# NOVEL WIRELESS RF-BIOMEMS IMPLANT SENSORS OF METAMATERIALS

A THESIS SUBMITTED TO
THE DEPARTMENT OF ELECTRICAL AND ELECTRONICS ENGINEERING
AND THE INSTITUTE OF ENGINEERING AND SCIENCES
OF BILKENT UNIVERSITY
IN PARTIAL FULLFILMENT OF THE REQUIREMENTS
FOR THE DEGREE OF
DOCTOR OF PHILOSOPHY

**By**

**Rohat Melik**

**August 2010**

I certify that I have read this thesis and that in my opinion it is fully adequate, in scope and in quality, as a dissertation for the degree of doctor of philosophy.

Assoc. Prof. Dr. Hilmi Volkan Demir (Supervisor)

I certify that I have read this thesis and that in my opinion it is fully adequate, in scope and in quality, as a dissertation for the degree of doctor of philosophy.

Prof. Dr. Ergin Atalar

I certify that I have read this thesis and that in my opinion it is fully adequate, in scope and in quality, as a dissertation for the degree of doctor of philosophy.

Prof. Dr. Ayhan Altıntaş

I certify that I have read this thesis and that in my opinion it is fully adequate, in scope and in quality, as a dissertation for the degree of doctor of philosophy.

Assoc. Prof. Dr. M. Özgür Oktel

I certify that I have read this thesis and that in my opinion it is fully adequate, in scope and in quality, as a dissertation for the degree of doctor of philosophy.

Prof. Dr. Birsen Saka

Approved for the Institute of Engineering and Science:

Prof. Dr. Levent Onural
Director of the Institute of Engineering and Science

# ABSTRACT

# NOVEL WIRELESS RF-BIOMEMS IMPLANT SENSORS OF METAMATERIALS

Rohat Melik

PhD in Electrical and Electronics Engineering

Supervisor: Assoc. Prof. Dr. Hilmi Volkan Demir

August 2010

Today approximately one out of ten patients with a major bone fracture does not heal properly because of the inability to monitor fracture healing. Standard radiography is not capable of discriminating whether bone healing is occurring normally or aberrantly. To solve this problem, we proposed and developed a new enabling technology of implantable wireless sensors that monitor mechanical strain on implanted hardware telemetrically in real time outside the body. This is intended to provide clinicians with a powerful capability to asses fracture healing following the surgical treatment. Here we present the proof-of-concept *in vitro* and *ex vivo* demonstrations of bio-compatible radio-frequency (RF) micro-electro-mechanical system (MEMS) strain sensors for wireless strain sensing to monitor healing process. The operating frequency of these sensors shifts under mechanical loading; this shift is related to the surface strain of the implantable test material. In this thesis, for the first time, we developed and demonstrated a new class of bio-implant metamaterial-based wireless strain sensors that make use of their unique structural advantages in sensing, opening up important directions for the applications of metamaterials. These custom-design metamaterials exhibit better performance in remote sensing than traditional RF structures (e.g., spiral coils). Despite their small size, these meta-sensors feature a low enough operating frequency to avoid otherwise strong background absorption of soft tissue and yet yield higher Q-factors (because of their splits with high electric field density) compared to the spiral structures. We also designed and fabricated flexible metamaterial sensors to exhibit a high level of linearity, which can also conveniently be used on non-flat surfaces. Innovating on the idea of integrating metamaterials, we proposed and implemented a novel architecture of ‘nested metamaterials’ that incorporate multiple split ring

resonators integrated into a compact nested structure to measure strain telemetrically over a thick body of soft tissue. We experimentally verified that this nested metamaterial architecture outperforms classical metamaterial structures in telemetric strain sensing. As a scientific breakthrough, by employing our nested metamaterial design, we succeeded in reducing the electrical length of the sensor chip down to $\lambda_o/400$ and achieved telemetric operation across thick soft tissue with a tissue thickness up to 20 cm, while using only sub-cm implantable chip size (compatible with typical orthopaedic trauma implants and instruments). As a result, with nested metamaterials, we successfully demonstrated wireless strain sensing on sheep's fractured metatarsal and femur using our sensors integrated on stainless steel fixation plates and on sheep's spine using directly attached sensors in animal models. This depth of wireless sensing has proved to suffice for a vast portfolio of bone fracture (including spine) and trauma care applications in body, as also supported by ongoing *in vivo* experiments in live animal models in collaboration with biomechanical and medical doctors. Herein, for all generations of our RF-bioMEMS implant sensors, this dissertation presents a thorough documentation of the device conception, design, modeling, fabrication, device characterization, and system testing and analyses. This thesis work paves the way for "smart" orthopaedic trauma implants, and enables further possible innovations for future healthcare.

*Keywords:* metamaterials, nested metamaterial, split ring resonators; microwave resonators; bioMEMS sensors, RF-MEMS; telemetry, remote sensing; mechanical loading, strain; sensitivity, linearity, resonance frequency, quality factor (Q-factor), frequency shift; bio-implant, biocompatibility.

# ÖZET

# METAMALZEME ÖZGÜN KABLOSUZ RF-BİYOMEMS İMPLANT SENSÖRLER

Rohat Melik
Elektrik ve Elektronik Mühendisliği Doktora
Tez Yöneticisi: Doçent Dr. Hilmi Volkan Demir
Agustos 2010

Günümüzde kemik kırıklarının iyileşmesi takip edilemediğinden dolayı büyük kemik kırığı olan yaklaşık on hastadan biri düzgün bir şekilde iyileşmemektedir. Standart radyografi kemiğin iyileşmesinin normal mi anormal mi geliştiğini ayıramamaktadır. Bu problemi çözmek için, implant donanımın üzerindeki mekanik gerinimi vücut dışından kablosuz olarak gerçek zamanlı ölçmeye imkân veren vücut içerisine yerleştirebilecek yenilikçi sensör teknolojisini önerdik ve geliştirdik. Bu, cerrahi tedaviden sonra doktorların güçlü bir kapasiteyle kırığın iyileşmesini değerlendirmesini sağlayacak güçlü bir yeti sunar. Burada kırıkların iyileşmesini takip etmek için gerinimi kablosuz olarak algılayan biyo-uyumlu radyo frekansı (RF) mikro-elektro-mekanik sistem (MEMS) gerinim sensörlerini laboratuar ve ölü hayvan modeli ortamında gösteriyoruz. Bu sensörlerin çalışma frekansı mekanik yükleme altında kayar; bu kayma implant olabilecek test malzemesinin yüzey gerinimi ile bağlantılıdır. Bu tezde, algılamadaki kendine has yapısal avantajlarından faydalanan kablosuz yeni bir sınıf metamalzeme-tabanlı biyo-implant sensörleri ilk kez geliştirdik ve kullandık; bu metamalzeme kullanımıyla ilgili yeni yönler açtı. Bu özel tasarım metamalzemeler, geleneksel RF yapılarına (spiral bobinler) göre daha iyi kablosuz algılama sergilerler. Küçük boyutlarına rağmen, bu meta-sensörler yeterince düşük çalışma frekansı göstererek yumuşak dokunun aksi taktirde güçlü soğurmasından sakınır ve yine de spiral yapılara göre yarıklarında çok yüksek elektrik alan yoğunluğu olduğu için daha yüksek kalite faktörü gösterir. Ayrıca yüksek düzeyde doğrusallık gösteren ve ayrıca düz olmayan yüzeylere elverişli biçimde kullanılabilen esnek tabanlı metamalzeme sensörlerini tasarlayıp ürettik. Kalın yumuşak doku üzerinden gerinimi kablosuz ölçmek için metamalzemeleri birleştirme fikrine

dayanan bir buluşla çok çatallı halka rezonatörlerini kompakt bir yapıda toplayan özgün içiçe metamalzeme yapısını önerdik ve gerçekleştirdik. Bu içiçe metamalzeme mimarinin kablosuz gerinimi algılamada klasik metamalzemelerden daha iyi çalıştığını deneysel olarak kanıtladık. Büyük bir bilimsel ilerleme olarak, içiçe metamalzeme tasarımlarımızı kullanarak sensörün elektriksel boyunu $\lambda_o/400$'e kadar düşürmeyi başardık ve sadece cm-altı implant olabilecek (tipik ortopedik travma implantları ve enstrumanları ile uyumlu) çip boyutuyla 20 cm kalınlığa kadar yumuşak doku içinden kablosuz ölçümü başardık. Sonuç olarak, içiçe metamalzemelerle sensörlerimizi koyunun metatarsal ve femurunda paslanmaz çelik sabitleme plakası ile bütünleşmiş biçimde kullanarak ve koyunun omuriliğinde de hayvan modeline doğrudan tutturarak kablosuz gerinim algılamasını başarılı biçimde gösterdik. Bu kablosuz algılamada derinliği, biyomekanik ve tıp doktoru olan ortaklarımızla birlikte devam eden canlı hayvan modelleri deneylerince de desteklendiği üzere, vücuttaki kemik (omuririlik dahil) kırık ve travma uygulamalarında geniş bir portföy için yeterli olmuştur. Burada, bu doktora tezi RF-biyoMEMS implant sensörlerin farklı nesillerini tümüyle aygıt kavramından, tasarım, modelleme, üretim, aygıt karakterizasyonu, sistem testi ve analizine kadar her aşamayı dökümente etmektedir. Bu tez akıllı ortopedik travma implantları için kaldırım taşları döşemekte, gelecekte sağlık için muhtemel yeni buluşlara olanak sağlamaktadır.

*Anahtar Sözcükler:* metamalzeme, içiçe metamalzeme, çatallı halka rezonatörleri; mikrodalga rezonatörleri; biyoMEMS sensörleri, RF-MEMS; uzaktan algılama; mekanik yükleme, gerinim; hassaslık, doğrusallık, rezonans frekansı, kalite faktörü (Q-factor), frekans kayması; biyo-implant, biyo uyumluluk.

# Acknowledgements

I would first like to thank Prof. Hilmi Volkan Demir for his endless support during my PhD study. A phone call may change a person's life. After receiving my BS degree at METU Electrical and Electronics Engineering Department, I wanted to work as a research assistant since I wanted to pursue an academician career. When nobody gave me a chance of becoming an academician, he did. He gave me a call and took me as his research assistant. During my PhD, I have never forgotten his favor any time and I will never forget this in the future. I will be thankful to him in my whole life. He gave me the chance of becoming a scientist, supported and nurtured me scientifically, gave me the chance to show my potential and changed my life.

I would like to thank Prof. Ergin Atalar for his support, for discussions during the project and for giving useful comments and suggestions as being a member of my thesis committee. I also want to thank Prof. Ayhan Altıntaş, Prof. Özgür Oktel and Prof. Birsen Saka for their useful comments and suggestions as members of my thesis committee.

During the course of this work at Bilkent University (2005-2010), I was supported by the TÜBİTAK National Scholarship Programme-2211 for PhD Students for which I owe special thanks. This work is supported by TÜBA-GEBİP, ESF-EURYI, and TÜBİTAK EEEAG 105E066, 105E065, 106E020, 107E088, 107E297, 109E002, and 109E004, and EU MOON 021391. This work is also supported by a subcontract from the United States National Institutes of Health (NIH) 5R01EB010035.

I would like to thank my dear friend, my project teammate Emre Unal. I would like to give him my special thanks. Long days and nights, we worked together and these moments are special moments for me. He has made a great contribution to this project. His dynamism and talent were very important for the project. I would like to thank Dr. Nihan Kosku Perkgoz for her help during my thesis, especially in the writing of our articles. I would like to thank Dr. Zeynep Dilli who helped me a lot especially in the first stages of the project technically and during writing the

articles. I also would like thank Prof. Christian Puttlitz for supervising biocompatibility studies and *ex-vivo* experiments.

I would like to give my deepest thanks to my wife Bahar. She always supported me, she always gave me confidence and she always trusted me. She brings me luck, after our meeting, my work all went well. She gave me her endless love, supported me and showed patience during preparation of my thesis defense.

I would like to thank my family members, my mother Senay and my brother Serhat. From my childhood and on, they always gave me their endless support. They are very special for me. Without their endless support and patience towards me, I would not be able to achieve my goals. I also would like to thank my uncle Sedat, who gave endless support to my family and me since my teenage. I also want to thank Bahar's parents Mehmet Ali and Vecihe, and her sisters, Ruşa, Dılşa, Dilan, and Nazvan for always being kind to me and sharing their valuable child and sister with me.

Our office was like a family and my office mates are like my family members. Tuncay Özel has always been like a brother and helped me as I am his elder brother. Evren Mutlugün has also been like a brother and always make me happy when I feel sad. İlkem Özge Özel, Tuncay's wife, has been like a niece and helped me all the time during my thesis work. I want to thank Evren's wife, Sümeyye, and Tuncay's wife, Özge, for making my friends very happy. I want to thank Sedat Nizamoğlu, who is always very kind and positive, and I also want to thank Özgür Çakmak, who is always positive and made discussions with me during my research and helped me for training.

I would like to thank Dr. Aşkın Kocabaş for his endless help and support during my PhD work. I also would like to thank Prof. Coşkun Kocabaş for his help during my PhD. I would like to thank my friend Bawer Okutmuştur, who helped me with everything especially in the first year, and I also want to thank my dear friends Mustafa Durukal and Erdinç Ircı, who gave me endless support during all my PhD study. I want to thank my friends Onur Taşçı, Mehrdad Atabak,

Özhan Ünverdi, and Haydar Çelik for their positive and helpful attitude towards me. I want to give my special thanks to my young teammates Sayım Gökyar, and Hatice Ertuğrul, who have always run for my help when I needed. I want to thank Mustafa Yorulmaz for his assistance in using Coventorware, and Prof. Aykutlu Dana and Ergün Karaman for their help in the construction of our experimental setup.

I would like to thank all former and recent group members of Devices and Sensors Group, who work under the supervision of Dr. Hilmi Volkan Demir. I would like to thank Özgün Akyüz, Aslı Yılmaz, Neslihan Çiçek, Gülis Zengin, Emre Sarı, Can Uran, Gürkan Polat, Akın Sefünç, Onur Akın, Olga Samarska, Sina Toru, Talha Erdem, Burak Güzeltürk, Veli Tayfun Kılıç, Kıvanç Güngör, Uğur Karatay, Urartu Şeker, Cüneyt Eroğlu, İrfan Bulu, Bora Alıcı, Yaşar Kemal Alp, Salih Kılıç, Evrim Çolak, Makbule Pehlivan, Murat Güre, Ergün Hırlakoğlu, Engin Zeydan, Halis Yerlikaya, Hikmettin Demir, Şerafettin Ay, Mehmet Paydaş, Faruk Aydoğdu, Ünal Deniz, Ömer Faruk Yekdeş, Mehmet Melik, Hasan Yeter, and many other friends helped to keep my spirits high all the time which I appreciate very much.

Finally, I dedicate this dissertation to my father, Muhsin…

# Table of Contents

# List of Figures

# List of Tables

*To my father…*

# Chapter 1

# Introduction

The ability to telemetrically measure strain is important in many aspects of daily life. However, such a task brings about important scientific and technological challenges. In many sectors such as in civil engineering, measuring the strength of materials (e.g., concrete) remotely in real time will help us understand their transient structural behavior better (e.g., before and after an earthquake). Similarly, real-time measurement of the flexural rigidity of aircraft components during service in avionics is also an important application of telemetric strain sensing. Another unrealized, yet critical, application area is human medicine and healthcare.

One important clinical issue in which we are currently interested is objectively monitoring the healing processes of fractured long bones [1]. Orthopaedic extremity injuries currently present a large medical and financial burden around the globe as can be seen for the United States in [2]. Severely comminuted fracture patterns, those commonly seen in high energy fractures, are difficult to treat due to the inherent absence of mechanical support through the native osseous tissue. In these cases, the implanted hardware (intramedullary rods, bone plates, screws, etc.) must assume the total mechanical load in the early post-operative term, which frequently results

in an aberrant course of healing and the onset of delayed union or non-union. The most common treatment for these complications is additional surgery. These types of orthopaedic injuries require prolonged time before patients return to full activity [3].

Approximately six million long bone fractures are reported per annum in the United States. Surprisingly, approximately 10% of these fractures do not heal properly. Though the exact mechanism through which the healing progression becomes impaired is poorly understood, many of these non-unions or pseudoarthroses result when there is a severe or communited condition that does not proceed through a stabilized (intramembranous ossification) healing pathway [4]. Currently, clinicians may monitor healing visually by radiographs, and may examine the mechanical condition of the union through manually bending the bone at the fracture [5]. Unfortunately, the course of aberrant fracture healing is not easily diagnosed in the early time period when standard radiographic information of the fracture site is not capable of discriminating the healing pathway. Reference 6 shows us that manual assessment of fracture healing is also subjective and, therefore, inadequate as a diagnostic tool in the early stages of healing.

It has been shown in animal models that healing is critically important in the early time period. Animal studies have demonstrated that the callus and bone assume an increasing proportion of the load as healing proceeds, reducing the load carried by the implanted hardware [1]. However, to date, many of the technologies that seek to exploit this bone-implant load sharing phenomena have been considered too large in dimension or involve implantation of an associated power supply. Previous investigations have been successful in determining forces in the hip [7]-[9], spine [10]-[12], and femur [13], [14]. However, due to the relatively large size of the sensors and associated hardware (signal conditioning, modulation, etc.), most of the aforementioned telemetry systems have been implanted inside of joint replacement components or bulky internal fixators. The result is that these devices have produced data that has been useful in the understanding of bone-implant loading, but have not been advantageous for large-scale implementation as diagnostic and prognostic tools. Also, due to the complexity of the designs and requisite interconnectivity, manufacture of these systems could only be performed on a

custom basis. The resulting expense could not justify their large-scale production.

To overcome the aforementioned shortcomings, we have developed wireless radio frequency (RF) micro-electro-mechanical (MEMS) strain sensors. By using such a remote sensor, it is expected that a continuous healing profile of an individual patient can be recorded during the activities of daily life.

We present a bio-MEMS strain sensor for implantation using a RF-MEMS approach. The operating principle is based on a concomitant operating frequency shift with mechanical deformation. We aim to sense biological data and transfer it effectively to an antenna outside the body. To interpret the biological data, the input is denoted by the physical load (F), and the output is denoted by the operating frequency readout ($f_0$). As the load is applied to the stainless steel plate, it deforms (strains) under the applied stress [1]. Eventually this strain decreases (due to the temporal shift in the load distribution) and modifies the operating frequency, thus allowing for real-time observation of the healing process in the fracture. Therefore, with the sensor chip we propose and demonstrate, it is possible to measure the change in the strain and hence to assess the healing process by means of this operating frequency shift. This $f_0$ shift results primarily from the change in the capacitance of the film between the metal and the substrate because of the modified area with the applied force.

In healthcare applications, we are typically constrained with the limited area of the sensors. In order to miniaturize the sensors, we first developed high Q-factor wired on-chip resonator in Chapter 2. We used this resonator concept throughout the thesis, and designed, and fabricated our wireless sensors based-on this concept at subsequent stages. We showed high Q-factor on-chip resonators operating at 7 GHz and at 15 GHz in this chapter.

In Chapter 3, we subsequently applied mechanical load to these on-chip resonators and observed the shift of their resonance frequency in response to mechanical deformation. We developed and demonstrated first accounts of the sensing mechanism in this chapter. We then developed

circular geometry and later suspended architecture and increased the performance of the sensors in both approaches. We also examined the triplet idea in detail in this chapter.

In Chapter 4, we showed the proof of concept demonstration of fully telemetric sensing using spiral RF coil architecture. In this chapter, we studied single type, array type, hybrid array type, and multi turn type of spiral sensors. We experimentally showed the importance of sensitivity, Q-factor and linearity for sensing operation, and discussed approaches to increase sensitivity, Q-factor and linearity.

In Chapter 5, we proposed and developed wireless strain sensing using metamaterials for the first time. We discovered a very promising new application area for metamaterials, one in which metamaterials offer unique benefits compared to conventional RF coils. We showed wireless strain sensing with silicon-based and vacuum tape-based flexible sensors. We also showed wireless strain sensing for different industrial testing materials and examined important design parameters of metamaterials in wireless strain sensing.

In Chapter 6, we introduced our novel structure, nested metamaterials, and demonstrated wireless strain sensing with these nested metamaterials. We also discussed metamaterial related RF expertise developed in this thesis in this chapter. We experimentally achieved the wireless strain sensing at 100 MHz using 0.8 cm sensor with different thicknesses of soft tissue and demonstrated *ex vivo* strain sensing in sheep's metatarsal, femur and spine telemetrically.

In Chapter 7, we finally conclude the thesis with a summary of our achievements and future prospects.

# Chapter 2

# High Quality-Factor On-Chip Resonators

In this chapter, we will examine the concept of high Q-factor on-chip resonators, and present design, implementation and experimental characterization for operation at 7 GHz and at 15 GHz.

## 2.1 Implementation of High Quality-Factor On-Chip Tuned Microwave Resonators at 7 GHz

This section is based on the publication "Implementation of High Quality-Factor On-Chip Tuned Microwave Resonators at 7 GHz" **R. Melik** and H.V. Demir, *Microwave and Optical Technology Letters 51, 497-501 (2009).* Reproduced (or 'Reproduced in part') with permission from Wiley Periodicals, Inc. Copyright 2008 Wiley Periodicals, Inc.

In this section [15], we report on the design, analytical modeling, numerical simulation, fabrication, and experimental characterization of chip-scale microwave resonators that exhibit high quality-factors in the microwave frequency range (at 7 GHz). We demonstrate high quality-

factors by tuning these microwave resonators with the film capacitance of their LC tank circuits rather than the conventional approach of using external capacitors for tuning. Our chip-scale resonator design further minimizes energy losses and reduces the effect of skin depth leading to high quality factors even for significantly reduced device areas. Using our new design methodology, we observe that despite the higher resonance frequency and smaller chip size, the quality-factor is improved compared to the previous literature using traditional approaches. For our 540 μm× 540 μm resonator chip, we theoretically compute a quality -factor of 52.40 at the calculated resonance frequency of 6.70 GHz and experimentally demonstrate a quality-factor of 47.10 at the measured resonance frequency of 6.97 GHz. We thus achieve optimal design for on-chip microwave resonators with the highest quality-factor in the smallest space for operation at 6.97 GHz.

## 2.1.1 Introduction

High quality-factor (Q-factor) resonators are required for good performance in applications such as microwave devices, mobile phones, radars, wireless universal serial buses (USB), and wireless local area networks (WLAN). In such applications, on-chip resonators are preferred because they reduce power consumption, prevent connection losses, and facilitate on-chip integration. These lead to compact, low-cost systems. However, it is difficult to produce chip-scale, small-size resonators that exhibit high Q-factors at high frequencies. In general, smaller resonators yield lower Q-factors. To date, microwave resonators based on on-chip spiral coils have been successfully demonstrated, with unloaded Q-factors of inductors up to a maximum of 40 at 5 GHz [16] and 50 at 2 GHz [17]. In these studies, to realize resonators using inductors, external capacitors are used to tune the inductors, which undesirably increase the effective device area and decrease the resonator Q-factor. The use of such an externally connected capacitor further results in longer propagation times and fewer operating channels for communication. Also, it has been shown that higher Q-factors can be achieved using cavity geometries. But, this also comes at the cost of significantly increased size, resulting in much larger chips (as long as several millimeters on one side) [18] and in more complicated fabrication steps. Therefore, these are not

ideal methods to obtain a compact and high Q-factor microwave resonator operating at a high frequency. In addition, there is a strong demand for bio-implant resonators in medical applications that would satisfy the bio-compatibility constraints [19], which is the focus of this thesis work here. Therefore, herein with the motivation to address the need for compact high-Q bio-implantable microwave resonators, we develop and demonstrate on-chip bio-compatible resonators with high Q-factors of about 50 in the microwave frequency range, despite their chip-scale, small size (sub-millimeter on one side).

In the literature, Q-factors are typically stated in unloaded cases, excluding the external loading effects [20]-[21]. In this section, we report the measured Q-factors including the loading effects and the associated losses instead of merely citing unloaded Q-factors. Thus, we present the worst case Q-factor values, with the probe loading and related losses all included. Furthermore, we implement the resonator aiming for a minimal device size while operating with a high Q-factor at a high frequency. To do so, we develop a new design methodology that reduces the effect of skin depth in attaining high Q-factors. In our device, although the metal layer is very thin, we can achieve high Q-factors because of our new design approach. The area of our microwave resonator is demonstrated to be as small as 540 μm × 540 μm while the Q-factor is still kept high at 47.10, which is not possible with previous approaches in the literature.

The resonator architecture is based on a spiral coil structure with a few turns tuned with the on-chip capacitance to obtain the highest Q-factor from the smallest lateral chip size. This approach relies on minimizing energy losses in the coil and also on using the film capacitance for tuning. We develop a two-port circuit model design for our on-chip coil. We support our analytical model with numerical simulations. Our analytical model obtains targeted resonance frequencies that are very close to the resonance frequencies we obtained with numerical simulations and those that are later measured experimentally on our fabricated chips.

Although we implement our resonator chips using a standard micro-electro-mechanical-systems (MEMS) fabrication procedure, we design them to be compatible with complementary metal oxide semiconductor (CMOS) processing, while also using only bio-compatible materials. Our

resonators are of a size (a half millimeter by a half millimeter with 100 nm thick metal lines) to possibly be fabricated in large quantities, at a low per-unit cost, by standard CMOS processes and conveniently be integrated on-chip with CMOS electronics.

In subsequent sections, we present the design, analytical modeling, numerical simulation, fabrication, and experimental characterization of such compact high-$Q$ microwave resonators. The rest of this section is organized accordingly as follows. We first present the theoretical background in Section 2.1.2, then describe the microfabrication of our on-chip resonators and their experimental characterization along with our theoretical analysis in Section 2.1.3, and finally summarize in Section 2.1.4.

## 2.1.2 Theoretical Background

We develop our circuit model for a spiral coil starting with the circuit model of a general transmission line [22]. We consider the coil as being composed of many transmission line segments in serial connection [23]. For each of these transmission lines, with half of their capacitance terminated both at the beginning and the end of each segment, we put together all of these transmission line segments and include the admittance to ground through the dielectric capacitance and substrate to construct the coil [24]. For further simplification, we convert this coil model into a conventional circuit that matches the coil structure. The circuit conversion is illustrated step by step from Fig. 2.1.1(a) to Fig. 2.1.1(c). In the literature, one of the ports is commonly taken as ground especially for the analysis of the measured S parameters, which significantly simplifies the analysis [25]. In our case, we produce the final circuit model using two ports as shown in Fig. 2.1.1(d). We perform all of our analytical modeling and simulations as well as our designs based on this final two-port circuit model representation. The standard way of calculating a resonator Q-factor is based on measuring the 3-dB bandwidth ratio of $S_{21}$ magnitude [26], which is different from calculating an inductor Q-factor by measuring reflectivity after grounding one port of the circuit.

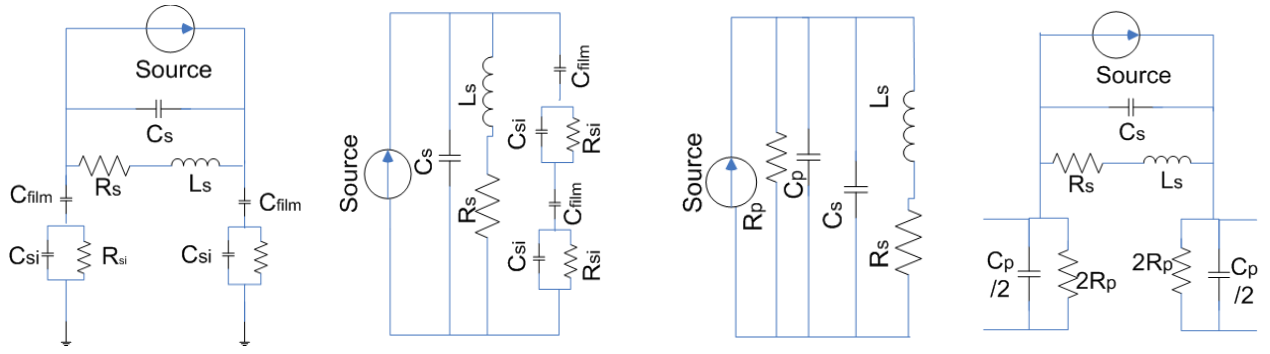


(a) (b) (c) (d)

**Figure 2.1.1. Our circuit model conversion: We first consider a source driving the conventional circuit of the coil with two ports in (a), then consider one of these ports to be grounded in (b), from which we obtain the common representation of a parallel RLC circuit in (c). Unlike other approaches, here we expand this model further into a simple two-port circuit representation in (d) to be used for all of our analytical simulations.**

To calculate the circuit components for the coil model, we use the equations listed together for convenience in Table 2.1.1. These equations relate our structural design parameters to the circuit components of our coil resonator (and thus to the resonator specifications). Our on-chip microwave resonator consists of metal layers (Au) that make up the spiral coil structure and the insulator layers ($Si_3N_4$) that isolate the metal layers from each other and the substrate (Si). In our circuit model, $L_S$ is the inductance of the spiral coil; $C_{film}$ is the capacitance of the dielectric thin film between the coil and the substrate; $C_{Si}$ is the capacitance from the coil trace to the substrate for a half turn; $C_S$ is the capacitance between adjacent coil segments; $R_{Si}$ is the resistance of the substrate; and $R_S$ is the resistance of the spiral coil. Additionally, in Table 2.1.1, in the inductance equation (2.1.1), $L_{self}$ is the self-inductance, $M^+$ and $M^-$ are the positive and negative mutual inductance, respectively; and in the coil resistance equation (2.1.6), $\delta$ is the skin depth. Moreover, device design parameters used in these equations include the total length of the spiral coil ($l$), the metal width ($w$), the separation between metal lines ($s$), the dielectric thin film thickness ($t_{film}$), the coil metal thickness ($t$), the total length and width of the resonator chip ($L_C$ and $W_C$), and the number of turns ($N$).

**Table 2.1.1. List of empirical equations used to calculate circuit components from design parameters.**

$$L_S = |L_{self}| + |M^+| - |M^-| \tag{2.1.1}$$

$$C_{film} = \frac{\varepsilon_o \varepsilon_r lw}{t_{film}} \tag{2.1.2}$$

$$C_{Si} = 0.5 lwC_{sub}, \text{where } C_{sub} = 1.6\times10^{-10}\,\frac{\text{F}}{\text{cm}^2} \tag{2.1.3}$$

$$C_S = \frac{\varepsilon_0 lt}{s} \tag{2.1.4}$$

$$R_{Si} = \frac{2}{lwG_{sub}}, \text{where } G_{sub} = 0.4\,\frac{1}{\Omega\text{cm}^2} \tag{2.1.5}$$

$$R_S = \frac{\rho l}{w\delta \times \left(1 - e^{\frac{t}{\delta}}\right)} \tag{2.1.6}$$

$$\delta = \sqrt{\frac{2\rho}{\omega\mu_0}}, \text{where } \omega = 2\pi f \tag{2.1.7}$$

$$R_P = \frac{1}{\omega^2 {C_{film}}^2 R_{Si}} + \frac{R_{Si}(C_{film} + C_{Si})^2}{{C_{film}}^2} \tag{2.1.8}$$

$$C_P = C_{film}\,\frac{1 + \omega^2 (C_{film} + C_{Si}) C_{Si} {R_{Si}}^2}{1 + \omega^2 (C_{film} + C_{Si})^2 {R_{Si}}^2} \tag{2.1.9}$$

$$Q_{ind} = \frac{\omega L_S}{R_S} \times \frac{2R_P}{2R_P + \left[\left(\frac{\omega L_S}{R_S}\right)^2 + 1\right] R_S} \times \left[1 - \frac{{R_S}^2\left(\frac{C_P}{2} + C_S\right)}{L_S} - \omega^2 L_S \left(\frac{C_P}{2} + C_S\right)\right] \tag{2.1.10}$$

$$f_0 = \frac{1}{2\pi\sqrt{LC}} \tag{2.1.11}$$

$$Q = \frac{f_0}{\Delta f} \tag{2.1.12}$$

In Table 2.1.1, the inductance parameters $L_S$, $L_{self}$, $M^+$, and $M^-$ are calculated following [27]. For calculating $C_{Si}$ and $R_{Si}$, experimental characterization results are used in the method given in Lee [28]. For $R_P$ and $C_P$, the relations in Bahl [19] are utilized. We obtain $R_P$ and $C_P$ through the circuit conversion from Fig. 2.1.1(b) to Fig. 2.1.1(c). Here $R_P$ and $C_P$ represent the combined impedances of $R_{Si}$, $C_{Si}$, and $C_{film}$. $R_P$ is particularly important for the computation of substrate losses and $C_P$ is significant for the resonance frequency and the self-resonance factor.

Our design guidelines rely on the objective of maximizing Q-factor of our on-chip microwave resonators. Thus, the Q-factor definition is important. The quality-factor of a resonator is defined in the most general sense in (2.1.13) [29]:

$$Q = 2\pi \frac{\text{energy stored}}{\text{energy loss in one oscillation cycle}} \tag{2.1.13}$$

The empirical form of this Q-factor definition is presented in (2.1.12) in Table 2.1.1. However, this equation does not identify the lumped elements that store energy and those that dissipate energy. Therefore, it does not provide guidance on how to increase the Q-factor. For that reason, in our design methodology, we utilize the definition of the Q-factor of the inductor (rather than the entire $LC$ tank circuit of the resonator). We can obtain the resonator quality factor using both the inductor quality factor ($Q_{ind}$) and capacitor quality factor ($Q_c$) as given in Ludwig and Bretchko [26]: $\frac{1}{Q_{res}} = \frac{1}{Q_{ind}} + \frac{1}{Q_c}$. Structural design and material selection does not affect $Q_c$ very much. However, $Q_{ind}$ is directly affected by geometrical design and the material selection. As a result, we can maximize the resonator Q-factor by using the classical resonance definition and the methods to increase $Q_{ind}$. The inductor Q-factor is given by (2.1.14) and (2.1.15) [30].

$$Q_{ind} = 2\pi \frac{\text{peak magnetic energy} - \text{peak electric energy}}{\text{energy loss in one oscillation cycle}} \tag{2.1.14}$$

$$Q_{ind} = \frac{R}{\omega L}\left[1 - \left(\frac{\omega}{\omega_o}\right)^2\right] \tag{2.1.15}$$

The open form of this equation is presented in (2.1.10) in Table 2.1.1, which explicitly shows the design factors that affect the inductor Q-factor (i.e., the elements that store energy and those that dissipate energy). As shown in (2.1.14) and (2.1.15), $Q_{ind}$ is proportional to the difference between peak magnetic energy and peak electric energy, and the resonance frequency is the one where these two energies are equal, i.e., where the inductor's Q-factor is zero. This is the point where the tank circuit has the minimum transmitted power. (2.1.11) of Table 2.1.1 gives the basic definition of the resonance frequency $f_0$, which corresponds to the point where $Q_{ind}$ is zero and alternatively to the point where the transmitted power is minimum. When using the

numerical or experimental data, we compute the resonance frequency from the point of minimum transmitted power. Since the device we fabricate is an on-chip resonator that does not require any tuning with an external capacitor, we calculate the Q-factor theoretically as given in (2.1.12) of Table 2.1.1.

## 2.1.3 Experimental Implementation, Characterization and Analysis

We design our devices to have a resonance frequency in the microwave frequency range in accordance with the criterion of maximum feasible Q-factor while maintaining the minimal size for targeted applications. To maximize the Q-factor of our microwave resonator we construct our design methodology based on maximizing the inductor's Q-factor. As discussed in Section 2.1.2, $Q_{ind}$ explicitly includes the effect of design parameters on resonance and identifies the energy loss and storage elements. Given these guidelines, we set the device parameters. Table 2.1.2 summarizes two of our designs to demonstrate the effect of different design parameters for comparison purposes.

**Table 2.1.2. Our device design parameters.**

| Design | $L_C$ (μm) | $W_C$ (μm) | $N$ | $w$ (μm) | $s$ (μm) | $t_{film}$ (μm) | $t$ (μm) |
|---|---|---|---|---|---|---|---|
| 1 | 540 | 540 | 2 | 100 | 10 | 0.1 | 0.1 |
| 2 | 520 | 520 | 2 | 100 | 5 | 0.1 | 0.1 |

We use silicon as substrate and Au as metal layer since they are bio-compatible (so that our resonator can be used as bio-MEMS sensors at future stages). We directly lay down the first metal layer used for contacts directly on the substrate to decrease substrate losses. We choose $Si_3N_4$ thin film, which is also bio-compatible while featuring a low loss tangent (as low as $5\times10^{-4}$) and a high dielectric constant (as high as 8) in the microwave frequency range. The

low loss tangent significantly decreases the loss, while the high dielectric constant increases the dielectric film capacitance. To increase the resonance frequency and $Q_{ind}$, and to make a compact resonator, we reduce the resonator chip area; $L_C$ and $W_C$ are thus as short as possible. By increasing the metal width ($w$), we decrease the sheet resistance and, hence, increase the Q-factor. An increase in the metal width with constant spacing between metal lines ($s$) increases the lateral area; we thus optimize the metal width and spacing, considering the Q-factor and compactness. The higher the metal spacing is, the lower the resonance frequency is. Generally, although smaller metal spacing increases $Q_{ind}$, one should also consider the effect of the ratio between $w$ and $s$. This ratio should not be too large; otherwise, the parasitic capacitance eventually decreases $Q_{ind}$. The first design with 10 µm spacing features higher $Q_{ind}$ since the $w/s$ ratio of the other device is too large and thus the parasitic capacitance decreases the Q-factor.

In Fig. 2.1.2, we show $Q_{ind}$ computed for both designs (with $s$ = 10 µm and $s$ = 5 µm). Here we observe that the maximum inductor quality-factor of the first design with $s$ = 10 µm is higher than that of the second one with $s$ = 5 µm. At resonance frequencies, their inductor quality-factors cross the zero line; the first design with $s$ = 10 µm has a resonance frequency of 6.70 GHz and the second design with $s$ = 5 µm has a resonance frequency of 7.00 GHz.

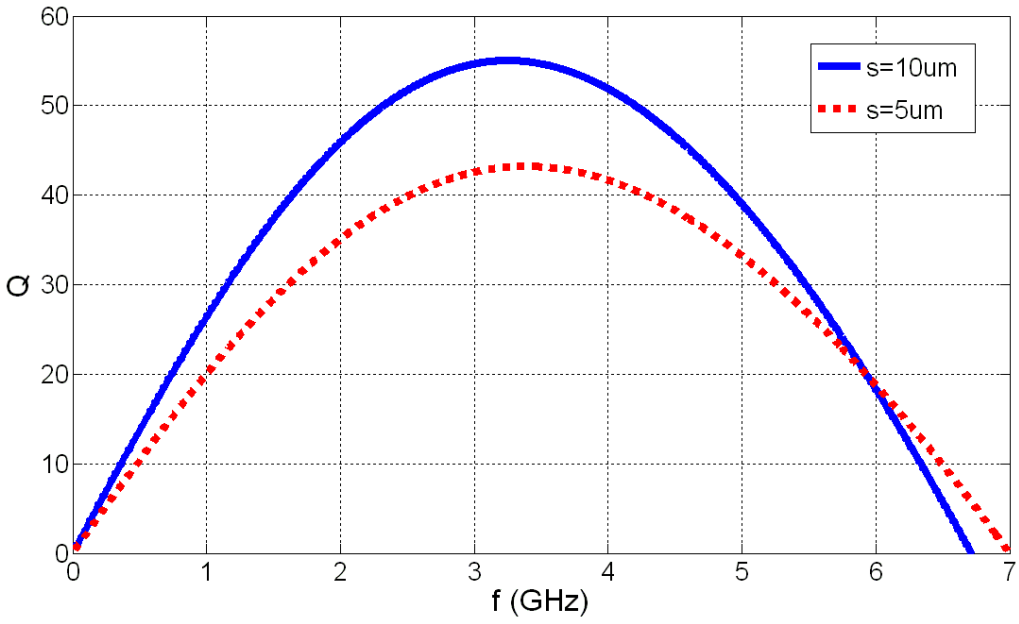


**Figure 2.1.2. $Q_{ind}$ computed for our designs with $s$ = 10 µm and $s$ = 5 µm.**

High-Q factor in our designs is achieved because we use the capacitance of the dielectric thin film between the coil and the substrate for on-chip tuning and obtain an all on-chip, small-size microwave resonator. In fact, because we use the high dielectric capacitor instead of an external capacitor, the spiral inductor is utilized the way that a cavity resonator would be. Thus we obtain a high Q-factor, comparable to the results of cavity resonator studies, but here without sacrificing the small chip area. Therefore, this study effectively combines two different approaches: The spiral inductor concept and cavity resonator design techniques. In addition, considering the factors that reduce the losses and enhance the Q-factor by a careful inspection each of the circuit parameters in Fig. 2.1.1(a), the losses are minimized and the Q-factor is maximized at a resonance frequency of 7 GHz. Also, if we further modify our resonator design to operate at even higher frequencies, the chip size becomes smaller and the Q-factor is enhanced because of our design methodology, which is again different from the traditional approaches.

The first step in the fabrication procedure includes standard lithography and liftoff directly on a Si substrate to lay down the first metal layer made of Au with a thickness of 0.1 μm. We then deposit a $Si_3N_4$ thin film using a plasma-enhanced chemical vapor deposition (PECVD) system; this film is 0.1 μm thick. To pattern the $Si_3N_4$ film, we perform a second lithography to open vertical interconnection areas using a wet etching process with HF (hydrofluoric acid). In the subsequent Au metallization step, we erect the interconnection layer. In the third lithography and Au metallization steps, we construct the top coil and contact pads and finally obtain our on-chip microwave resonator. Figure 2.1.3 summarizes our process flow to fabricate our devices and shows one of the fabricated devices. We characterize these fabricated devices using a vector network analyzer (HP8510C). We calibrate our setup using the ISS (impedance standard substrate). In our measurements, we take 801 points and perform 128-point averaging both in calibration and measurement.

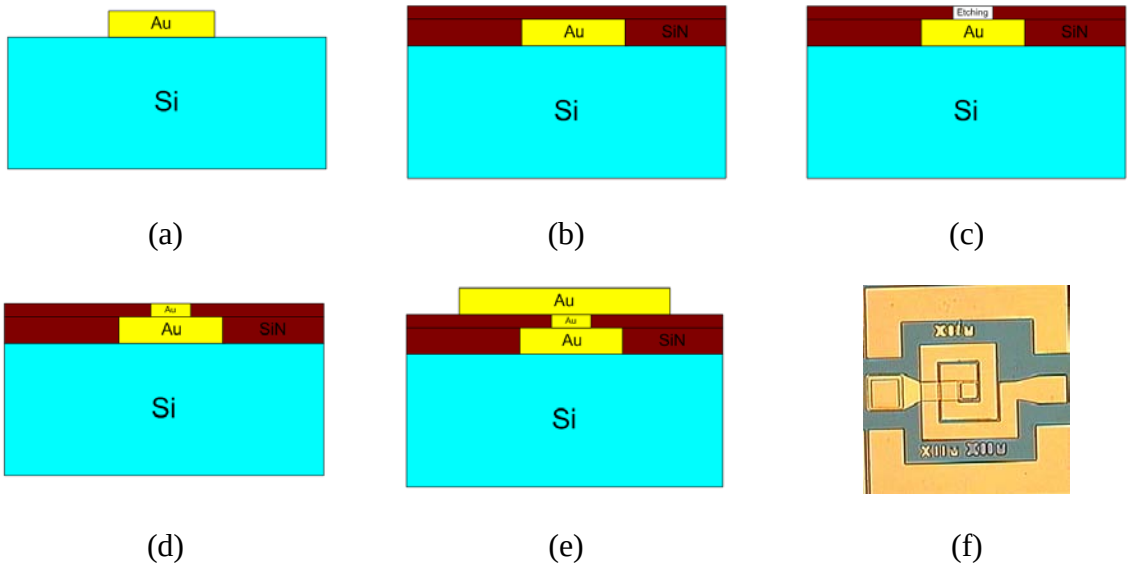


**Figure 2.1.3. The process flow for the microfabrication of our on-chip microwave resonators shown in cross-sectional view at the stages of (a) metallization on the substrate, (b) dielectric film coating, (c) film patterning (wet etching), (d) interconnect metallization, and (e) final top coil metallization, along with (f) a top-view micrograph of our fabricated device.**

Figures 2.1.4 and 2.1.5 show $S_{21}$ parameters (in dB) that are experimentally measured and numerically simulated (in CST Microwave Studio) together for our first and second designs ($s$ = 10 µm and 5 µm), respectively. We measure the Q-factors of the microwave resonators from the 3-dB bandwidth ratio of the $S_{21}$ magnitude by taking transmission measurements [26]. Therefore, we obtain the loaded Q-factor including the external effects, which is different from calculating the Q-factor of an inductor alone by measuring reflectivity after grounding one port of the circuit. We observe sharp dips in the transmitted power at the resonance frequencies both in Fig. 2.1.4 (a) and Fig. 2.1.5 (a). We measure the resonance frequencies (where $S_{21}$ is minimum) to be 6.97 GHz and 7.12 GHz for our first and second designs, respectively. These experimental results match very well with the theoretical values of 6.70 GHz and 7.00 GHz. Our theoretical and experimental results are summarized in Table 2.1.3.

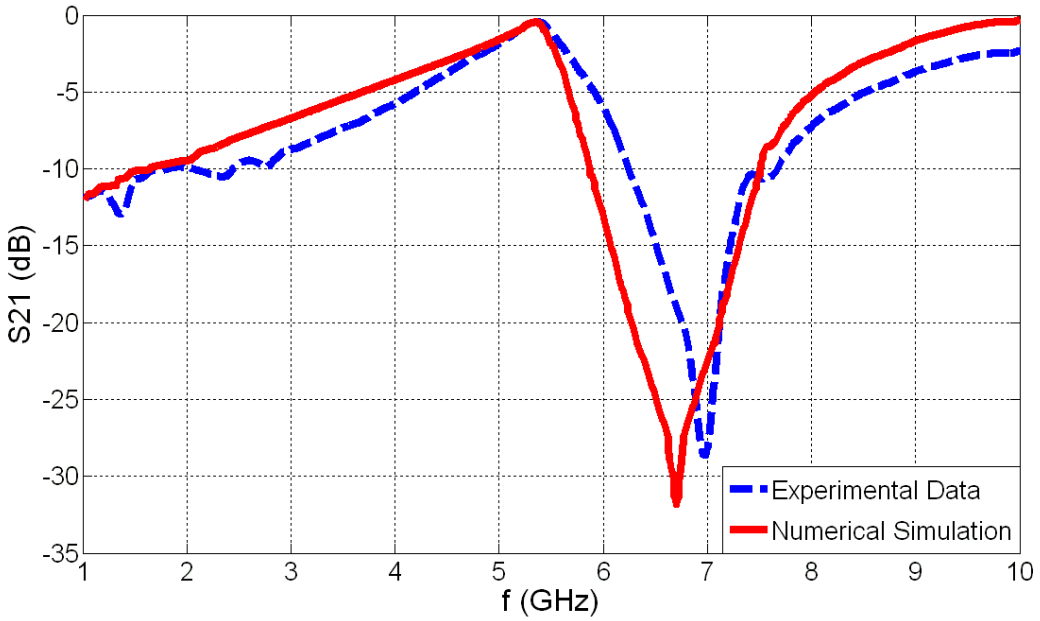


(a)

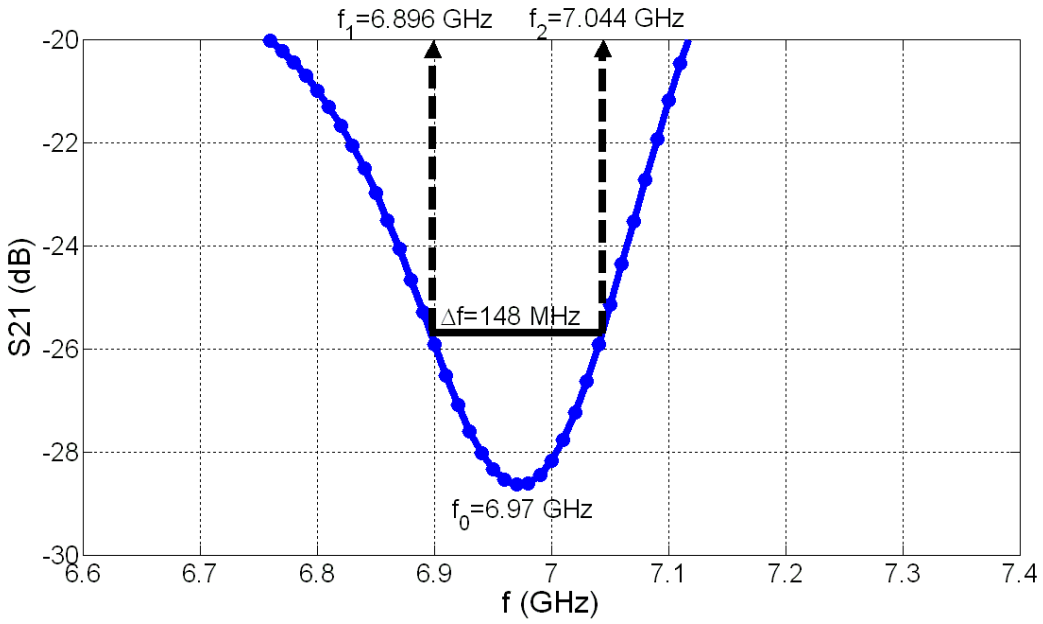


(b)

**Figure 2.1.4. For our first device, (a) experimental measurement and numerical simulation of $S_{21}$ parameter and (b) zoom-in experimental $S_{21}$ data to illustrate the resonance frequency $f_0$ and the 3-dB bandwidth $\Delta f$.**

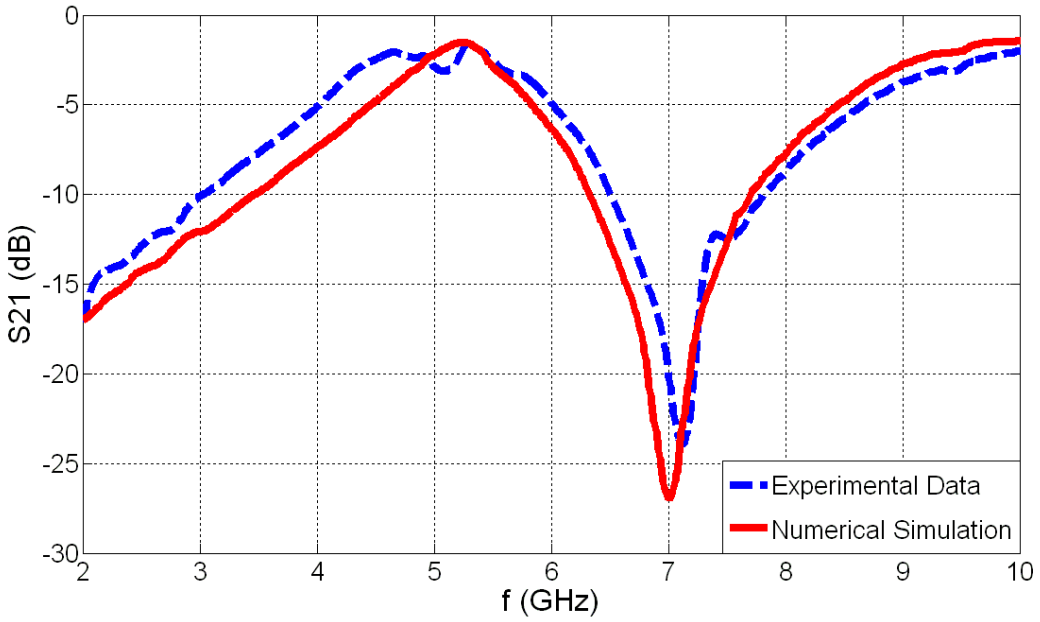


(a)

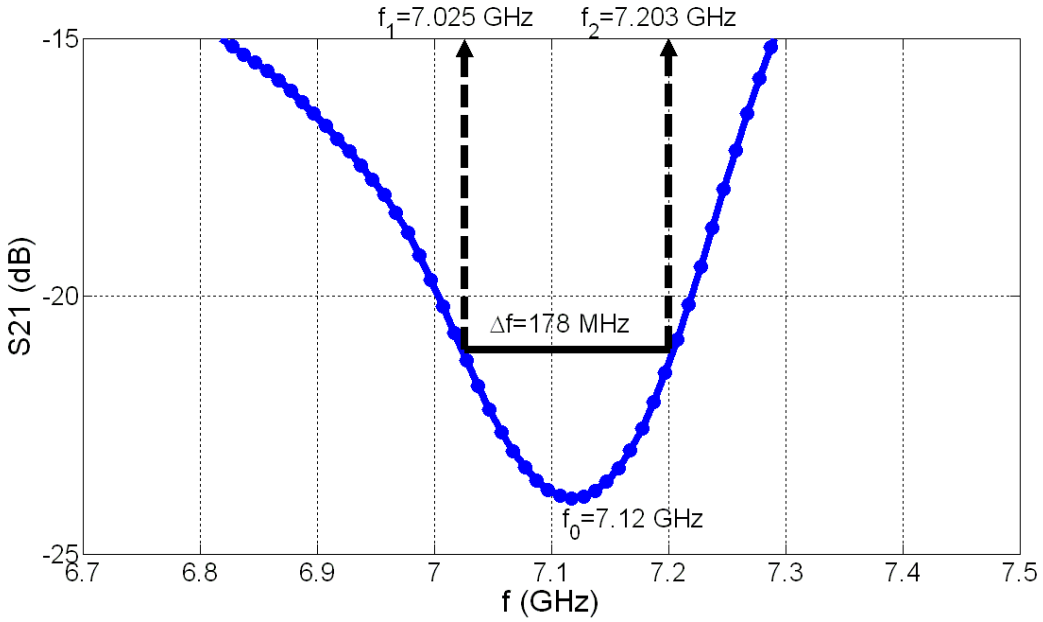


(b)

**Figure 2.1.5. For our second device, (a) experimental measurement and numerical simulation of $S_{21}$ parameter and (b) zoom-in experimental $S_{21}$ data to illustrate the resonance frequency $f_0$ and the 3-dB bandwidth $\Delta f$.**

To clearly illustrate 3-dB bandwidth measurements, Fig. 2.1.4 (b) and Fig. 2.1.5 (b) depict the same experimental $S_{21}$ data presented in Fig. 2.1.4 (a) and Fig. 2.1.5 (a), zooming in the resonance regions. As can be clearly seen in Fig. 2.1.4 (b) and Fig. 2.1.5 (b), we measure $\Delta f$ of the first and second devices to be 148 MHz and 178 MHz; these closely match the numerically-calculated $\Delta f$ values of 128 MHz and 169 MHz, respectively. Using (2.1.12), we then experimentally obtain Q-factors for the first and second devices of 47.10 and 38.48; these are also in close agreement with the numerical results of 52.40 and 41.30, presented in Table 2.1.3.

**Table 2.1.3. Theoretical and experimental resonance frequencies, 3-dB bandwidths, and quality-factors of our devices.**

| | $f_0$ (GHz) | | Δf (MHz) | | Q-factor | |
|---|---|---|---|---|---|---|
| | Theory | Experiment | Theory | Experiment | Theory | Experiment |
| Device 1 | 6.70 | 6.97 | 128 | 148 | 52.40 | 47.10 |
| Device 2 | 7.00 | 7.12 | 169 | 178 | 41.30 | 38.48 |

Here it is worth noting that we take all of our measurements loaded with standard microwave probes on the chips and then extract the Q-factors from these measurements in the loaded case including the losses coming from the probes. For example, for cavity resonators [20]-[21], typically unloaded Q-factors are cited; these are calculated using the relation $\frac{1}{Q_l} = \frac{1}{Q_u} + \frac{1}{Q_e}$, where $Q_u$ is the unloaded Q-factor, $Q_l$ is the loaded Q-factor, and $Q_e$ is the external Q-factor. In these works, $Q_u$ and $Q_e$ are larger than $Q_l$. In our case, we obtain and cite only the loaded Q-factors ($Q_l$) in our experiments by placing the microwave probes on the chips and measuring the $S_{21}$ parameters with the probes. In our experimental characterization, the minimum point of this $S_{21}$ measurement gives the resonance frequency $f_0$; the points that are 3 dB above this minimum point give the 3-dB frequencies ($f_1$ and $f_2$); the difference between $f_1$ and $f_2$ gives the 3-dB bandwidth Δf; and finally the ratio of $f_0$ to Δf gives the loaded Q-factor as in (2.1.12), which is also explicitly shown on the plots of Fig. 2.1.4 (b) and Fig. 2.1.5 (b). Therefore, the Q-factors cited here present the worst case with probe loading (and thus related losses) included in the measurements and extraction of the Q-factors.

Using our new design approach, we also increase the Q-factor by decreasing the device size and increasing the resonance frequency as also stated in (2.1.10). However, with the conventional design techniques, the Q-factor would rather decrease with increasing frequencies. In our experimental study, after achieving a considerably high Q-factor at 7 GHz using a small footprint of 540 µm × 540 µm, we further modify our design for $L_C$ = 270 µm, $W_C$ = 270 µm, $N$ = 2, $w$ = 50 µm, $s$ = 5 µm, $t_{film}$ = 0.1 µm, and $t$ = 0.1 µm. We use our analytical model to predict the operating resonance frequencies and we find out that the Q-factor is further improved despite the smaller chip size, while the resonance frequency is increased (13.08 GHz), as shown in Fig. 2.1.6. This is a unique feature of our self-tuning design methodology, which is not possible with the traditional approaches.

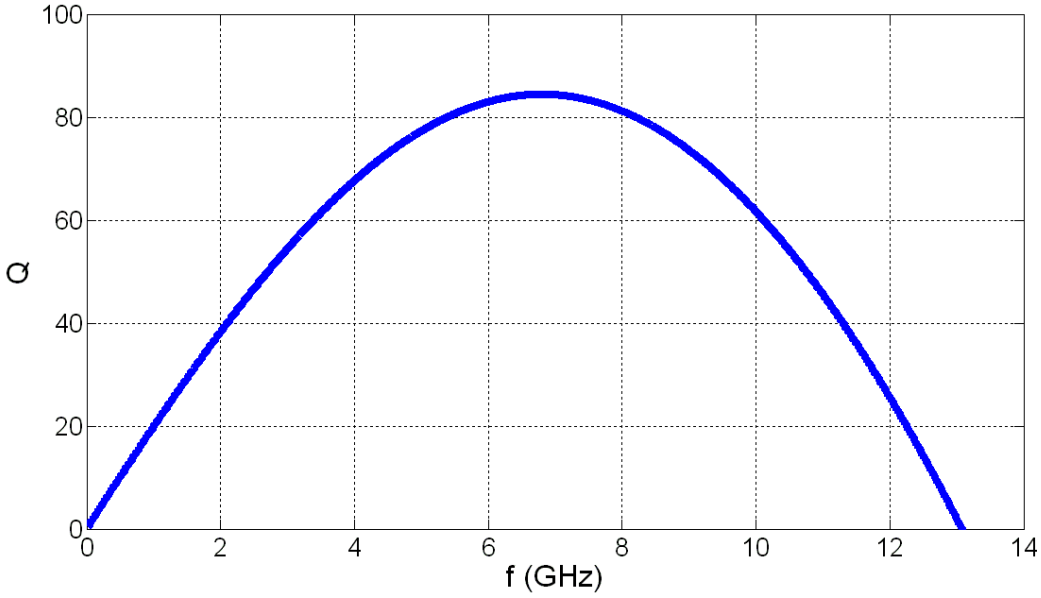


**Figure 2.1.6. $Q_{ind}$ computed for our design with $L_C$ = 270 µm.**

The loaded quality-factors experimentally obtained with our all-on-chip microwave resonator using our new design methodology in this work are considerably larger than the current state-of-the-art for similar-size microwave resonators that are implemented without cavity geometries in traditional approaches. The excellent agreement between our experimental measurement results

and theoretical simulation results (both analytical and numerical) verifies our theoretical models and techniques.

## 2.1.4 Conclusion

We have designed, fabricated, and demonstrated 540×μm540 μm on -chip microwave resonators working at 6.97 GHz with a Q-factor of 47.10. These hold great promise for use as high-Q chip-scale microwave resonators in different high-frequency applications, e.g., in implant RF sensors. To achieve high Q-factors, our design methodology focused on tuning the on-chip coil inductance with the increased on-chip dielectric thin film capacitance and minimizing energy losses. Also, we developed a two-port coil model representation, which we verified with our experimental results and numerical simulations. This model allows us to design and implement all-on-chip resonators whose resonance frequencies and Q-factors are precisely set and controlled with the device parameters in the design phase. As an interesting feature in our design approach, the effect of skin depth on the Q-factor is relatively reduced. Additionally, if our resonator design is modified to operate at an increased frequency, the chip size becomes smaller and the Q-factor is enhanced, which is again a different feature from the traditional approaches. Here in this study, the well-known spiral geometry, which is commonly utilized in inductors, is implemented as an all-on-chip microwave resonator for the first time.

## 2.2 Design and Realization of a Fully On-Chip High-Q Resonator at 15 GHz on Silicon

This section is based on the publication "Design and Realization of a Fully On-Chip High-Q Resonator at 15 GHz on Silicon" **R. Melik,** N.K. Perkgoz, E. Unal, Z. Dilli and H.V. Demir, *IEEE Transactions on Electron Devices 55, 3459-3466 (2008).* Reproduced (or 'Reproduced in part') with permission from IEEE. Copyright 2008 IEEE.

In this section [31], we develop and demonstrate an on-chip resonator working at 15 GHz with a high Q-factor of 93.81 while only requiring a small chip size of 195 μm x 195 μm on Si by using our new design methodology. In our design, unlike previous approaches, we avoid the need for any external capacitance for tuning; instead we utilize the film capacitance as the capacitor of the LC tank circuit and realize a fully on-chip resonator that shows a strong transmission dip of >30 dB on resonance as required for telemetric sensing applications. We present the design, theory, methodology, microfabrication, experimental characterization, and theoretical analysis of these resonators. We also demonstrate that the experimental results are in excellent agreement with the theoretical (both analytical and numerical) results. Based on our proof-of-concept demonstration, such high-Q on-chip resonators hold great promise for use in transmissive telemetric sensors.

### 2.2.1 Introduction

Improving the quality of the resonators is a major concern for satellite communications in the super high frequency (SHF) band. High-performance resonators operating in this frequency range are also required for other wireless applications such as mobile phones. Additionally, such resonators find applications in sensing. However, it is not a simple task to increase the quality factor (Q-factor) while satisfying the other specifications including small size and low cost. In

general, to fulfill these requirements, micromachined cavity resonators are used [18], [32]. Although these cavity architectures exhibit sufficiently high Q-factors, their sizes are quite large (on the order of 10 mm on one side with a minimum volume of 24.5 $mm^3$) [32]. Thus, as an alternative, structures based on spiral-coil inductors are investigated to satisfy the minimal area requirement while increasing the Q-factor [33]-[37]. But, these previous studies reported Q-factors only up to ~50. In this section, we develop and demonstrate an on-chip resonator on silicon, working in the $K_u$ band (at 15 GHz) with a very high Q-factor (93.81) while only requiring a small chip size (195 μm x 195 μm) by using our new design methodology. In our design, unlike previous approaches, we do not treat the spiral coil as only an inductor and do not use an external capacitor for tuning. Instead, we make use of the intrinsic capacitances and LC-tank behavior of the structure to set the resonance.

Avoiding the need for an external capacitor to develop such an on-chip resonator was first reported in our previous work [15]. However, this previous work led to only a Q-factor of 47 at 7 GHz. In this study here, we implement a self-tuning spiral coil based architecture without a cavity on the chip using improved design parameters at a higher operating frequency. Thus, we achieved significantly small-size and high-Q resonators in comparison with those of previous reports of our group and others [15], [19], [23], [30]. Typically, the resonator Q-factor decreases as the frequency increases. By our novel design, we realize the highest Q-factor with the smallest lateral area of 3.8 x $10^{-2}$ $mm^2$ (and with the smallest volume of 1.9 x $10^{-2}$ $mm^3$) at 15 GHz reported to date.

Furthermore, considering the high demand for good-quality resonators in medical applications and BioMEMS sensors, we design our on-chip resonators with bio-compatible materials (Si as the substrate, Au as the metal layers, and $Si_3N_4$ as the thin dielectric film). Also, we restrict our device designs to thin enough metal layers to avoid the need for using specially-thick high metal layers, sometimes called “RF layers”, which further reduces fabrication cost, if implemented in CMOS technology. These designs can also use the standard CMOS metal layer thicknesses, if desired. This is particularly important if such resonators are to be manufactured in high volumes as a part of sensors.

Given these restrictions, we start our resonator design by theoretical computations and numerical simulations for verification (using the CoventorWare RF Package). We further study the design *S*-parameters (using Microwave Studio). Fabricating the designs and characterizing the resulting devices, we observe an excellent agreement between the experimental and the numerical results, with a good conformity between theoretical and experimental resonance frequency and Q-factor.

The rest of the section is organized as follows. We first describe the physical and mathematical background in Section 2.2.2. We then explain our new design methodology, including numerical RF simulations, in Section 2.2.3. We describe the fabrication and experimental characterization in Section 2.2.4 and finally conclude in Section 2.2.5.

## 2.2.2. Review of Theory

The theory was discussed in Section 2.1.1, here we review the theoretical background for the sake of completeness of the design methodology of this 15 GHz chip.

Spiral-coil structures are used as on-chip inductors. Thanks to the parasitic capacitances of the coil metal with the substrate and the air bridge, such structures display a built-in resonance behavior. This resonance is normally considered to be past the structure's useful range of operation as an inductor. To utilize this structure as a resonator, here we model its behavior around this natural resonance point.

To form a circuit model, we analyze a rectangular spiral coil as consisting of segments. We conceive each segment of the coil as a transmission line and proceed according to established transmission line theory [22], [38]. To model the device, we consider the following design parameters: $L_c$ and $W_c$ as the outer lengths of the coil, $l$ as the total coil length, $w$ as the line width, $s$ as the line spacing, $N$ as the number of turns, $t$ as the coil thickness, and $t_{film}$ as the thickness of the dielectric thin film between the substrate and the Au metal layer. The

geometrical design parameters $L_c$, $W_c$, $N$, $w$, and $s$ set the coil inner diameter. These device parameters are used to calculate the parameters for the conventional lumped-element model illustrated in Fig. 2.2.1 [15].

In the figure, $L_s$ and $R_s$ correspond to the coil inductance and resistance, respectively. $C_{film}$ represents the capacitance between the substrate and the coil. $C_{si}$ and $R_{si}$ are the substrate capacitance and resistance, respectively. $C_s$ denotes the capacitance between coil segments.

$L_s$ is calculated by taking into account the self inductance $L_{Self}$, the positive mutual inductance $M^+$, and the negative mutual inductance $M^-$ as given in (2.2.1) [27].

$$L_S = \left|L_{Self}\right| + \left|M^+\right| - \left|M^-\right| \tag{2.2.1}$$

The coil resistance ($R_s$) is a function of the skin depth δ, where $R_s$ and δ are given in (2.2.2) and (2.2.3).

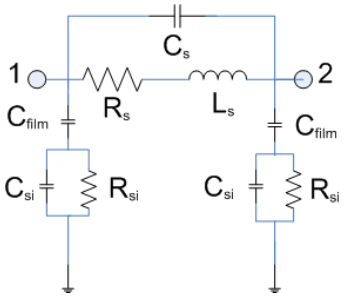


**Figure 2.2.1. Conventional lumped-element circuit model.**

$$R_S = \frac{\rho \ell}{w\delta \times \left(1 - e^{-\frac{t}{\delta}}\right)} \tag{2.2.2}$$

$$\text{where } \delta = \sqrt{\frac{2\rho}{\omega\mu_0}},\ \omega = 2\pi f \tag{2.2.3}$$

$C_{film}$ and $C_s$ are calculated using the parallel plate capacitor formula [28].

$$C_{film} = \frac{\varepsilon_0 \varepsilon_r \ell w}{t_{film}} \tag{2.2.4}$$

$$C_S = \frac{\varepsilon_0 \ell t}{s} \tag{2.2.5}$$

The elements $C_{si}$ and $R_{si}$, which represent substrate effects, are calculated by (2.2.6) and (2.2.7), respectively. (Our special design approach for $R_{si}$ will be explained in detail in Section 2.2.3.)

$$C_{Si} = 0.5 \ell w C_{Sub},\ C_{Sub} = 1.6 \times 10^{-10} \frac{F}{cm^2} \tag{2.2.6}$$

$$R_{Si} = \frac{2}{\ell w G_{Sub}},\ G_{Sub} = 0.4 \frac{1}{\Omega \text{cm}^2} \tag{2.2.7}$$

Here, $C_{sub}$ and $G_{sub}$ are fitting parameters as defined in [28] and obtained from measurements.

The quality factor can be defined in two different ways. The first is the basic quality factor definition for a resonator [30]:

$$Q = 2\pi \frac{\text{energy stored}}{\text{energy loss in one oscillation cycle}} \tag{2.2.8}$$

The above gives the total resonator Q-factor. Another form for this equation is given as follows [26]:

$$Q = \frac{f_0}{\Delta f} \tag{2.2.9}$$

$\Delta f$ is the full width at 3 dB above the minimum $S_{21}$, which is at $f_0$, the resonance frequency. Using $S_{21}$ measurements taken with microwave probes, we can calculate the loaded quality

factor.

Although (2.2.9) is useful to extract the resonator quality factor from experimental characterization (e.g., from the experimental data of $S_{21}$ as in Section 2.2.4), it does not give us information about which elements store or dissipate energy. To design a high-quality, on-chip resonator, we need a better grasp of the system. Therefore, we exploit the definition of the Q-factor for the inductor instead of the entire LC tank circuit. For the inductor, only the energy stored in the magnetic fields is of interest. So, when the difference between the peak magnetic field and the peak electric field is at the maximum value, we get the maximum $Q_{max}$ of the inductor quality factor $Q_{ind}$, [30].

$$Q_{ind} = 2\pi \frac{\text{peak magnetic energy-peak electric energy}}{\text{energy loss in one oscillation cycle}} \tag{2.2.10}$$

By this definition, we can ascertain which elements store and dissipate the energy and how we can improve the design.

An alternate form for $Q_{ind}$ is [30]:

$$Q_{ind} = \frac{\mathrm{R}}{\omega \mathrm{L}}\left[1-\left(\frac{\omega}{\omega_0}\right)^2\right] \tag{2.2.11}$$

The above equation reveals that $Q_{ind}$ is zero at the structure's self-resonance frequency. This frequency in a classical LC circuit is given by (2.2.12) [30]:

$$f_0 = \frac{1}{2\pi\sqrt{LC}} \tag{2.2.12}$$

The resonator quality factor can be obtained by combining the inductor and capacitor quality factors [26]: $\frac{1}{\mathrm{Q_{res}}} = \frac{1}{Q_{ind}} + \frac{1}{Q_c}$. $Q_c$ is not affected extensively by structural design once a material

system has been selected. $Q_{ind}$, on the other hand, depends on geometrical design as well as the materials. Thus by using the classical resonance definition and the design techniques for better $Q_{ind}$, we can maximize the resonator Q-factor for our small on-chip resonator.

For optimizing $Q_{ind}$, we start by simplifying the equivalent lumped circuit model whose parameters we use to calculate $Q_{ind}$ . In the literature, one of the ports of the two port model in Fig. 2.2.1 is shorted to obtain a one-port circuit [25], [28]. By simplifying this circuit to a parallel RLC circuit, we get the circuit shown in Fig. 2.2.2. Here $R_p$ and $C_p$ represent the combination of $C_{film}$, $C_{si}$ and $R_{si}$ as shown in (2.2.13) and (2.2.14), respectively.

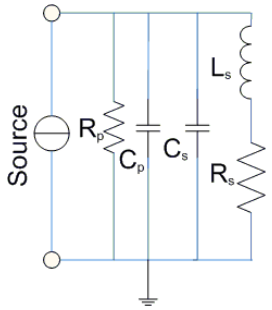


**Figure 2.2.2. The conventional simplified one-port parallel RLC circuit.**

$$R_P = \frac{1}{\omega^2 C_{film}{}^2 R_{Si}} + \frac{R_{Si}\left(C_{film}+C_{Si}\right)^2}{C_{film}{}^2} \tag{2.2.13}$$

$$C_P = C_{film}\frac{1+\omega^2\left(C_{film}+C_{Si}\right)C_{Si}R_{Si}{}^2}{1+\omega^2\left(C_{film}+C_{Si}\right)^2 R_{Si}{}^2} \tag{2.2.14}$$

At this point, we change the model in Fig. 2.2.2 into a two-port model as shown in Fig. 2.2.3 and proceed with the calculations. Combining all the concepts explained so far, $Q_{ind}$ becomes:

$$Q_{ind} = \frac{\omega L_S}{R_S} \times \frac{2R_P}{2R_P + \left[\left(\frac{\omega L_S}{R_S}\right)^2 + 1\right] R_S} \times \left[1 - \frac{R_S{}^2\left(\frac{C_P}{2} + C_S\right)}{L_S} - \omega^2 L_S\left(\frac{C_P}{2} + C_S\right)\right] \quad (2.2.15)$$

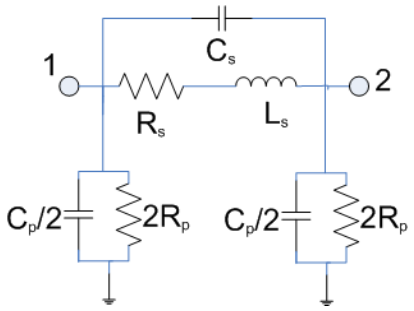


**Figure 2.2.3. Our two-port circuit model to calculate the Q-factor.**

From (2.2.15), we identify the two factors, which affect $Q_{ind}$ and $Q_{max}$: The substrate loss factor and the self-resonance factor, both given below. Here we note that the substrate loss factor mainly affects $Q_{max}$ and the self resonance mainly affects the resonance frequency.

$$\text{Substrate Loss Factor} = \frac{2R_P}{2R_P + \left[\left(\frac{\omega L_S}{R_S}\right)^2 + 1\right] R_S} \quad (2.2.16)$$

$$\text{Self Resonance Factor} = \left[1 - \frac{R_S{}^2\left(\frac{C_P}{2} + C_S\right)}{L_S} - \omega^2 L_S\left(\frac{C_P}{2} + C_S\right)\right] \quad (2.2.17)$$

## 2.2.3 Design

Our main objective is to design the smallest resonator working at 15 GHz with the highest

possible Q-factor. To this end, understanding each of the device parameters correctly allows us to accomplish a superior design. In the literature, ways to increase $Q_{max}$ are sought as in [19] and [23], with $Q_{ind}$ as the target Q-factor to be maximized. (The difference between Q and $Q_{ind}$ was given in Section 2.2.2.)

In the literature, the film capacitance is considered as a parasitic capacitance [30]. However, our approach is to use this built-in capacitance as the capacitor of LC tank so that there is no need to tune the circuit with an external capacitor; thus we can obtain a small, fully on-chip resonator that can be used, e.g., for transmissive telemetric sensing. We presented the physical design factors in Section 2.2.2. Here we examine the effects of these parameters.

*A. Effect of the Substrate*

Minimizing substrate losses is important to achieve a considerable increase in $Q_{ind}$ and $Q_{max}$, as the substrate is the main lossy component in the system. In general, to prevent substrate loss in resonators, it is preferred to use GaAs, which is harmful to the human body and would render the BioMEMS sensor non-biocompatible. Here we chose Si as the substrate for a biocompatible device.

For low loss, a high $R_{si}$ (and thus a highly resistive substrate) is required. However, a completely nonconductive substrate would hinder the formation of a parallel plate capacitor between the metal layer and substrate, contradicting the on-chip resonator concept. Thus, we select a substrate at 5-10 Ω.cm, which is resistive enough to prevent excessive loss, but still conductive enough to serve as the second plate of a parallel-plate capacitor. Fig. 2.2.4 displays the relationship between $Q_{ind}$ and the substrate resistivity as obtained by our simulations.

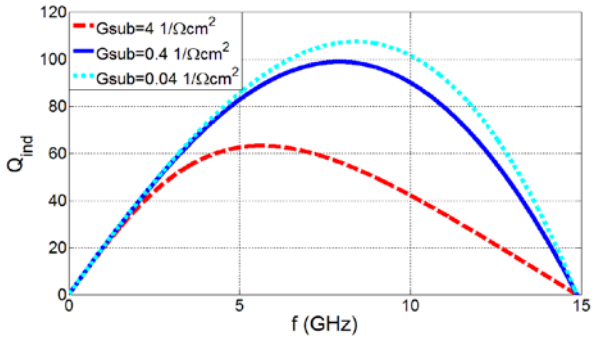


**Figure 2.2.4. The relationship between $Q_{ind}$ and substrate resistivity.**

*B. Effect of the Dielectric Thin Film*

The dielectric layer is also an important factor for a high quality-factor design. To optimize the capacitor between the metal and the substrate, which serves as the C of the LC circuit, we need a dielectric layer with a high dielectric constant. On the other hand, to minimize the loss, a low loss dielectric is required. Therefore $Si_3N_4$, with a dielectric constant of 8 and a loss tangent of $5x10^{-4}$, is chosen as the dielectric film to satisfy these conditions.

*C. Effect of the Film Thickness*

The thickness of the dielectric layer ($t_{film}$) is another effective parameter to design a high Q-factor resonator. For our target resonance frequency of 15 GHz, we set the dielectric layer thickness to 0.1 μm.

*D. Effect of the Metal Layer Parameters*

The metal type used in the design is critical, particularly for the BioMEMS sensor applications where biocompatibility is crucial. There are several metals (e.g., Al and Cu) being used in the generic CMOS or MEMS processes. However, since these restrict biocompatibility, instead Au, which is biocompatible, is chosen as the metal layer.

The thickness of the metal layer is also significant to determine $Q_{ind}$. The thicker the metal is, the higher $Q_{ind}$ and $Q_{max}$ are. However, as we aim for an RFIC resonator achievable without the need

for special fabrication steps in a CMOS-process, we set the metal thickness to 0.1 μm. In spite of the thin layer, we can achieve a high $Q_{ind}$ by decreasing the substrate loss sufficiently. In that case increasing the metal thickness would still affect the Q-factor, but not as significantly as it would in a structure with a too-low substrate resistance.

*E. Effect of the Line Width and the Spacing*

Optimizing the line width (*w*) and spacing (*s*) is critical for our design. Although increasing the width improves $Q_{ind}$, it also results in a larger area. In addition, an excess increase in the width with respect to the spacing, *s*, further increases the parasitic capacitance and diminishes $Q_{ind}$. On the other hand, by decreasing the spacing, both the resonance frequency and $Q_{ind}$ can be increased. However, continuing to decrease the spacing with respect to the line width causes an increase in the parasitic capacitance and a decrease in the Q-factor. Considering these constraints, we chose the width and the spacing as thick as 35 μm and 5 μm, respectively.

*F. Effect of the Number of Turns*

To increase $Q_{ind}$ while keeping the size small, we decrease the number of turns (*N*). This decreases the net inductance, pushing the self-resonance frequency higher. Thus, we restrict the number of turns to 2.

*G. Effect of the Area*

The chip size is influential to adjust the resonance frequency and $Q_{ind}$. As we intend to have resonance at 15 GHz, which is in the super high frequency range, we need to decrease the area as much as possible. This is also consistent with our aim of a compact resonator. A smaller area also increases $Q_{ind}$. As in (2.2.15), $Q_{ind}$ is related to the ratio of $\omega L_s/R_s$ and the substrate loss factor. (The self resonance factor mainly affects the resonance frequency.) In our design methodology, the substrate loss factor is almost one and generally the ratio of $L_s/R_s$ is almost the same, so a higher ω increases $Q_{ind}$. If we have a smaller area, we have higher resonance frequency and as a result, we can see $Q_{ind}$ at higher frequencies. (We can observe $Q_{ind}$ up to the self-resonance frequency.) So we have higher ω and thus higher $Q_{ind}$. As a result, we set the area ($L_c x W_c$) to the minimum value possible with the limiting factors such as *N*, *w*, and *s*.

*H. Effect of the Inner Diameter*

If all the other design parameters are fixed, the increase in inner diameter increases area. This decreases the resonance frequency and hence $Q_{ind}$. So a smaller inner diameter enhances $Q_{ind}$ and increases the resonance frequency. However, we can only decrease the inner diameter down to the thickness of the spacing, *s*, since decreasing below this value causes the parasitic capacitance to dominate and degrade $Q_{ind}$. Therefore, our inner diameter is set equal to *s*.

*I. Effect of $R_p$*

$R_p$, representing the combined impedances of $C_{film}$, $C_{si}$ and $R_{si}$, as in (2.2.13) is one of the most important factors in determining the substrate loss. If $R_p$ is high, the substrate loss factor becomes almost unity, as indicated by (2.2.16). On the other hand, since energy loss is more apparent at higher frequencies, we need to optimize $R_p$ to minimize these losses.

Targeting 15 GHz operation, we already need to fix *w* and *l* at low values. Also, we adjust the other parameters to minimize the coil size. So the total *l* also decreases, which enhances $R_{si}$. As a result we obtain a high $R_{si}$ giving rise to a high $R_p$ almost independent of the frequency. Because of the increased frequency and smaller dimensions, we obtain a higher $R_p$ and observe a smaller change in $R_p$ as a function of the frequency compared to $R_p$ in our previous design [15].

We notice that $R_p$ is rather high with a slight decrease at higher frequencies. Hence, the substrate loss factor is also high and it decreases from 1 to nearly 0.75 with the frequency increasing from 1 GHz to 15 GHz as shown in Fig. 2.2.5. With our design parameters we obtain high $Q_{ind}$ and high $Q_{max}$. Because of the high substrate loss, $Q_{max}$ is observed at higher frequencies. If the substrate loss factor decreases, $Q_{max}$ shifts to lower frequencies. The substrate loss factor does not have a significant effect on the resonance frequency whereas it mainly affects $Q_{ind}$, $Q_{max}$, and the frequency at which $Q_{max}$ is detected. If we had an $R_p$ of infinity, the substrate loss factor would become unity and we would observe a minimal increase in $Q_{max}$.

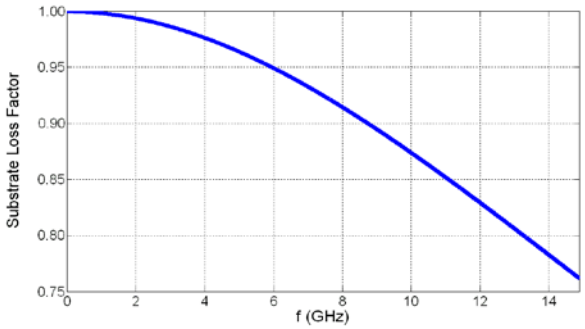


**Figure 2.2.5. The substrate loss factor as a function of the operating frequency.**

*J. Effects of $C_p$*

$C_p$ is a compound of $C_{film}$, $C_{si}$ and $R_{si}$, as presented in (2.2.14). It mainly depends on $C_{Si}$ and $C_{film}$. It is essentially a function of $w$ and $l$. $C_p$ determines the resonance frequency. For a higher resonance frequency, a low $C_p$ is required. Therefore, $l$ is decreased to attain a low $C_p$ and a high resonance frequency with a small device-volume. Thus, by reducing the size, we decrease $C_p$ and increase the resonance frequency. As in (2.2.14), $R_{si}$ should be high for $C_p$ to be independent of the frequency. How to obtain a high $R_{si}$ is explained above. In comparison with the $C_p$ in [15] we realize a lower $C_p$ and observe a slight decrease in $C_p$ with the increasing frequency and smaller dimensions. As a result, the substrate loss factor decreases to zero at 14.88 GHz. With a low $C_p$, the self resonance frequency factor slowly decreases to zero at 15 GHz and we obtain a high frequency resonator. Fig. 2.2.6 shows the self resonance frequency factor with respect to the frequency.

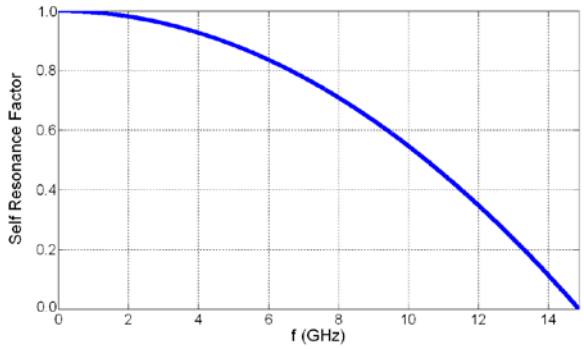


**Figure 2.2.6. The self resonance frequency factor as a function of the operating frequency.**

By combining all these effects, we obtain the design parameters as shown in Table 2.2.1.

**Table 2.2.1. The parameters of our device.**

| $L_c$ (μm) | $W_c$ (μm) | $N$ | $w$ (μm) | $s$ (μm) | $t_{ox}$ (μm) | $t$ (μm) |
|---|---|---|---|---|---|---|
| 195 | 195 | 2 | 35 | 5 | 0.1 | 0.1 |

To design our device, we compute the inductance $L_s$ by simulating in the RF simulation tool of CoventorWare and compare these values with our theoretical calculations. The calculated and simulated $L_s$ values are almost identical as shown in Table 2.2.2. Our theoretical calculation for $L_s$ is carried out as in (2.2.1) where $L_{self}$, $M^+$, and $M^-$ are calculated as in [27].

**Table 2.2.2. Theoretical and numerical $L_S$ values for our device.**

| | Theoretical | Numerical |
|---|---|---|
| $L_s$ (nH) | 2.54 | 2.56 |

In Fig. 2.2.7, we present the theoretical $Q_{ind}$ as a function of the operating frequency. At the resonance frequency (15 GHz), the inductor quality factor crosses the zero line.

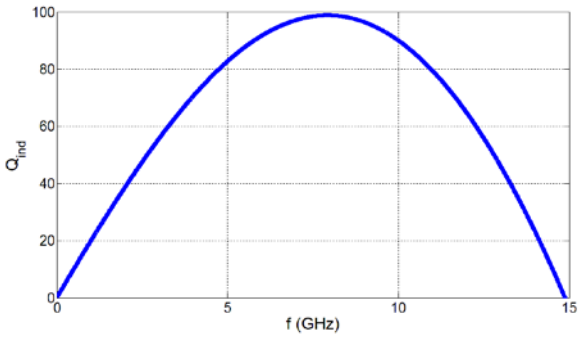


**Figure 2.2.7. $Q_{ind}$ versus the operating frequency.**

## 2.2.4 Experimental Realization, Characterization, and Analysis

Our fabrication process follows standard photolithography, metallization, wet etching, and plasma enhanced chemical vapor deposition (PECVD) steps [15]. We use lithography to pattern the first metal layer (0.1 μm thick Au) on the Si substrate with lift-off following the metallization by evaporator. We deposit a 0.1 μm-thick dielectric $Si_3N_4$ film with PECVD. Then we again perform lithography to open the holes in $Si_3N_4$ film using wet etching in HF. After this process, we carry out vertical interconnect metallization by evaporating a 0.1 μm thick Au film. Finally, we lay down the spiral coil using lithography, metallization, and lift-off of a top 0.1 μm thick Au layer. Fig. 2.2.8(a)-(c) show the resulting fabricated device in top view and its cross-sectional layer diagram to show these different layers of the device from the side.

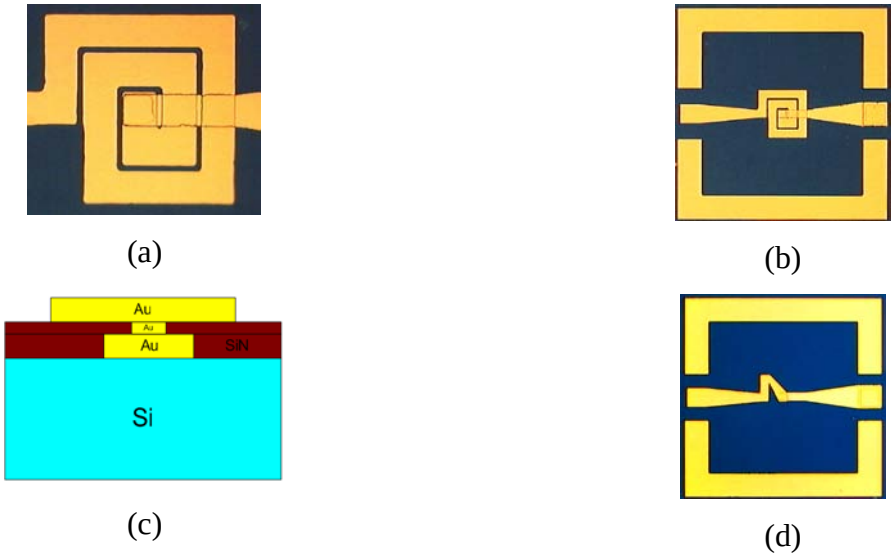


**Figure 2.2.8. Micrographs of one of our fabricated devices showing (a) the spiral coil zoomed at the center and (b) in its entirety, along with (c) its cross-sectional layer diagram, and (d) that of the "thru" structure used for calibration purposes.**

The network analyzer is used to obtain the spectral transmission response of the fabricated

devices. We use GSG microwave probes for *S* parameter measurements after performing an impedance standard substrate (ISS) calibration. In a further calibration process before measuring the $S_{21}$ parameters, we first measure the response of the through ("thru") calibration structure given in Fig. 2.2.8(d), which consists of just the GSG probe pads and interconnects, to exclude the effect of parasitic capacitance when later measuring the values of the device under test. The measurements were taken using the maximum number of points (801 point), with an averaging factor of 128.

Fig. 2.2.9 shows the experimentally measured $S_{21}$ parameter (in dB) along with the numerically simulated one up to a maximum operating frequency of 18 GHz (which is the upper limit of the measurement range in our setup). We observe an excellent agreement between the experimental and theoretical results. In particular, we observe very good matches between the experimental and theoretical resonance frequency ($f_0$) and the experimental and theoretical resonator Q-factor.

Here the resonator Q-factor is calculated from the experimental results by examining the dip in the transmitted power. The minimum point of $S_{21}$ is presented in Fig. 2.2.9. This corresponds to $f_0$ (at ~15 GHz). Here we observe a very strong dip of >30 dB in transmission. To calculate the resonator Q-factor from the experimental data as defined in (2.2.9), we use those frequencies with $S_{21}$ parameters 3 dB above the resonance frequency. Here we find $\Delta f$ to be 160 MHz, yielding a Q-factor of 93.81. This is the Q-factor of the entire resonator for the case when the chip is loaded with microwave probes.

In summary, Table 2.2.3 lists the resonance frequencies and the resonator Q-factors obtained both experimentally and theoretically. The theoretically calculated resonance frequency is 14.88 GHz, whereas the experimental resonance frequency is 15.01 GHz. The theoretical Q-factor is 98.77, while the experimental Q-factor is 93.81. This experimental demonstration shows that such a fully on-chip resonator leads to a very high Q-factor and a very strong dip in transmission, making it possible to use for telemetric sensing applications.

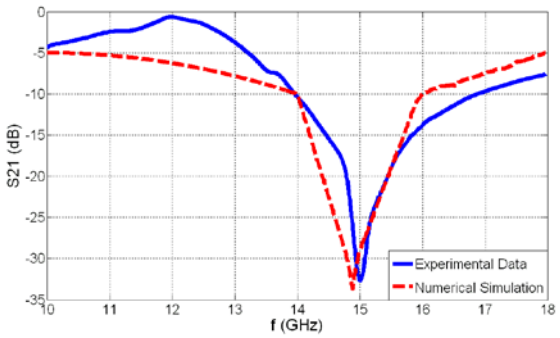


**(a)**

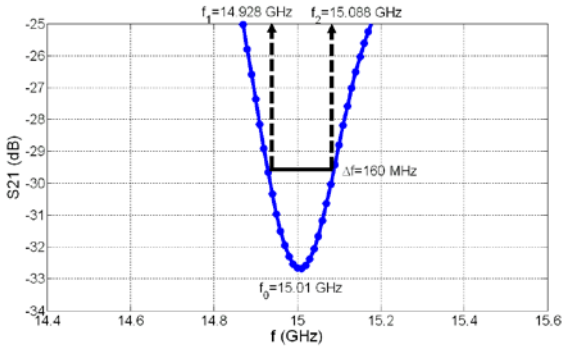


**(b)**

**Figure 2.2.9. (a) Experimental data and numerical simulation results for $S_{21}$ parameters, and (b) zoom-in experimental $S_{21}$ data to illustrate the Q-factor extraction from the experimental data.**

**Table 2.2.3. The theoretical and experimental resonance frequency and Q-factor.**

| $f_0$ (GHz) | | Q-Factor | |
|---|---|---|---|
| Theoretical | Experimental | Theoretical | Experimental |
| 14.88 | 15.01 | 98.77 | 93.81 |

We also consider other design parameter sets given in Table 2.2.4. In this table, Device-1 and Device-2 are the devices that have lower resonance frequencies than our device, which are optimally designed for their operating resonance frequencies with our design methodology. Also,

we used and inspected Device-1 in [15]. Device-3, Device-4, and Device-5 are the devices that have the same resonance frequency as our device in this section. In Fig. 2.2.10(a), we present the $Q_{ind}$ factors of Device-1 and Device-2. In Fig. 2.2.10(b), we show the experimental $S_{21}$ parameters of Device-1 as a function of operating frequency and in Fig. 2.2.10(c), we depict the experimental $S_{21}$ parameters of Device-2 with respect to frequency. From Fig. 2.2.10(b) and Fig. 2.2.10(c), we find out that Device-1 has a resonance frequency of 6.97 GHz with a Q-factor of 47.1 while Device-2 has 3.58 GHz resonance frequency and 28.1 Q-factor. By comparing these results with our device results, we observe that when the resonance frequency increases, the Q-factor increases. In Fig. 2.2.11, we show the $Q_{ind}$ factors of our device, Device-1, Device-3, Device-4, and Device-5. We see that Device-3, 4 and 5 have almost the same resonance frequency as our device but their $Q_{max}$ is smaller than even Device-1, which has lower resonance frequency. From these results, we observe that Device-3, 4 and 5 will have lower Q-factors than our device. These results show that designs that are made using our design methodology yield higher Q-factors with higher $Q_{max}$ levels for the same resonance frequency.

**Table 2.2.4. The design parameters of some exemplary devices with N=2, $t_{ox}$=0.1 µm and $t$=0.1 µm. Device-1 and Device-2 are optimally designed for their resonance frequencies with our design methodology. The $f_0$ of Device-1 and Device-2 are experimental values while those of Device 3-4 and 5 are theoretical values. The Q values are experimental and $Q_{max}$ values are theoretical.**

| | $L_c$ (µm) | $W_c$ (µm) | $w$ (µm) | $s$ (µm) | $f_0$ (GHz) | $Q$ | $Q_{max}$ |
|---|---|---|---|---|---|---|---|
| Device-1 | 540 | 540 | 100 | 10 | 6.97 | 47.1 | 55.0 |
| Device-2 | 1080 | 1080 | 200 | 20 | 3.58 | 28.1 | 33.3 |
| Device-3 | 212 | 212 | 10 | 10 | 14.95 | N.A. | 41.9 |
| Device-4 | 270 | 270 | 5 | 20 | 15.05 | N.A | 23.7 |
| Device-5 | 332 | 332 | 3 | 30 | 14.96 | N.A | 14.9 |

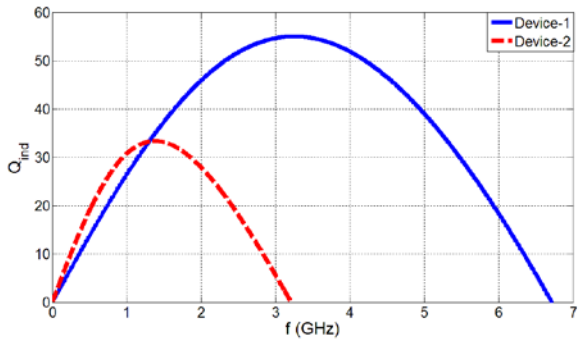


**(a)**

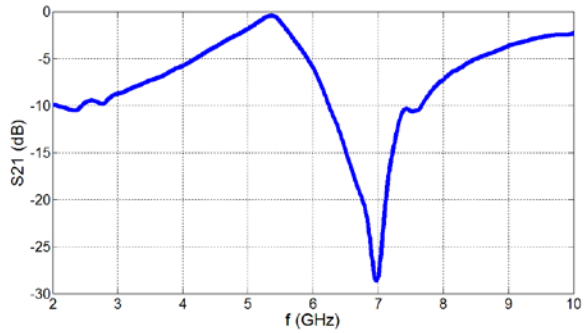


**(b)**

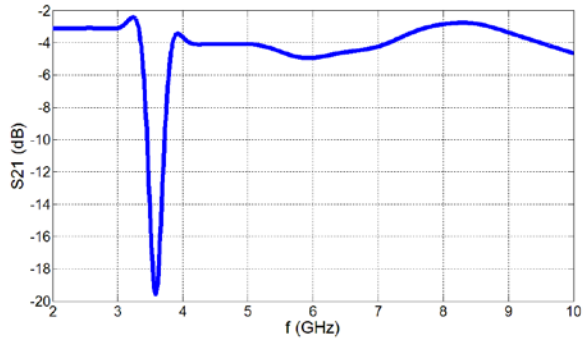


**(c)**

**Figure 2.2.10. (a) $Q_{ind}$ of Device-1 and Device-2 (b) the experimental $S_{21}$ parameter of Device-1, and (c)the experimental $S_{21}$ parameter of Device-2.**

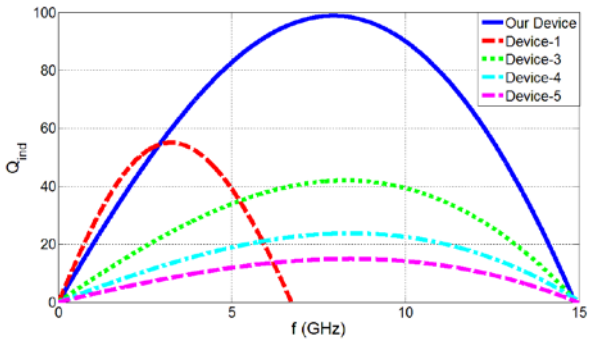


**Figure 2.2.11. The $Q_{ind}$ values of Our Device, Device-1 (where Our Device and Device-1 are optimally designed with our design methodology for their resonance frequencies), Device-3, Device-4 and Device-5.**

## 2.2.5 Conclusion

We have designed, fabricated, and demonstrated the operation of a 195 μm x 195 μm on-chip resonator on Si working at 15 GHz with a Q-factor of 93.81, which is much larger than the Q-factors of the current state-of-the-art on-chip resonators that have been realized without cavity geometries. Also, in the experimental transmission characterization, we observed a very strong dip of >30 dB, which renders our design particularly useful for sensing applications. By using the two-port circuit model, we precisely set and controlled the device resonance frequency and Q-factor with the device parameters at the design stage. We observed an excellent agreement between our experimental measurement results and theoretical simulation results. Our approach is unique in its Q-factor optimized even for very high frequencies while avoiding the need for the use of an external capacitor. Thus we have realized a fully on-chip resonator. In a typical design of such a device, increasing frequency decreases the Q-factor. However, using our new design technique, we achieved higher Q-factors at increasing frequencies even with smaller chip sizes. Such a high-Q, on-chip resonator has a high potential for use in different high-frequency applications, particularly for telemetric sensing applications where the changes in the transmission and resonance frequency are monitored.

# Chapter 3

# Resonance Frequency Shift of Resonators Loaded with Probes

In this chapter, we will externally apply mechanical load to the on-chip resonators loaded with probes and observe their resonance frequency shift under mechanical deformation. We will present proof of concept demonstration of sensing based on resonance frequency shift and understand the sensing mechanism in this chapter. We will use circular geometry and later suspended architecture, by both of which we increase the performance of the sensors. We will also study the triplet idea in detail in this chapter.

# 3.1 Bio-implantable Passive On-Chip RF-MEMS Strain Sensing Resonators for Orthopaedic Applications

This section is based on the publication "Bioimplantable passive on-chip RF-MEMS strain sensing resonators for orthopeadic applications" **R. Melik**, N.K. Perkgoz, E. Unal, C.M. Puttlitz, and H.V. Demir, *Journal of Micromechanics and Microengineering 18, 115017 (2008)*. Reproduced (or 'Reproduced in part') with permission from IOP Publishing Ltd. Copyright 2008 IOP Publishing Ltd.

One out of ten bone fractures does not heal properly due to improper load distribution and strain profiles during the healing process. In this section [39], to provide implantable tools for the assessment of bone fractures, we have designed novel, bio-implantable, passive, on-chip, RF-MEMS strain sensors that rely on the resonance frequency shift with mechanical deformation. For this purpose, we modeled, fabricated, and experimentally characterized two on-chip sensors with high quality-factors for *in vivo* implantation at the future stages. One of the sensors has an area of ~0.12 $mm^2$ with a quality-factor of ~60 and the other has an area of ~0.07 $mm^2$ with a quality-factor of ~70. To monitor the mechanical deformation by measuring the change in the resonance frequencies with the applied load, we employed a controllable, point load applying experimental setup designed and constructed for *in vitro* characterization. In the case of the sensor with the larger area, when we apply a load of 3920 N, we obtain a frequency shift of ~330 MHz and a quality-factor of ~76. For the smaller sensor, the frequency shift and the quality-factor are increased to 360 MHz and 95, respectively. These data demonstrate that our sensor chips have the capacity to withstand relatively high physiologic loads, and that the concomitant and very large resonance frequency shift with the applied load is achieved while maintaining a high signal quality factor. These experiments demonstrate that these novel sensors have the capacity for producing high sensitivity strain readout, even when the total device area is considerably small. Also, we have demonstrated that our bio-implantable, passive sensors deliver a telemetric, real-time readout of the strain on a chip. Placing two more resonators on the

sides of the sensor to serve as transmitter and receiver antennas, we achieved to transfer contactless power and read out loads in the absence of direct wiring to the sensor. With this model, where telemetric measurements become simpler due to the fact that all sensor system is built on the same chip, we obtain a frequency shift of ~190 MHz with an increase in the quality-factor from ~38 to ~46 when a load of 3920 N is applied. Therefore, as a preliminary demonstration, we have showed the feasibility of our on-chip strain sensors for monitoring the mechanical deformation using telemetry-based systems.

## 3.1.1 Introduction

Treatment of complicated bone fractures continues to be a challenge for modern medicine [40]. In fact, approximately 10% of all bone fractures will not heal properly [41]. Most operative treatment schema typically requires the implantation of stainless steel or titanium plates. The hardware serves to resist high stresses and bear a majority of the load during the early phase of bone tissue healing. As the healing tissue starts to ossify, the load is gradually transferred from the implanted plate to the tissue. Monitoring of the healing process in the acute phase (approximately first 30 days) via radiographic assessment (typically by X-rays) does not have sufficient fidelity to determine if the healing is normal or aberrant. To date, in vivo, real-time monitoring of the healing process at the wide scale via monitoring the hardware-to-tissue load transfer has not been possible due to a lack of technological advancement. To address this problem, we hereby introduce a bioimplantable wireless sensor system capable of monitoring the change in loading of an implantable plate in order to determine the quality of the healing process. By using such a remote sensor, it is expected that a continuous healing profile of an individual patient can be recorded during the activities of daily life.

Although biosensors have been studied for a wide range of applications and a good deal of research has been conducted by various groups, there exists limited data with respect to implantable microelectromechanical systems (MEMS) based biosensors due to various challenges [42]. One of the drawbacks of current wireless sensors is production of a low quality-

factor (Q-factor), which can be described as the ratio of the stored to lost energy. To monitor physiological parameters using telemetry-based implantable sensing systems, implantable bio-MEMS based capacitive pressure sensors have only been able to achieve Q-factors of approximately 10 [43], [44]. An important requirement on these sensors is that they maintain a fully on-chip resonator with a high transmission dip at resonance for telemetric sensing applications. Reducing the size of a sensor is another major issue because of the limited space for *in vivo* implantation. In our previous chapter, we demonstrated the implementation an on-chip resonator operating at 15 GHz with a Q-factor of 93.81 and a small chip size of 195 μm x 195 μm [31]. We effectively utilized a spiral coil geometry and cavity resonator concept, which provided a reduced area and practical implementation with a high Q-factor [31]. In this previous work of our group and the others, we developed RF resonators that were studied and designed from microwave perspective, especially focusing on high-Q performance. These resonators were not previously designed or characterized as MEMS-sensors for mechanical deformation (under applied force), unlike this current work.

In this chapter for the first, we present a bio-MEMS strain sensor for implantation using a RF-MEMS approach. The operating principle is based on a concomitant resonant frequency shift with mechanical deformation. We aim to sense biological data and transfer it effectively to an antenna outside the body. To interpret the biological data, the input is denoted by the physical load (F), and the output is denoted by the resonance frequency readout ($f_0$). As the load is applied to the stainless steel plate, it deforms (strains) under the applied stress [1]. Eventually this strain decreases (due to the temporal shift in the load distribution) and modifies the resonance frequency, thus allowing for real-time observation of the healing process in the fracture. Therefore, with the sensor chip we propose and demonstrate, it is possible in principle to measure the change in the strain and hence to assess the healing process by means of this resonance frequency shift. This $f_0$ shift results from the change in the capacitance of the film between the metal and the substrate because of the modified area with the applied force. Here it is worth noting that the resonator and the capacitive strain sensor are on the same chip in a compact form, which is unique to our design. Previous literature has reported on changes in the capacitance of the chip and resultant resonance frequency shifts [44]-[47]; however, the area of

these devices is relatively large because an additional external capacitor is used to tune the resonator. Also, these previous devices were constrained to very narrow load ranges.

To design and fabricate a bio-implantable RF-MEMS sensor based upon resonance frequency shifts, a number of difficult issues need to be addressed. First, human lower extremity loading can be approximately four or five times of its body weight. The implication of this is that a person with a weight of 100 kgf (i.e., 980 N) can apply a load up to 500 kgf (i.e., 4900 N) to an implanted stainless steel plate. Therefore, the chip has to withstand relatively high stresses while remaining sufficiently sensitive to indicate the resonance frequency as a function of the applied force. We apply this force to the chip using our experimental setup to have controllable resonance frequency with the applied load. Another constraint to be considered is the device size, since the area of the chip is limited by the plate area (in the range of $cm^2$). Additionally the materials are required to be biocompatible and not costly. Considering all these constraints, a biocompatible, sensitive, high Q-factor chip with smallest possible area is required to be modeled and produced as the first proof-of-concept.

## 3.1.2 Theoretical background

To design the sensor circuit, we use a coil structure with spiral geometry for the distributed inductor and capacitor shown in top view and side view in Fig. 3.1.1(a)-(b), and apply the transmission line theory to model this structure as a resonator. We presented a complete description of our circuit model given in Fig. 3.1.1(c), and the characterization of the RF device in our previous chapter [30], [31]. In this work, to achieve a high Q-factor, we used the same methodology from microwave perspective [15], [31]; further details of parts of the RF design can also be found in the literature [19], [22], [23], [25], [27], [28], [30], [38]. In this circuit model, $C_{film}$ is the capacitance between the coil and the substrate as in (3.1.1), as depicted in Fig. 3.1.1(b), and $C_S$ and $L_S$ denote the capacitance between adjacent coils and the inductance of the spiral coil, respectively. $R_S$ and $R_{Si}$ are the resistances of the coil and the substrate, respectively.

We use $R_P$ and $C_P$ for the circuit conversions [15], [31] and calculate them as in (3.1.2) and (3.1.3). Finally combining all these, we find the Q-factor of the inductor ($Q_{ind}$) as in (3.1.4).

$$C_{film} = \frac{\varepsilon_0 \varepsilon_r \ell w}{t_{film}} \tag{3.1.1}$$

$$R_P = \frac{1}{\omega^2 C_{film}{}^2 R_{Si}} + \frac{R_{Si}\left(C_{film} + C_{Si}\right)^2}{C_{film}{}^2} \tag{3.1.2}$$

$$C_P = C_{film} \frac{1 + \omega^2 \left(C_{film} + C_{Si}\right) C_{Si} R_{Si}{}^2}{1 + \omega^2 \left(C_{film} + C_{Si}\right)^2 R_{Si}{}^2} \tag{3.1.3}$$

$$Q_{ind} = \frac{\omega L_S}{R_S} \times \frac{2R_P}{2R_P + \left[\left(\frac{\omega L_S}{R_S}\right)^2 + 1\right] R_S} \times \left[1 - \frac{R_S{}^2 \left(\frac{C_P}{2} + C_S\right)}{L_S} - \omega^2 L_S \left(\frac{C_P}{2} + C_S\right)\right] \tag{3.1.4}$$

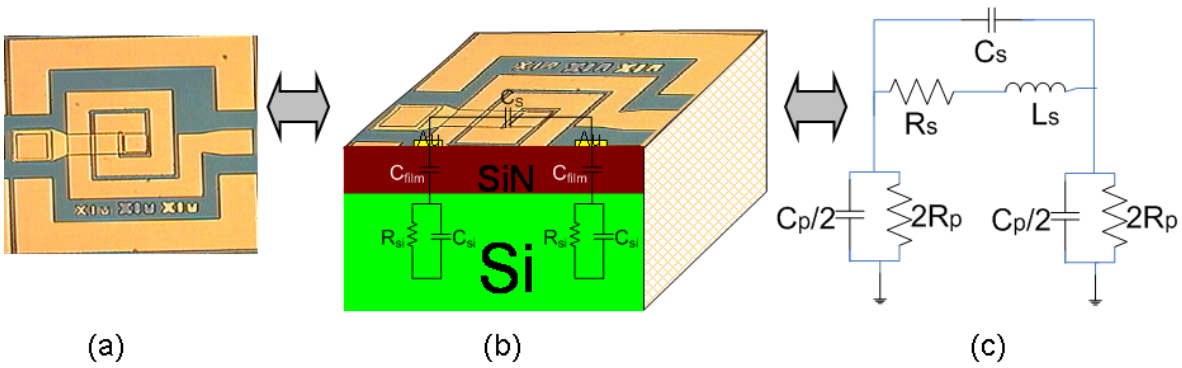


**Figure 3.1.1. (a) The top-view micrograph of a fabricated resonator, (b) a side-view schematic of the resonator shown along with the lumped element representations of its physical model, and (c) our equivalent circuit model of the resonator.**

To determine the change in the resonance frequency readout we start from the force ($F$) and stress ($\sigma$) relationship. When a force is applied to the structure, it creates stress as given in (3.1.5), where $A$ denotes the cross-sectional area of the plate. The stress causes strain (ε) in the structure as in (3.1.6) where the strain is calculated from the relationship in (3.1.7). $E$ and $l$ represent the Young's modulus (Pa) and length of the plate, respectively. The strain changes the sensor behavior mainly as a result of the modification in the capacitance. As a result we observe a change in the resonance frequency. We apply a point load to our structure to mechanically deform the active device area with the applied load. As we already know the parameters of the deflection, we determine our controllable load from (3.1.8) [48]. Here $x$, $y$, and $L$ represent the positions along beam length, the deflection and the beam length (m), respectively. $I$ is the moment of inertia ($m^4$).

$$\sigma = \frac{F}{A} \tag{3.1.5}$$

$$\sigma = E\varepsilon \tag{3.1.6}$$

$$\varepsilon = \frac{\Delta l}{l} \tag{3.1.7}$$

$$y(x) = \frac{F}{6EI}(3x^2L - x^3) \tag{3.1.8}$$

## 3.1.3 Sensor Design and Fabrication

With the aim of designing a biocompatible, high Q-factor sensor resonator chip with a small size and high frequency shift, we first need to determine the circuit that measures the change in the resonance frequency to operate either in a passive or active mode. In the case of an active circuit, minimization of the circuit space is restricted by the power supply and the device size becomes larger with a limited deformation of the device. Therefore, we prefer to use a passive circuit. Although using GaAs as the substrate material would enhance the Q-factor, we use Si for its better biocompatibility characteristics. Nonconductive Si hinders the parallel plate capacitance

and the proper operation of the resonator. On the other hand, conductive Si decreases the Q-factor. Therefore, we employ a highly resistive Si substrate.

The selection of the dielectric layer affects the capacitance and the Q-factor. $Si_3N_4$ has a relatively high dielectric constant (as high as 8) and low loss, and also it is biocompatible. There are some dielectric materials that feature lower Young's moduli than $Si_3N_4$, however, they have higher loss and lower dielectric constants, resulting in a low Q-factor and the change of resonance frequency would not be as high as that of $Si_3N_4$. As a result, considering the trade-off between high Q-factor, small dimensions and high shift of resonance frequency, we select $Si_3N_4$ as the dielectric layer.

To observe the change in the resonance frequency ($\Delta f_0$) easily, we need to have a sufficiently low Young's modulus of the dielectric material as given in (3.1.6) since the stress is set to a fixed value and Young's moduli of Si and metal are already high. Therefore, when the area of the dielectric layer is changed, the capacitance is modified as in (3.1.1) and we realize a shift in the resonance frequency, which also affects the Q-factor as in (3.1.4). In the case of metals, their Young's moduli are nearly the same, which means that the choice of the metal is trivial for the shift of resonance frequency. Although Al and Cu are mostly utilized as metal layers, they are not biocompatible. Therefore, for future *in vivo* applications in mind, we prefer to use Au as the metal layer.

When deciding on the film thickness, once again we are required to consider the critical constraints such as a high Q-factor and small allowable dimension. Thus, our approach is to favor the high capacitance, which can be obtained from the tank circuit capacitance [15], [31] as opposed to considering this element as a parasitic capacitance (as it has been previously typically treated by other research groups). Hence, we choose a film thickness ($t_{film}$) as low as $0.1\,\mu m$. Using the film capacitance for self-tuning the resonator will also increase the resonance frequency shift and improve the sensor sensitivity compared to the approach of using an external capacitor for tuning.

To realize a high-performance sensor, the width of metal line is a critical design issue because an increase in the width would also increase the Q-factor and the resonance frequency, but this would produce an associated increase in the area at the same time. Therefore, considering these constraints, we choose an optimal value for the width. Also the metal line spacing affects the device performance. A lower spacing increases resonance frequency and leads to a more compact chip. However, an increased width and decreased spacing lead to parasitic effects which would decrease the Q-factor. So the value of the spacing should be carefully adjusted. With our design methodology, we find that we do not need to consider the effect of the skin depth as much as in conventional structures, as this effect is relatively reduced and high Q-factors are still obtained; the derivation of this conclusion can be found elsewhere [15].

Increasing the number of turns of the coil decreases the Q-factor and the resonance frequency and increases the area of the chip. Two turns is the minimum number needed to produce a full coil and this is the geometry used in our design. Decreasing the total area leads to an improved Q-factor and a higher resonance frequency. Also, a smaller inner diameter increases the Q-factor and resonance frequency. However, decreasing the inner diameter to a point where it is smaller than the spacing causes additional parasitic effects. Therefore, considering the width, the spacing, the inner diameter, and the number of turns, we choose an optimal area. $R_p$, which was given in (3.1.2), represents the combined resistance of our coil model and is an effective component to determine the substrate losses. We choose a high-resistivity substrate to get a high $R_{Si}$ and thus a high $R_P$. Therefore, in our model, the substrate loss factor is nearly independent of the frequency, and also, we obtain a high Q-factor. $C_{p,}$ corresponding to the capacitive component of the combined impedance and calculated as in (3.1.3), has a significant effect on the self resonance factor. Lower $C_p$ results in an increased resonance frequency.

Taking all these different factors into account, we designed two sensor chips with the parameters determined as shown in Table 3.1.1. Here $L_C$ and $W_C$ represent total length and total width of the device, respectively. $N$ is the number of turns, $w$ is the width of each coil, and $s$ is the spacing between coils. Also $t_{film}$ and $t_{metal}$ represent the thickness of the dielectric film and the thickness of the metal, respectively.

**Table 3.1.1. Our device parameters.**

| | $L_c$ (μm) | $W_c$ (μm) | $N$ | $w$ (μm) | $s$ (μm) | $t_{film}$ (μm) | $t_{metal}$ (μm) |
|---|---|---|---|---|---|---|---|
| Sensor-1 | 340 | 340 | 2 | 60 | 10 | 0.1 | 0.1 |
| Sensor-2 | 270 | 270 | 2 | 50 | 5 | 0.1 | 0.1 |

Based on the parameters for Sensor-1, we ran a simulation using a commercially-available finite element software package (Coventorware) to monitor the strain induced in the device when a load of 1960 N is applied. Fig. 3.1.2 shows the resulting displacement field. From the simulation, we observe that the area of the dielectric film changes, modifying the value of $C_{film}$. We notice that the change in the area is not uniform, which results in a nonlinear change in $C_{film}$, and thus, in the resonance frequency, as a function of the applied load (where the resonance frequency is calculated from the point that $Q_{ind}$ becomes zero as in (3.1.4)).

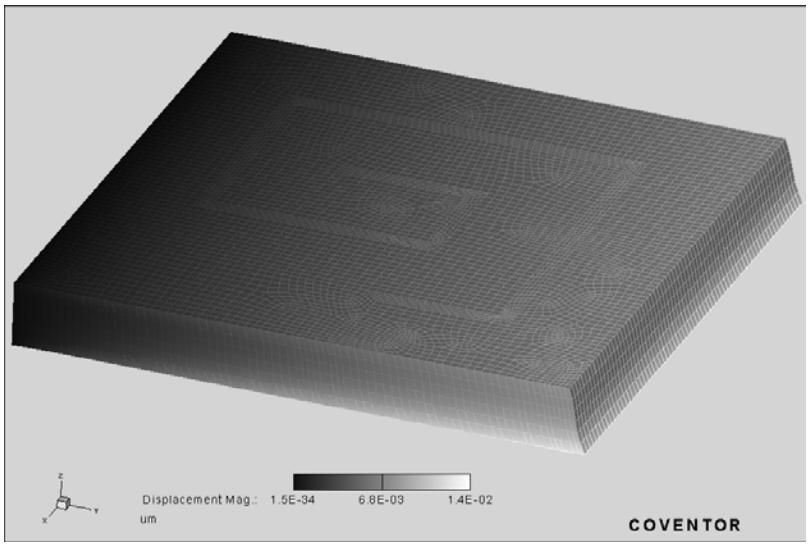


**Figure 3.1.2. Illustration of the deformed device when a load of 1960 N is applied from the bottom. The area and the thickness of the device are fixed to 340 μm x 340 μm and 500 μm, respectively. z-direction is scaled down by a factor of 10 for better visualization.**

We numerically calculated the inductance of the spiral coil ($L_s$), which is obtained by the addition of self-inductance with the positive mutual inductance and subtracted by the negative mutual inductance. We observe a very good agreement with the results obtained by the MemHenry suite of Coventorware (Table 3.1.2).

**Table 3.1.2. The theoretical and numerical $L_S$ values for Sensor-1 and Sensor-2.**

| | Theoretical $L_S$ (nH) | Numerical $L_S$ (nH) |
|---|---|---|
| Sensor-1 | 2.854 | 2.842 |
| Sensor-2 | 2.260 | 2.244 |

We fabricate our sensors using standard MEMS fabrication processes. For fabrication, the substrate is initially patterned with lithography and metallization is performed to obtain a thickness of 0.1 μm using Au. Then the structure is coated by a 0.1 μm thick $Si_3N_4$ layer using PECVD. Patterning is realized with lithography and holes are opened using wet etching by HF. The open parts are metallized with the boxcoater at a thickness of 0.1 μm (Au). Finally, the shape of the device is given by a third lithography step and the process is completed with a 0.1 μm-thick Au metallization. The fabricated device is presented in the inset of Fig. 3.1.3(a).

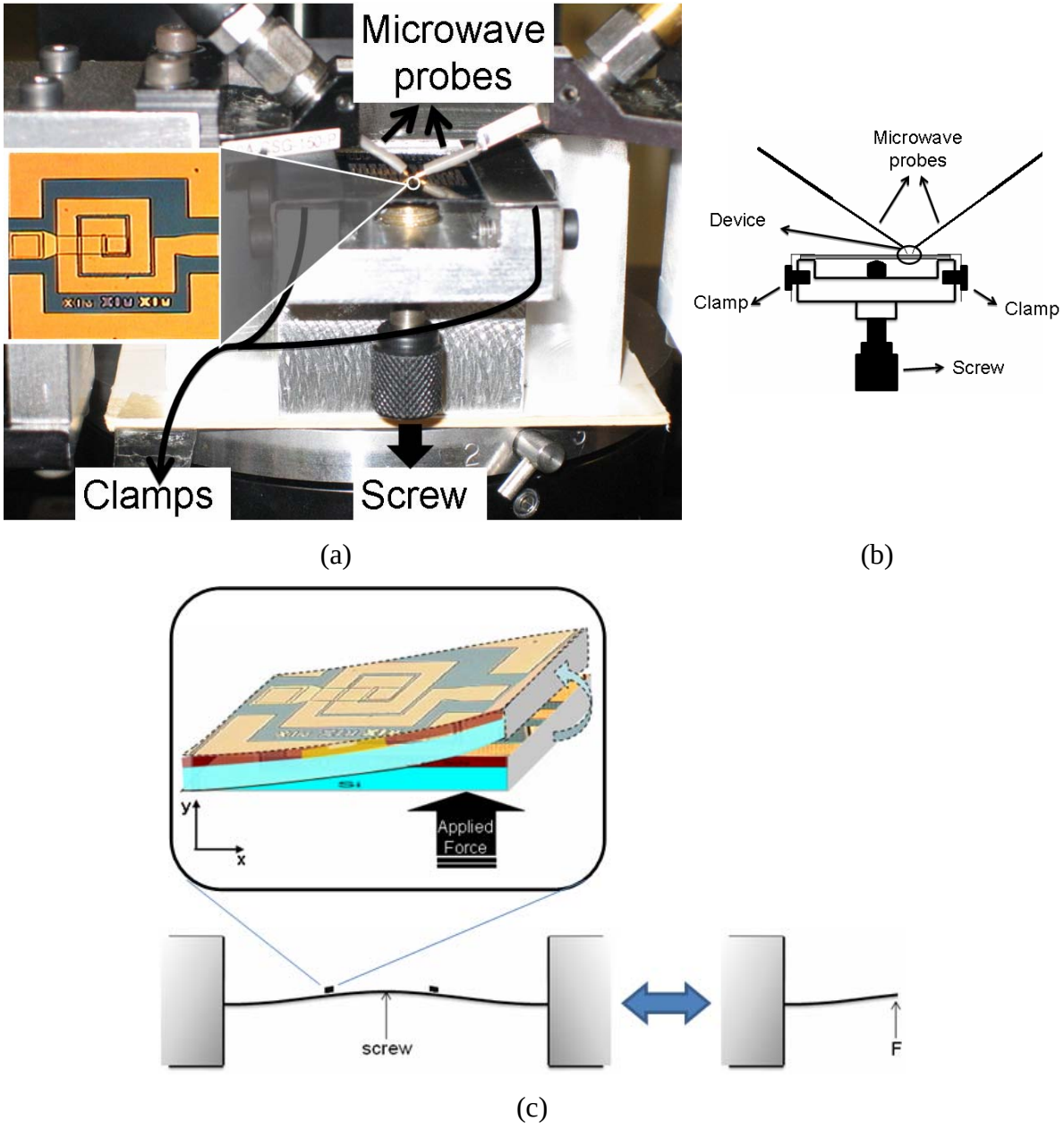


**Figure 3.1.3. (a) The experimental setup along with the fabricated sensor in the inset, (b) the cross sectional sketch of our experimental setup and its components, and (c) illustration of the mechanical deformation when the force is applied.**

## 3.1.4 Experimental Characterization

The experimental characterization consists of applying a point load in a controlled manner (Fig. 3.1.3). We use two thin clamps at the edges to fix the silicon substrate as shown in Fig. 3.1.3(a) and Fig. 3.1.3(b). There is a hole in the middle and we placed the silicon substrate into this aperture, fixing the substrate to the edges of the experimental apparatus sketched in Fig. 3.1.3(b). We used the screw below the silicon substrate to control and modify the load in a predictable manner. We used an ultra fine adjustable screw so that we could easily modify the applied load. The tip of the screw is a critical part as it should not penetrate or cause failures in the silicon substrate when applying high loads. After fixing our substrate, we measure $S_{21}$ parameters of our device with microwave probes as presented in Fig. 3.1.3(a) and Fig. 3.1.3(b). When we apply load to the whole chip by using screw, a point load is applied to our device while it deforms on the chip as shown in Fig. 3.1.3(c).

In Fig. 3.1.4(a) and Fig. 3.1.4(b), $S_{21}$ parameters (in dB) are given as a function of the frequency for Sensor-1 and Sensor-2, respectively. In Fig. 3.1.4(c) and Fig. 3.1.4(d) magnified views of the resonance regions are also shown for Sensor-1 and Sensor-2, respectively. One can clearly see the differences between the sensor responses without any deformation (no load) and then also these with deformation. In the case of no deformation for Sensor-1, the resonance frequency was measured to be 11.48 GHz, also given in Table 3.1.3, with a Q-factor of 59.98. When we apply 1960 N, the resonance frequency changes to 11.72 GHz, indicating a 240 MHz shift (also summarized in Table 3.1.4). When we apply a load of 2940 N, the resonance frequency increases to 11.78 GHz and for 3920 N, it becomes 11.81 GHz (Table 3.1.3). Therefore, for a load of 2940 N, we obtain a shift of 2940 MHz and for 3920 N, a shift of 330 MHz in the resonance frequency as compared to the initial condition (Table 3.1.4). Also, the Q-factor of the sensor changes from 59.98 to 70.35 when 1960 N load is applied. For a load of 2940 N, the Q-factor is 74.32 and for 3920 N, the Q-factor is 76.00 (Table 3.1.5).

Fig. 3.1.4(b) shows $S_{21}$ parameter of Sensor-2 in decibels as a function of the frequency. Similar to Sensor-1, the resonance frequency increases with the applied load. For the no-deformation case, the resonance frequency is 13.59 GHz (Table 3.1.3) and the Q-factor is 69.91 (Table 3.1.5). After application of 3920 N load, the resonance frequency becomes 13.95 GHz, representing a resonance frequency shift of 360 MHz (Table 3.1.4) with a Q-factor of 95.39. For 1960 N a 13.84 GHz resonance frequency was measured (Table 3.1.3) with an 87.87 Q-factor (Table 3.1.5).

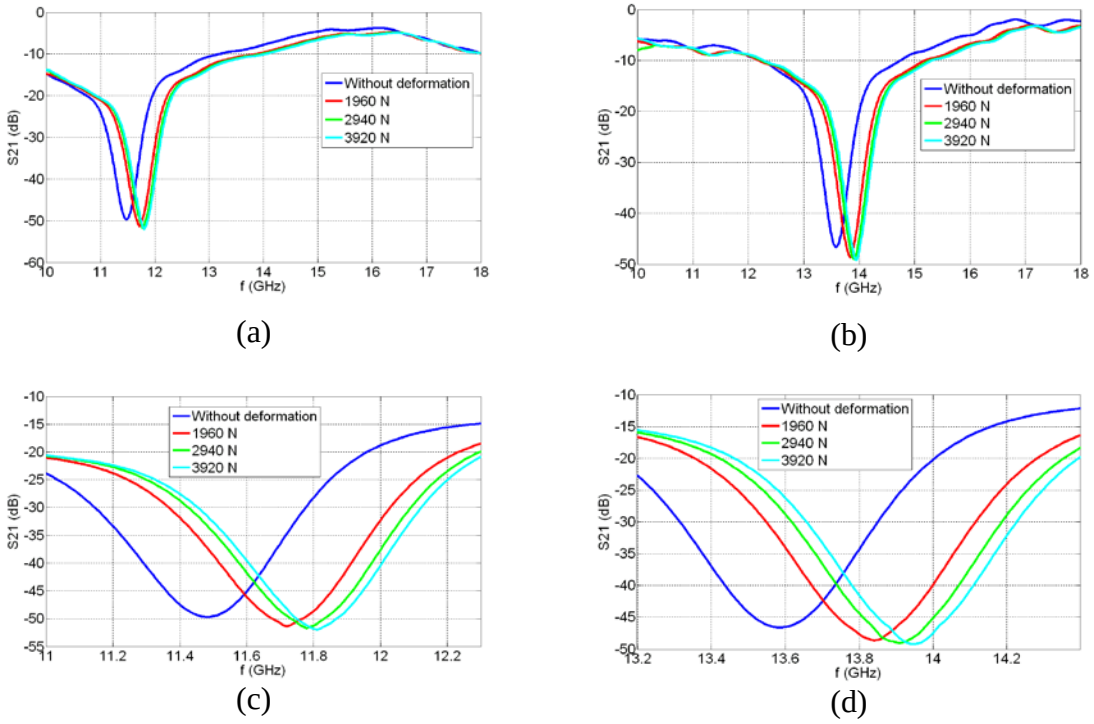


**Figure 3.1.4. Experimental measurements of $S_{21}$ parameters as a function of frequency for (a) Sensor-1 and (b) Sensor-2, along with their zoom-in resonance regions for (c) Sensor-1 and (d) Sensor-2, respectively, for the cases without deformation and when loads of 1960 N, 2940 N and 3920 N are applied.**

**Table 3.1.3. The resonance frequencies of the sensors with the changing load values.**

| Load | No load | 1960 N | 2940 N | 3920 N |
|---|---|---|---|---|
| Sensor-1 | 11.48 GHz | 11.72 GHz | 11.78 GHz | 11.81 GHz |
| Sensor-2 | 13.59 GHz | 13.84 GHz | 13.91 GHz | 13.95 GHz |

**Table 3.1.4. The shift of resonance frequencies of the sensors with the changing load values.**

| Δ Load | 1960 N | 2940 N | 3920 N |
|---|---|---|---|
| Sensor-1 | 240 MHz | 300 MHz | 330 MHz |
| Sensor-2 | 250 MHz | 320 MHz | 360 MHz |

**Table 3.1.5. Q-factors with the changing load values.**

| Load | No load | 1960 N | 2940 N | 3920 N |
|---|---|---|---|---|
| Sensor-1 | 59.98 | 70.35 | 74.32 | 76.00 |
| Sensor-2 | 69.91 | 87.87 | 89.22 | 95.39 |

From these experimental results, it is clear that the resonance frequency increases with the applied load. This can be explained by the decrease in the area, and hence the resulting decrease in the capacitance (Fig. 3.1.2), leading to an increase in the resonance frequency with the applied load, as was also numerically verified by Coventorware. In this experiment, we also observe that the shift is not linear with respect to the applied load and thus the induced strain (which is experimentally obtained in the reference strain measurements using high-quality semiconductor based wired strain gauges, made of Kyowa, Japan, with a gauge factor of 178) (Fig. 3.1.5). The decrease in the area of the capacitance is not linear so the change in the capacitance is not linear and also capacitance affects the resonance frequency nonlinearly as in (3.1.4), and, accordingly, our observation that the change in the resonance frequency is nonlinear with the applied load is congruent with our numerical simulations.

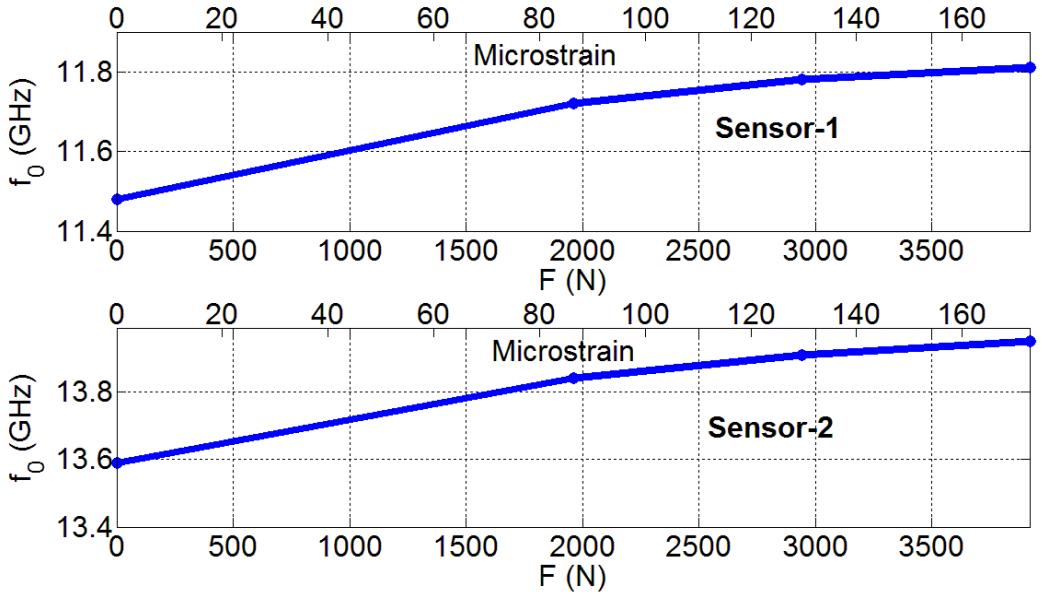


**Figure 3.1.5. Resonance frequency ($f_0$) as a function of the externally applied load and the induced strain (microstrain) for Sensor-1 and for Sensor-2.**

We can consider the shift of resonance frequency from other perspectives. For example, we can define sensitivity with respect to the applied force as $\frac{\Delta f_0}{F}$. Since we have similar geometries in Sensor-1 and Sensor-2, which are both rectangular, and they are fabricated using the same fabrication procedure, they are expected to have nearly the same level of sensitivity. For Sensor-1 we have 330 MHz resonance frequency shift with 3920 N of applied load. So we have 0.0842 MHz/N sensitivity. For Sensor-2 we have 360 MHz resonance frequency shift with 3920 N of applied load, and hence, 0.0918 MHz/N sensitivity. The sensor with a higher $f_0$ will tend to slightly have a higher sensitivity since a higher frequency means a slightly higher shift. Also, we can define sensitivity with respect to the induced strain as $\frac{\Delta f_0}{\varepsilon}$. Because of the structure of our load setup, which is explained in detail and illustrated in Fig. 3.1.2, the minimum strain that we can reproducibly apply is 81.5 microstrain, while the maximum strain that we can controllably apply is 172.8 microstrain. For Sensor-1 we have 330 MHz resonance frequency shift with an induced strain of 172.8 microstrain while we have 360 MHz resonance frequency shift with

172.8 microstrain for Sensor-2. So for Sensor-1, we have 1.9 MHz/microstrain sensitivity while we have 2.1 MHz/microstrain sensitivity for Sensor-2. Similar to the sensitivity defined with respect to the applied load, the sensor with higher $f_0$ expectedly yields a slightly higher sensitivity also with respect to strain. For another comparison, we can use another definition: relative shift, which is $\frac{\Delta f_0}{f_0}$ at a given applied load. For Sensor-1, under 3920 N, we have a shift of 330 MHz at 11.48 GHz resonance frequency; thus we have a relative shift of 2.88%. For Sensor-2 we have 360 MHz shift at 13.59 GHz resonance frequency; thus we have a relative shift of 2.65%. From these results, we observe that we have nearly the same sensitivities and relative shifts. Also, theoretically we consider that if two sensors exhibit the same relative shift, the sensor that has a higher resonance frequency will have a higher change of resonance frequency, and hence a higher sensitivity. Experimentally, we find out that although Sensor-2 has a slightly lower relative shift compared to Sensor-1, Sensor-2 has a slightly higher sensitivity. By using different geometries, different fabrication procedures and different frequencies, we obtained higher sensitivity levels, as presented in subsequent sections.

Another important conclusion of our experiments is that the Q-factor of the device is different for each applied load and the resulting strain, as was predicted theoretically. The increase is shown in Fig. 3.1.6. When $L_C$ decreases, the resonance frequency and the Q-factor are increased while the area decreases, as calculated in (3.1.4). Therefore, it is expected that Sensor-2 has a higher resonance frequency and Q-factor compared to Sensor-1. When the capacitance is decreased, the Q-factor is improved as calculated from (3.1.4). Therefore experimentally we observe an increase both in the resonance frequency and the Q-factor together as shown in Fig. 3.1.6. Also, since the capacitance change is not linear with applied load and change of the capacitance affects the Q-factor nonlinearly from (3.1.4), the Q-factor change is theoretically expected to be nonlinear with the applied load. From Table 3.1.5, we also experimentally observe that the increase in the Q-factor with applied load is not fully linear.

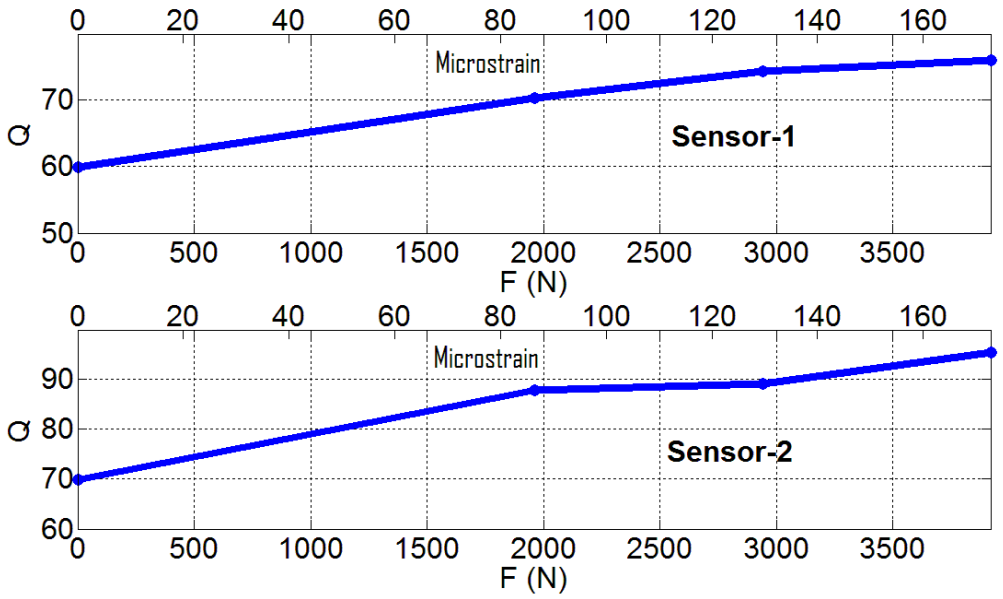


**Figure 3.1.6. Q-factor as a function of the applied load and the induced strain (microstrain) for Sensor-1 and Sensor-2.**

There is a strong demand for implantable chips that measure the change in hardware stress without any external wiring. This would allow the treating clinician to remotely measure and report the information. Therefore, to verify the wireless performance of our sensor, we utilized a telemetry-based implantable sensing system to monitor the resonance frequency shift as a function of the physical load (Fig. 3.1.7). This system consists of two antennas on the chip to serve as external antennas. Between these antennas there is the device under test used as the sensor. The telemetric sensor and the antennas have the same dimensions as those of Sensor-2.

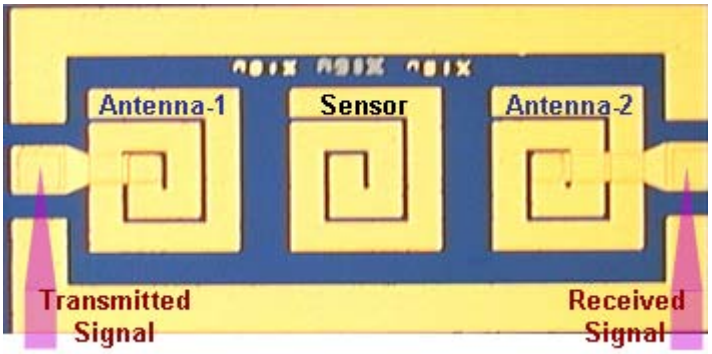


**Figure 3.1.7. A plan-view micrograph of our fabricated 270 µm×270 µm on -chip sensor along with the on-chip antennas for communication.**

Similar to the previous cases, we detected strain by measuring the resonance frequencies of the system without any applied load and after applying different loads to the sensor chip. By using three similar resonators, we set up a telemetric system on the same chip. The $S_{21}$ parameter is plotted as a function of the frequency in Fig. 3.1.8. Just like the previous cases, the area of the chip decreases and the resonance frequency increases with the applied load. Without deformation, the resonance frequency and the Q-factor were found to be 13.71 GHz and 38, respectively. After applying a 3920 N, the resonance frequency and the Q-factor were measured to be 13.9 GHz and 46, respectively, representing a resonance frequency shift of 190 MHz. Although this triplet configuration on the same chip does not fully represent a truly free-space telemetric setup, this experiment provides us with a preliminary measurement towards targeted telemetric demonstration.

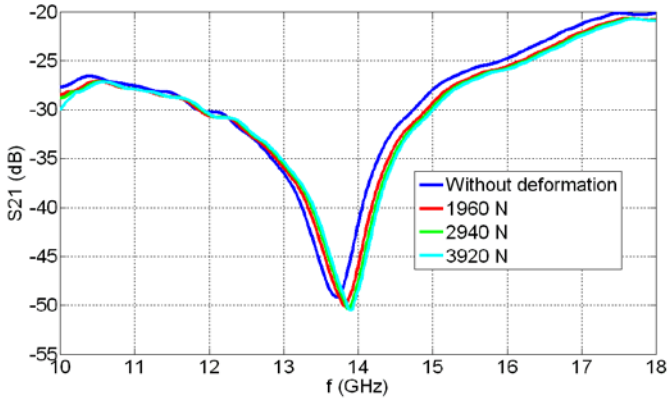


**Figure 3.1.8. Experimental measurement of $S_{21}$ parameters for the sensor under different loads taken by using the transmitter and receiver antennas.**

## 3.1.5 Conclusion

We designed, fabricated, and experimentally characterized a high Q-factor, bio-implantable RF-MEMS strain sensor to monitor the fracture healing process by measuring the change in the strain. Such a sensor of our design can withstand loads up to 3920 N without deterioration in the Q-factor, even for chip areas smaller than 0.1 $mm^2$. When a load of 3920 N is applied to the sensor with an area of 340 μm x 340 μm (Sensor-1), the resonance frequency is shifted by 330 MHz and the Q-factor is increased from ~60 to ~76. As the area is decreased to 270 μm x 270 μm (Sensor-2), we observe that the resonance frequency shift becomes 360 MHz and the Q-factor is increased from ~70 to ~95. We both theoretically and experimentally showed that our sensors can be utilized for assessing the osseous fractures through monitoring the shift in the resonance frequency. We also showed that our approach can be modified to work telemetrically. By fabricating three devices, one sensor and two antennas on the same chip, to set up a telemetric system, we demonstrated that the wireless measurement of the resonance frequency shift is possible. In this case, the resonance frequency and the Q-factor are increased when a load is applied. As a result of this pilot study, we believe that, by observing the change in resonance frequency, surgeons can evaluate the fracture healing process longitudinally. This thesis work presents the first theoretical and experimental proof of this concept. For human implantation

applications, the resonance frequency needs to be shifted to a lower range where absorption becomes less considerable in soft tissue. Our subsequent work in this thesis includes improving our sensors to operate within the constraints of the implantation applications.

## 3.2 Circular High-Q Resonating Isotropic Strain Sensors with Large Shift of Resonance Frequency under Stress

This section is based on the publication "Circular High-Q Resonating Isotropic Strain Sensors with Large Shift of Resonance Frequency under Stress" **R. Melik**, E. Unal,N. K. Perkgoz, C.M. Puttlitz, and H. V. Demir, *Sensors 9, 9444-9451 (2009).* Reproduced (or 'Reproduced in part') with permission from Molecular Diversity Preservation International, Basel, Switzerland. Copyright 2009 Molecular Diversity Preservation International, Basel, Switzerland.

In this section [49], we present circular architecture bioimplant strain sensors that facilitate a strong resonance frequency shift with mechanical deformation. The intended clinical application area of these sensors is for *in vivo* assessment of bone fractures. Using a rectangular geometry, we obtain a resonance shift of 330 MHz for a single device and 170 MHz for its triplet configuration (with three side-by-side resonators on chip) under an applied load of 3,920 N. Using the same device parameters with a circular isotropic architecture, we achieve a resonance frequency shift of 500 MHz for the single device and 260 MHz for its triplet configuration, demonstrating substantially increased sensitivity.

### 3.2.1. Introduction

Fixation plates are routinely used for major bone fracture cases. As the healing tissue develops stiffness and strength, the load borne by the plate decreases [1]. During this process, a sensor capable of monitoring strain telemetrically and in real time is highly desirable. When force is applied to the sensor via its attachment to the fixation plate, the resulting strain is observed via a resonance frequency ($f_o$) shift. Using this emerging technology, physicians would be able to assess the healing process by examining these temporal changes in strain.

In the previous section, we presented high quality factor (Q-factor) on-chip resonators [31] and demonstrated the proof-of-concept for utilizing the resonance frequency shift as an indirect measure of strain [39]. In this section, we demonstrate sensors with significantly increased Q-factor and resonance frequency shift compared to the architectures used in the previous sections. Here we present a circular architecture RF-MEMS bioimplantable strain sensor that demonstrates a substantially higher Q-factor and larger frequency shift compared to a rectangular architecture.

## 3.2.2. Design and Fabrication

For our resonators, we aim for a high Q-factor by using bio-compatible materials with a maximum possible resonance frequency shift. To design the resonator in a distributed spiral coil architecture with a high Q-factor (Fig. 3.2.1), we consider the effects of substrate, dielectric material, dielectric thickness ($t_{film}$), metal material, metal layer thickness ($t_{metal}$), metal width (w) and spacing (s), number of turns (N), and area ($W_c$ x $L_c$) as explained in [31]. Further details of the formulas and techniques for Q-factor enhancement can also be found in [19], [22]-[25], [27]-[30], [38]. For biocompatibility, we choose to use silicon as the substrate, gold as the metal layer, and $Si_xN_y$ as the dielectric layer. Our main design strategy in achieving a maximum Q-factor with minimum spacing relies on the use of the distributed film capacitance as the LC tank circuit capacitance. The dominant parameter driving the resonance frequency shift is the on-chip capacitance change with mechanical deformation, allowing for strain measurement from the sensor without requiring additional circuitry. Although strain sensors using digital electronics [50], [51] have been reported in the archival literature, this section represents the first account of an RF-based MEMS strain sensor in different architectures (circular geometries).

The following details using a circular architecture that better optimizes the aforementioned design aims. We compare two sensors with the same design parameters in rectangular and circular geometries shown in Fig. 3.2.1. In both cases, the total size ($W_c \times L_c$) is 340 µm × 340

μm. In addition, both architectures have 2 turns (N), 60 μm wide metal width (w) and 10 μm wide spacing between coil segments (s). Their metal film thickness ($t_{metal}$) is 0.1 μm while their dielectric film thickness ($t_{film}$) is also 0.1 μm. The circular architecture has an effectively reduced total area compared to the rectangular geometry with the same dimensions. Thus, for the circular architecture, we obtain smaller film capacitance and coil inductance, yielding a higher $f_o$. Also, we have lower coil resistance, lower loss, higher substrate resistance, and lower substrate capacitance. This produces a higher substrate loss factor and self-resonance factor, which is discussed in detail in [31]. As a result, with smaller spacing and higher $f_o$ in the circular geometry, we achieve a higher inductor $Q_{ind}$-factor (and thus a higher resonator Q-factor).

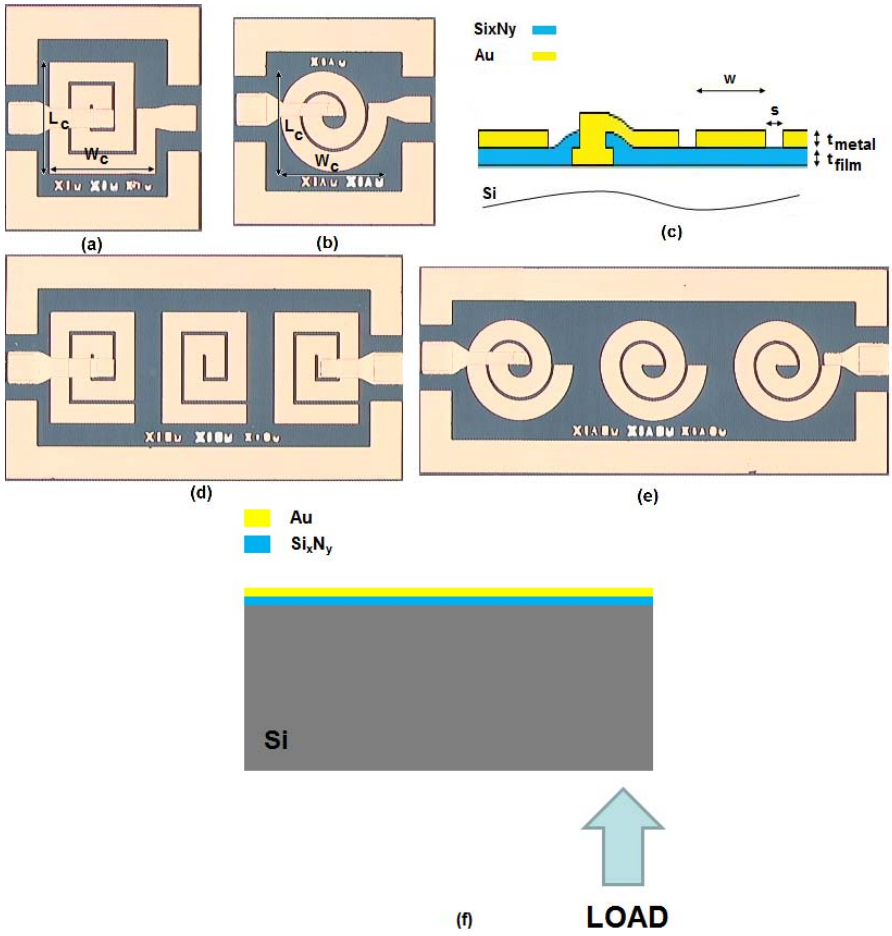


**Figure 3.2.1. (a) Top-view single rectangular device, (b) top-view single circular device, and (c) cross-sectional view of the device. (d) Top-view rectangular triplet configuration and (e) top-view circular triplet configuration. (f) Schematic illustration of the externally applied load from the side.**

We approach the increase in the resonance frequency shift from two perspectives. First, the deformation is equally effective in any direction, thanks to the isotropic geometry as depicted in Fig. 3.2.2(a). On the contrary, in a rectangular geometry, there is a preferential, anisotropic deformation, which dominates unilaterally (effective on only one side at a time) as illustrated in Fig. 3.2.2(b). In Fig. 3.2.2, we can see that the maximum deformation of circular and rectangular shapes are the same but in rectangular geometry, one side is not deformed while in circular geometry, the whole geometry deformation is nearly the same. Therefore, the capacitance change in the circular case is higher than that in the rectangular case with the same starting initial capacitance value because the deformation acts to change the whole geometry. Hence, the associated resonance frequency shift is expected to be larger. Next, even if we have the same frequency shift ratio, $\Delta f_o/f_o$ (relative shift), the frequency shift is higher in the circular geometry since it possesses a higher $f_o$. If we combine these two aspects, we have much higher shift for the circular case. Therefore, using the circular architecture, we expect to obtain a higher $\Delta f_o$ and a higher sensitivity, e.g., defined as $\partial f_o/\partial F$ (or as $\partial f_o/\partial \varepsilon$) with respect to the applied load (F) [or the induced strain ($\varepsilon$)]. Simulating $S_{21}$ parameters for the rectangular and circular devices and their triplet configurations, we also obtain higher resonance frequencies and higher Q-factors for the circular geometry. Thus, we predict better performance with the circular architecture.

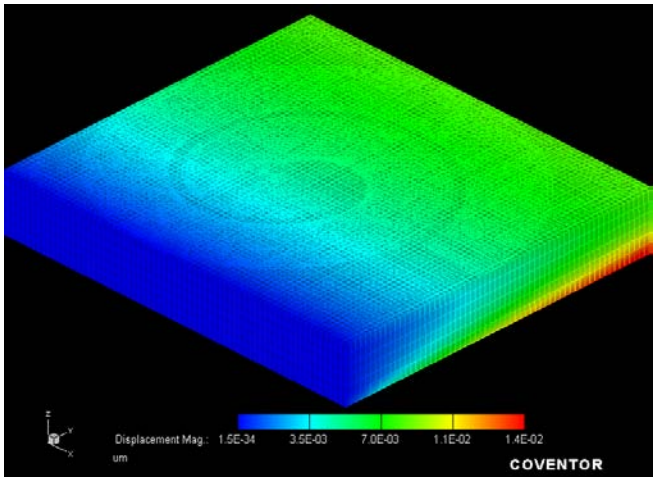


(a)

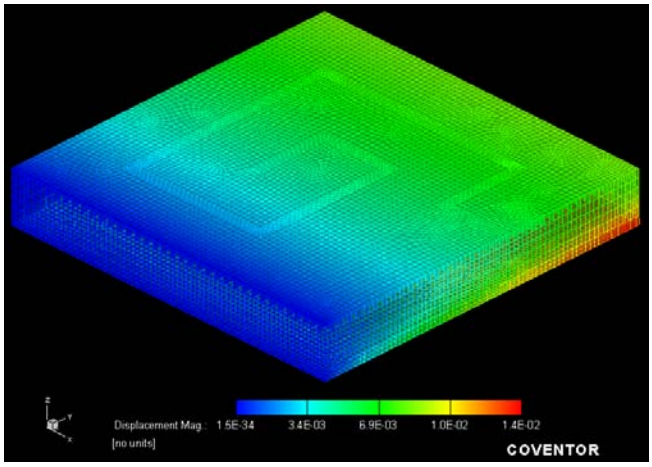


(b)

**Figure 3.2.2. Coventorware simulations of the strain distribution of the deformed devices when a load of 1,960 N is applied from the bottom (a) in a circular geometry and (b) in a rectangular geometry. The z-direction is scaled down by a factor of 10 for a better visualization of the image.**

For the implementation of our devices, our fabrication process begins with deposition and patterning of a 0.1 μm thick metal contact layer (Au) on the substrate (Si), and subsequent deposition of a 0.1 μm thick dielectric layer ($Si_xN_y$), a cross-sectional view of which is shown in Fig. 3.2.1(c). We obtained the specific patterning with lithography and wet etching by hydrofluoric acid (HF). Subsequently, we metalized the open parts with 0.1 μm thick Au layer.

Finally, another 0.1 μm thick final metal layer (Au) is deposited on top. The fabricated devices can be seen in Fig. 3.2.1(a),(b),(d),(e).

## 3.2.3. Experimental Characterization and Analysis

To characterize our fabricated devices, we apply a point load to our devices in a controllable manner using the same method as explained in [39], where its schematic illustration is given in Fig. 3.2.1(f), and measure the device $S_{21}$ parameter in response to the applied load. Thus, the change in resonance frequency and the Q-factor due to the applied load are determined. Our experimental setup includes an adjustable ultrafine-screw that can be adjusted to push towards the backside of the sensor. When the tip of this screw just touches the sensor backside, no load is applied, as verified by our reference strain gauge (made by Kyowa, Japan, with a gauge factor of 178). The screw is further twisted to apply load and induce strain. We confirmed the levels of strain induced with the position of the ultrafine-screw using our reference strain gauge.

For bioimplant sensing applications, there is an absolute requirement to measure and report strain remotely in the absence of wiring. Thus, for the current and future evaluations of this technology we need to measure and compare the telemetric performance of these sensors. To this end, we configure three resonators side by side on the same chip (in triplet configuration) and obtain an on-chip telemetry system. Although this on-chip system does not fully comply with the actual clinical application, it provides a robust methodology to compare different devices with respect to their telemetric operation. In this triplet configuration, the middle device serves as the sensor, with the lateral devices serving as the transmitter and receiver antennas. For calibration purposes, we measure the $S_{21}$ parameter of the case where there are only transmitter and receiver antennas, and then measure the $S_{21}$ parameters of our triplet configuration to obtain the resonance frequency and Q-factor of the whole measurement system. When the load is applied to the chip, the calibrations are again repeated with the same procedure as explained above to observe the changes in the resonance frequency and Q-factor. Also, using identical antennas guarantee to see the resonance frequency of the sensor since the working band of the antenna will definitely catch

the resonance frequency of the sensor. Since the triplet method is used for easy coupling, using the antennas identical to the sensor makes our measurements further easier. A more detailed description of the triplet configuration operating principles is given in previous sections and [39].

The human body presents a more complex environment compared to the lab environment. This side-by-side testing scenario (in triplet configuration) is an idealized one, as this configuration provides merely an *in vitro* characterization platform. Having characterized the operation of these sensors in a side-by-side configuration, our subsequent research work includes performing animal model experiments as discussed later. We anticipate that there will be differences in the performance of our sensor when placed in the *in vivo* environment. Specifically, we expect reduced sensitivity levels due to the complex nature of the *in vivo* measurement medium. We also expect that the circular architecture will greatly enhance some of the proposed application areas for this sensor thanks to the significantly improved sensing performance of the circular designs.

Fig. 3.2.3(a) through Fig. 3.2.3(d) present $S_{21}$ (in dB) as a function of operating frequency for the single rectangular, single circular, triplet rectangular, and triplet circular configurations, in respective order. All of these figures also include a zoom-in view (in the inset) of the data around the resonance frequencies.

Table 3.2.1 lists the measured resonance frequencies in response to the applied loading, clearly showing that the resonance frequency increases with the applied force due to decreasing area, and hence, decreasing capacitance. Also, all of these experimental $S_{21}$ data measured under zero external load are in agreement with our numerical simulations (in CST Microwave Studio).

In Table 3.2.1, we also present the resonance frequency changes. The resulting resonance frequency increase is higher for all of the circular device geometries as explained above. Since the area decrease is not linear and the capacitance is not linearly proportional to the resonance frequency, the resulting frequency increase is expectedly nonlinear. In addition, since the

frequency shift is much higher in the circular cases compared to the rectangular cases, we observe higher relative shift and higher sensitivity for the circular cases in Table 3.2.1.

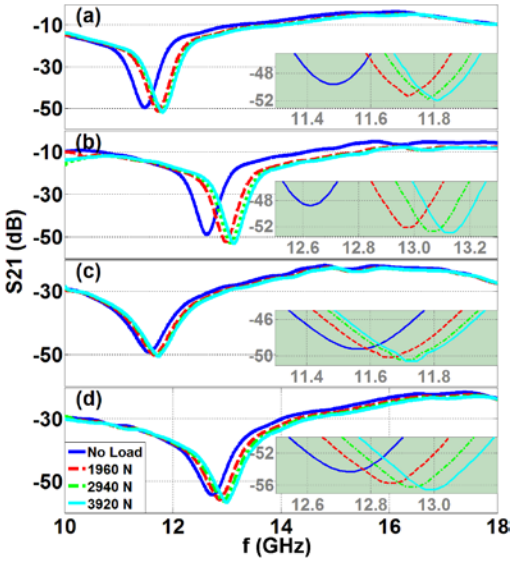


**Figure 3.2.3. Experimental measurements of $S_{21}$ parameters (dB) as a function of operating frequency (GHz) for (a) the single rectangular device, (b) the single circular device, (c) the rectangular triplet configuration, and (d) the circular triplet configuration under the applied loads of 1,960 N, 2,940 N, and 3,920 N, along with their zoom-in $S_{21}$ parameters (dB) *vs.* operating frequency (GHz) (where the numbers of inset axes are grey colored) given around their resonances in the insets.**

**Table 3.2.1. Resonance frequencies, resonance frequency shifts, relative shifts, Q-factors, and sensitivities of our devices given as a function of changing load and induced strain levels.**

| Load (N) | | No load | 1960 | 2940 | 3920 |
|---|---|---|---|---|---|
| **Microstrain** | | **0** | **81.5** | **127.7** | **172.8** |
| **Single rect.** | $f_o + \Delta f_o$ (GHz) | 11.48 | 11.72 | 11.78 | 11.81 |
| | $\Delta f_o$ (MHz) | -- | 240 | 300 | 330 |
| | $\Delta f_o/f_o$ (%) | -- | 2.1 | 2.6 | 2.9 |
| | Q | 59.979 | 70.348 | 74.324 | 76.000 |
| | Sensitivity | 0.0842 MHz/N or 1.9 MHz/microstrain | | | |
| **Single circ.** | $f_o + \Delta f_o$ (GHz) | 12.63 | 12.98 | 13.07 | 13.13 |
| | $\Delta f_o$ (MHz) | -- | 350 | 440 | 500 |
| | $\Delta f_o/f_o$ (%) | -- | 2.8 | 3.5 | 4.0 |
| | Q | 72.461 | 91.667 | 93.025 | 93.786 |
| | Sensitivity | 0.1276 MHz/N or 2.9 MHz/microstrain | | | |
| **Triplet rect.** | $f_o + \Delta f_o$ (GHz) | 11.56 | 11.66 | 11.71 | 11.73 |
| | $\Delta f_o$ (MHz) | -- | 100 | 150 | 170 |
| | $\Delta f_o/f_o$ (%) | -- | 0.9 | 1.3 | 1.5 |
| | Q | 33.801 | 36.347 | 38.243 | 39.231 |
| | Sensitivity | 0.0434 MHz/N or 1.0 MHz/microstrain | | | |
| **Triplet circ.** | $f_o + \Delta f_o$ (GHz) | 12.73 | 12.86 | 12.93 | 12.99 |
| | $\Delta f_o$ (MHz) | -- | 130 | 200 | 260 |
| | $\Delta f_o/f_o$ (%) | -- | 1.0 | 1.6 | 2.0 |
| | Q | 44.033 | 50.431 | 53.364 | 55.442 |
| | Sensitivity | 0.063 MHz/N or 1.5 MHz/microstrain | | | |

Table 3.2.1 also provides Q-factor data, which are observed to be high despite the relatively small chip sizes. These Q-factors are particularly higher in the circular case with a smaller area. The Q-factor is increased as the load magnitude is increased due to a lower $C_{film}$, as discussed in [31] and [39]. The Q-factor also increases for the telemetric case of the circular case compared to the rectangular case. However, in the telemetric operation, due to coupling between resonators, the signal is decreased and Q-factors are reduced for both of the rectangular and circular cases compared to the single device cases. Our experimental apparatus can reproducibly apply a minimum strain of 81.5 microstrain, while the maximum strain is 172.8 microstrain. Therefore, it is not possible to make a direct measurement of the minimum detectable strain level for our sensors. Since the resolution of the network analyzer that we use in our experiments is 1 Hz

(given the typical noise level in our experiments), we find the resolution of our sensors in the strain range across which they are tested by dividing this minimum detectable frequency to their sensitivities. From this calculation, we obtain 526.3 femtostrain for single rectangular device and 344.8 femtostrain for single circular device. These resolutions are better than those reported in [51].

Another interesting point for discussion is the hysteresis behavior. When different levels of external load are successively applied without allowing the mechanical setup to fully relax into the new loading conditions (typically in a time scale of minutes), we observe a memory effect and see a hysteresis in the experimental characterization of these sensors. The sensors in circular geometry exhibit a wider hysteresis loop as expected because they are more sensitive sensors, compared to those in the rectangular geometry. However, if one waits long enough (minutes) between successive force levels, mechanical relaxation is completed and no hysteresis is observed. The experimental data presented here is for the case of no hysteresis.

## 3.2.4. Conclusion

In summary, we have designed, fabricated, and experimentally characterized isotropic circular strain sensor resonators that allow for higher Q-factors with smaller spacing compared to rectangular designs. The circular architecture enables a significantly higher resonance frequency shift and sensitivity (both with respect to applied force and induced strain) because of its isotropic geometry. This results in a substantial improvement in the performance of these resonators for use as bioimplant strain sensors. With their promising properties and biocompatibility, our sensors are good candidates for the investigation and assessment of osseous fractures through monitoring the shift in the resonance frequency in response to the acting load.

## 3.3 RF-MEMS Load Sensors with Enhanced Q-factor and Sensitivity in a Suspended Architecture

This section is based on the submission to Microelectronic Engineering as "RF-MEMS Load Sensors with Enhanced Q-factor and Sensitivity in a Suspended Architecture" **R. Melik,** E. Unal, N. K. Perkgoz, C.M. Puttlitz, and H. V. Demir. Reproduced (or 'Reproduced in part') with permission from Molecular Elsevier B.V. Copyright 2010 Elsevier B.V.

In this section [52], we present and demonstrate RF-MEMS load sensors designed and fabricated in a suspended architecture that increases their quality-factor (Q-factor), accompanied with an increased resonance frequency shift under load. The suspended architecture is obtained by removing silicon under the sensor. We compare two sensors that consist of 195 μm × 195 μm resonators, where all of the resonator features are of equal dimensions, but one's substrate is partially removed (suspended architecture) and the other's is not (planar architecture). The single suspended device has a resonance of 15.18 GHz with 102.06 Q-factor whereas the single planar device has the resonance at 15.01 GHz and an associated Q-factor of 93.81. For the single planar device, we measured a resonance frequency shift of 430 MHz with 3920 N of applied load, while we achieved a 780 MHz frequency shift in the single suspended device. In the planar triplet configuration (with three devices placed side by side on the same chip, with the two outmost ones serving as the receiver and the transmitter), we observed a 220 MHz frequency shift with 3920 N of applied load while we obtained a 340 MHz frequency shift in the suspended triplet device with 3920 N load applied. Thus, the single planar device exhibited a sensitivity level of 0.1097 MHz/N while the single suspended device led to an improved sensitivity of 0.1990 MHz/N. Similarly, with the planar triplet device having a sensitivity of 0.0561 MHz/N, the suspended triplet device yielded an enhanced sensitivity of 0.0867 MHz/N.

## 3.3.1. Introduction

In the case of major fractures in humans, fixation plates are commonly implanted to facilitate bony healing. When the plate is implanted, it assumes a majority of the load and demonstrates a relatively high associated strain. During the course of healing, the tissue consolidates and the strain in the plates decreases. The strain change profile over time can be found in [1]. To monitor the healing process, a bio-implantable sensor is needed to observe the strain change in real-time. For this purpose, we present RF-MEMS resonator sensors that shift their resonance frequency when an external force is applied and strain occurs. The structure of these sensors is based on spiral RF coil architecture that provides a distributed LC tank circuit. The operating principle of these sensors relies on the resonance frequency shift as a result of the dielectric area (and thus the film capacitance between the metal and the substrate) changing with the externally applied load. Therefore, using these RF-MEMS load sensors, the induced strain can in principle be monitored in real time to observe the fracture healing process by tracking the shift of resonance frequency. While there are also some other bio-sensor reports in the literature [44]-[47], [53], our sensors are unique in that they provide the ability to monitor the strain telemetrically and with small dimensions.

Previously, we developed on-chip resonators [15], [31]. In [31], the highest Q-factor with the smallest size at high frequency (15 GHz) was demonstrated. We also showed proof-of-concept of resonator-based sensors in [39]. Here, we show and demonstrate RF-MEMS load sensors designed and fabricated in a suspended architecture to achieve a higher shift in resonance frequency and an enhanced level of Q-factor and sensitivity compared to the previous resonators.

In this section, we introduce the effects of suspended architecture on a resonator for RF-MEMS bio-implant sensors, which rely on resonance frequency shift to monitor fracture healing. Using a silicon substrate to fabricate our chips, we describe the suspended architecture obtained by etching the silicon though a carefully designed mask. This new design, which is obtained by partially removing the substrate of the single planar device, is called the single suspended device. Applying load to both of these devices (planar *vs.* suspended), we observed their resonance

frequencies, change in their resonance frequencies, and their Q-factors. We found a higher Q-factor for the single suspended device compared to single planar device. Further, the single suspended device led to a higher resonance frequency ($f_0$) shift compared to the single planar device. We also achieved a higher $f_0$ shift compared to our previously published data in [39] as a result of partially etching the substrate. The rest of this section presents our theoretical background and design process, fabrication processes, and experimental characterization and analysis sections.

## 3.3.2. Theoretical Background and Design

Our aim is to design bio-compatible sensors with maximum Q-factor and maximum resonance frequency shifts. By using the circuit model in [15], the formulas in [15], [31], and techniques available in the literature [19], [22]-[23], [25]-[28], [30], [38], we design our devices to maximize the Q-factor. The formulas in [39], [48] are used during device design process to have maximum frequency shift. We use gold as the metal layer, $Si_3N_4$ as the dielectric and silicon (identical to the ones used in [31]) as the substrate so that our chip is fully bio-compatible and has a high Q-factor. To obtain a high Q-factor with minimum spacing, our technique leverages the film capacitance ($C_{film}$) as the main capacitance change in the LC tank circuit with the spiral geometry, as in [15], [31]. In order to obtain a high Q-factor, dielectric, dielectric thickness, effects of substrate, metal layer, metal layer thickness, metal layer width, spacing, number of turns and area should also be considered carefully. The other important aspect of the design is the resonance frequency shift. The main driver of the resonance frequency shift is the change in the area of the dielectric, and, as a result, the change in the value of the capacitance. When the load is applied, since the Young's modulus of silicon and gold is high, the main change occurs in the dielectric area as verified by the Coventorware simulation, which is also described in detail in [39].

The parameters of the single planar device are presented in Table 3.3.1. We remove the substrate of another chip, with all the same parameters, to obtain the single suspended device. By

using this technique, we theorize that higher Q-factors and shifts of resonance frequency will result. When we etch the substrate, we decrease the substrate loss. As a result, we increase the silicon resistance ($R_{si}$) and decrease the silicon capacitance ($C_{si}$). Hence, the overall result is an increase in the parallel resistance ($R_P$). By engineering a higher substrate loss factor, a higher inductor quality-factor ($Q_{ind}$) and hence a higher Q-factor of the device are obtainable, as explained in details in [15], [31]. The resonator quality factor (Q) is obtained from the inductor quality factor ($Q_{ind}$) and capacitor quality factor ($Q_c$) as given in [15] by: $\frac{1}{Q} = \frac{1}{Q_{ind}} + \frac{1}{Q_c}$. From this relation, it is possible to observe that increasing the inductor quality-factor will increase the resonator quality factor. Due to the higher $R_{si}$ and lower $C_{si}$, we have a lower parallel capacitance ($C_p$); therefore, a higher self resonance factor is obtained at the same frequency compared to the case with single planar device. Thus, the resonance frequency is also higher. Combining all these effects, we obtain higher Q-factors and higher resonance frequencies with silicon removal. Fig. 3.3.1 presents the $Q_{ind}$-factors of the single suspended device and the single planar device.

**Table 3.3.1. The parameters of the resonator device.**

| $L_c$ (µm) | $W_c$ (µm) | N | w (µm) | s (µm) | $t_{ox}$ (µm) | t (µm) |
|---|---|---|---|---|---|---|
| 195 | 195 | 2 | 35 | 5 | 0.1 | 0.1 |

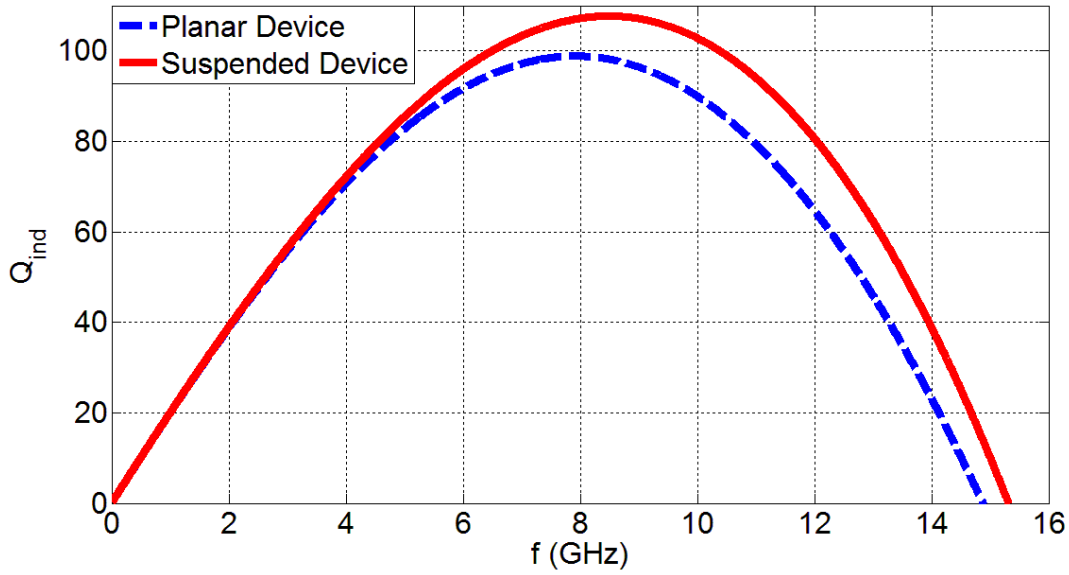


**Figure 3.3.1. The $Q_{ind}$ of the singular devices with respect to frequency.**

By etching the substrate, we will also have higher shift of resonance frequency. This can be examined from two aspects. As a result of etching the substrate, the strain propagation will be higher. Since the strain first occurs in the substrate and is then propagated to the dielectric and metal layers, with an etched substrate, there will be more strain and consequently, there will be more capacitance change. Hence, there will be a higher $f_0$ shift. If we apply the same load to the single planar device and the single suspended device, assuming that they have the same resonance frequency, we will have higher shift of resonance frequency ($\Delta f_0$) in the single suspended device as a result of higher strain in dielectric and metal layer. Secondly, if we have two chips with the same relative shift ($\frac{\Delta f_0}{f_0}$), the chip with the higher $f_0$ will have the higher $\Delta f_0$ as well. Thus the chip with etched substrate, with its higher $f_0$, also has a higher $\Delta f_0$. If we combine these two rationales, we expect to have a higher $\Delta f_0$ in the chip with the etched substrate. Also, because of the strain amplification effect we also expect that the silicon-etched

chip has a higher sensitivity ($\frac{\partial f_0}{\partial F}$). Considering all these factors, we postulate that the suspended architecture yields a higher $f_0$ shift and higher sensitivity.

## 3.3.3. Fabrication

Fig. 3.3.2 provides a detailed schematic view of our fabrication procedure. We use an n-type 500 μm thick substrate with a <100> orientation. We deposit a $Si_3N_4$ thin film using a plasma-enhanced chemical vapor deposition (PECVD) system; this film is 0.1 μm thick (Fig. 3.3.2(b)). We then lay down the first metal layer (contact layer) made of Au with a thickness of 0.1 μm (Fig. 3.3.2(c)). A 0.1 μm thick $Si_3N_4$ thin film is subsequently deposited (Fig. 3.3.2(d)). This film is patterned and vertical interconnection areas are opened using a wet etching process with HF (Fig. 3.3.2(e)). We also perform an Au (gold) metallization step to make the interconnects and top coil construction (Fig. 3.3.2(f)). A 0.8 μm thick $Si_3N_4$ film is deposited (Fig. 3.3.2(g)) and this layer is patterned and etched by HF (Fig. 3.3.2(h)). Finally, using potassium hydroxide (KOH), we partially etch the silicon as shown in Fig. 3.3.2(i).

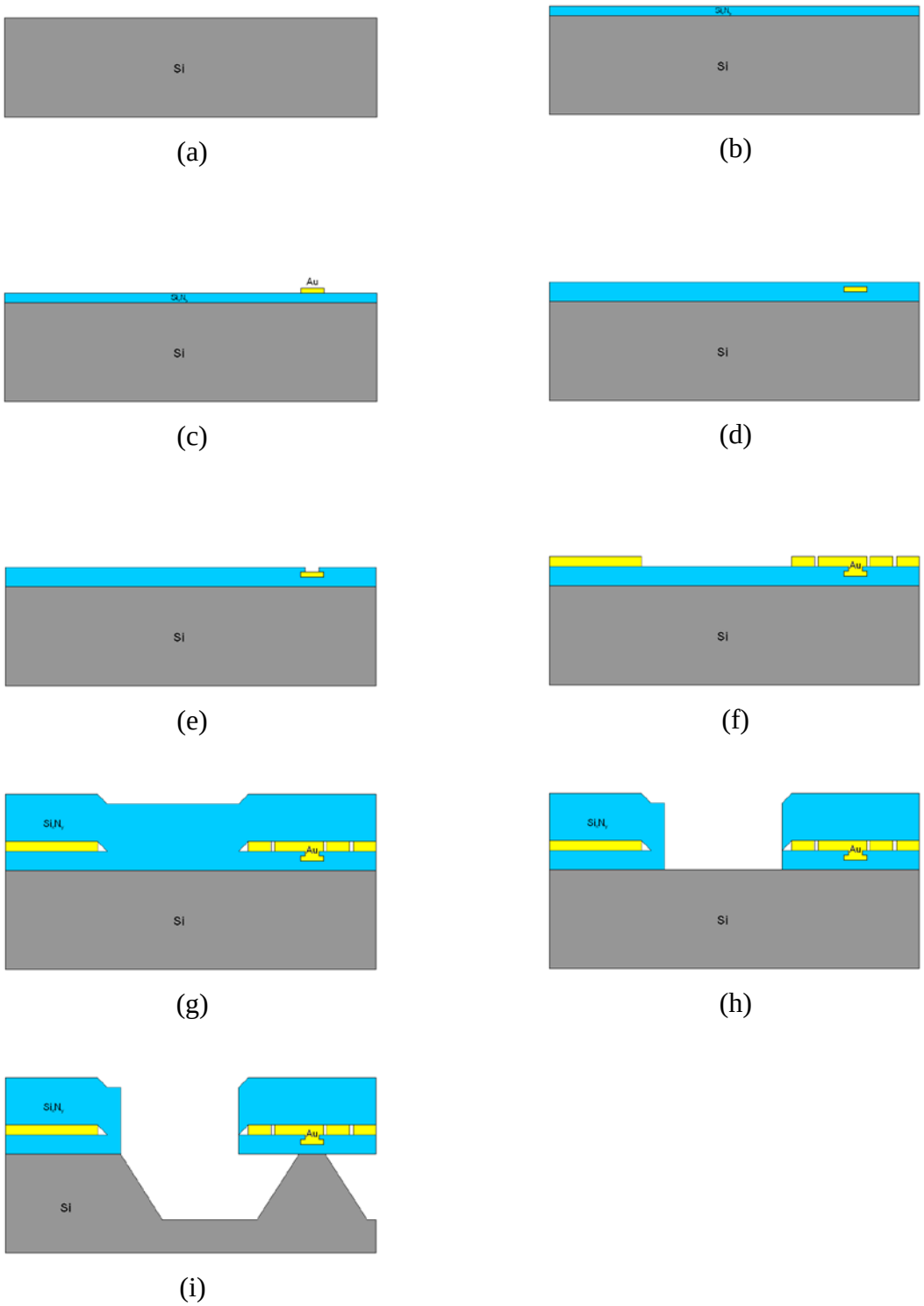


**Figure 3.3.2. The fabrication procedure.**

Unlike other process flows used in [15], [31], [39], here we initially put down the $Si_3N_4$ thin film to protect the contact metal layer while silicon is being etched. Since KOH also etches the metal layer, we use the first and third $Si_3N_4$ layers as etch-stop layers. The second $Si_3N_4$ layer acts as our dielectric layer. For silicon etching, we use a process simulation (ACES), with its simulation results shown in Fig. 3.3.3. Using a KOH solution with a concentration of 30% at 65$^o$C gives an etch rate of 1.1 μm/min, as expected from our chemical kinetics simulation. Thus, after 70 minutes, a depth of 77 μm is etched. This is the maximum feasible etch depth that avoids damaging the device given the architecture and size of the sensor. Since etching the substrate deep enough increases the Q-factor and sensitivity, we used the maximum feasible etching to obtain the best possible performance for this sensor geometry in practice. Here it is worth noting that, although etching helps especially at the beginning, etching has a diminishing effect in improving the Q-factor and sensitivity after a certain point. In our case, this etch depth of 77 μm is practically good enough for a proof-of-concept demonstration of the resulting improvements. The final structures are visualized in Fig. 3.3.4 and the associated SEM image of the single suspended device is presented in Fig. 3.3.5.

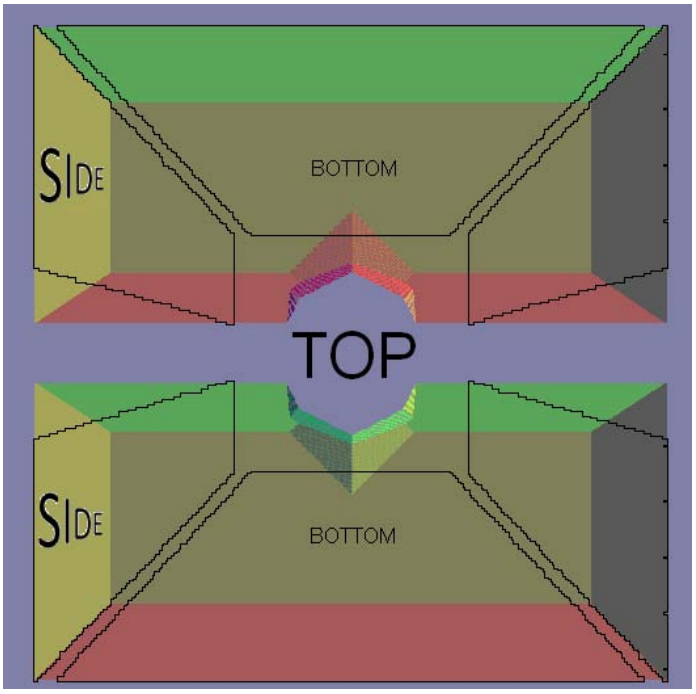


**Figure 3.3.3. Simulation of the silicon etching. The trapezoids represent areas where there are no $Si_3N_4$. KOH solution etches the silicon through these regions.**

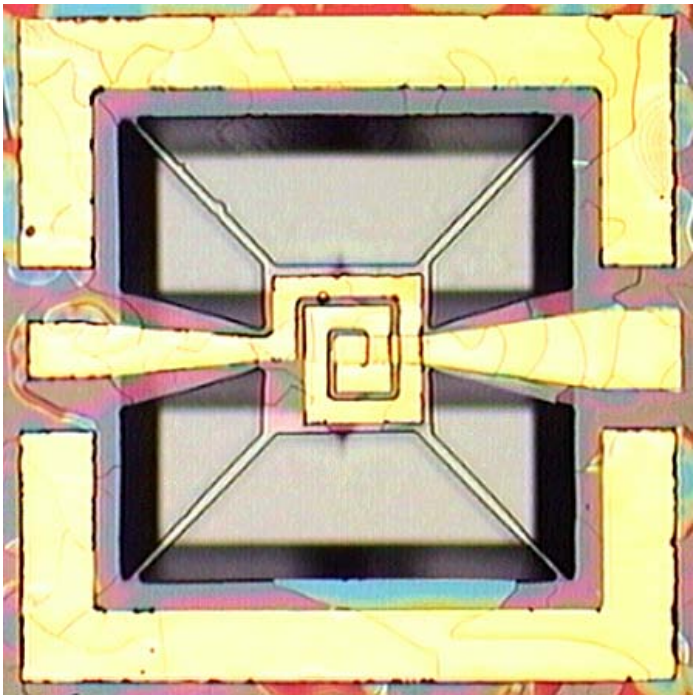

(a)

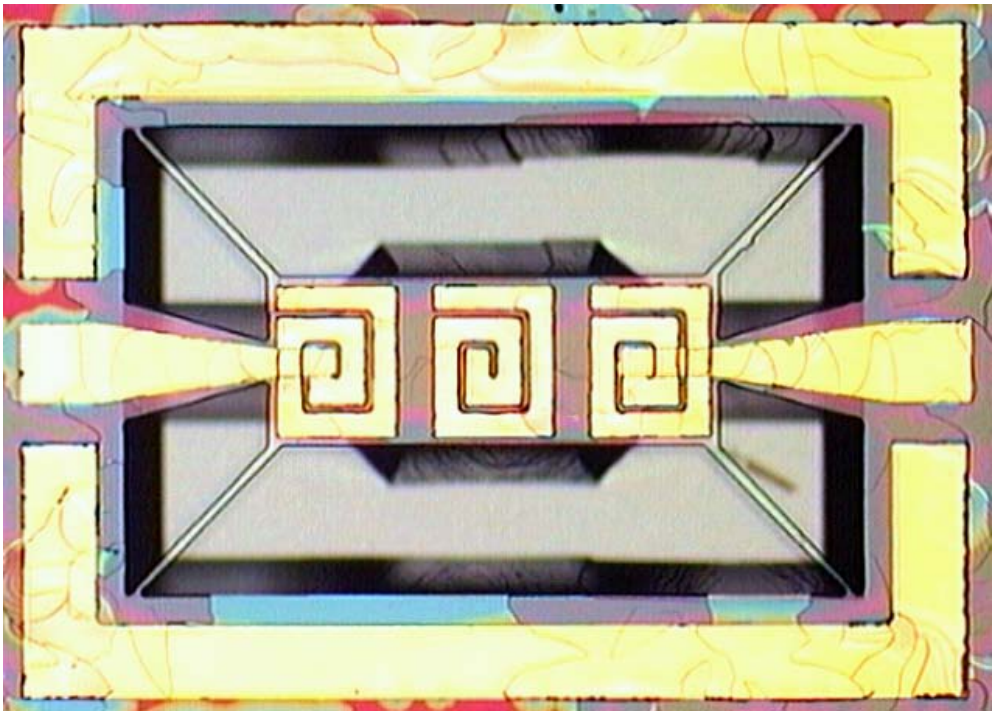

(b)

**Figure 3.3.4. Planar images of the devices: a) the fabricated single suspended device and b) the fabricated suspended triplet device.**

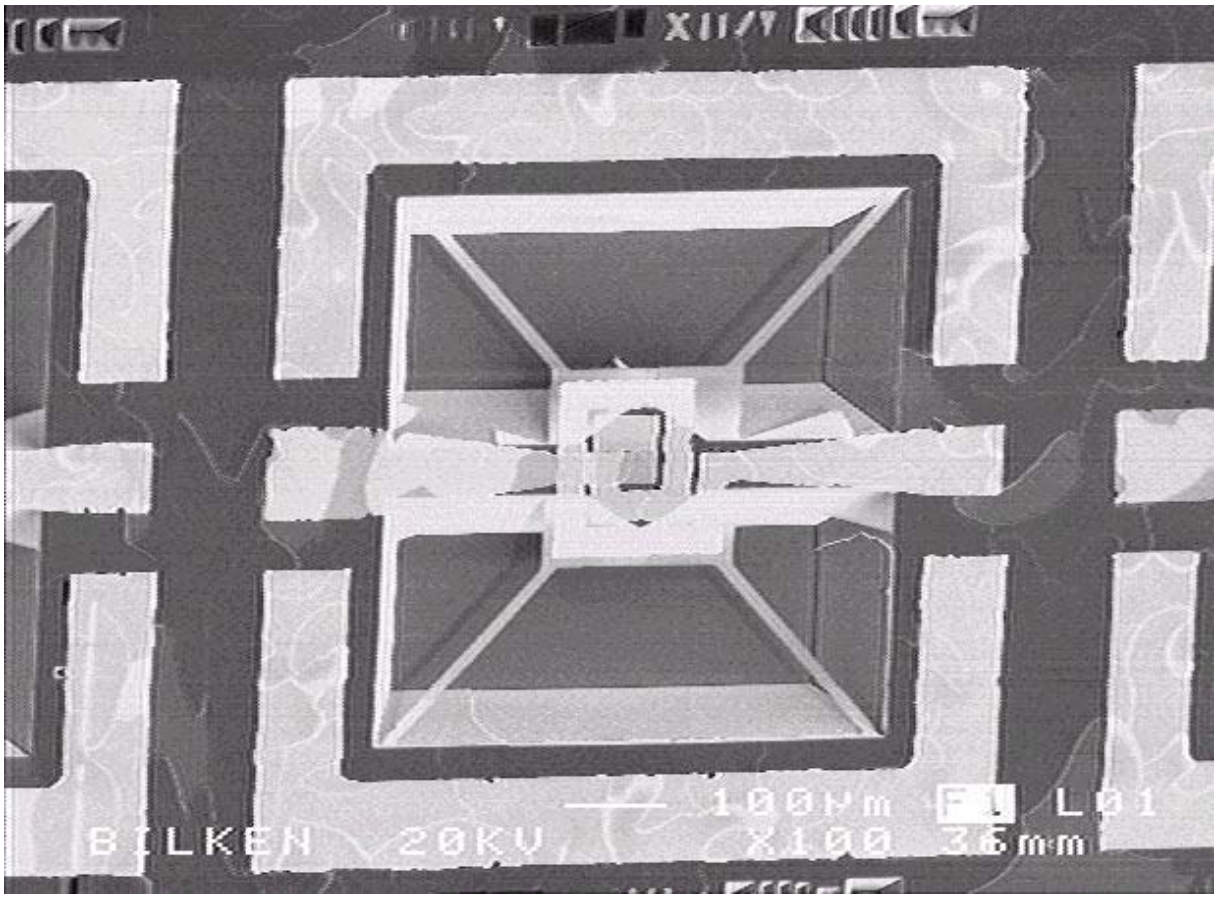


**Figure 3.3.5. SEM image of the single suspended device.**

## 3.3.4. Experimental Characterization and Analysis

We characterize our resonator sensors with a custom-design apparatus; details of the setup can be found in [39]. We first measure $S_{21}$ parameters of our devices by the network analyzer when there is no load. The $S_{21}$ parameters are also then recorded when applying loads of 1960, 2940 and 3920 N (i.e., 200, 300 and 400 kgf). Using this experimental protocol, the resonance frequencies ($f_0$), Q-factors, and $f_0$ shifts are determined under different levels of applied loads. In our characterization, we apply up to 400 kgf (3920 N) because the human body can effectively

apply about 4 times of its weight to a bone; for example, a human body with a weight of 100 kgf can generate a mechanical loading of 400 kgf for a bone. During operation, in one frequency scan of the network analyzer, there are only a limited number of data points; it is thus easier to track smaller shifts in the transmission spectra in response to the applied load when the sensitivity is higher. Therefore, higher sensitivity, which results in larger shifts in transmission with the same level of induced strain, is highly preferred to read out the strain correctly. In this work, we characterized the single suspended device, the single planar device, the suspended triplet device and the planar triplet device to compare their performances with respect to each other including their resonance frequencies, Q-factors, and sensitivities. Here with the "triplet" configuration, we refer to a method of characterizing the sensor on the chip telemetrically where all the receiver and transmitter antennas are placed on the same chip side by side with the sensor; further details can also be found in [39].

Fig. 3.3.6 shows the $S_{21}$ parameters of the single suspended device and the single planar device under different applied load values. Fig. 3.3.6(a) gives the $S_{21}$ parameters of the single planar device under different loads and Fig. 3.3.6(b), provides a magnified view of this information. The $S_{21}$ parameters of the single suspended device under different applied loads are shown in Fig. 3.3.6(c) and Fig. 3.3.6(d). There is a considerable increase of the resonance frequency for single suspended devices.

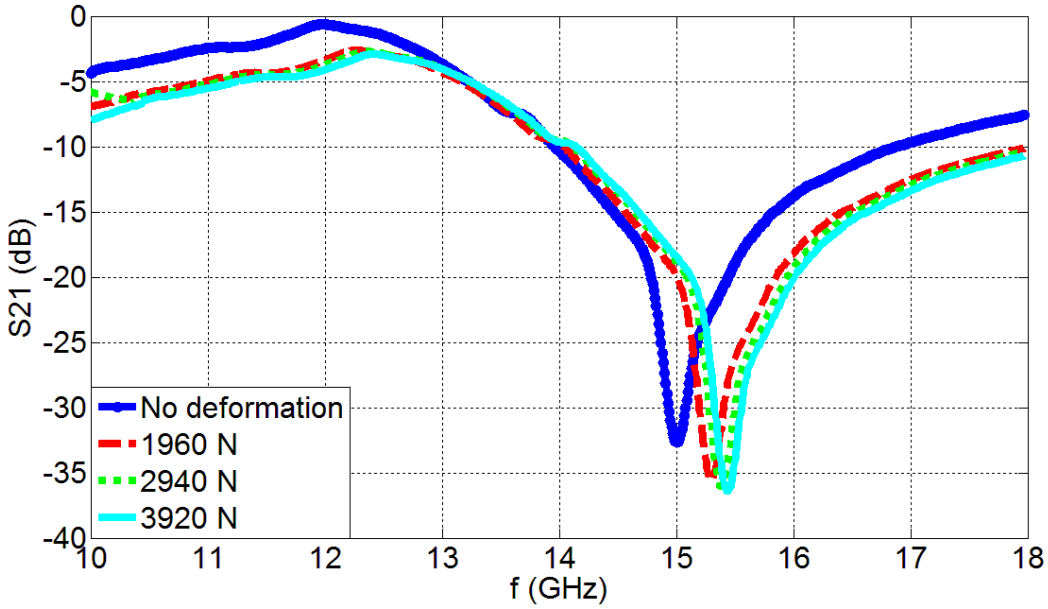
0
-5
-10
-15
-20
-25
-30
-35
-40
S21 (dB)
10
11
12
13
14
15
16
17
18
f (GHz)
No deformation
1960 N
2940 N
3920 N

(a)

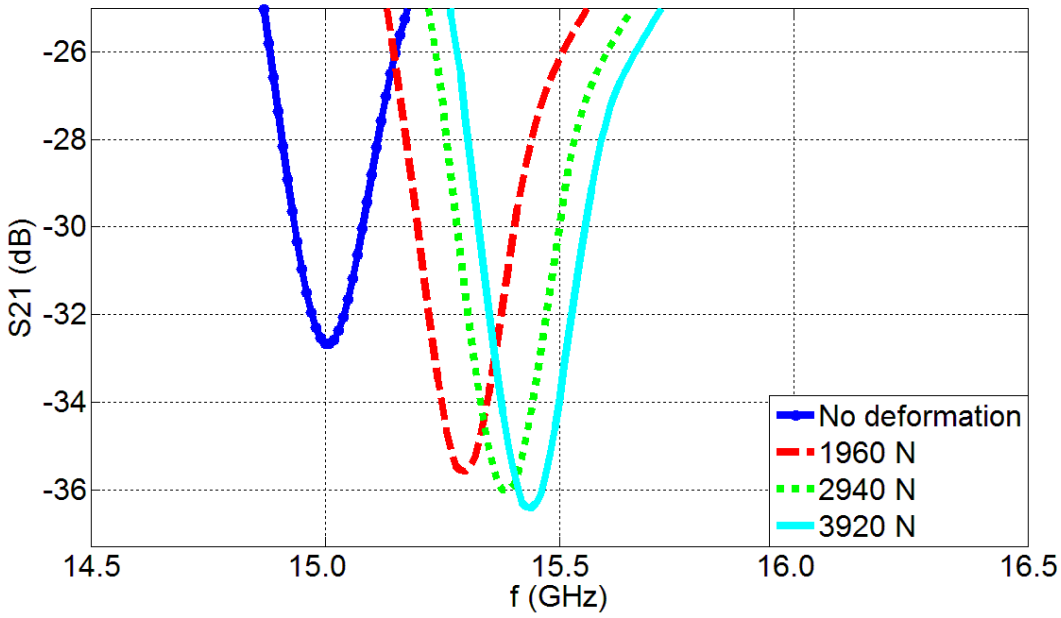
-26
-28
-30
-32
-34
-36
S21 (dB)
14.5
15.0
15.5
16.0
16.5
f (GHz)
No deformation
1960 N
2940 N
3920 N

(b)

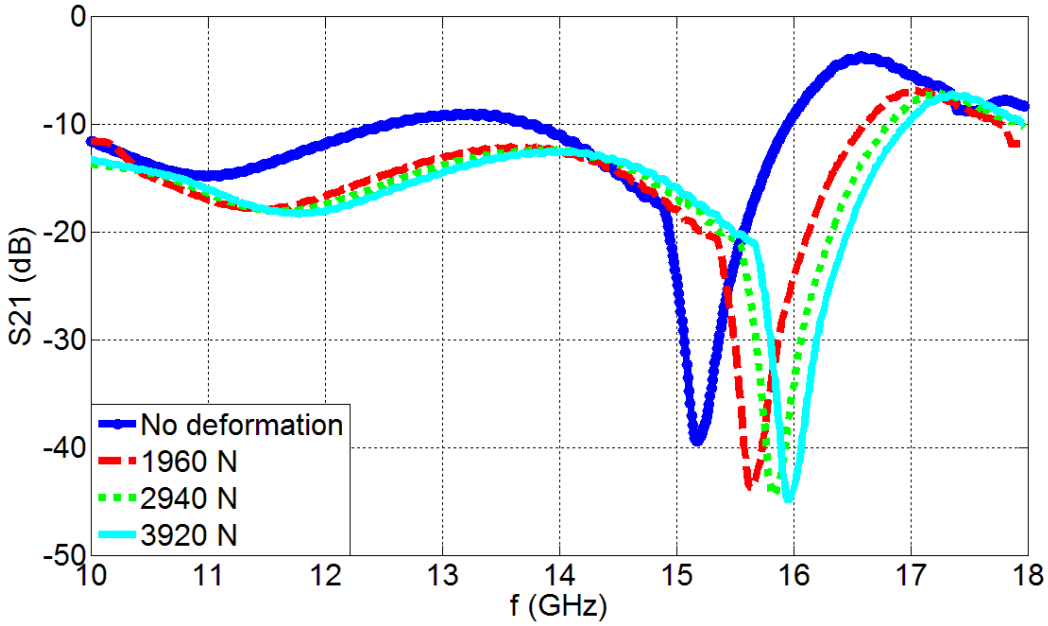


(c)

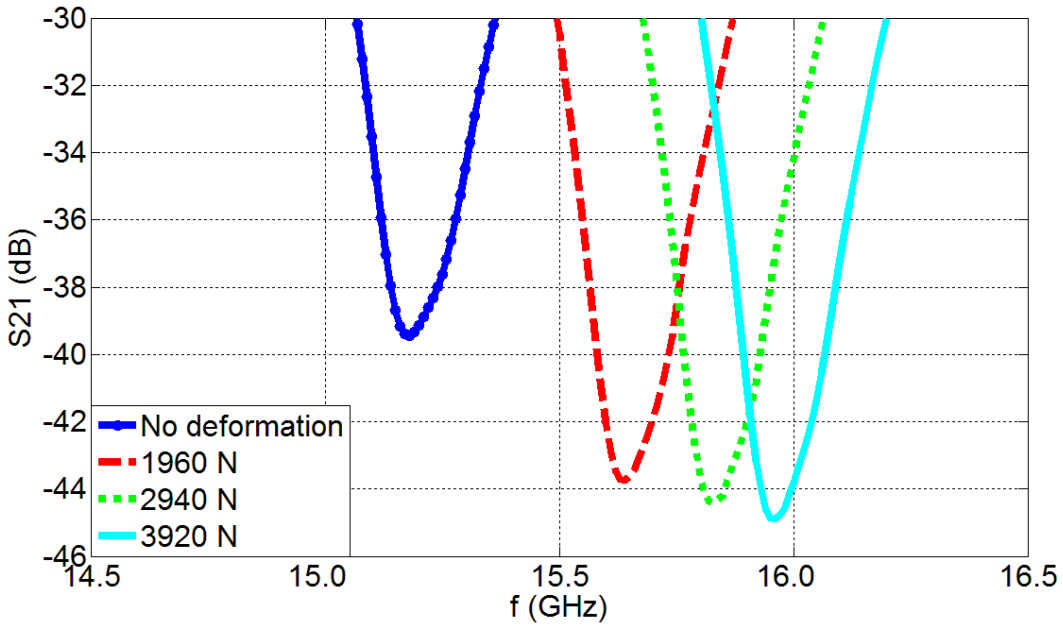


(d)

**Figure 3.3.6. Experimental measurements of $S_{21}$ parameters as a function of frequency for: (a) the single planar device and (b) zoom in for the single planar device, (c) the single suspended device and (d) zoom in for the single suspended device. Data is presented for the cases of no deformation and also when loads of 1960 N, 2940 N and 3920 N are applied.**

Table 3.3.2 displays the resonance frequencies of the single planar devices under different loads. The single planar device has a resonance frequency of 15.01 GHz under no deformation and demonstrates 430 MHz shift with 3920 N applied.

**Table 3.3.2. Resonance frequencies of the device variants with different loads.**

| Load | No load | 1960 N | 2940 N | 3920 N |
|---|---|---|---|---|
| Single Planar Device | 15.01 GHz | 15.30 GHz | 15.39 GHz | 15.44 GHz |
| Single Suspended Device | 15.18 GHz | 15.64 GHz | 15.83 GHz | 15.96 GHz |
| Planar Triplet | 15.06 GHz | 15.17 GHz | 15.23 GHz | 15.28 GHz |
| Suspended Triplet | 15.41 GHz | 15.56 GHz | 15.66 GHz | 15.75 GHz |

For the single suspended device, it demonstrates a 15.18 GHz resonance frequency with no deformation (Table 3.3.2). Its resonance frequency increases by 780 MHz with 3920 N applied load. There is an increase in resonance frequency for the single suspended device compared to single planar device with no load, as expected and hypothesized in the theoretical background and design section. The table also shows a significant increase in the resonance frequency shift in the single suspended device compared to the single planar device.

Table 3.3.2 shows the increase in resonance frequency with applied load. The underlying reason is that, under load, the dielectric area decreases and the capacitance decreases. Hence, there is a concomitant resonance frequency increase. In addition, since the relation between the capacitance change and resonance frequency is nonlinear, then the resonance frequency shift is nonlinear.

For the triplet case, we can see the $S_{21}$ parameters of the suspended triplet device and the planar triplet device under different applied loads in Fig. 3.3.7. The figures display a considerable increase of the resonance frequency for suspended triplet devices compared to the planar triplet devices. If we observe the resonance frequencies for triplet cases, we will see that the planar triplet device has a resonance frequency of 15.06 GHz with no deformation, and the suspended

triplet device displays 15.41 GHz with no deformation (Table 3.3.2). The resonance frequency shift of the planar triplet device is 220 MHz under 3920 N load while the resonance frequency shift of the suspended triplet device is 340 MHz under 3920 N load. In all cases of single and triplet devices, we measured each device 5 times. The presented points of resonance frequency correspond to the averages of these points of all 5 measurements. In these measurements, we also observed that the difference between the maximum and the minimum measured $f_0$ (variable range of $f_0$) is 0.02 GHz while their standard deviation is only ~0.01 GHz.

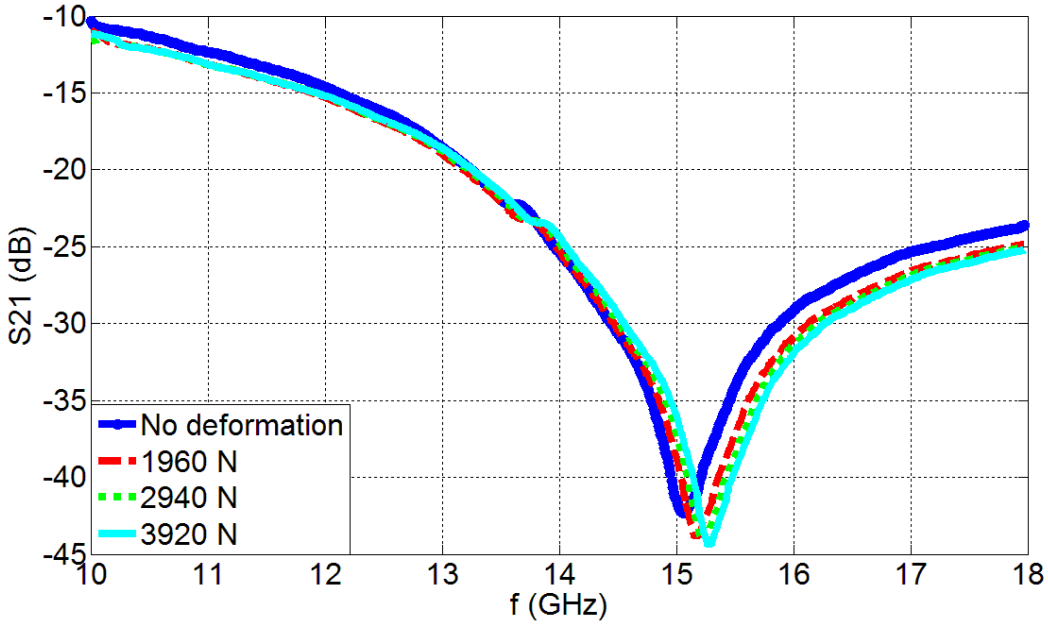


(a)

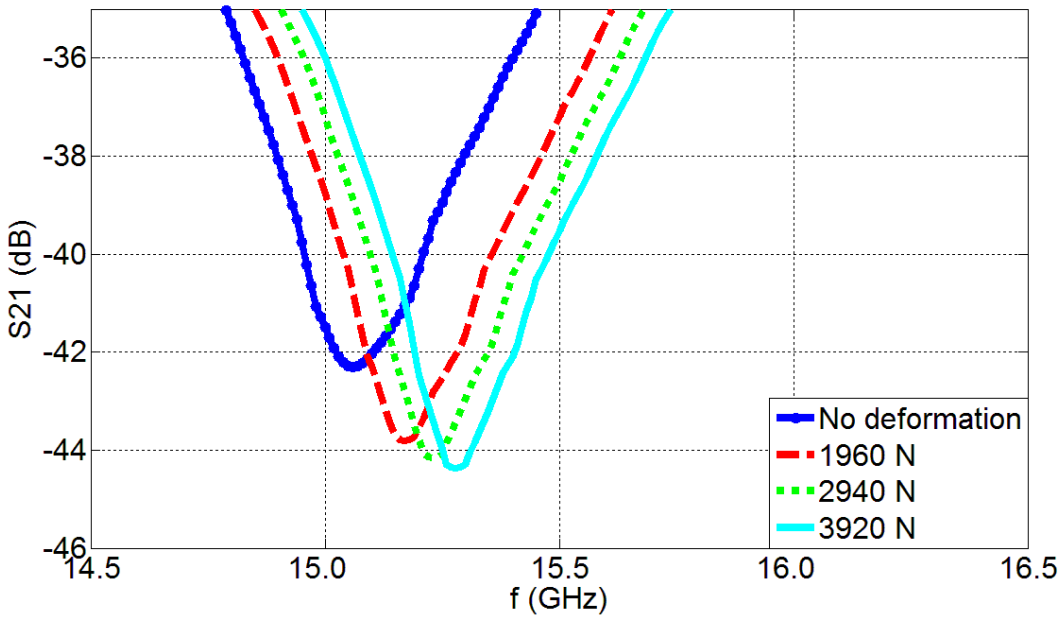
-36
-38
-40
-42
-44
-46
S21 (dB)
14.5
15.0
15.5
16.0
16.5
f (GHz)
No deformation
1960 N
2940 N
3920 N

(b)

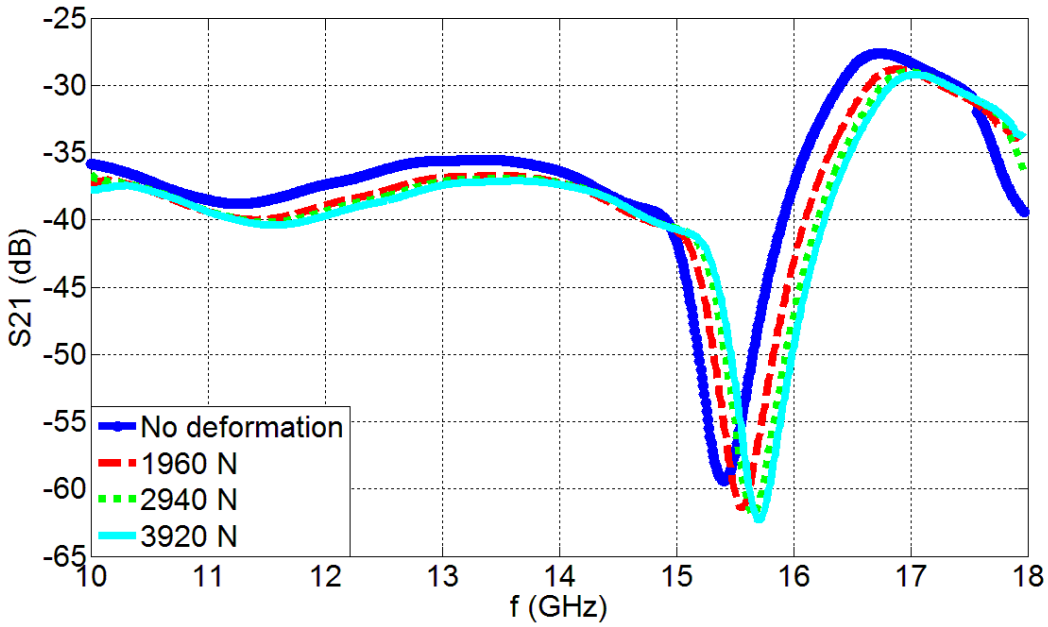
-25
-30
-35
-40
-45
-50
-55
-60
-65
S21 (dB)
10
11
12
13
14
15
16
17
18
f (GHz)
No deformation
1960 N
2940 N
3920 N

(c)

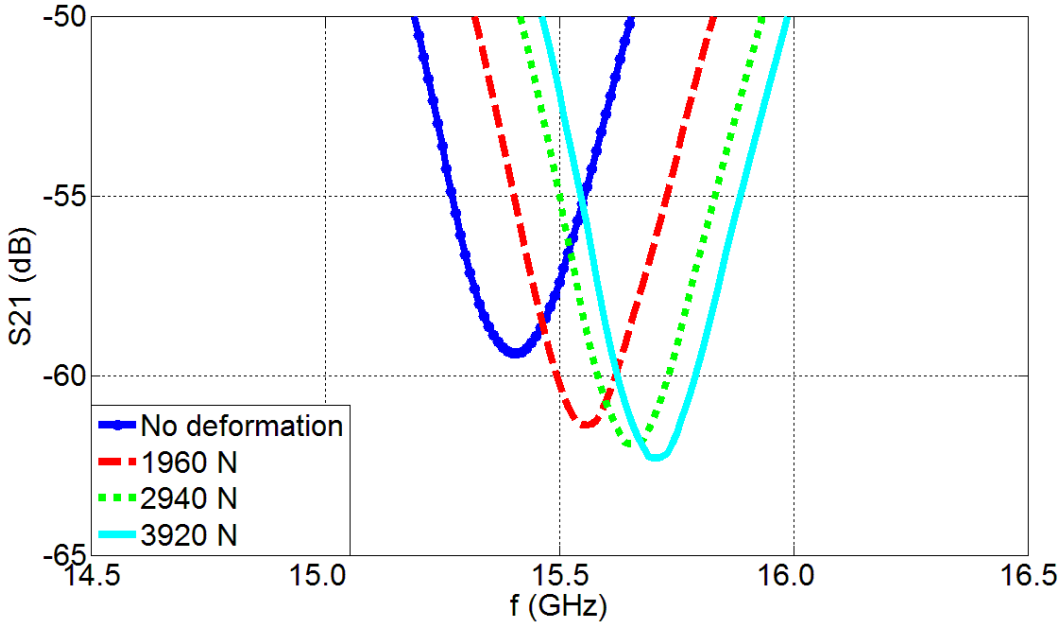


(d)

**Figure 3.3.7. Experimental measurements of $S_{21}$ parameters as a function of frequency for: (a) the planar triplet device and (b) zoom in for planar triplet device, (c) the suspended triplet device and (d) zoom in for suspended triplet device. Data for the case of no deformation and also when loads of 1960 N, 2940 N and 3920 N are applied are presented.**

Table 3.3.3 shows the device Q-factors that are obtained from Fig. 3.3.6 and Fig. 3.3.7. We see that the single planar device has Q-factors of 93.81 under no load, and 111.08 under 3920 N load. The single suspended device yields an increase in Q-factor compared to the single planar device case. The single suspended device has Q-factors of 102.64 under no load, and 120.02 under 3920 N. The suspended triplet device has higher Q-factors compared to the planar triplet device case. The Q-factors of the planar triplet device are 51.90 when there is no load, and 62.55 when 3920 N load is applied. However, the Q-factors of the suspended triplet device are 67.15 with no load, and 80.45 when 3920 N load is applied. These data show that the Q-factor rises with the applied load, as expected from the load-related capacitance decrease.

**Table 3.3.3. The Q-factors of the variant devices with different loads.**

| Load | No load | 1960 N | 2940 N | 3920 N |
|---|---|---|---|---|
| Single Planar Device | 93.81 | 109.21 | 110.96 | 111.08 |
| Single Suspended Device | 102.06 | 116.54 | 119.47 | 120.02 |
| Planar Triplet | 51.90 | 57.38 | 60.82 | 62.55 |
| Suspended Triplet | 67.15 | 79.51 | 80.31 | 80.45 |

The sensitivity ($\frac{\partial f_0}{\partial F}$) and relative shift ($\frac{\Delta f_0}{f_0}$) are important parameters for a sensor. The sensitivity and relative shift of the sensors are presented in Table 3.3.4. We see that the single suspended device has higher sensitivity and relative shift compared to the single planar device case. The single planar device has a sensitivity of 0.1097 MHz/N while the single suspended device has a sensitivity of 0.1990 MHz/N. The single planar device has a 2.9% relative shift whereas the single suspended device has a 5.1% relative shift. The same comparison occurs for the triplet case, the suspended triplet device has both higher sensitivity and relative shift compared to the planar triplet device. The planar triplet device has a 0.0561 MHz/N sensitivity and a 1.5% relative shift while the suspended triplet device has a 0.0867 MHz/N sensitivity and a 2.2% relative shift. These data demonstrate that the single suspended device has a higher Q-factor compared to the single planar device presented in [31] and has a higher resonance frequency shift, higher sensitivity and higher relative shift compared to the case in [39].

**Table 3.3.4. The sensitivities of the variant devices.**

| | Sensitivity | Relative Shift |
|---|---|---|
| Single Planar Device | 0.1097 MHz/N | 2.9% |
| Single Suspended Device | 0.1990 MHz/N | 5.1% |
| Planar Triplet | 0.0561 MHz/N | 1.5% |
| Suspended Triplet | 0.0867 MHz/N | 2.2% |

If we compare the case of triplet and single devices, we observe that we have different experimental performance results in terms of signal level, resonance frequency, Q-factor and sensitivity. Since there is a distance between antennas on the chip, the signal level of the triplet device case is lower than that of the single device case. Besides, because of the interaction between antennas, the resonance frequency of the single device and triplet device is slightly different. Also in the single device case, the signal is directly fed to the device whereas in the triplet device case, it is sent via the external antennas on the same chip. As a result, the Q-factor of the triplet device is lower than that of the single device as expected. The shift of resonance frequency is observed to be lower in the case of triplet device compared to the single device case. The reason is that the external load is applied across a larger area in the triplet device, whereas it is applied to a smaller area in the single device case. Consequently, the shift of resonance frequency in the single device for the same level of external loading is higher compared to the triplet device, making its measured sensitivity to be higher in the single device case.

We also numerically simulate S parameters of our devices for the no-load case in CST Microwave Studio. The simulation results are given in Fig. 3.3.8. We observe generally good agreement between theoretical and experimental results from these figures. Table 3.3.5 gives the theoretical and experimental resonance frequencies and Q-factors in Table 3.3.5. The single planar device theoretically has a 14.88 GHz resonance frequency and a 98.77 Q-factor (experimentally it demonstrates a 15.01GHz resonance frequency and 93.81 Q-factor). The single suspended device has a theoretical 15.31 GHz resonance frequency and a 117.41 Q-factor at the same time (experimentally it has a 15.18 GHz resonance frequency and 102.06 Q-factor). For triplet cases, we have a theoretical 14.9 GHz resonance frequency and a 57.62 Q-factor for the planar triplet device. The planar triplet device has a 15.06 GHz resonance frequency and a 51.90 Q-factor. For the suspended triplet device, we have a theoretical 15.22 GHz resonance frequency while the experimental resonance frequency is 15.41 GHz. The theoretical Q-factor for this device is 80.32 while the experimental one is 67.15. The theoretical and experimental resonance frequencies and Q-factors are observed to be reasonably close, but not identical. There is a slight difference between each pair of the simulated and measured values, which is attributed to the assumptions we make in our computations. In numerical simulations, we treat all

components to be ‘ideal’; we assume perfect contact of the probes, perfect plane wave, perfect grounds, perfectly the same dimensions in design, and perfect environment with no external conditions affecting the signal or noise level. However, in real life, we experimentally face with all of these complications and measure all non-idealities in effect together, along with some degree of experimental error. Hence, the theoretical and experimental results differ slightly.

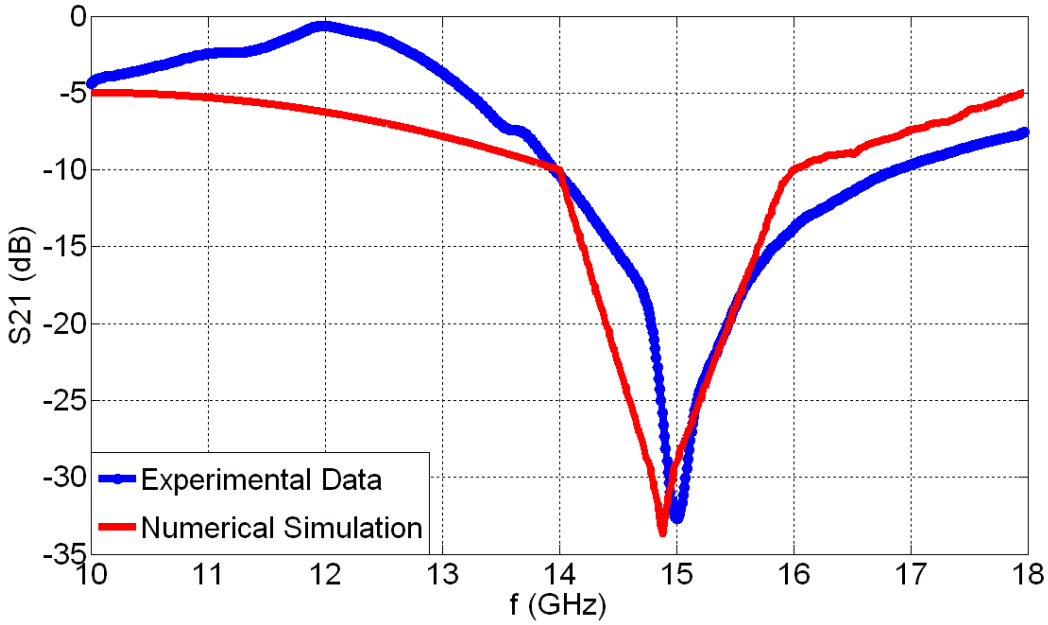


(a)

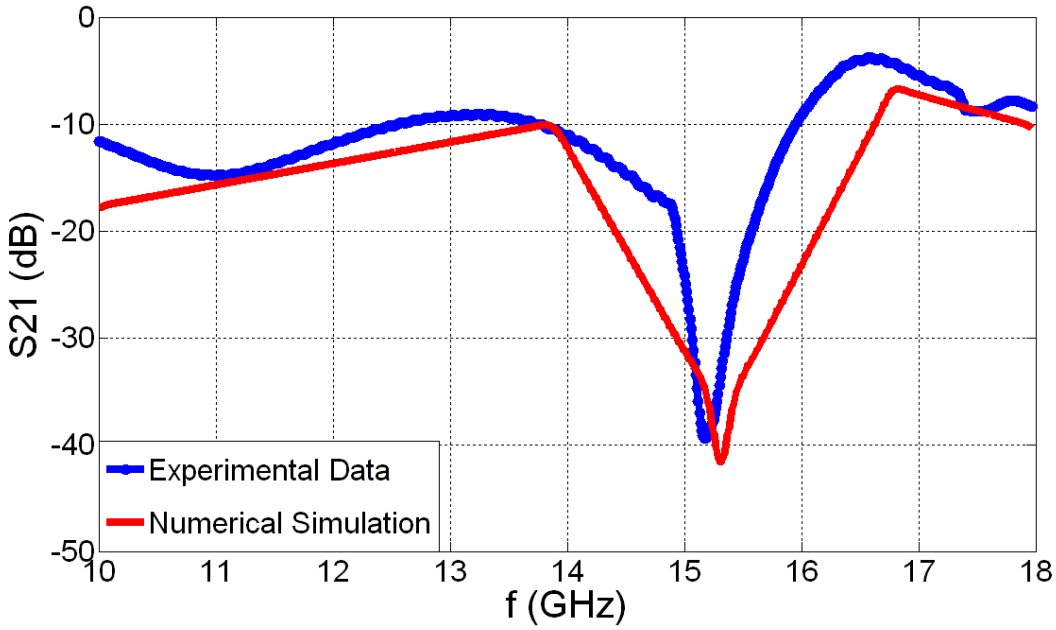
0
-10
-20
-30
-40
-50
S21 (dB)
10
11
12
13
14
15
16
17
18
f (GHz)
Experimental Data
Numerical Simulation

(b)

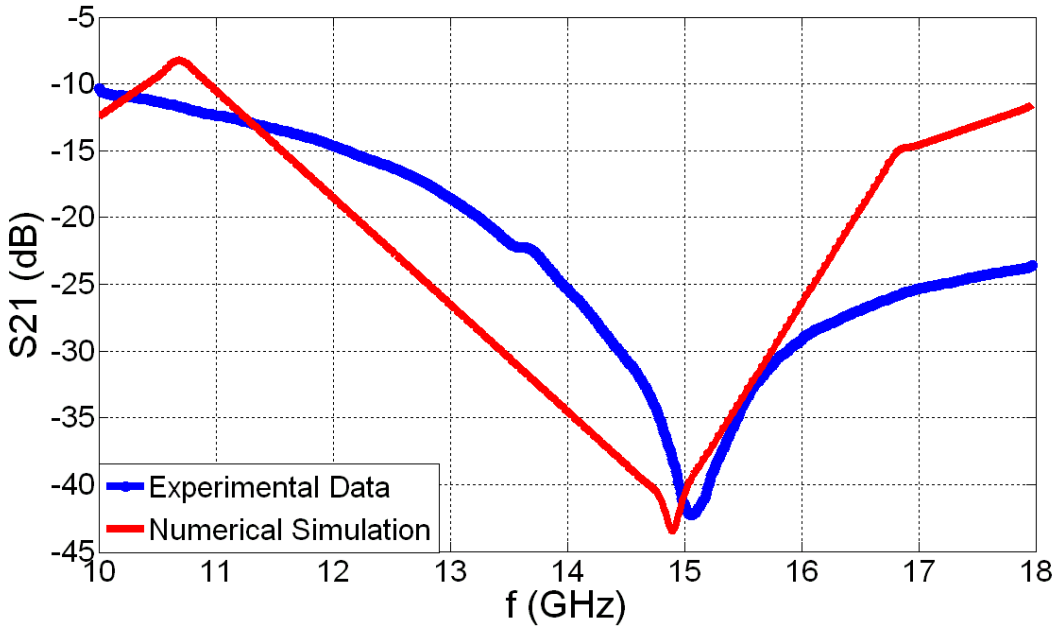
-5
-10
-15
-20
-25
-30
-35
-40
-45
S21 (dB)
10
11
12
13
14
15
16
17
18
f (GHz)
Experimental Data
Numerical Simulation

(c)

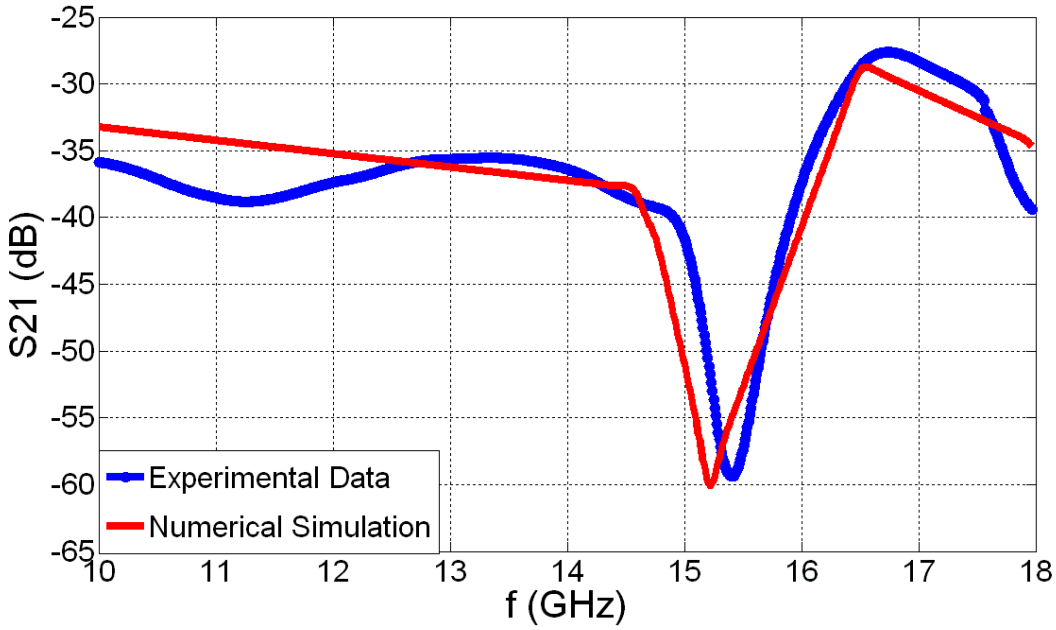


(d)

**Figure 3.3.8. Numerical simulations for $S_{21}$ parameters when there is no load (a) for the single planar device, (b) for the single suspended device, (c) for the planar triplet device, and (d) for the suspended triplet device.**

**Table 3.3.5. The theoretical and experimental resonance frequencies and Q-factors of the variant devices.**

| | $f_0$ (GHz) | | Q-Factor | |
|---|---|---|---|---|
| | Theoretical | Experimental | Theoretical | Experimental |
| Single Planar Device | 14.88 GHz | 15.01 GHz | 98.77 | 93.81 |
| Single Suspended Device | 15.31 GHz | 15.18 GHz | 117.41 | 102.06 |
| Planar Triplet | 14.90 GHz | 15.06 GHz | 57.62 | 51.90 |
| Suspended Triplet | 15.22 GHz | 15.41 GHz | 80.32 | 67.15 |

## 3.3.5. Conclusion

In conclusion, we designed, numerically and analytically simulated, fabricated and experimentally characterized suspended RF-MEMS load sensors that achieve higher Q-factors and higher resonance frequency shifts compared to planar devices (devices without substrate etching). The single suspended device has a 102.06 Q-factor, a 780 MHz frequency shift, a 0.1990 MHz/N sensitivity and a 5.1% relative shift whereas the single planar device has a 93.81 Q-factor, 430 MHz frequency shift, they 0.1097 MHz/N sensitivity and a 2.9% relative shift. For triplet cases, the suspended triplet device has a 340 MHz frequency shift, a 0.0867 MHz/N sensitivity and a 2.2% relative shift while the planar triplet device has a 220 MHz frequency shift, a 0.0561 MHz/N sensitivity and a 1.5% relative shift. The suspended structures have greater resonance frequency shifts, sensitivities and relative shifts compared to all other cases presented heretofore. Therefore, the suspended architecture represents an improved geometry for monitoring strain in real time. This improvement can be useful for the application of assessing the progression of healing osseous fractures.

## 3.4 Wireless BioMEMS Sensor to Detect Fracture Healing

In this section, we report the development of a new class of bio-implant wireless passive RF sensors for the reading out in-body load telemetrically in real time. By using the “triplet” idea, we test our implantable chip in a wireless way easily. In this section, we examine the triplet idea in a detailed way. We designed, modeled, fabricated, experimentally characterized and theoretically analyzed bio-implant wireless RF sensors. The experimental results are in agreement with our theoretical and numerical simulation results. We also demonstrated that our wireless RF sensors exhibit resonance frequency shift with the external application of load.

### 3.4.1. Introduction

We demonstrate experimentally the proof of concept of a wireless bio-implant RF-MEMS sensor to detect fracture healing using the principle of resonance frequency shift. We demonstrate the experimental telemetric proof of concept using the “triplet” idea. This is basically an antenna system implemented on the same chip as the sensor. There are two external antennas at the edges of the same chip and the main device, which will be implanted into human beings, is between the antennas. The two antennas and the main device have similar structures. By using the triplet, we easily test our implantable chip wirelessly.

When major fractures occur in human beings, plates are implanted and come under strain. Then strain decreases in time since the tissue builds up [1]. Because of this, monitoring strain wirelessly in real time is an important issue to observe the healing process of the patient. Using a sensor with the resonance frequency shift with the applied load is a solution for this problem.

In literature, the RF telemetric readout of miniaturized antennas and their application is an active research area. There are some works on this problem with different aims and applications. As a result, telemetric study is very important for wireless bio-MEMS sensors. It is difficult to establish power coupling between an external antenna and an implanted sensor. In some previous studies [43]-[47], wireless power coupling between the external antenna and the implanted antenna could not be obtained. The implanted antenna is then wired to the network analyzer for measurements. However, in our case, the implanted antenna can be completely wireless. The aim of wireless bio-implant sensor is also rather specific and different from works so far in the literature. For example, in [43]-[47], the aim is to see the physiological effects of the space to the human body. In [53], the target is ingestible devices. In [54], an intraocular pressure sensor is used. In [55], the chip is used for visual prosthesis for epi-retinal stimulation. In [56], the aim is to record peripheral neural signals from axons. There are also reports to examine the coupling between spiral structures, as in [36]. In [40], the attempt is to monitor the structure's strain using active telemetry, but no results are available.

Previously, we developed high Q-factor on-chip resonators in [15], [31] and showed the proof of concept of resonance frequency shift in [39]. Then we presented increased Q-factor and frequency shift in [49], [52]. In this section, we examine the telemetric case in detail, implementing passive telemetry. We investigate the triplet idea in terms of the calibration procedure of the triplet, the distance between antennas, the signal level, the Q-factor, the resonance frequency ($f_0$) and Q-factor behavior of the triplet configuration with the applied load, the quantity of the shift of $f_0$ ($\Delta f_0$) of the triplet, and the sensitivity ($\frac{\partial f_0}{\partial F}$) and relative shift ($\frac{\Delta f_0}{f_0}$) of the triplet.

## 3.4.2. Fabrication, Experimental Characterization and Analysis

We examine five different single devices and their triplet devices. We design our single and triplet devices according to the formulas and design techniques discussed previously and also in [15], [31], [39], [49], [52]. The design parameters are given in Table 3.4.1. The $L_c$ and $W_c$ are width and length of the single devices, $N$ is the number of turns, $w$ is width of the one coil spiral structure, $s$ is the spacing, $t_{film}$ is the height of the dielectric and $t$ is the height of the metal layer. The single device and triplet device cases are fabricated using the same fabrication procedure. We first deposit 0.1 μm thick metal contact layer (gold) on the substate (silicon), then deposit a 0.1 μm dielectric layer ($Si_3N_4$). Finally another 0.1 μm thick final metal layer (gold) is put on top. By this technique, the planar, rectangular, circular single devices and single device previously investigated cases are fabricated. The suspended single device is fabricated by etching the substrate of the planar single device. The details of the fabrication procedure are given in [52]. The dimensions of the rectangular single device and circular single device cases are the same but the geometry is different. Also the dimensions of the planar single device and suspended single device cases are the same but the substrate of the planar single device case is etched in the suspended single device case.

**Table 3.4.1. The parameters of our device.**

| | $L_c$ (μm) | $W_c$ (μm) | $N$ | $w$ (μm) | $s$ (μm) | $t_{film}$ (μm) | $t$ (μm) |
|---|---|---|---|---|---|---|---|
| Planar Single Device | 195 | 195 | 2 | 35 | 5 | 0.1 | 0.1 |
| Suspended Single Device | 195 | 195 | 2 | 35 | 5 | 0.1 | 0.1 |
| Rectangular Single Device | 340 | 340 | 2 | 60 | 10 | 0.1 | 0.1 |
| Circular Single Device | 340 | 340 | 2 | 60 | 10 | 0.1 | 0.1 |
| Single Device Investigated | 270 | 270 | 2 | 50 | 5 | 0.1 | 0.1 |

We can see two antennas on the same chip in Fig. 3.4.1(a). One of them is used as the transmitting antenna and the other one as the receiving antenna. To obtain $S_{21}$ parameters of the sensor to be placed between these two antennas as in Fig. 3.4.1(b), we perform de-embedding using this structure in Fig. 3.4.1(a). Thus $S_{21}$ parameters of the structure in Fig. 3.4.1(a) is measured as zero line. Then we look at the $S_{21}$ parameters of the case as in Fig. 3.4.1(b) where our wireless bio-implant sensor is in the middle of two antennas and study the resonance frequency and Q-factor of the sensor. When the load is applied to the chip, again the calibration is performed with the procedure as explained above and the changes appear in the resonance frequency and Q-factor. The distance between the antennas and the sensor is also an important concern. If the distance is smaller than width plus spacing, then the sensor will act as a part of the transmitting or receiving antenna. Then $S_{21}$ parameters of the sensor cannot be understood in a reliable way. If the distance between antenna and sensor is bigger than the total length of the sensor, the signal level will be too low and we cannot see the resonance frequency easily. So the distance between antenna and sensor should be bigger than the width plus spacing and it should be smaller than the total length of the sensor. Another important point is that since the spiral structure is omnidirectional, the angle between antennas is not important; so, using the spiral structure, the triplet idea works.

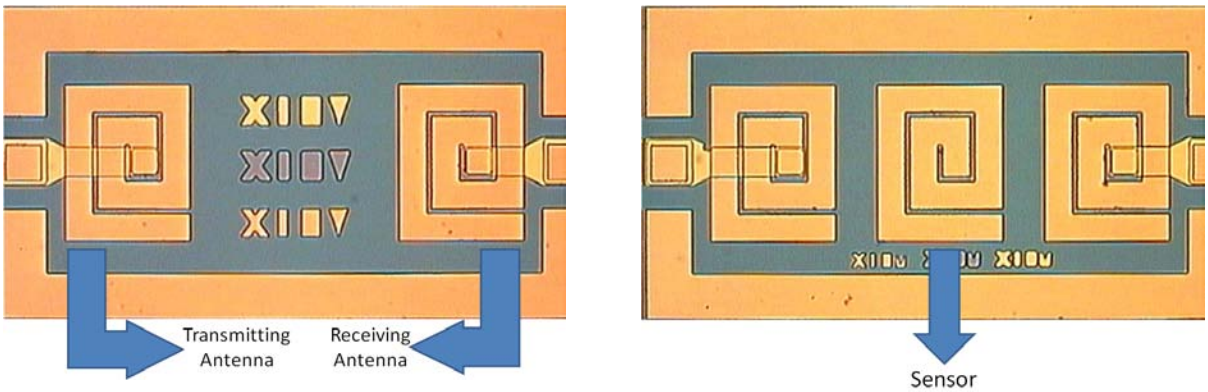


(a) (b)

**Figure 3.4.1. (a) The de-embedding structure for triplet configuration (b) the triplet structure, where the sensor is in the middle of the transmitting antenna and receiving antenna.**

We measure $S_{21}$ parameters of the devices with different geometries and fabricated with different fabrication techniques. We numerically simulate the $S_{21}$ parameters and compare the resonance frequencies and Q-factors of the devices. We experimentally and numerically examine the $S_{21}$ parameters of the planar single device in Fig. 3.4.2(a), planar triplet device in Fig. 3.4.2(b), suspended single device in Fig. 3.4.2(c) and suspended triplet device in Fig. 3.4.2(d). (Note that these devices are the devices in [52], these results are reproduced here for the reader's convenience) The $f_0$ and Q-factor values can be seen in Table 3.4.2. The figures demonstrate that since there is a distance between antennas, the signal level of the triplet device case is lower than the single device case. Besides, as a result of the interaction between antennas, the resonance frequency of the single device and triplet device is a bit different as can be seen in Table 3.4.2. Also in the single device case, the signal is directly fed to the device whereas in the triplet device case, it is sent to the external antennas on the same chip. Thus since the signal does not go directly to device, the Q-factor of the triplet device is lower than the single device case as expected.

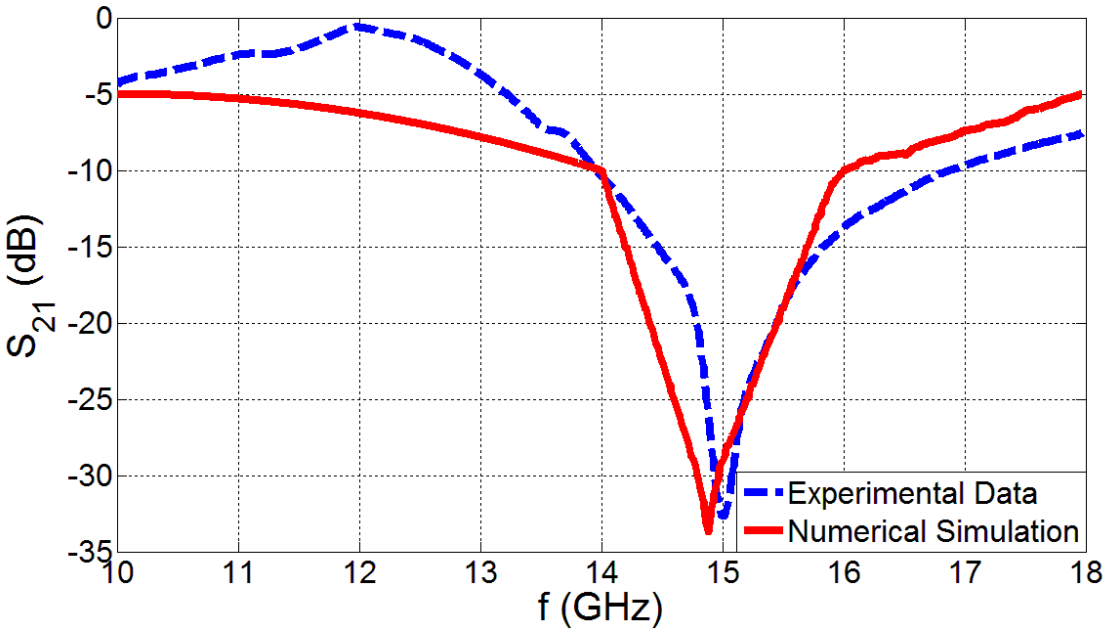


(a)

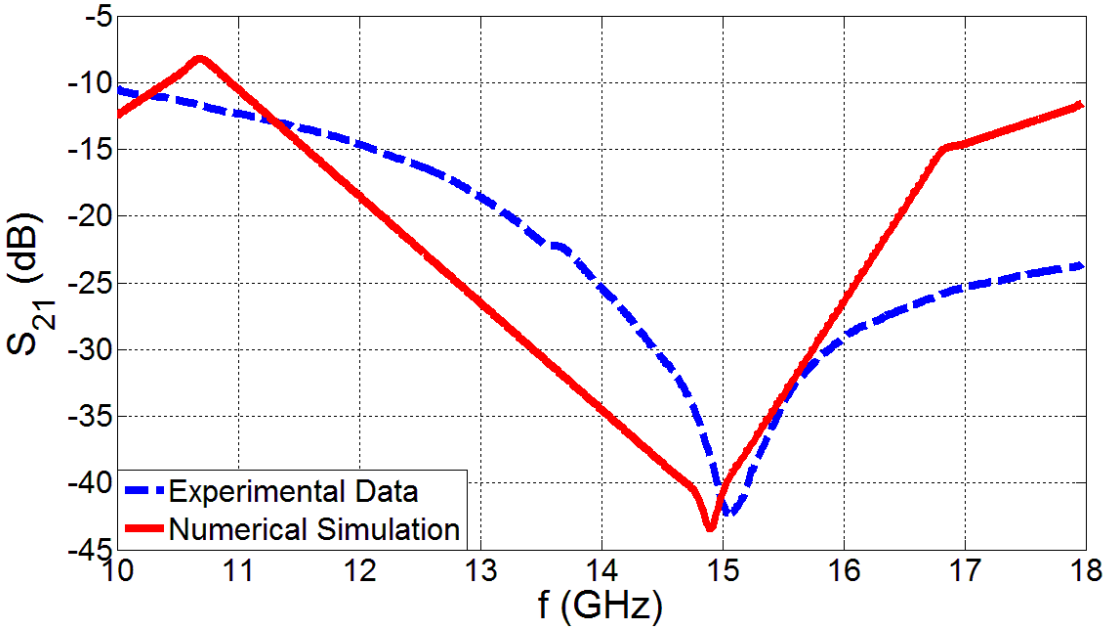
-5
-10
-15
-20
-25
-30
-35
-40
-45
10
11
12
13
14
15
16
17
18
S21 (dB)
f (GHz)
Experimental Data
Numerical Simulation

(b)

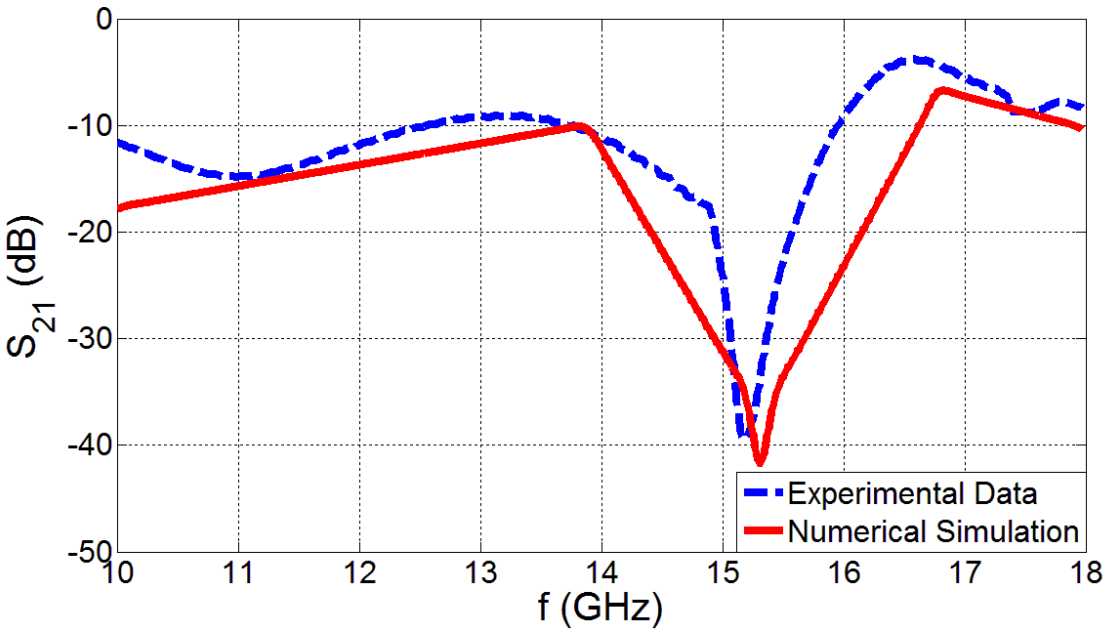
0
-10
-20
-30
-40
-50
10
11
12
13
14
15
16
17
18
S21 (dB)
f (GHz)
Experimental Data
Numerical Simulation

(c)

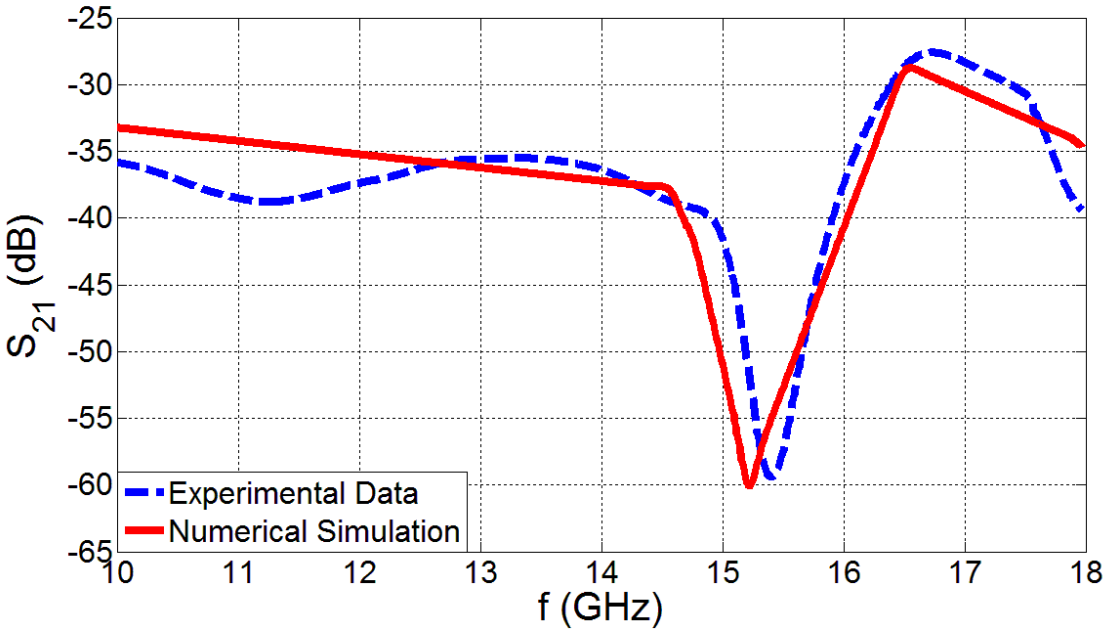


(d)

**Figure 3.4.2. Experimental measurement and numerical simulation of $S_{21}$ parameters with respect to frequency (a) for planar single device (b) for planar triplet device (c) for suspended single device (d) for suspended triplet device.**

**Table 3.4.2. The theoretical and experimental resonance frequencies and Q-factors of the planar and suspended devices.**

| | *$f_0$ (GHz)* | | Q-Factor | |
|---|---|---|---|---|
| | Theoretical | Experimental | Theoretical | Experimental |
| Planar Single Device | 14.88 GHz | 15.01 GHz | 98.770 | 93.810 |
| Suspended Single Device | 15.31 GHz | 15.18 GHz | 117.408 | 102.064 |
| Planar Triplet Device | 14.90 GHz | 15.06 GHz | 57.618 | 51.895 |
| Suspended Triplet Device | 15.22 GHz | 15.41 GHz | 80.317 | 67.146 |

For different geometries, we examine experimentally and numerically the $S_{21}$ parameters of the rectangular single device in Fig. 3.4.3(a), rectangular triplet device in Fig. 3.4.3(b), circular

single device in Fig. 3.4.3(c) and circular triplet device in Fig. 3.4.3(d). The $f_0$ and Q-factor values can be seen in Table 3.4.3. As for the different fabrication case, for the different geometry case the triplet device signal level and Q-factor are also lower than the single device case and the resonance frequency is a bit different than single device case. From Table 3.4.2 and Table 3.4.3, we see that the theoretical and experimental results agree with each other.

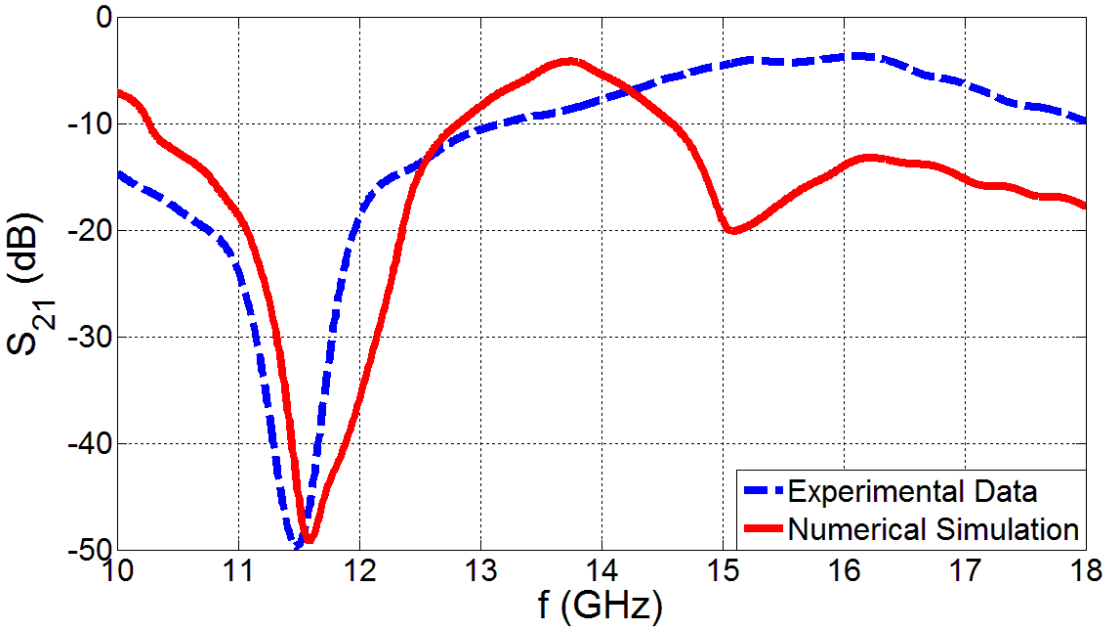


(a)

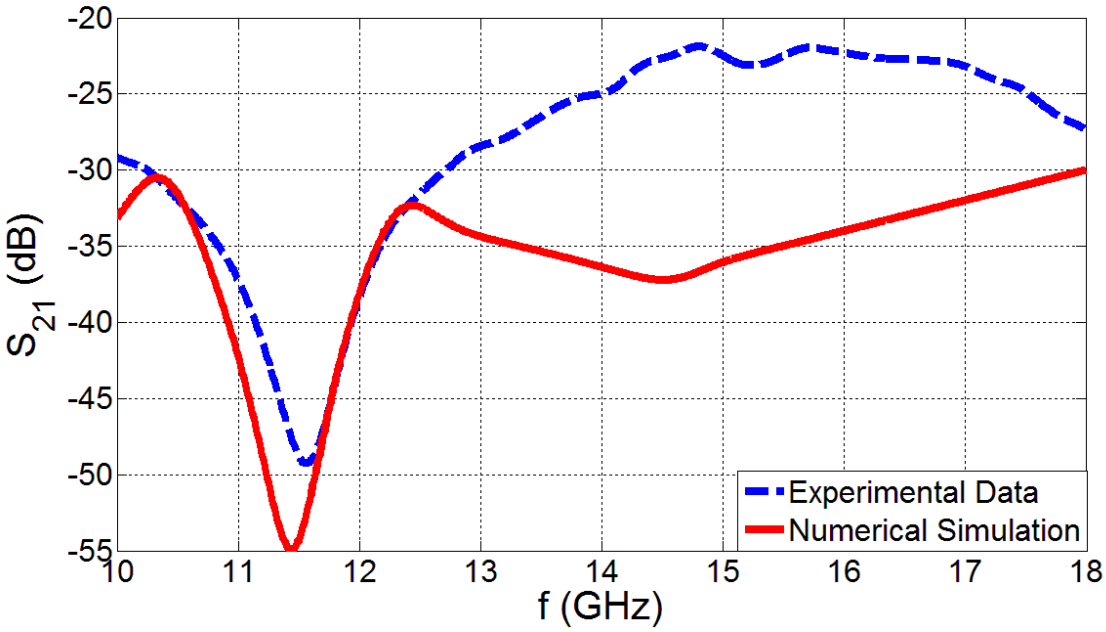
-20
-25
-30
-35
-40
-45
-50
-55
10
11
12
13
14
15
16
17
18
S21 (dB)
f (GHz)
Experimental Data
Numerical Simulation

(b)

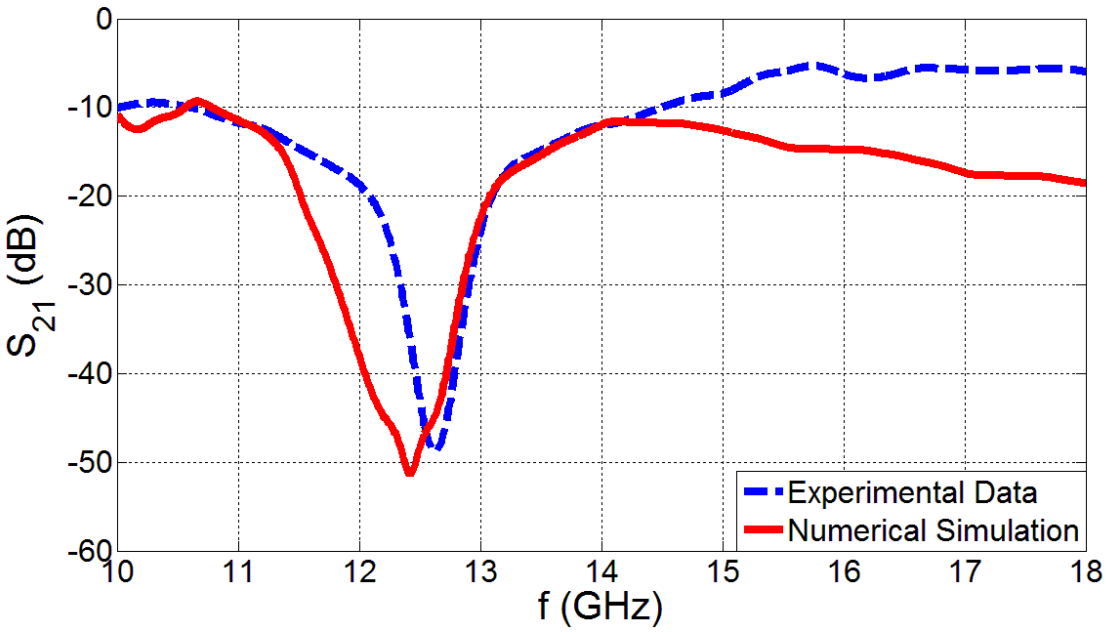
0
-10
-20
-30
-40
-50
-60
10
11
12
13
14
15
16
17
18
S21 (dB)
f (GHz)
Experimental Data
Numerical Simulation

(c)

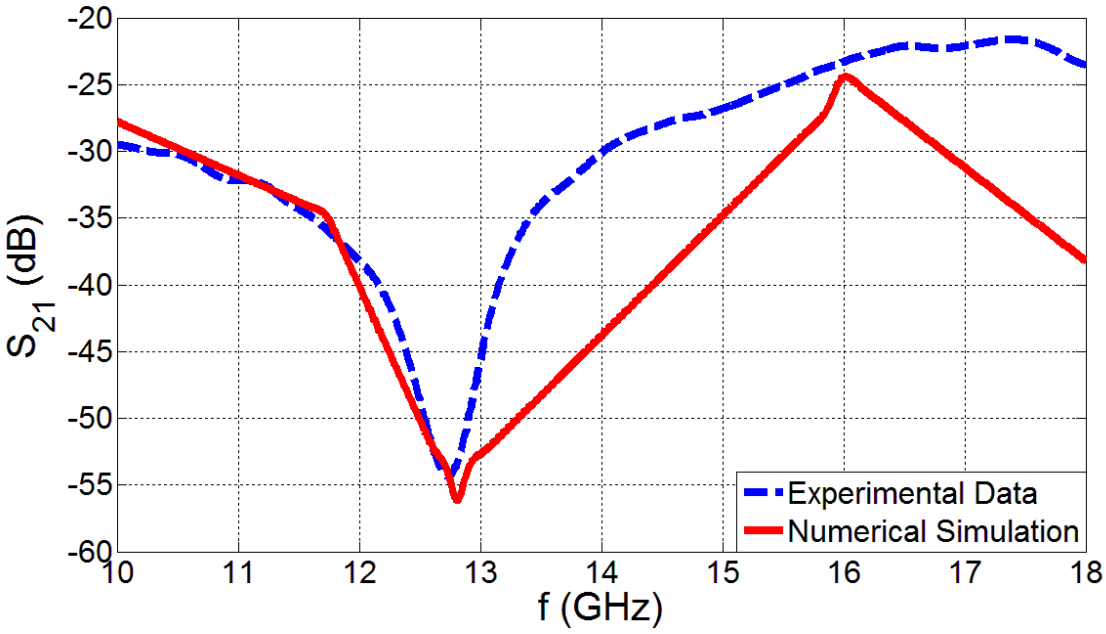


(d)

**Figure 3.4.3. Experimental measurement and numerical simulation of $S_{21}$ parameters with respect to frequency (a) for rectangular single device (b) for rectangular triplet device (c) for circular single device (d) for circular triplet device.**

**Table 3.4.3. The theoretical and experimental resonance frequencies and Q-factors of the rectangular and circular devices.**

| | *$f_0$ (GHz)* | | Q-Factor | |
|---|---|---|---|---|
| | Theoretical | Experimental | Theoretical | Experimental |
| Rectangular Single Device | 11.59 GHz | 11.48 GHz | 66.84 | 59.979 |
| Circular Single Device | 12.42 GHz | 12.63 GHz | 78.459 | 72.461 |
| Rectangular Triplet Device | 11.44 GHz | 11.56 GHz | 38.819 | 33.801 |
| Circular Triplet Device | 12.82 GHz | 12.73 GHz | 49.825 | 44.033 |

We apply load to the single device investigated with the setup in [39] constructed at Bilkent University. We observe $S_{21}$ parameters under different loads of the single device investigated and

triplet device investigated. In Fig. 3.4.4(a), we show the $S_{21}$ parameters of the single device investigated under different loads; and in Fig. 3.4.4(b), we present the zoom-in for the $S_{21}$ parameters of single device investigated. In Fig. 3.4.5(a), we depict the $S_{21}$ parameters of the triplet device investigated under different loads; and in Fig. 3.4.5(b), we display the zoom-in of the $S_{21}$ parameters of triplet device investigated. The resonance frequencies of single device investigated and triplet device investigated can be seen in Table 3.4.4. These results demonstrate that the resonance frequency of the triplet device case is increased as in the single device case.

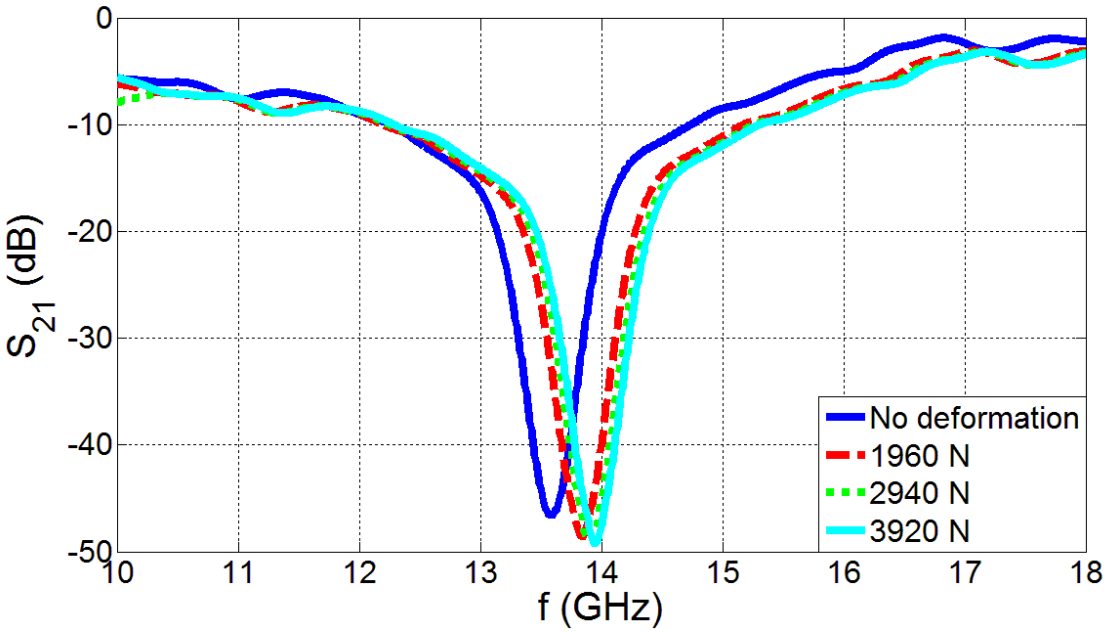


(a)

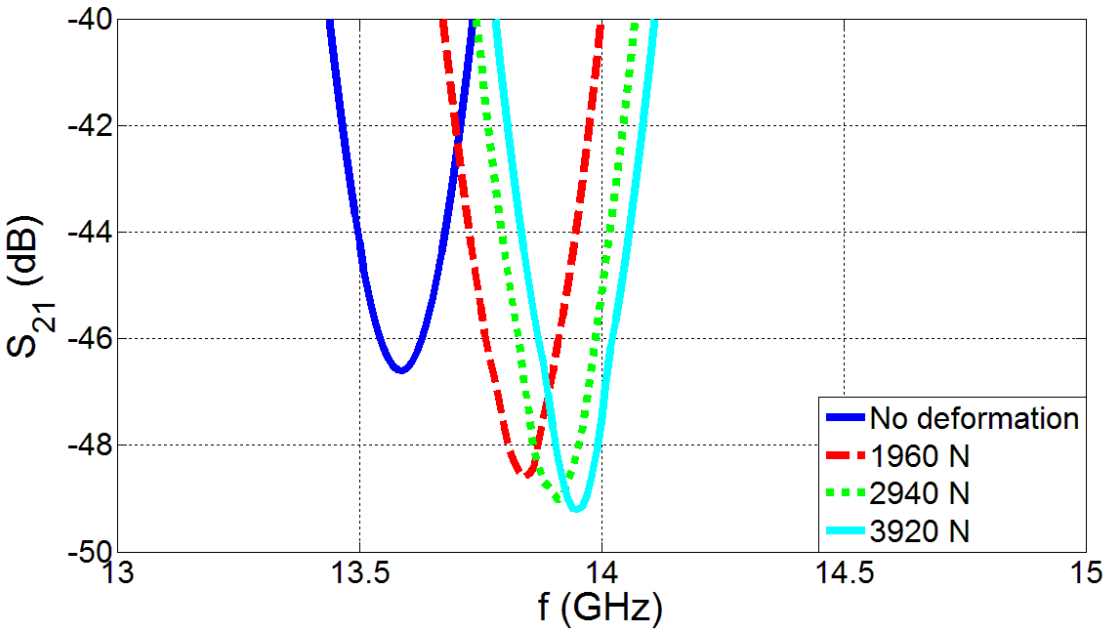


(b)

**Figure 3.4.4. Experimental measurements of $S_{21}$ parameters as a function of frequency (a) for single device investigated and (b) zoom-in of $S_{21}$ parameters for single device investigated, for the cases of no deformation and when loads of 1960 N, 2940 N and 3920 N are applied.**

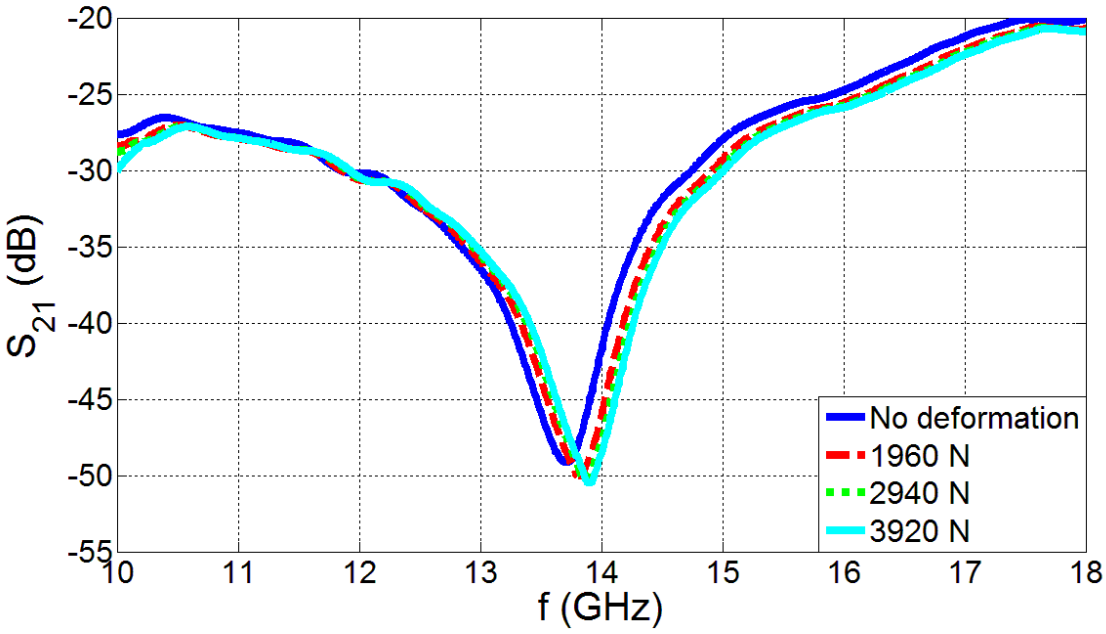


(a)

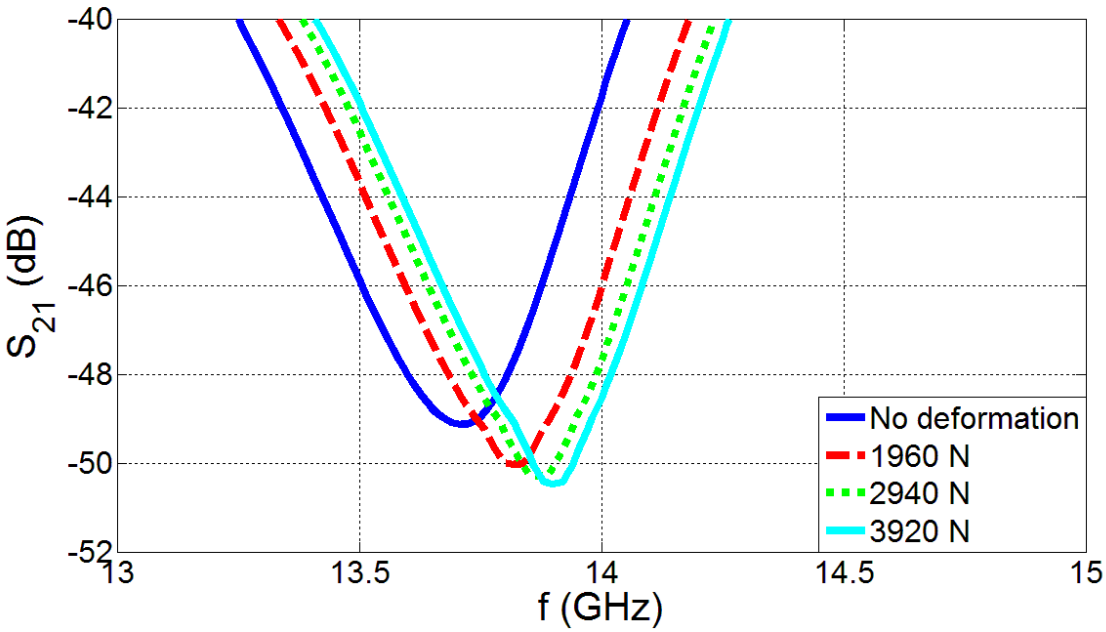


(b)

**Figure 3.4.5. Experimental measurements of $S_{21}$ parameters as a function of frequency (a) for triplet device investigated and (b) zoom-in of $S_{21}$ parameters for triplet device investigated, for the cases of no deformation and when loads of 1960 N, 2940 N and 3920 N are applied.**

**Table 3.4.4. The resonance frequencies of the devices with different loads.**

| Load | No load | 1960 N | 2940 N | 3920 N |
|---|---|---|---|---|
| Single Device Investigated | 13.59 GHz | 13.84 GHz | 13.91 GHz | 13.95 GHz |
| Triplet Device Investigated | 13.71 GHz | 13.82 GHz | 13.87 GHz | 13.9 GHz |

Table 3.4.5 gives the change of the resonance frequency, demonstrating that the shift of $f_0$ is lower in the triplet device case compared to the single device case. The reason is that load is applied to a larger area in the triplet device, whereas it is applied to a smaller area in the single device case. Then the shift of resonance frequency of the single device case for the same load is higher compared to the triplet device case.

**Table 3.4.5. The shift of the resonance frequencies of the devices with different loads.**

| Load | 1960 N | 2940 N | 3920 N |
|---|---|---|---|
| Single Device Investigated | 250 MHz | 320 MHz | 360 MHz |
| Triplet Device Investigated | 110 MHz | 160 MHz | 190 MHz |

When we observe the Q-factors under different loads in Table 3.4.6, we see that there is an increase in Q-factor with the applied load for both cases, which again shows the validity of the telemetrical measurement with the parallel behavior of single device and triplet device cases in terms of the Q-factor.

**Table 3.4.6. The Q-factors of the devices with different loads.**

| Load | No load | 1960 N | 2940 N | 3920 N |
|---|---|---|---|---|
| Single Device Investigated | 69.907 | 87.873 | 89.224 | 95.386 |
| Triplet Device Investigated | 33.998 | 41.765 | 44.172 | 45.514 |

We also examine the sensitivity (shift of resonance frequency per applied load) and relative shift (ratio of the shift of resonance frequency to the resonance frequency) in Table 3.4.7. The results show that the sensitivity and relative shift of the single device are higher than the triplet device case. This arises from the facts that the applied load is the same and the shift of the resonance frequency is higher in single device case. Therefore the sensitivity is higher in the single device case. Also, since the resonance frequencies are nearly the same and the resonance frequency shift is higher in the single device case, the relative shift of the single device is higher than the triplet device case.

**Table 3.4.7. The sensitivities of the devices.**

| | Sensitivity | Relative Shift |
|---|---|---|
| Single Device Investigated | 0.0918 MHz/N | 2.650% |
| Triplet Device Investigated | 0.0485 MHz/N | 1.390% |

# 3.4.3. Conclusion

In conclusion, we designed, numerically simulated, fabricated and experimentally characterized wireless bio-implant RF-MEMS sensors using the triplet idea. This is a telemetry system on the same chip where the transmitting and receiving antennas are placed at both ends of the chip and the sensor is in the middle. We examined sensors with different geometries, fabricated with different techniques and in different dimensions. In all cases, the triplet idea worked. We

observed that the signal level and the Q-factor in triplet device are lower than the single device case. The resonance frequency and Q-factor behavior of the triplet device with the applied load is the same as in the single device case, and the shift of $f_0$, the sensitivity and relative shift of the triplet device are lower than those of the single device case. The triplet idea facilitates device testing.

# Chapter 4

# Wireless Strain Sensing with Spiral Structure

In this chapter, we will present the proof-of-concept demonstration of fully telemetric sensing using spiral architecture. In this chapter, we will examine single type, array type, hybrid array type, and multi-turn spiral sensor. We will also discuss tension in spiral structure. We will experimentally investigate important parameters for sensing operation including sensitivity, Q-factor and linearity, and demonstrate the ways to improve these figure-of-merits. This chapter will show us the different characteristics of different types of sensors to telemetric sensing.

## 4.1 Wireless Bio-implantable RF-MEMS Strain Sensors

This section is based on the submission as “Wireless bio-implantable RF-MEMS strain sensors” **R. Melik**, E. Unal, C.M. Puttlitz, and H. V. Demir.

In many bone fracture cases, the healing process does not continue to form a solid fusion. Standard radiography is not capable of discriminating whether bone healing is occurring normally or aberrantly. In this section [57], we propose to use an implantable sensor that monitors strain on implanted hardware in real-time and telemetrically. To provide implantable tools for the assessment of bone fractures, we modeled, fabricated, and experimentally characterized on-chip sensors for telemetrically strain sensing and monitored strain fully telemetrically as a proof-of-concept demonstration. Due to the capacitance change of the sensors with the applied load, the operating frequency of the sensor shifts. By observing this change, we indirectly measure strain wirelessly. We implemented two types of fully telemetric sensors called single type and array type and compared their performances. With our single type of fully telemetric sensor, we obtain 0.218 MHz/kgf or 10.3 kHz/microstrain sensitivity with a maximum error of 24%. Using array type of fully telemetric sensor, although the sensitivity decreased to 0.155 MHz/kgf or 7.3 kHz/microstrain, the maximum error reduced to 11%. These data document that a single-type sensor has 1.5 fold increase in sensitivity compared to an array-type sensor. In contrast, the data indicated that an array-type sensor has more than a 2-fold reduction in error percentage compared to single-type sensors.

## 4.1.1. Introduction

Measuring strain telemetrically presents a difficult challenge; however, wireless strain recording holds important advantages. Treatment of complicated bone fractures is a technical challenge [40], and approximately 10% of all fractures do not heal properly [41]. Major fractures are usually treated by internal plate fixation. These plates deform (strain) under physiological loading (stress), and as the tissue mineralizes, the strain on the plate decreases [1]. Altered temporal load distribution and strain profiles are indicators of aberrant healing. We develop a technique to report the strain on the implanted plate using wireless technology. Specifically, in this section we demonstrate our RF-MEMS strain sensor designs that detect the strain on the implantable plate wirelessly.

The working principle of our sensor is based on operating frequency shift. When the load is applied to the implantable plate, the plate undergoes deformation. This deformation produces a concomitant change in the capacitance of the sensor. Hence, the operating frequency of the sensor changes, and by monitoring this change, we can observe the strain in real time and telemetrically.

Telemetric study is very important for wireless bio-MEMS sensors. In literature, there are some reports about RF telemetric readout of miniaturized antennas for different aims and applications. From these studies, we can see that the power coupling between external antenna and implanted sensor in limited space is difficult. Wireless power coupling between external antenna and implanted sensor could not be obtained in [43]-[47], where the aim is to see the physiological effect of the space in human beings, and the implanted sensor is connected to the network analyzer for measurements. There are also other works [53]-[56] that the telemetric measurement results could not be observed where in [53] the aim is to investigate ingestible devices, in [54] they used an intraocular pressure sensor, in [55] they used the chip for visual prosthesis for epi-retinal simulation, and in [56], the target is recording peripheral neural signals from axons.

Previously, we developed high Q-factor on-chip resonators [15], [31], and using on-chip probes, we demonstrated the proof of concept of operating frequency shift in [39], and showed the increase of the performance of the sensors measured by probes in [49]. In this section, we present the proof of concept of the operating frequency shift fully telemetrically. In our previous works in [39] and [49], we used probes to measure strain using operating frequency shift, however, in this section, we measure strain fully telemetrically. We observe the transmission of our sensor without any wires or other connections and our sensors are remotely located away from our external antennas. We apply load to our sensor using a custom-designed compression setup and detect the strain telemetrically. We explore the effects of different parameters to the quality of telemetric sensing such as sensitivity and error, by comparing single-type and array-type sensors.

## 4.1.2. Design, Fabrication and Experimental Characterization

Our aim is to make high Q-factor, biocompatible sensors with relatively small size (with total chip size 1.5 cm × 1.5 cm). The size of the sensor is limited by the implantable plate size. For miniaturization purposes, the sensor should be passively powered; otherwise, the space will be limited by power supply. We make on-chip sensors and use distributed capacitance (as opposed to utilizing the external capacitance as in [44]-[47], which undesirably increases the area substantially) to tune the operating frequency, and miniaturize the sensor dimensions. We use $Si_3N_4$ as the dielectric thin film with its high dielectric constant (~8) and obtain a high film capacitance ($C_{film}$), which is the capacitance between the substrate and metal layer. We use $C_{film}$ as the parallel plate LC tank circuit capacitance. The details of the on-chip resonator concept can be found in [31], [39]. We need sensors with sufficiently high Q-factor to track the operating frequency shift. The details of the high Q-factor sensor design can be found in [31], [39]. Since our sensor will be implanted within the human body, we are restricted to using bio-compatible materials. We use a Si substrate instead of a GaAs substrate (although using GaAs substrate would increase the Q-factor) and we use Au as metal layer instead of Al or Cu. We use highly resistive Si substrate to have parallel plate capacitor ($C_{film}$) because nonconductive Si hinders $C_{film}$. We also design our coil with minimum number of turns (N) as 2, with large width (w) and low spacing (s). All the details of the coil design can be seen in [15], [31]. By considering all these factors, we obtain the design parameters as shown in Table 4.1.1 where $L_c$ is the total length of the sensor, $W_c$ is the total width of the sensor, w is the width of each coil, s is the spacing between coils, N is the number of turns, $t_{metal}$ is the thickness of Au and $t_{film}$ is the thickness of the $Si_3N_4$. In this section, we compare two types of sensors that are composed of spiral coils with the same dimensions and fabricated in a consistent manner.

**Table 4.1.1. Our device parameters.**

| $L_c$ (μm) | $W_c$ (μm) | $N$ | $w$ (μm) | $s$ (μm) | $t_{film}$ (μm) | $t_{metal}$ (μm) |
|---|---|---|---|---|---|---|
| 1040 | 1040 | 2 | 200 | 10 | 0.1 | 0.1 |

For the fabrication of our sensors, we first deposit 0.1 μm thick $Si_3N_4$ film onto the silicon substrate using plasma enhanced chemical vapor deposition (PECVD). Subsequently, by utilizing lithography, metallization using a box-coater, and lift-off, we deposit and pattern a 0.1 μm Au layer onto the $Si_3N_4$ dielectric thin film and finalize our structure. Fig. 4.1.1(a) presents the top view of a single-type spiral coil resonator, and Fig. 4.1.1(b) depicts the whole structure. Our total chip size is 1.5 cm × 1.5 cm and includes 4 spiral coils, 2 spiral coils in the horizontal direction and 2 spiral coils in the vertical direction. Fig. 4.1.1(c) shows the top view of an array-type spiral coil resonator, and Fig. 4.1.1(d) demonstrates the whole structure. In this case, we have 6×5 array structure, resulting in a total of 30 spiral coils.

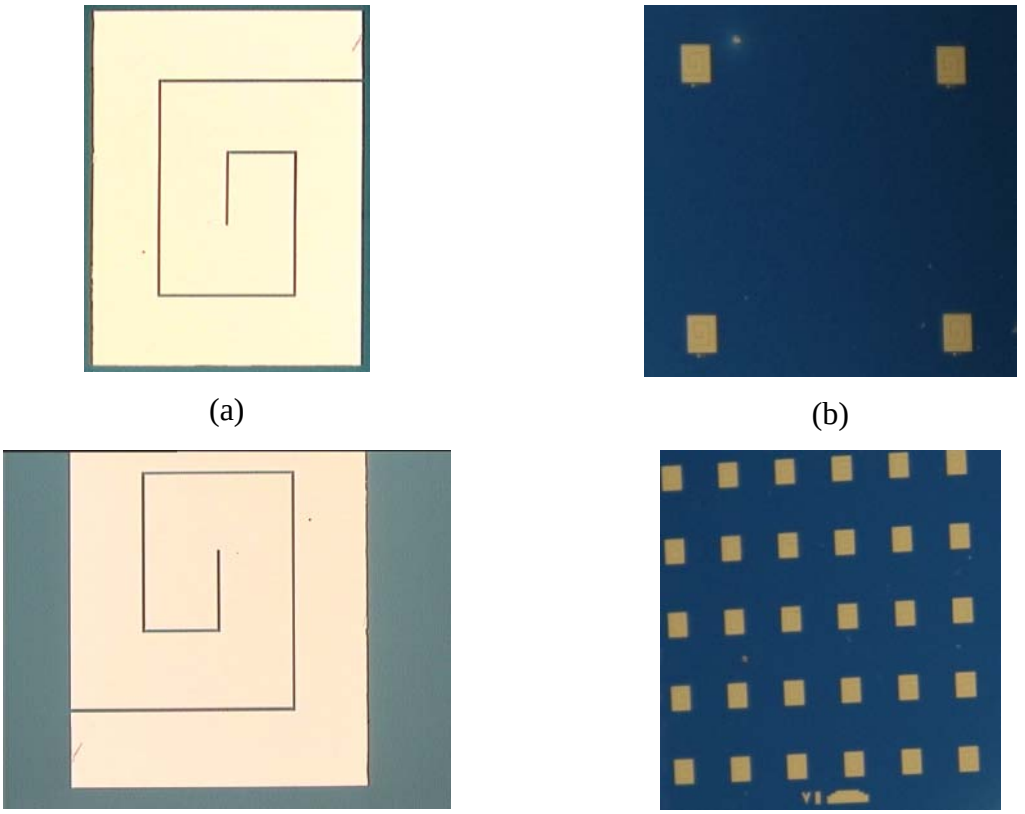

(a) (b)

(c) (d)

**Figure 4.1.1. (a) The top-view micrograph of a single-type fabricated resonator, (b) the whole single-type fabricated sensor, (c) the top-view micrograph of an array-type fabricated resonator, and (d) the whole array-type fabricated sensor.**

We fix our sensor to the implantable plate by using hard epoxy. We use a cast polyamide test material to represent the implantable plate and it is fixed to the testing apparatus with a rail system as demonstrated in Fig. 4.1.2. We apply load to the cast polyamide rod in a controllable manner using this setup. In our compression setup, the pneumatic piston applies load to the cast polyamide and varies between 0-300 kgf. The load is measured by a load cell at the bottom of the compression setup. We use standard gain horn antennae, one of which acts as the transmitter and the other of which as the receiver. The horn antennae are connected to a standard network analyzer with low loss cables. For calibration purposes, we first measure the inherent transmission of the cast polyamide rod when there is no sensor attached to it. Afterwards, we

repeat the same measurement with the sensor attached under no load and then under variable loading. We obtain the transmission spectra referenced relative to the no sensor condition as a function of the applied load.

The operating principle of the sensor is that mechanical deformation of the sensor shifts the operating frequency. Specifically, under compressive deformation the dielectric area is reduced, and hence the dielectric capacitance is subsequently decreased. Therefore, the operating frequency increases. The theoretical explanation of this concept is explained in detail in [39].

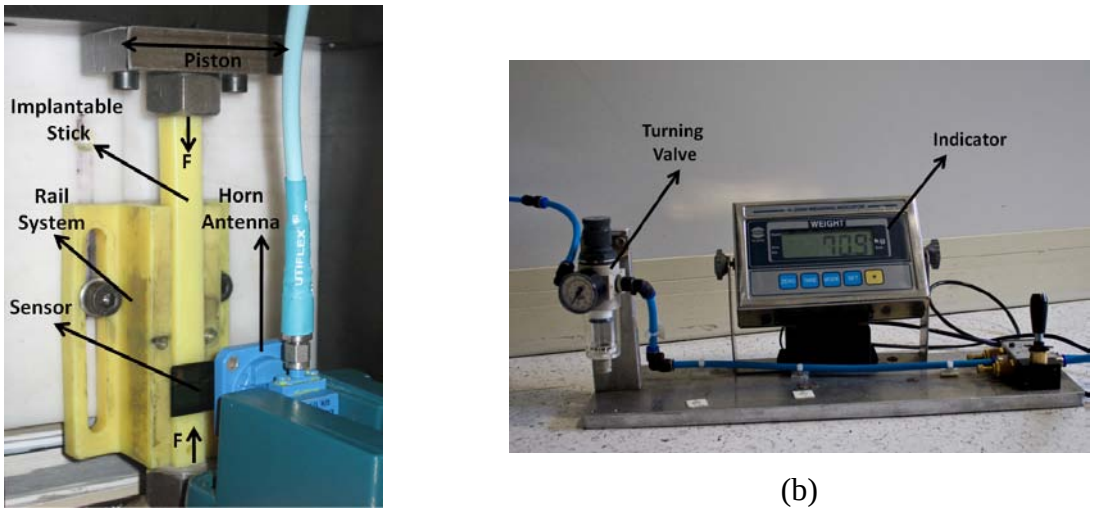


(a) (b)

**Figure 4.1.2. The experimental setup: (a) the compression apparatus and (b) the force adjustment component.**

Fig. 4.1.3(a) shows the transmission of the single-type sensor parameterized with respect to the applied load while Fig. 4.1.3(b) illustrates the zoom-in of the transmission of the sensor parameterized with respect to the applied load. We see a definite trend of operating frequency increase with the increased applied load in Fig. 4.1.3(a) and Fig. 4.1.3(b). The applied load (F) versus operating frequency shift ($\Delta f_0$) is depicted in Fig. 4.1.3(c) from the transmission spectra of our single-type sensor. We obtain the operating frequency shift ($\Delta f_0$) by subtracting the operating frequency of the zero load condition (16.537 GHz) from the operating frequency of the sensor

under different applied loads. By using commercially available wired strain gauges (Tokyo Sokki Kenkyujo Co., Ltd. Strain Gauges with a gauge factor of 2.1), we determine the Young's modulus of the cast polyamide as 3.287 GPa and characterize the induced strain from the applied load (via transformation of the strain values using the material geometry). Then we obtain the induced strain of the implantable plate from the sensor telemetrically by using the operating frequency shift as shown in Fig. 4.1.3(d). From Fig. 4.1.3(c) and Fig. 4.1.3(d), we acquire sensitivities of 0.218 MHz/kgf or 10.3 kHz/microstrain, which is relatively high. Fig. 4.1.3(e) demonstrates the errors in terms of microstrain and Fig. 4.1.3(f) presents the errors in terms of percentages. Here these errors are the horizontal distances of the data points from the best linear fit (using the least square error) in microstrain. From these graphs, we can see that the wireless sensor is observed to have error of less than 701 microstrain or less than 24%.

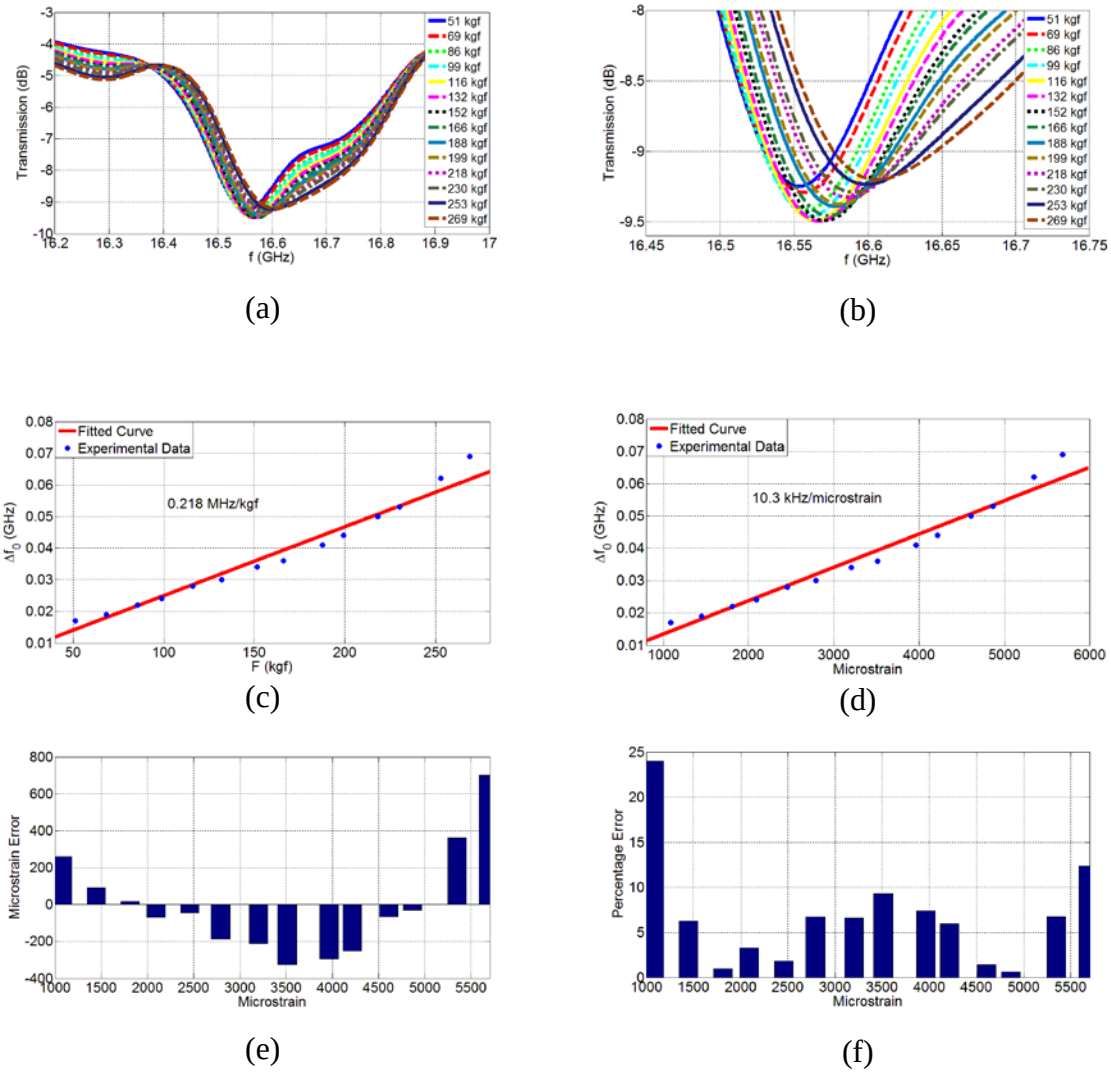


**Figure 4.1.3. Experimental measurements of single-type sensor (a) transmission as a function of frequency with different applied loads, (b) the zoom-in of the transmission as a function of frequency with different applied loads, (c) F *vs.* $\Delta f_0$, (d) microstrain *vs.* $\Delta f_0$, (e) the error in terms of microstrain, and (f) the error in percentages.**

We can see the experimental measurements of the array-type sensor in Fig. 4.1.4. The transmission spectra and zoom-in of the transmission spectra of the sensor is depicted in Fig. 4.1.4(a) and Fig. 4.1.4(b), respectively. The Q-factors and transmission minima are higher as compared to the single-type sensor. There is also a definite trend of increasing operating

frequency with the increasing applied load (as was the case for the single-type sensor). Fig. 4.1.4(c) presents the operating frequency shift (with no load operating frequency of 16.534 GHz) with respect to the applied load and results in a 0.155 MHz/kgf sensitivity. Fig. 4.1.4(d) shows the induced strain in terms of microstrain as a function of the applied load and this data indicates a 7.3 kHz/microstrain sensitivity. The sensitivities we obtain from array-type sensors are high enough to show the induced strain of the implantable rod telemetrically, however these sensitivities are lower than the single-type sensor. Fig. 4.1.4(e) illustrates the errors in terms of microstrain and denotes less than a 440 microstrain error while Fig. 4.1.4(f) demonstrates the errors that are less than 11%. The errors obtained from the array-type sensor are less than the ones obtained from the single-type sensor.

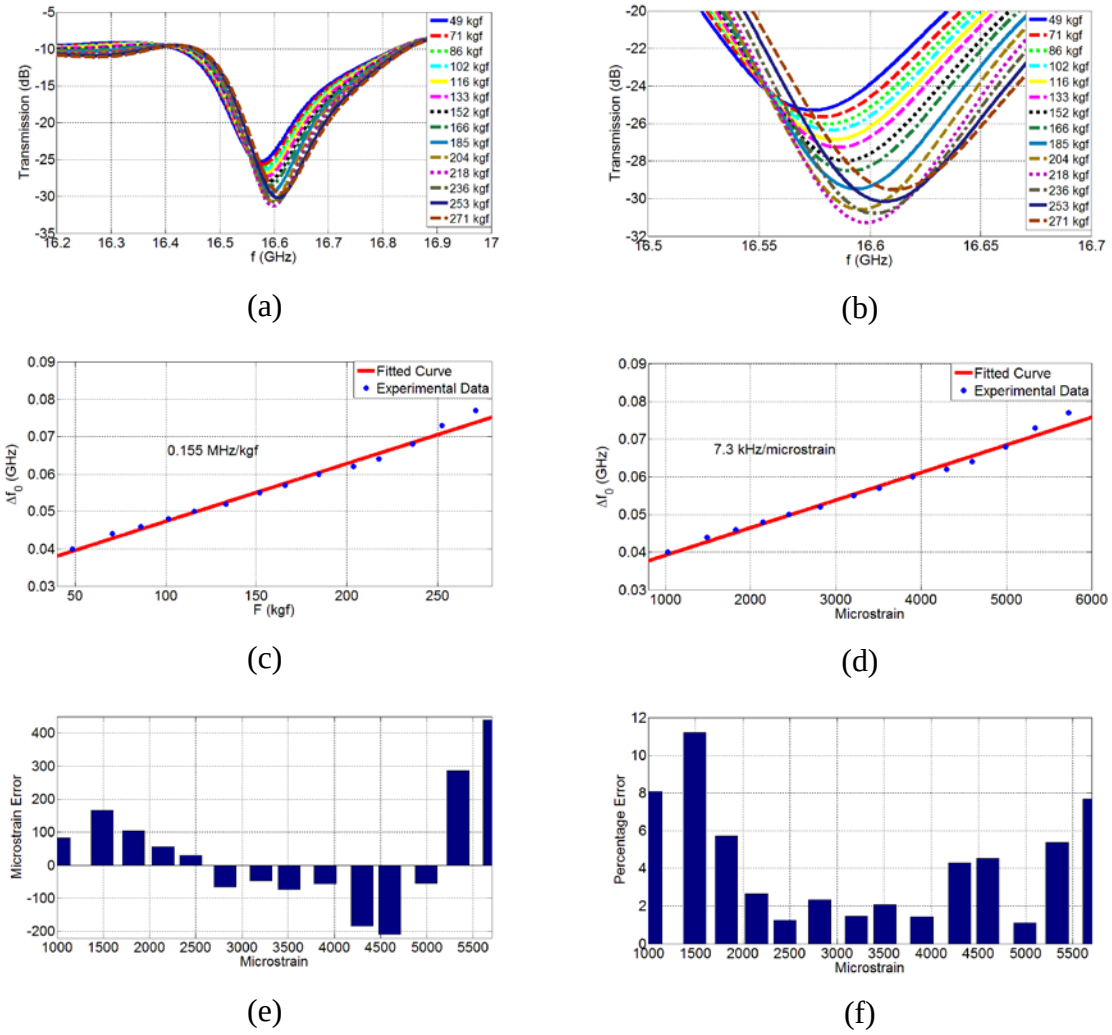


**Figure 4.1.4. Experimental measurements of array-type sensor (a) transmission as a function of frequency with different applied loads (b) the zoom-in of the transmission as a function of frequency with different applied loads (c) F *vs.* $\Delta f_0$, (d) microstrain *vs.* $\Delta f_0$, (e) the error in terms of microstrain, and (f) the error in percentages.**

We demonstrate that strain can be measured via telemetry using both of our sensors. However, these sensors demonstrate important differences in terms of sensing parameters, sensitivity, Q-factors, and errors. The single-type sensor shows higher sensitivity while array-type sensor exhibits higher Q-factors and lower errors. Sensitivity is an important parameter for our sensing

application. There are only limited number of datum points in one frequency scan using a network analyzer; therefore, it is easier to track smaller shifts in the transmission spectra with respect to the externally applied load when the sensitivity is higher. If the sensitivity is too low, then the shift of operating frequency will be insufficient and differences in strain will not be detectable. In this respect, the single-type sensor is more sensitive compared to the array-type sensor, and this is probably because since it has fewer structures on it. The same force is applied to the whole chip (the dimensions of whole chip is the same for both types) and since the single-type sensor has fewer structures on it, the applied force per structure is higher in a single-type sensor. As a result, changes due to deformation of the structure are higher hence the operating frequency shift is higher in a single-type sensor. The data confirms this wherein the single-type sensor shows approximately a 1.5-fold increase in sensitivity.

The Q-factor is another important concern for our application. If the sensor demonstrates a sufficiently high Q-factor, we can accurately track the shift of the operating frequency in the transmission spectra. Another important parameter for wireless sensing is the linearity of the strain detection. The errors depend on two parameters. The first one is sensitivity and the second one is a high Q-factor. If the sensitivity is too low, then the data will be stepwise, resulting in a greater error. If the Q-factor and transmission minima in the transmission spectra are low, then we cannot measure strain telemetrically as explained above. Inherently, the array-type sensor has more structures on it compared to a single-type sensor, and therefore, it emits a stronger signal and exhibits a higher Q-factor and greater minima magnitude. As a result, it has a relatively higher signal to noise ratio (SNR) and demonstrates lower errors. Array-type sensor leads to a more than 2-fold reduction in errors.

## 4.1.3. Conclusion

In conclusion, we showed the proof of concept of bio-implantable RF-MEMS strain sensors to monitor the fracture healing process by measuring the strain telemetrically. We did not use any probes, wires, PCB or any other hardwiring in our measurements and observed strain fully telemetrically by using both single-type and array-type sensors. We obtained 0.218 MHz/kgf or 10.3 kHz/microstrain sensitivity with a maximum 24% error from the single-type wireless strain sensors, and obtained 0.155 MHz/kgf or 7.3 kHz/microstrain sensitivity with a maximum 11% error from the array-type wireless strain sensors. By comparing the single-type sensor and array-type sensor, we explored what effects different parameters have on the quality of the telemetric measurement (such as sensitivity and errors). The single-type sensor shows approximately 1.5-fold increase in sensitivity compared to the array-type sensor since it has fewer structures on it. However, the array-type sensor represents a more than 2-fold reduction in errors because it has more structures, which produces a higher Q-factor, higher SNR, and lower errors.

## 4.2 Hybrid Arrays

In this section, we will explore the hybrid arrays and investigate the relation between Q-factor and linearity. In previous section, we experimentally demonstrated that when we use array structures, we have better linearity compared to single device structure; however, that when we use single device structure, we have better sensitivity. By using hybrid array structure, we can increase both sensitivity and linearity; hence, we can increase the overall sensor performance.

In this section, we investigate 4 devices whose dimensions are given in Table 4.2.1. In Fig. 4.2.1 we can see the fabricated devices. Each device has a unit cell with dimensions shown in Table 4.2.1 but with the same total chip size of 1.5 cm × 1.5 cm. The single circular device just has 4 circular spiral coils whereas the array-circular structure has 15 × 17 circular coils. The multiarray-circular device has 40 × 46 circular coils and the hybrid array structure has 29 × 29 spiral coils. The hybrid array structure has both circular and rectangular coils at the same time. In the hybrid array structure, after one rectangular spiral structure, we have one circular structure. The fabrication procedure of the sensors is the same as in Section 4.1 and the experimental setup and calibration procedure are also the same as those described in Section 4.1.

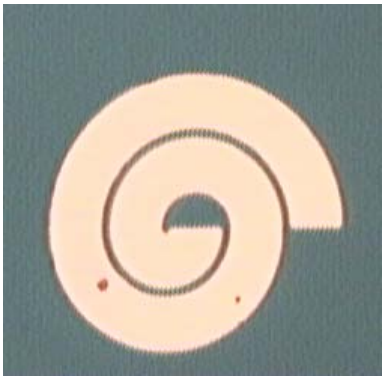

(a)

(b)

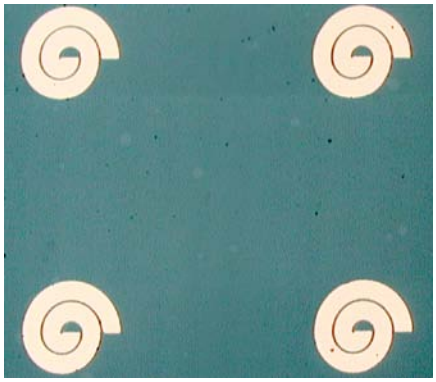

(c)

(d)

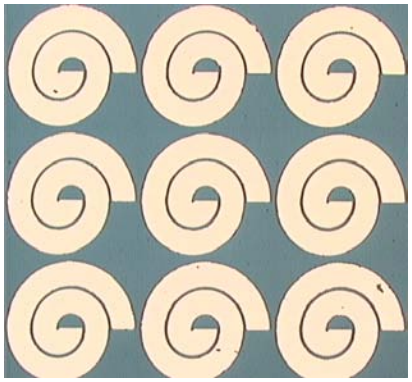

(e)

(f)

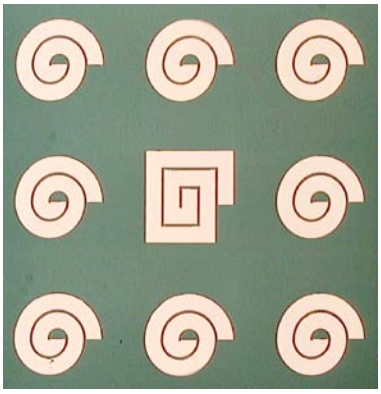

(g)

(h)

**Figure 4.2.1. (a) The top view of the micrograph single-circular device and (b) the whole single-circular device; (c) the top view of the micrograph array-circular device and (d) the whole array-circular device; (e) the top view of the micrograph multiarray-circular device and (f) the whole multiarray-circular device; and (g) the top view of the micrograph hybrid array device and (h) the whole hybrid array device.**

**Table 4.2.1. Our device parameters.**

| | $L_c$ (μm) | $W_c$ (μm) | $N$ | $w$ (μm) | $s$ (μm) | $t_{film}$ (μm) | $t_{metal}$ (μm) |
|---|---|---|---|---|---|---|---|
| Sensor-1 | 340 | 340 | 2 | 60 | 10 | 0.1 | 0.1 |

We show the experimental results of the single-circular device in Fig. 4.2.2. The no load resonance frequency of the circular-single device is 16.484 GHz, while it has the no load Q-factor of 99.35, which is the lowest Q-factor in all investigated devices. Also, it has the lowest transmission dip in all explored cases, however both the Q-factor and the transmission dip are enough for strain readout. The sensitivity of the device is 0.265 MHz/kgf, or 12.5 kHz/microstrain. It has an error less than 2000 microstrain. Since it has the lowest trasnsmission dip and the lowest Q-factor, it has the highest error. If the sensor has a lower Q-factor and transmission dip, then the noise will dominate the signal, it will have a lower SNR, which increases the error.

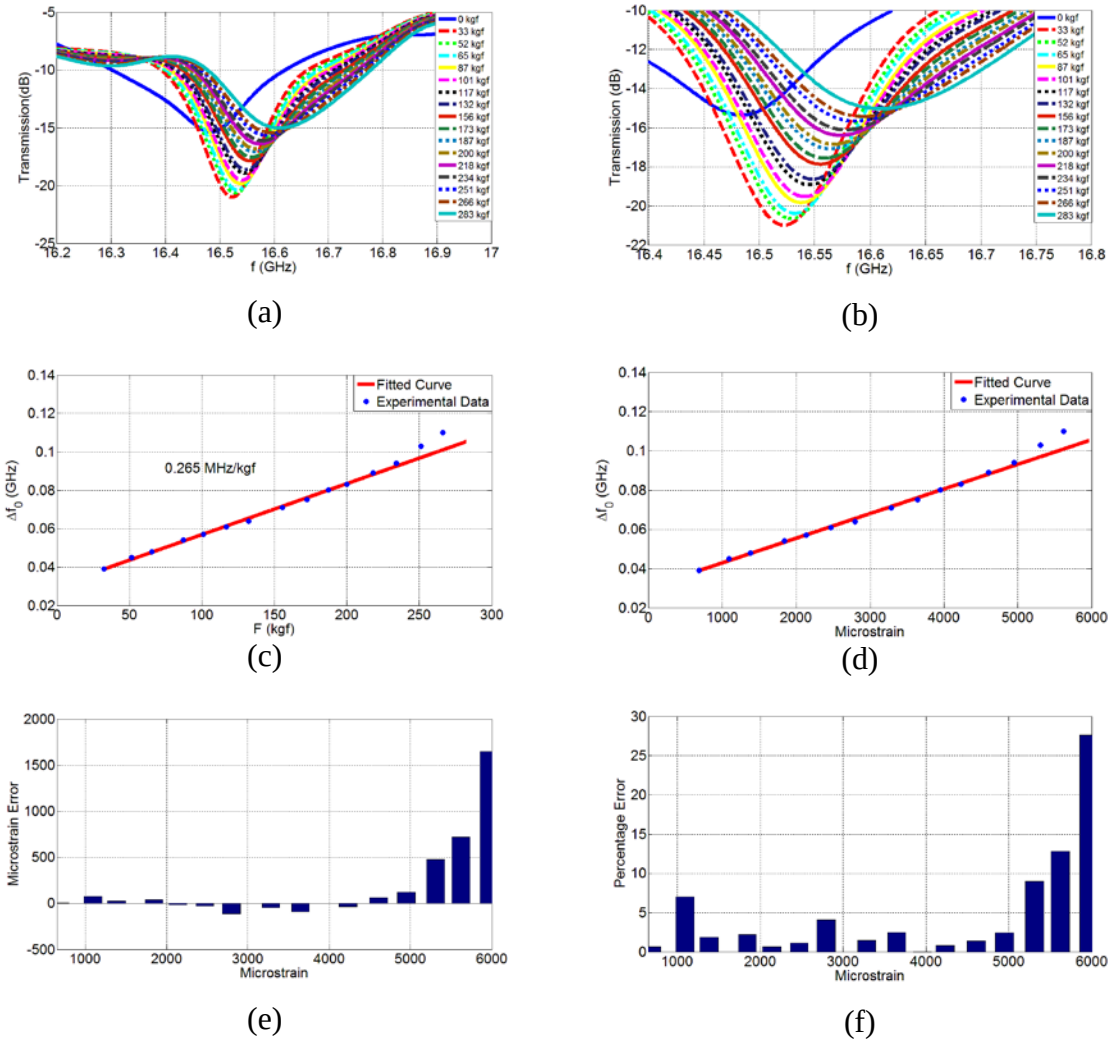


**Figure 4.2.2. Experimental measurements of the single-circular sensor: (a) Transmission spectra under different applied loads, (b) the zoom-in of the transmission spectra (c) F *vs.* $\Delta f_0$, (d) microstrain *vs.* $\Delta f_0$, (e) error in terms of microstrain, and (f) the error in terms of percentage.**

The experimental results of the array-circular device can be seen in Fig. 4.2.3. The no load resonance frequency of the array-circular device is 16.525 GHz while its no load Q-factor is 171.6. Since array structure has many more units on it, it radiates higher signal compared to the single-circular device. Hence it yields a higher Q-factor and transmission dip. The sensitivity of the array-circular device is 0.259 MHz/kgf, or 12.2 kHz/microstrain. Since the array-circular device contains more units compared to

the single-circular device, and we apply the same load to the whole chip, the singe-circular one deforms more; hence, it has a higher level of sensitivity as expected. The array-circular device has error less than 1200 microstrain. We can see that the array-circular device has a higher Q-factor and transmission dip, thus it exhibits small errors compared to the single-circular case.

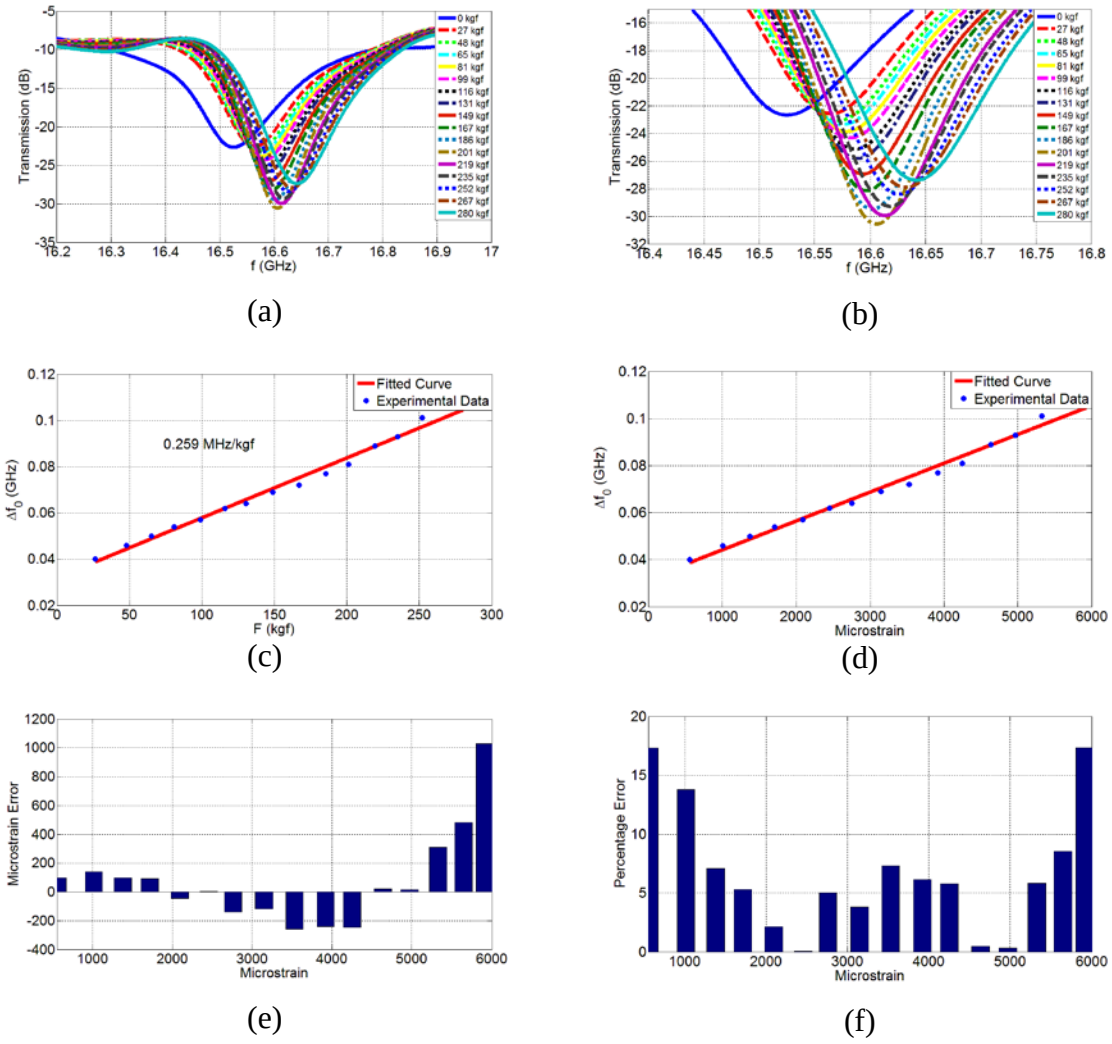


**Figure 4.2.3. Experimental measurements of the array-circular sensor: (a) Transmission spectra under different applied loads, (b) the zoom-in of transmission spectra, (c) F *vs.* $\Delta f_0$, (d) microstrain *vs.* $\Delta f_0$, (e) error in terms of microstrain, and (f) error in terms of percentage.**

We demonstrate the experimental results of the multiarray-circular device in Fig. 4.2.4. The no load resonance frequency of the device is 16.515 GHz, while the no load Q-factor is 265.1. Since it has the highest number of units on it, the multiarray-circular device has the highest Q-factor and the highest dip in all the investigated devices. Also, since each spiral coil effects the resonance, there is more mutual coupling between each pair of spiral coils, the no load resonance frequencies of each device investigated is slightly different. The sensitivity of the device is 0.203 MHz/kgf, or 9.6 kHz/microstrain. Since it contains the highest number of units on it, it shows the lowest sensitivity among all investigated devices. It exhibits an error less than 300 microstrain. Since it has the highest Q-factor and transmission dip, it features the lowest errors in all cases of the devices investigated.

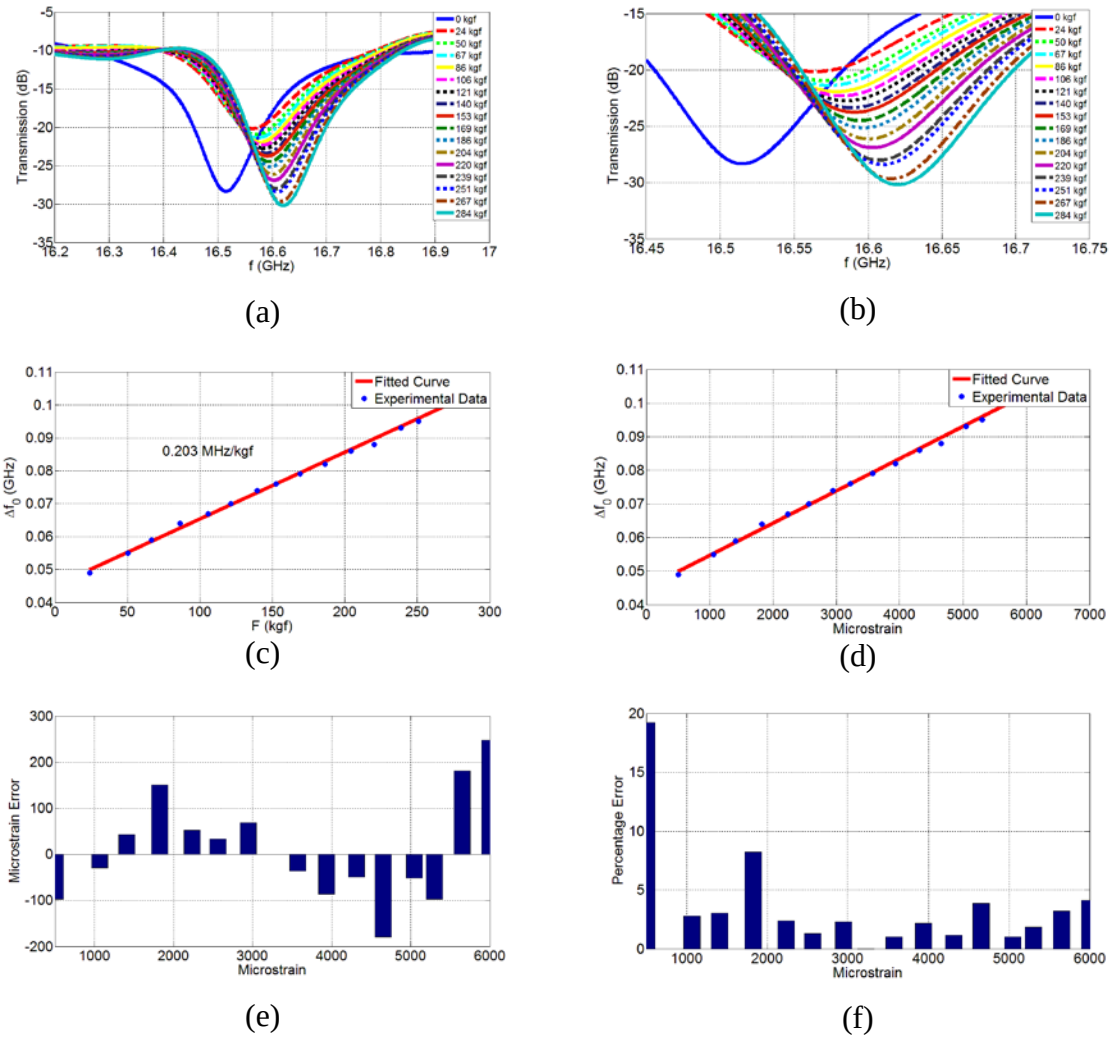


**Figure 4.2.4. Experimental measurements of the multiarray-circular sensor: (a) Transmission spectra under different applied loads, (b) the zoom-in of transmission spectra, (c) F *vs.* $\Delta f_0$, (d) microstrain *vs.* $\Delta f_0$, (e) error in terms of microstrain and (f) error in terms of percentage.**

We depict the experimental results of the hybrid array in Fig. 4.2.5. The no load resonance frequency of the hybrid array is 16.549 GHz and the no load Q-factor is 178.14. Since it has more units than array-circular and single-circular, it has a higher Q-factor and a higher dip compared to the array-circular and single-circular devices. However, it has fewer units than the multiarray-circular, and as a result, it has lower Q-factor and a lower transmission dip. The

sensitivity of the hybrid array is 0.326 MHz/kgf, or 15.4 kHz/microstrain. Because of its fewer units compared to the multiarray-circular case, it is expected to have a higher level of sensitivity. Although the hybrid array incorporates more units than the array-circular and single-circular, since it has a combination of rectangular and circular geometries, it is deformed more per unit force, as it has higher sensitivity. The circular isotropic structures tend to yield more deformation if the force is applied as in Section 3.2. However, in this case, the force is applied to the test material stick uniaxially. In Section 4.1, we can see that the difference between the array device and the single device in terms of the sensitivity level is high; however, in this case, there is no such a large difference because of the isotropic geometry. The strain is equally distributed in the circular case. However, in the rectangular case, the deformation is predominantly along one dimension and the amount of the deformation in this direction is higher compared to the circular case. Thus, if we place both rectangular and circular coils in the same chip, we will obtain higher deformation compared to the case of only circular coil. Also, since the area of the circular coil is smaller compared to rectangular coil, we cannot include the same number of coils in the same device; hence, we will have lower Q-factors. Thus, integrating circular and rectangular coils in the same device is the best way to increase sensitivity and Q-factor at the same time. The hybrid array shows an error less than 800 microstrain, which is smaller than those of the array-circular device and single circular device as expected. Since the Q-factor of the hybrid array is higher compared to these devices, its error is lower. However, it has higher errors compared to the multi-array case.

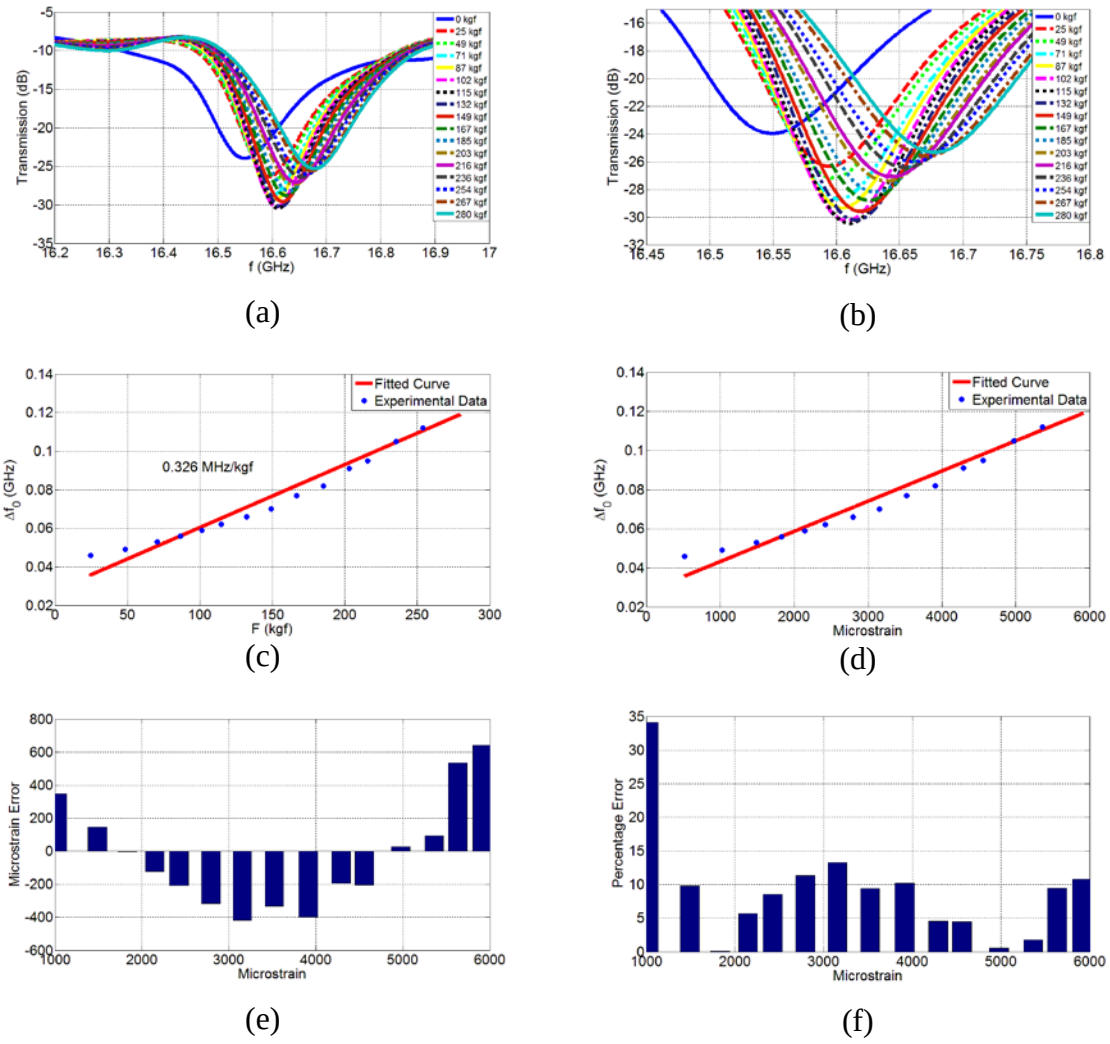


**Figure 4.2.5. Experimental measurements of the hybrid array sensor: (a) Transmission pectra under different applied loads, (b) the zoom-in of transmission spectra, (c) F *vs.* $\Delta f_0$, (d) microstrain *vs.* $\Delta f_0$, (e) error in terms of microstrain, and (f) error in terms of percentage.**

In conclusion, if a device features a higher Q-factor, it shows lower errors. Herein, by using hybrid array structures, we increased the sensitivity and Q-factor and decreased the errors at the same time compared to the single-circular and array-circular case.

## 4.3 Multi-turn Spirals

In this section, we will investigate the multi-turn spiral coils. We will show that the multi-turn spirals show the better sensing performance compared to the cases of other spiral structures. We will generate another device by adding a line to form a complete loop for spiral coils. We will compare the sensor performance of this device against the starting multi-turn device.

We explore three devices (Sensor -1, -2 and -3) in this section. We present the fabricated devices in Fig. 4.3.1. The total size of the chip is 1.5 cm × 1.5 cm. We list the device parameters in Table 4.3.1. The fabrication procedure of Sensor-1 and Sensor-2 is the same as in Section 4.1. By using the identical fabrication procedure we fabricate 50-turn spiral sensors. For Sensor-3, we additionally deposit a 0.1 μm thick $Si_3N_4$ on Sensor-2 using plasma enhanced chemical vapor deposition (PECVD). Then, by using lithography and wet etching, we open holes to the ends of Sensor-2. Subsequently, by utilizing lithography, metallization using a box-coater, and lift-off, we deposit and pattern a 0.1 μm Au layer and finalize our structure. In Sensor-3, we complete a full loop by connecting the ends. The experimental setup and calibration procedure are the same as described in Section 4.1.

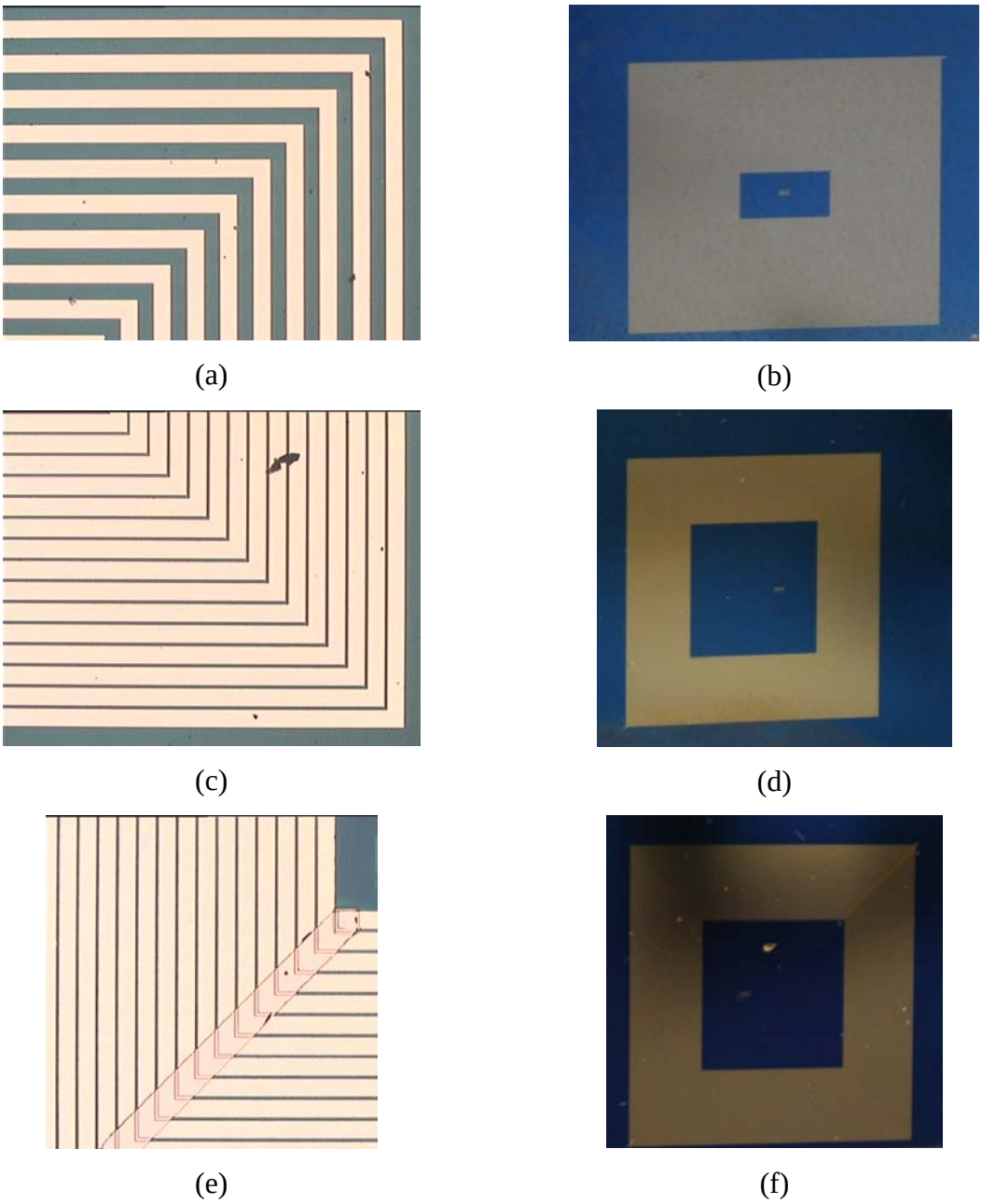


**Figure 4.3.1. (a) The top view micrograph of Sensor-1, and (b) the whole picture of Sensor-1; (c) the top view micrograph of Sensor-2, and (d) the whole picture of Sensor-2; and (e) the top view micrograph of Sensor-3 and (f) the whole picture of Sensor-3.**

**Table 4.3.1. Our device parameters.**

| | $L_c$ (μm) | $W_c$ (μm) | $N$ | $w$ (μm) | $s$ (μm) | $t_{film}$ (μm) | $t_{metal}$ (μm) |
|---|---|---|---|---|---|---|---|
| Sensor-1 | 12000 | 12000 | 50 | 50 | 50 | 0.1 | 0.1 |
| Sensor-2 | 12000 | 12000 | 50 | 50 | 10 | 0.1 | 0.1 |
| Sensor-3 | 12000 | 12000 | 50 | 50 | 10 | 0.1 | 0.1 |

We depict the experimental results of Sensor-1 in Fig. 4.3.2. Sensor-1 has a no load resonance frequency of 15.014 GHz with a no load Q-factor of 203.4. We can observe the high Q-factor and high transmission dip in multi-turn spirals compared to other spiral cases in telemetric measurements. The sensitivity of this device is 0.435 MHz/kgf, or 20.5 kHz/microstrain, which is higher compared to other spiral cases. Sensor-1 also has less than 130 microstrain error, which is smaller than those of other spiral cases. Considering all these parameters (sensitivity, Q-factor, and linearity), we can conclude that a multi-turn spiral is the best case among the investigated spiral coils because it resembles the single device case presented in the previous sections and exhibits a high level of sensitivity. Also, as it has many turns, the storage time of the induced current upon incident EM wave in the device is longer and so is the damping time. Thus, it radiates a stronger signal compared to the other cases hence it has a higher Q-factor. Therefore, it has a higher SNR and better linearity compared to other spiral cases.

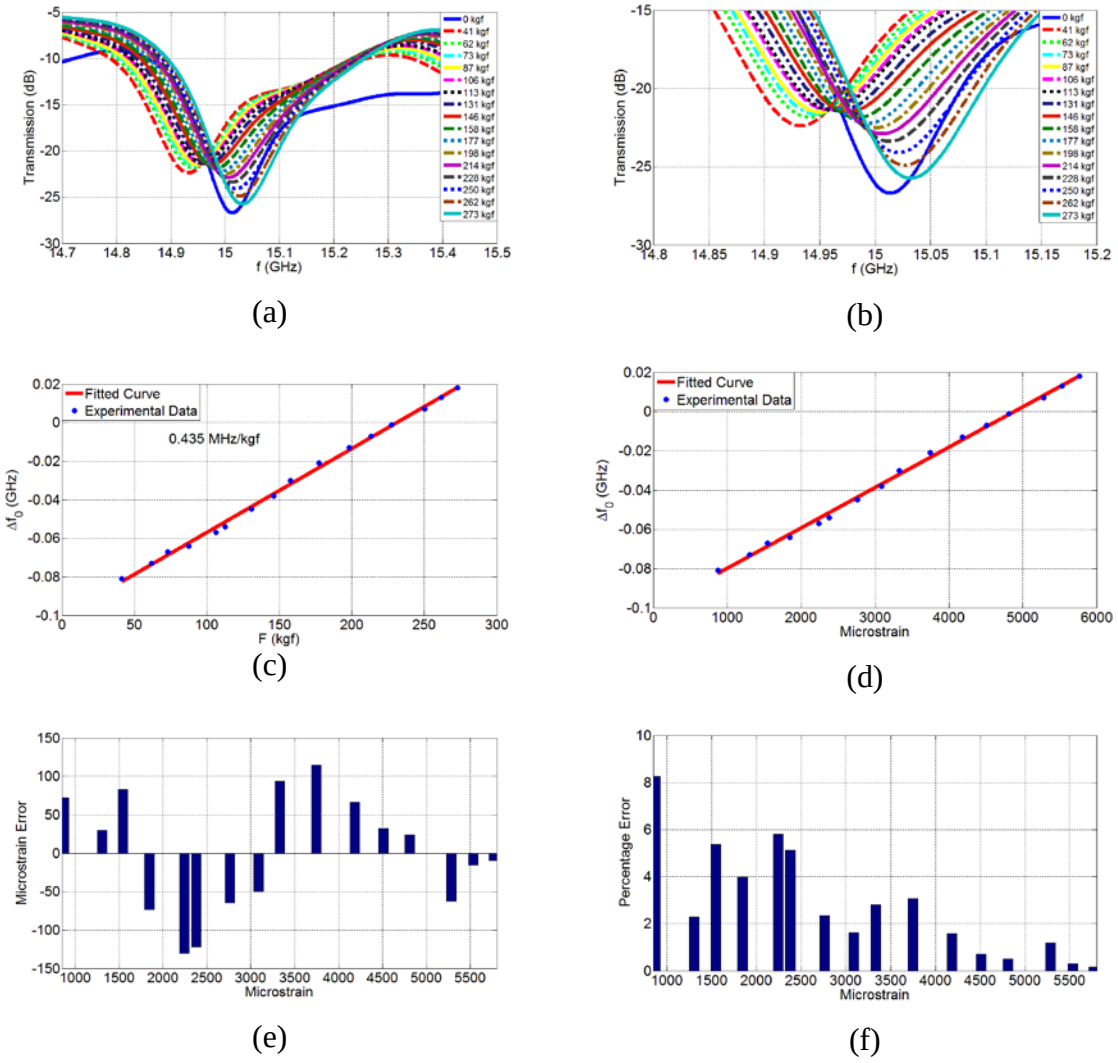


**Figure 4.3.2. Experimental measurements of Sensor-1: (a) Transmission spectra under different applied loads, (b) zoom-in of transmission spectra, (c) F *vs.* $\Delta f_0$, (d) microstrain *vs.* $\Delta f_0$, (e) error in terms of microstrain and (f) error in terms of percentage.**

Examining the performance of Sensor-2 as given in Fig. 4.3.3, we observe that the no load resonance frequency is 14.958 MHz, while the no load Q-factor is 174.3. It has a lower resonance frequency compared to that of Sensor-1 since its spacing is less than that of Sensor-2. It also has a lower Q-factor compared to Sensor-1 because of the w/s ratio as explained in detail in Section 2.1. Since the parasitic capacitance dominates in Sensor-2, its Q-factor is lower

compared to Sensor-1. Sensor-2 has 0.405 MHz/kgf or 19.1 kHz/kgf sensitivity. It exhibits less than 450 microstrain error, which is higher than Sensor-1. Since Sensor-2 has a lower Q-factor and lower transmission dip compared to Sensor-1, it has a lower SNR and higher errors compared to Sensor-2.

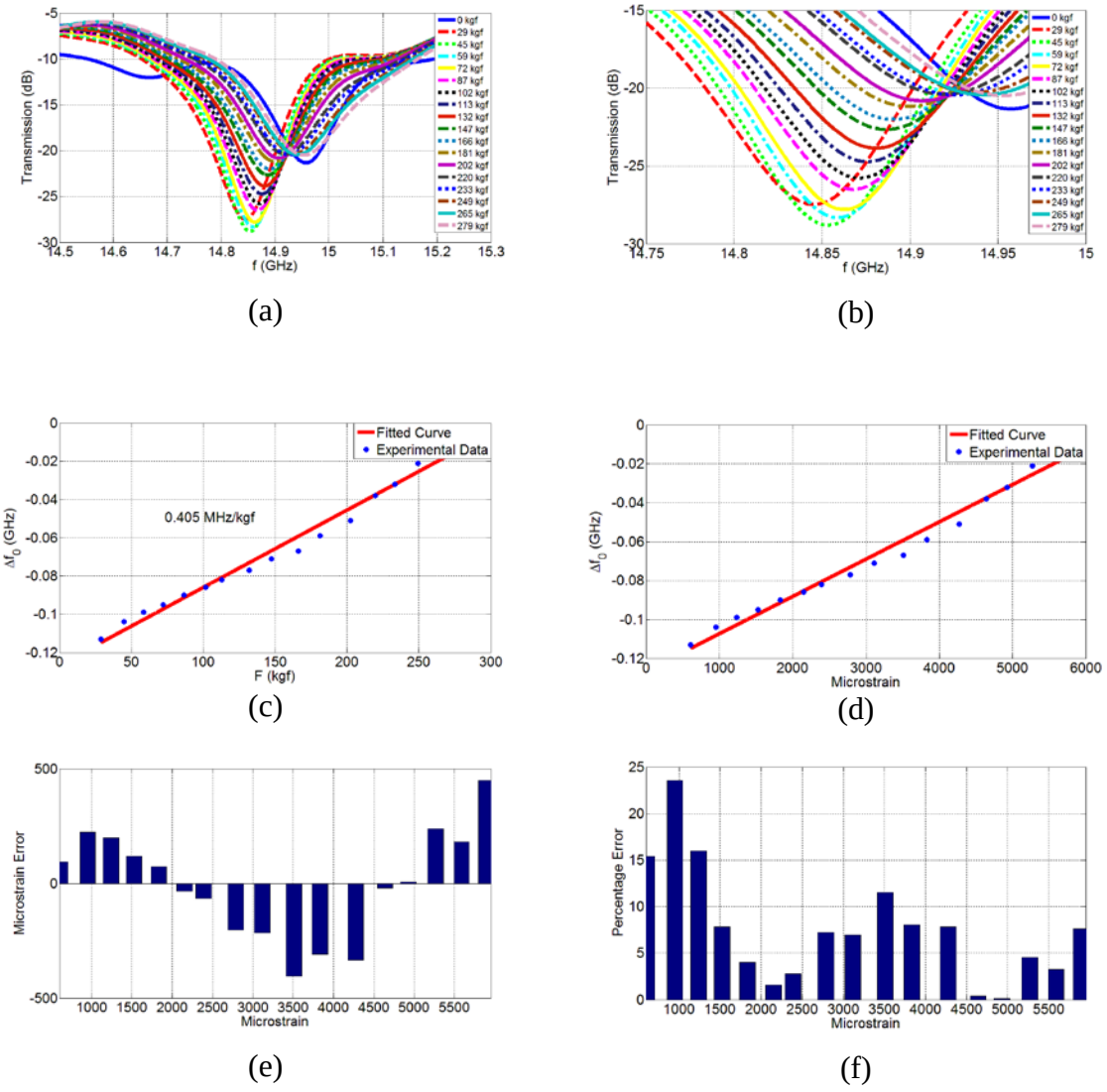


**Figure 4.3.3. Experimental measurements of Sensor-2: (a) Transmission spectra under different applied loads, (b) zoom-in of transmission spectra, (c) F *vs.* $\Delta f_0$, (d) microstrain *vs.* $\Delta f_0$, (e) error in terms of microstrain and (f) error in terms of percentage.**

We demonstrate the experimental results of Sensor-3 in Fig. 4.3.4. Sensor-3 has the same dimensions as Sensor-2 but we added a line to form a complete loop. We added extra two-fabrication process for this purpose. Sensor-3 has a no load resonance frequency of 15.016 GHz with a no load Q-factor of 211.4. As expected, Sensor-3 has a higher Q-factor and higher transmission dip compared to Sensor-2. Since Sensor-3 has a full loop, the incident EM wave induces current in the complete loop for a larger period; hence, the sensor radiates a stronger signal. Sensor-3 has 0.389 MHz/kgf or 18.4 kHz/microstrain sensitivity. To shift resonance frequency, the loop need also to be deformed and strain need to propagate to the loop. Hence, the change in the resonance frequency and thus the sensitivity are lower compared to Sensor-2. Sensor-3 demonstrates less than a 105 microstrain error which is smaller than Sensor-2. Since Sensor-3 has a higher Q-factor hence a higher SNR, it exhibits lower errors compared to Sensor-2.

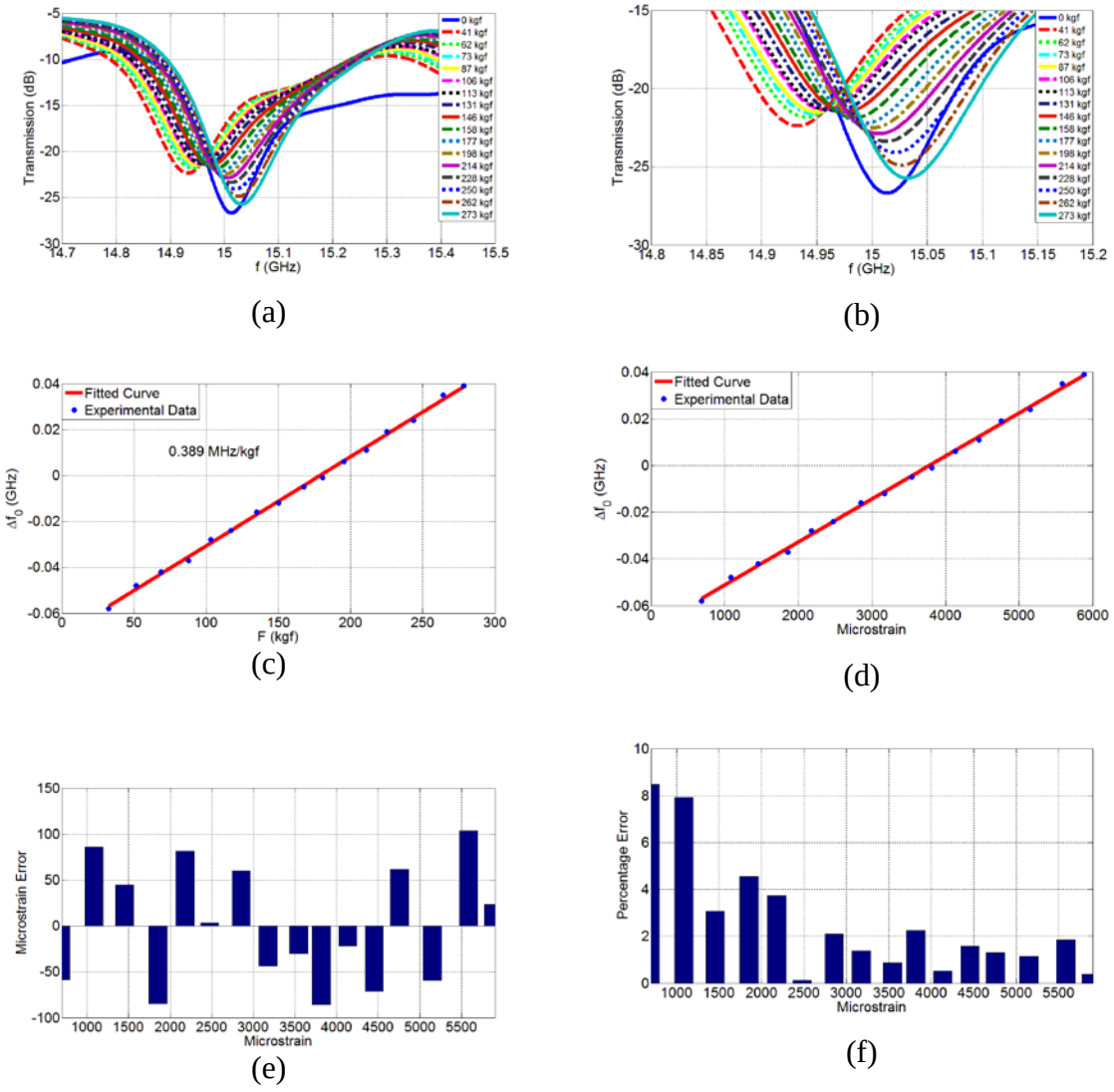


**Figure 4.3.4. Experimental measurements of Sensor-3: (a) Transmission spectra under different applied loads, (b) zoom-in of transmission spectra, (c) F *vs.* $\Delta f_0$, (d) microstrain *vs.* $\Delta f_0$, (e) error in terms of microstrain and (f) error in terms of percentage.**

In conclusion, multi-turn spirals make better sensors in wireless strain sensing compared to all of the investigated spiral cases. They exhibit a higher Q-factor because of the higher damping time and they demonstrate better sensitivity since the strain affecting the structure directly changes the resonance frequency. As a result of their higher Q-factor, they demonstrate lower errors compared to other spiral cases. By adding a line and forming a compete loop in multi-turn spirals

increases the Q-factor but decreases the sensitivity compared to the multi-turn spirals without a complete loop. The EM waves induce current in the structure for longer time because of the complete loop and radiate a stronger signal, and hence exhibit an increased Q-factor. However, since the loop is an extra part, in order to change the resonance frequency, this part need also be deformed. Hence, the strain should propagate to the loop as well; thus, the resulting sensitivity is lower.

## 4.4 Spiral Structure under Tension as Opposed to Compression

In this section, we will study the tension in spiral structures. Up to this section, all of the device characterization was carried out under compression. As opposed to the compression, the resonance frequency decreases with the applied load under tension hence the sensor is sensitive to the direction of the applied load (tension *vs.* compression). Moreover, since the tensile Young's modulus of our test material cast polyamide is lower than compressive Young's modulus, we measure larger sensitivities under tension in our setup. Here we made a comparison of single-type sensor and array-type sensor under tension. As in the compression case in Section 4.1, the single-type sensor is more sensitive whereas the array-type sensor has a higher Q-factor and better linearity. Thus, the sensors under tension behave in the same way as under compression in terms of sensor performance parameters including sensitivity, Q-factor and linearity.

We explore two devices: single-type sensor and array-type sensor. Their behavior under compression was previously examined in Section 4.1. They are composed of spiral structures whose design parameters are listed in Table 4.4.1. The single-type sensor is composed of four spiral structures while the array-type sensor is composed of 6×5 spiral structures. The fabrication procedure of the sensors, the experimental setup and the calibration procedure are completely the same as discussed in detail in Section 4.1.

**Table 4.4.1. Our device parameters.**

| $L_c$ (μm) | $W_c$ (μm) | $N$ | $w$ (μm) | $s$ (μm) | $t_{film}$ (μm) | $t_{metal}$ (μm) |
|---|---|---|---|---|---|---|
| 1040 | 1040 | 2 | 200 | 10 | 0.1 | 0.1 |

We show the tension setup in details in Fig. 4.4.1. In Fig. 4.4.1(a), we see the mechanical apparatus of the tension setup. The force is applied in reverse direction compared to the compression setup. In addition, we again use two external standard gain horn antennas for RF measurements. The measurement technique is explained in detail in Section 4.1.

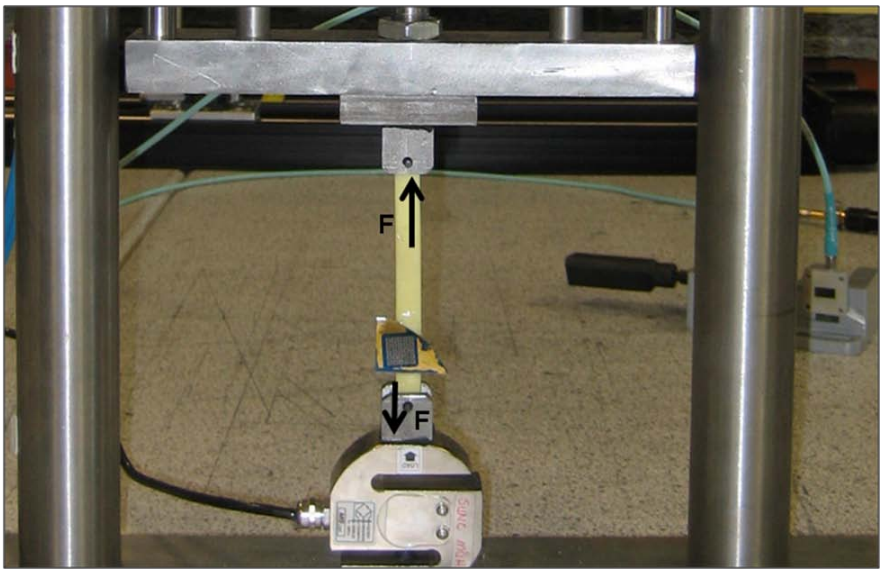


(a)

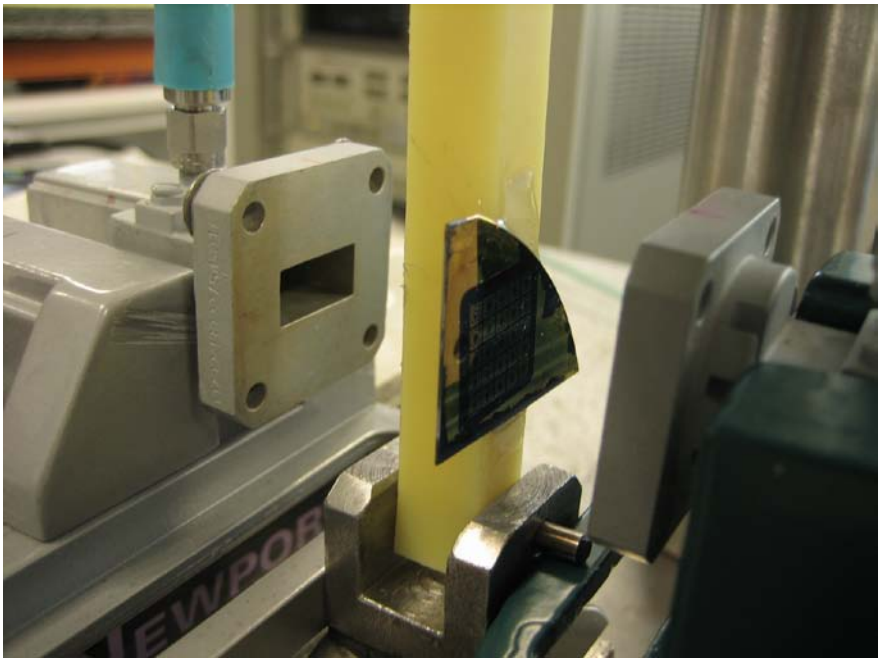

(b)

**Figure 4.4.1. Tension setup (a) mechanical apparatus and (b) antennas.**

We show the experimental results of the single-type sensor in Fig. 4.4.2. From the transmission data, we can observe that the resonance frequency decreases with the applied load as opposed to the compression case. The reason is that, when the load is applied, the dielectric area between substrate and metal layer is increased; hence, the dielectric capacitance ($C_{diel}$) is increased. Therefore, the resonance frequency is decreased with the applied loads. We measured the tensile Young's modulus of the test material, cast polyamide stick, with a commercially available wired strain gauge (Tokyo Sokki Kenkyujo Co., Ltd. Strain Gauges with a gauge factor of 2.1). We found out the tensile Young's modulus of cast polyamide to be 2.371 GPa, which is lower than the compression Young's modulus of the cast polyamide (3.288 GPa). Since we obtain more strain under the same applied load compared to the compression case, there exists more mechanical deformation in the sensor and the sensor therefore demonstrates larger measured sensitivity under tension compared to the compression case. The sensor exhibits -0.398 MHz/kgf sensitivity with less than 35% error. The error is sufficient for correct strain reading but it still needs to be decreased as in the compression case. The Q-factor is also modarete as in compression case.

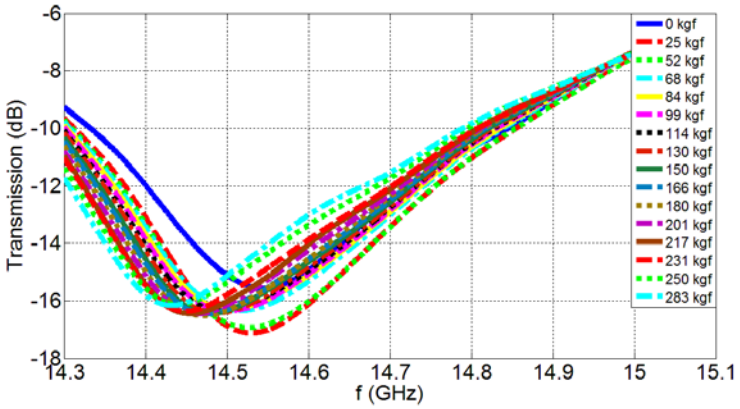


(a)

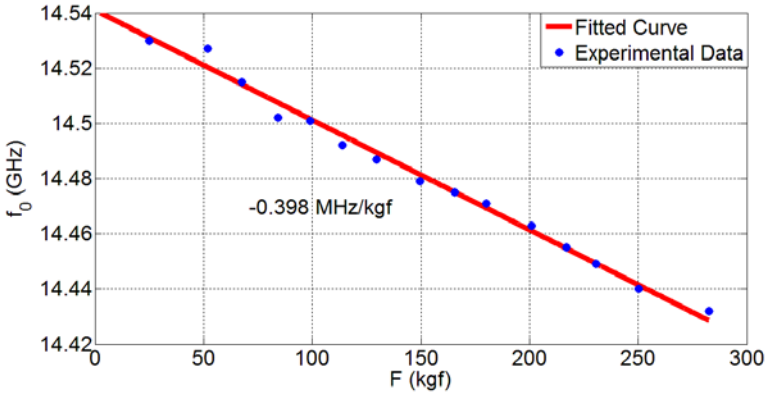


(b)

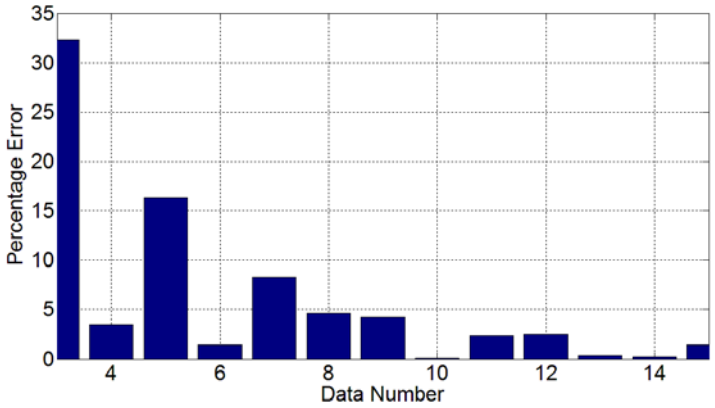


(c)

**Figure 4.4.2. Experimental characterization results of single-type sensor under tension: (a) Transmission spectra under different applied loads, (b) F *vs.* $\Delta f_0$, and (c) error in terms of percentage.**

The experimental behavior of the array-type sensor under tension can be seen in Fig. 4.4.3. The sensor has a higher Q-factor and a larger dip in transmission compared to the single-type sensor case as in the compression case. Since the array-type sensor has more units, it radiates a higher signal; hence, it has a higher Q-factor. It has -0.174 MHz/kgf sensitivity, which is higher in magnitude compared to compression case and opposite in sign. Since the Young's modulus of the test material is lower, than the sensitivity is bigger. Because the direction of the applied force is in reverse direction of the compression case, then the sign of the sensitivity is opposite. The sensitivity is lower compared to the single-type sensor case as in compression case. Since there are more structures in array-type sensor, with the same force applied, there is less effect of mechanical deformation per structure. Then the sensitivity is lower. The array-type sensor has less than 20% error, which is better than single-type case. Because the array-type sensor has higher Q-factor, then it has better SNR and better linearity. You can see the reasons of the differences of sensor performance in Section 4.1 in details.

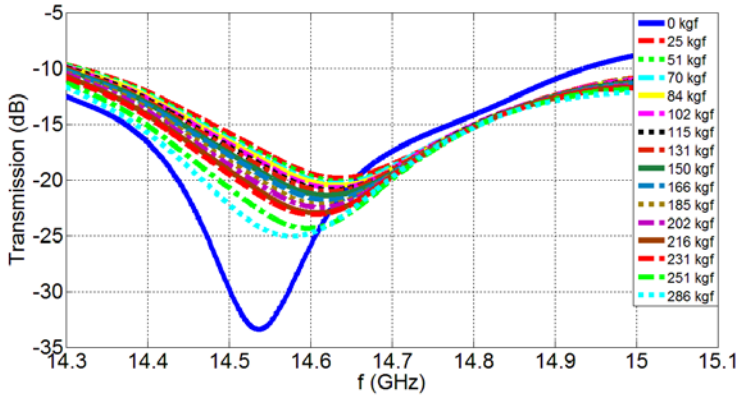


(a)

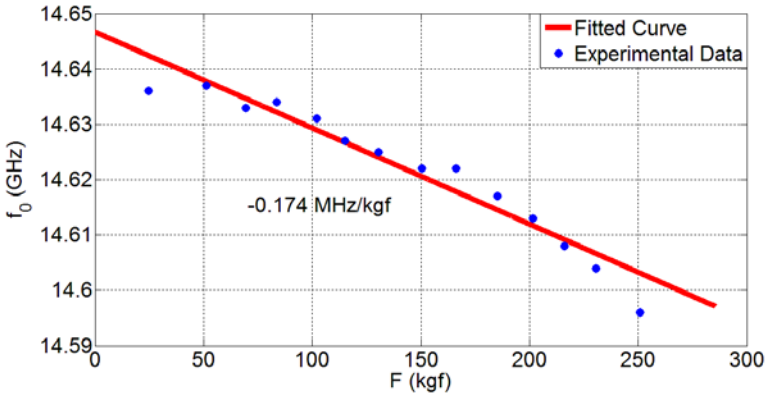


(b)

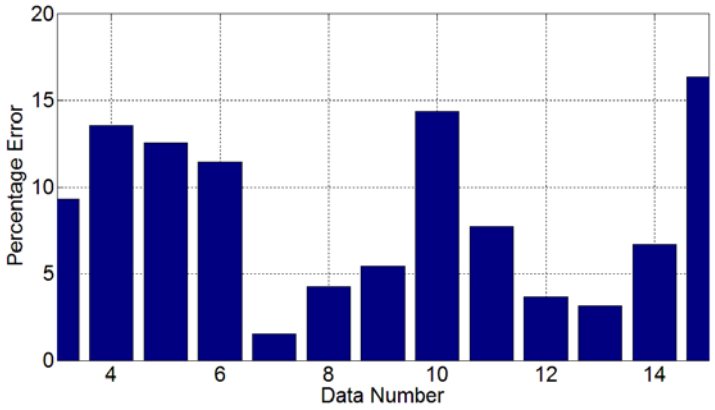


(c)

**Figure 4.4.3. Experimental characterization results of array-type sensor under tension: (a) Transmission spectra under different applied loads, (b) F *vs.* $\Delta f_0$, and (c) error in terms of percentage.**

In conclusion, the resonance frequencies of the single-type sensor and the array-type sensor are shown to decrease with the applied load as opposed to the compression case. Because of the lower tensile Young's modulus, they are measured to exhibit higher sensitivities compared to the compression case. These experiments show the ability of our sensors to wirelessly detect the strain in different directions of applied load and for different Young's modulus. The single-type and array-type sensors behave in the same way if we consider the sensor performance parameters as in the compression case.

# Chapter 5

# Wireless Strain Sensing Metamaterials

In this chapter, we will show wireless strain sensing using metamaterial-based RF-bioMEMS sensors for the first time. We will demonstrate that custom-design metamaterials make better sensors compared to conventional RF structures (spiral structures). By demonstrating metamaterial sensors, we develop a new application area for metamaterials and open up a new direction for innovative metamaterials. Herein we will demonstrate wireless strain sensing with silicon-based and flexible sensors. We will also show wireless strain sensing using different test materials and examine the parameters of metamaterials in their wireless strain sensing. We will also discuss metamaterial sensors under tension as opposed to compression.

## 5.1 Metamaterial-based Wireless RF-MEMS Strain Sensors

This section is based on the publication "Metamaterial-based wireless strain sensors" **R. Melik,** E. Unal, N. K. Perkgoz, C. Puttlitz and H. V. Demir, *Applied Physics Letters 95, 011106 (2009)*.

Reproduced (or ‘Reproduced in part’) with permission from American Institute of Physics. Copyright 2009 American Institute of Physics.

In this section [58], we proposed and demonstrated metamaterial-based RF-MEMS strain sensors that are highly sensitive to mechanical deformation. Their resonance frequency shift is correlated with the surface strain of our test material and the strain data are reported telemetrically. These metamaterial sensors are better than traditional RF structures in sensing for providing resonances with high Q-factors and large transmission dips. Using custom-design split-ring-resonator (SRR) architecture, we achieve lower resonance frequencies per unit area compared to other RF structures, allowing for bio-implant sensing in soft tissue (e.g., fracture healing). In 5×5 SRR architecture, our wireless sensors yield high sensitivity (109kHz/kgf, or 5.148kHz/microstrain) with low error (<200microstrain).

Measuring and reporting strain in structural components using telemetric methods represents a significant engineering challenge. In many fields, such as civil engineering, this measurement tool would be highly beneficial. For instance, measuring the strain in concrete to discern the temporal course of its strength and flexibility (e.g., before, during, and after an earthquake) would greatly advance our knowledge of concrete’s transient structural behavior (in an earthquake) [59]-[60]. Other possible applications include the real-time measurement of the flexural rigidity of aircraft components during service in avionics. While there is a large portfolio of possible applications in various applications in various industries, our interest currently lies in particular with using wireless sensing to observe the healing processes of fractured long bones in biomedical engineering [1]. When complicated fractures occur in humans, plates are implanted to impart stability to the fracture site during the acute postoperative period. In order to observe the healing process, wireless measurement of the strain on the plate could be utilized to indicate whether healing was proceeding through a normal or aberrant pathway. For this end goal (and other possible uses), we propose and demonstrate biocompatible metamaterial-based wireless RF-MEMS strain sensors that are highly sensitive to mechanical loading. The operating principle of these sensors relies on telemetrically monitoring shifts in their operating frequencies, which are a function of the strain imparted to the associated circuit, in response to externally applied

loads. In this chapter, we present the design, fabrication and *in vitro* characterization of these wireless metamaterial strain sensors.

To date metamaterials have been widely investigated [61]-[64] and exploited for numerous functions, e.g., to obtain negative refraction [65]-[67], cloaking [68], superlenses [69], antennas [70], plasmons with nanowires [71], laser output facets [72], and focused light [73]. However, metamaterial architectures have not been studied for sensing till date. In this work, for the purpose of sensing, we employ split ring resonator (SRR) architecture in the fabrication of our RF-MEMS sensors because of their benefits that are unique for the function of telemetric sensing. Among their advantages is the ability to obtain higher Q-factors, and sharper and deeper dips on resonance in their transmission using SRR compared to traditional RF structures that we previously used (e.g., rectangular coils, circular coils) [15], [31], [39]. This makes metamaterials very well suited for telemetric sensing applications. Furthermore, metamaterial architecture enables us to achieve higher operating frequency shifts, leading to higher sensitivity and better linearity, compared to our previous RF sensor structures. With regard to the aforementioned fracture plate application, by using metamaterials, we also manage to significantly reduce operating resonance frequencies per unit area. This is especially critical for sensing applications that involve transmission through soft tissue (e.g., muscle) because such tissue strongly absorbs electromagnetic waves at otherwise high operating frequencies.

Previously, we developed high Q-factor on-chip resonators at higher operating frequencies [15], [31]. Using microwave probes, we demonstrated the proof-of-concept principle of utilizing the resonance frequency shift [39] via on-chip resonators serving as sensors. In this section, we present the proof-of-concept demonstration of fully telemetric resonance frequency shifts using our metamaterial sensors. Specifically, we measure the transmission through our sensors without using any wires or other connections made to the sensors; our sensors are located away from our external antennas. In characterization, we also externally apply loads to our sensors using a compression apparatus and measure the resulting frequency shifts in response. We also measure the strain using commercially available wired strain gauges and compare the two data sets.

To fabricate our metamaterial sensors, we start with depositing 0.1 μm thick $Si_3N_4$ onto silicon substrate by plasma enhanced chemical vapor deposition (PECVD). Subsequently, standard lithography, metal evaporation, and lift-off techniques are utilized to deposit and pattern a 0.1 μm thick Au film to obtain our SRR structure on the top. Our final geometry is depicted in Fig. 5.1.1 (denoted as SRR sensor), with a 2220 μm outer length and a 1500 μm inner length. This design also has an 80 μm inner width and an 80 μm outer width, with a 280 μm inner spacing and a 280 μm outer spacing, respectively. The unit cell length of one SRR structure is 2780 μm. We have a 5 × 5 array of these SRR unit cells incorporated in the sensor, resulting in a total of 1.5 cm x 1.5 cm chip size. Our sensor is fixed to the test material via hard epoxy. A cast polyamide stick is employed as the test material. The apparatus applies compressive loads to the cast polyamide stick from 0 kgf to 300 kgf. Our sensor returns the strain on the cast polyamide stick. One antenna acts as the transmitter and another, as the receiver, for both of which standard gain horn antennae are used as shown in Fig. 5.1.1.

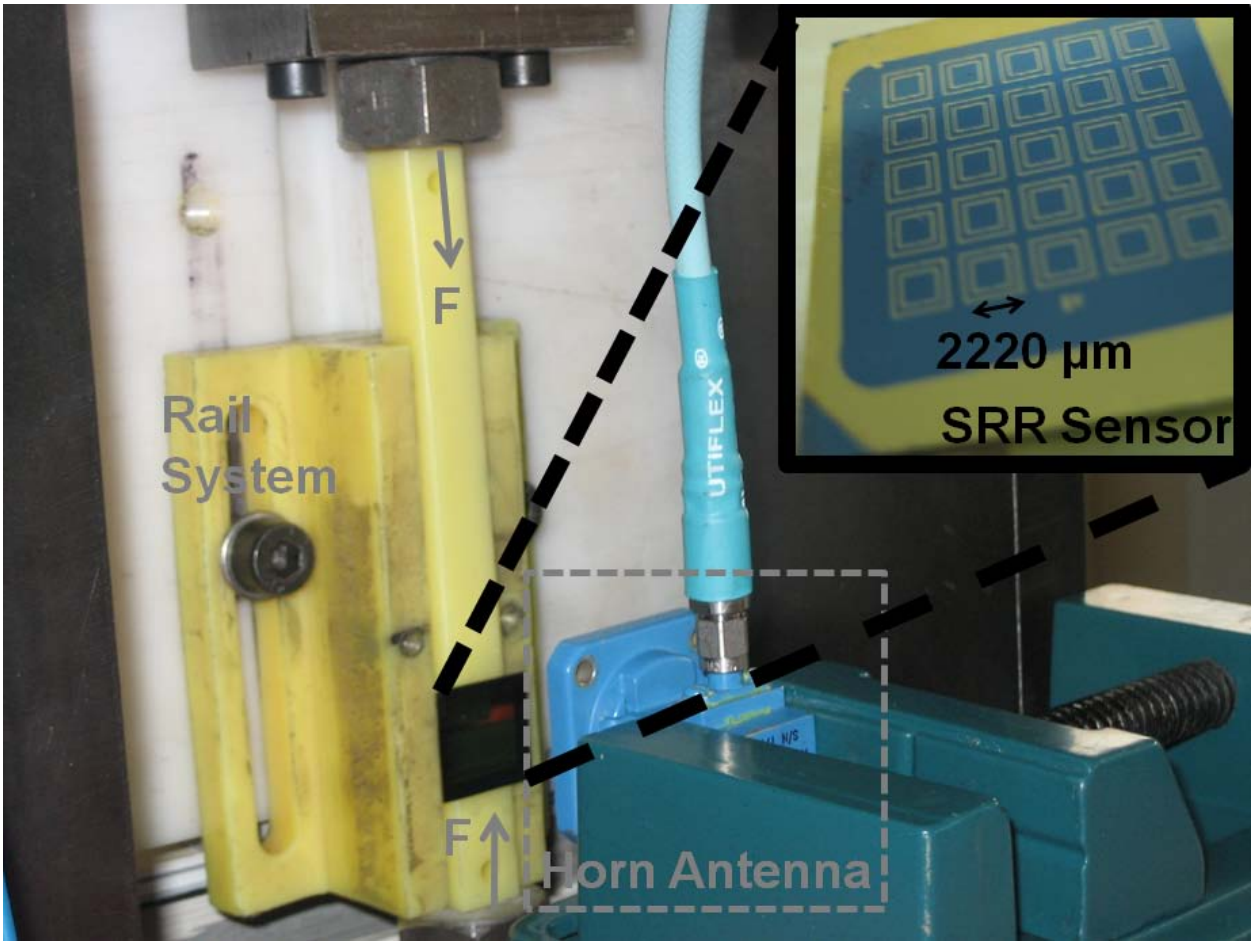


**Figure 5.1.1 Our microfabricated 5 × 5 split ring resonator (SRR) array based strain sensor under test in the compression apparatus.**

In operation, the sensor is mechanically deformed under stress and this shifts the operating frequency. For example, in compression, the dielectric area and capacitance (dielectric capacitance) are decreased, the spacing between the metals is increased, and the capacitance between metals is decreased. These changes result in an overall increase in the resonance frequency. The theoretical rationale of the design has been previously presented in detail for conventional spiral coil architecture [39]. $S_{21}$ parameter of the matematerial sensor is shown as a function of the frequency parameterized with respect to the applied load in Fig. 5.1.2(a). There is a definite trend of increasing resonance frequency with increased applied load shown in Fig. 5.1.2(a). Here in the transmission spectra, the dip represents the second harmonic of our

structure’s resonance frequency within our characterization range. This characterization demonstrates that we can use further lower resonance frequencies for sensing purposes. The device size is much smaller than the operating wavelength. This is particularly important for measuring the strain of instrumented and implanted sticks under soft tissue conditions. In Fig 5.1.2(b), we obtain the strain measured telemetrically from the resonance frequency shift and depict the microstrain versus the resonance frequency. From this measurement, we obtain a sensitivity level of 109 kHz/kgf, which corresponds to 5.148 kHz/microstrain. The wireless sensor is observed to have errors of less than 200 microstrain in this telemetric strain measuring experiment using the frequency shift data. This shows us that we can accurately read the strain wirelessly with metamaterials. For comparison, we also measure the stress versus microstrain of a semiconductor based wired strain gauge (Tokyo Sokki Kenkyujo Co., Ltd. strain gauges with a gauge factor of 2.1). Here we observe that the wired strain gauge also exhibits errors of less than 600 microstrain. Therefore, both the commercial wired gauge and our wireless strain sensor return equivalent results, with the difference that the wireless sensor provides an additional benefit of remote readout.

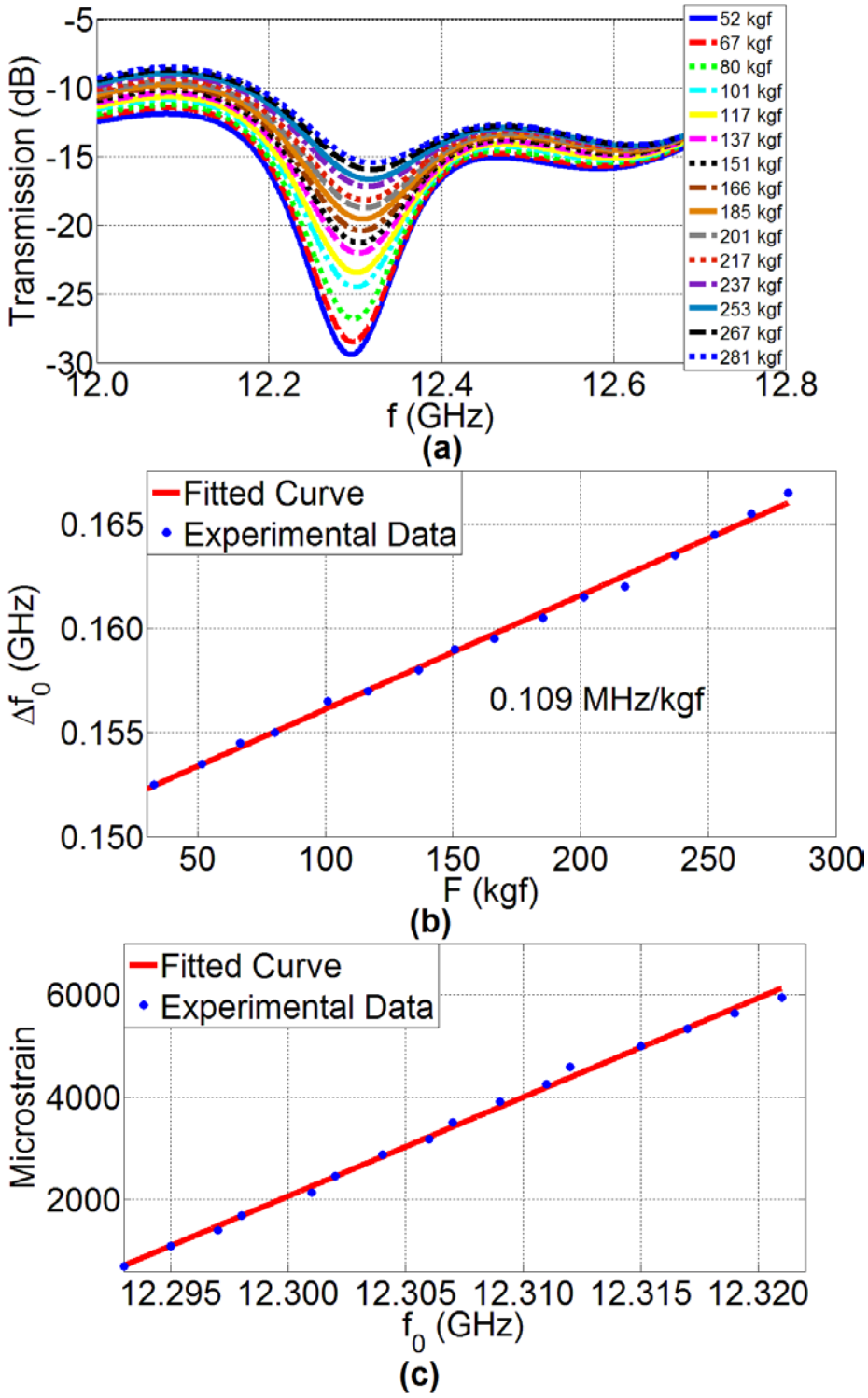


**Figure 5.1.2 (a) Transmission spectra of our metamaterial strain sensor parameterized with respect to the external force, (b) its resonance frequency shift versus the applied force, and (c) the microstrain versus resonance frequency.**

For comparison of this current work against previous ones, we are able to take fully telemetric data by using SRR structure in this work, instead of using wired spiral coil structure with a pair microwave probes in full contact with the coil. For wired devices, we took on-chip data and we did not use any external antenna. Here we use only external antennas and do not use any probes or any other wired connection, and therefore measure the strain wirelessly. In this work, the SRR geometry is more sensitive compared to the spiral case because of their additional gaps in their SRR structure. These gaps produce additional capacitance, which is changed when the load is applied. Hence, it makes SRR more sensitive than the spiral coil geometry. In addition, the electric field density is much higher in the gaps so these gaps are important to have strong resonances. When the load is applied, these gaps change and hence the resonance frequency changes. This leads to higher sensitivity in SRRs compared to spiral coil structure.

Also, as a result of these gaps, SRRs yield higher dips and higher Q-factors compared to the spiral structure. This enables us to measure telemetrically and observe the resonance frequency relatively more easily. As a result, SRR sensor is more linear than spiral coil sensor. Also, because of these gaps, we can lower resonance frequencies per unit area, which we need for our bio-implant applications. Therefore, because of the gaps in SRR structure, we obtain higher Q-factors, higher dips, higher sensitivities, better linearity and lower resonance frequency per unit area compared to spiral coil structure.

In spite of being fully wireless, our SRR sensors exhibit a very good level of sensitivity (109 kHz/kgf, or 5.148 kHz/microstrain) with a low error less than 6% while the wired sensor of similar dimensions in our previous work has a sensitivity level of 400 kHz/kgf with an error of 12%.

In conclusion, this is the first account of implementing metamaterials in wireless RF-MEMS strain sensors. By using metamaterials, we can obtain high Q-factors, high transmission dips on resonance, high resonance frequency shifts, high sensitivities, and very good linearity. These are highly desirable properties of an accurate wireless sensor. Furthermore, we achieve significantly

lower resonance frequencies per unit area with sharper dips by using metamaterials, which is very useful particularly for sensing applications involving soft tissue. Specifically, a sensitivity level of 109 kHz/kgf (corresponding to 5.148 kHz/microstrain) with an error of less than 200 microstrain in the strain reading is shown in the telemetric measurements. Our wireless sensor's strain readouts that are obtained telemetrically are found to be comparable to those obtained using commercially available wired strain sensors that are used in electrical contact.

## 5.2 Flexible Metamaterials for Wireless Strain Sensing

This section is based on the publication "Flexible Metamaterials for Wireless Strain Sensing" **R. Melik,** E. Unal, N. K. Perkgoz, C. Puttlitz and H. V. Demir, *Applied Physics Letters 95, 181105 (2009)*. Reproduced (or 'Reproduced in part') with permission from American Institute of Physics. Copyright 2009 American Institute of Physics.

In this section [74], we propose and demonstrate flexible metamaterial-based wireless strain sensors that include arrays of split ring resonators (SRRs) to telemetrically measure strain. For these metamaterial sensors, we showed that a flexible substrate (e.g., Kapton tape) delivers greater sensitivity and a more linear response as compared to using silicon substrates. Specifically, these tape-based flexible SRR sensors exhibit a significantly improved sensitivity level of 0.292 MHz/kgf with a substantially reduced error of 3% for externally applied mechanical loads up to 250 kgf. These data represent a 6-fold increase in sensitivity and a16-fold reduction in error percentage.

Telemetric strain measurement is important in many fields including civil engineering (e.g., to assess the strength of various concrete surfaces [60]) and the health sciences (e.g., to observe the healing process of fractures in bones [1], [39]). Many applications require that these measurements occur on curved or non-planar surfaces. To address these demands, we develop flexible metamaterial-based wireless strain sensors that telemetrically monitor strain in real time. The operating principle of these sensors relies on the shift of their operating frequency ($f_0$) with an externally applied load to read out the strain remotely from the frequency shift. From a feasibility viewpoint, wireless sensors that operate on this principle are required to have their resonance frequency to be easily measureable, exhibiting relatively high quality factors (Q-factors) with relatively large dips on resonance in their transmission spectra and being highly sensitive to the mechanical deformation with low errors.

For remote sensing, metamaterial based architectures provide the ability to achieve higher Q-factors and larger resonance dips in transmission, compared to conventional radio frequency (RF) structures, as demonstrated in our previous works with silicon-based metamaterial strain sensors [58], [75]. But, for enhanced sensitivity and linearity, these metamaterial sensors further need to be mechanically flexible. In this section, we designed, fabricated, and characterized flexible metamaterials for wireless strain sensing and demonstrated substantially increased sensitivity and significantly decreased errors, compared to our previous chapters [58], [75].

There are many previous reports with respect to the use of metamaterials in various applications including negative refraction indices [76]-[77], focusing light [78], making superlenses [79], and cloaking [80]. We have also previously used metamaterials in the fabrication of silicon wireless strain sensors in a double split ring resonator (SRR) architecture [58]. In this section, different from the previous works of our group, this section introduces flexible metamaterials that are designed and fabricated on Kapton tape. This is a polyimide tape, also known as vacuum tape, commonly used in fabrication and packaging, such as in metal deposition, wave soldering, lithography, powder coating, and insulating circuit boards because it is heat resistant and has silicone adhesive on the back side that does not leave any residue when the tape is removed [81].

The fabrication procedure of our Kapton-based flexible metamaterial is depicted in Fig. 5.2.1(a). The Kapton tape is first laid down and fixated on a dummy silicon piece to provide mechanical support during the fabrication process before the tape-based finished sensor is removed for use. Next, we deposit 0.1 μm thick Au on the tape using standard metallization techniques. Using plasma enhanced chemical vapor deposition (PECVD), we then deposit 0.1 μm thick $Si_3N_4$ as a dielectric thin film. Subsequently, we apply standard lithography, metal evaporation, and lift-off techniques to deposit and pattern a 0.1 μm thick Au layer as top strata and finalize our sensor fabrication. Finally, the completed sensor patterned on the tape is peeled off to be used on a test material. In our microfabrication process, we were able to incorporate the Kapton vacuum tape since it can withstand up to 260 °C, which is sufficient in our case as our highest temperature process (dielectric deposition in PECVD) is performed at 250 °C.

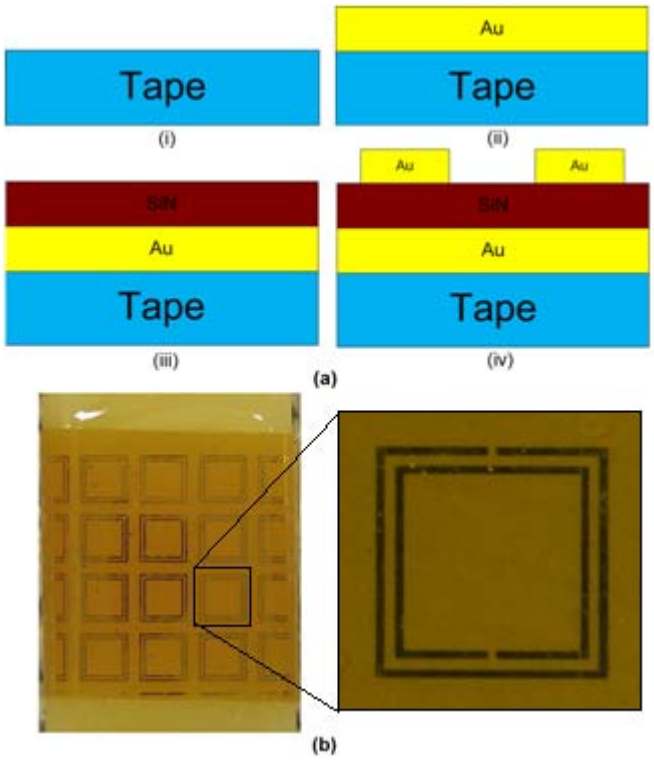


**Figure 5.2.1 (a) Fabrication procedure of the tape-based flexible sensor and (b) the final fabricated structure of the tape-based flexible sensor.**

The main difference in the fabrication procedure between these tape-based flexible sensors and the silicon-based sensors is the deposition of the first gold layer onto the vacuum tape substrate. This bottom gold layer increases the absorption of the sensor at the resonance frequency, producing a large dip at the resonance frequency. However, with the silicon substrate, the silicon inherently increases the absorption, so there is no need to deposit this extra Au layer. Deposition of the first gold layer also guarantees the presence of a parallel plate capacitor (between the first and final gold layers) of the tape-based flexible sensor. In the case of the silicon-based sensor, the silicon is doped; hence, there is no need for this additional Au layer to establish a parallel plate capacitor. The manufacture of a parallel plate capacitor is important for the operation of the sensor because, under loading, this capacitance will change and produce a resonance frequency shift [58]. The final fabricated flexible metamaterial sensor can be seen in Fig. 5.2.1(b). Our SRR geometry has a 2220 µm outer length and a 1380 µm inner length. The sensor also has a 140 µm

inner width and a 140 μm outer width, with a 280 μm inner spacing and a 280 μm outer spacing. The unit cell length of our SRR architecture is 2780 μm. The total resonator has 5 ×5 unit cells, producing a 1.5 cm × 1.5 cm chip size.

For the silicon-based sensor, we use a hard epoxy to fix the sensor to the test stick (made of cast polyamide in our case), which is used as the loading fixture. However, for the tape-based flexible sensor, there is no need for an additional epoxy layer because the tape has its own adhesive (silicone based epoxy) on the back side. Thus, the sensor is affixed to the test material directly. The goal of the characterization is to observe the shift of the operating frequencies under different loading magnitudes. Therefore, by observing this frequency change, the strain of the test material is measured telemetrically. In the experimental setup, we use one excitation transmitter and one receiver antenna to measure the spectral response of the sensors. We look at the transmission spectra (in $S_{21}$ configuration) to observe the resonance behavior.

Fig. 5.2.2(a) shows transmission characterization of the silicon-based metamaterial sensor (in dB), which demonstrates a -10dB transmission minimum or greater for all levels of loading in our experiment. Here we assign $\Delta f_0$ as the frequency shift with respect to the case of no load and denote the applied force as F, with $\Delta f_0$ *vs.* F illustrated in Fig. 5.2.2(b). The no load operating frequency of the sensor is 12.783 GHz. The Young's modulus of the cast polyamide is 3.287 GPa, which is measured by using data obtained from wired strain gauges (Tokyo Sokki Kenkyujo Co., Ltd. Strain Gauges with a gauge factor of 2.1) and simple elasticity theory. Using this data, we obtain a 0.0487 MHz/kgf sensitivity, or correspondingly $2.303 \times 10^{-3}$ MHz/microstrain sensitivity, as shown in Fig. 5.2.2(b). In Fig. 5.2.2(c), we obtain less than a 600 microstrain error, and this corresponds to less than a 50% error [82].

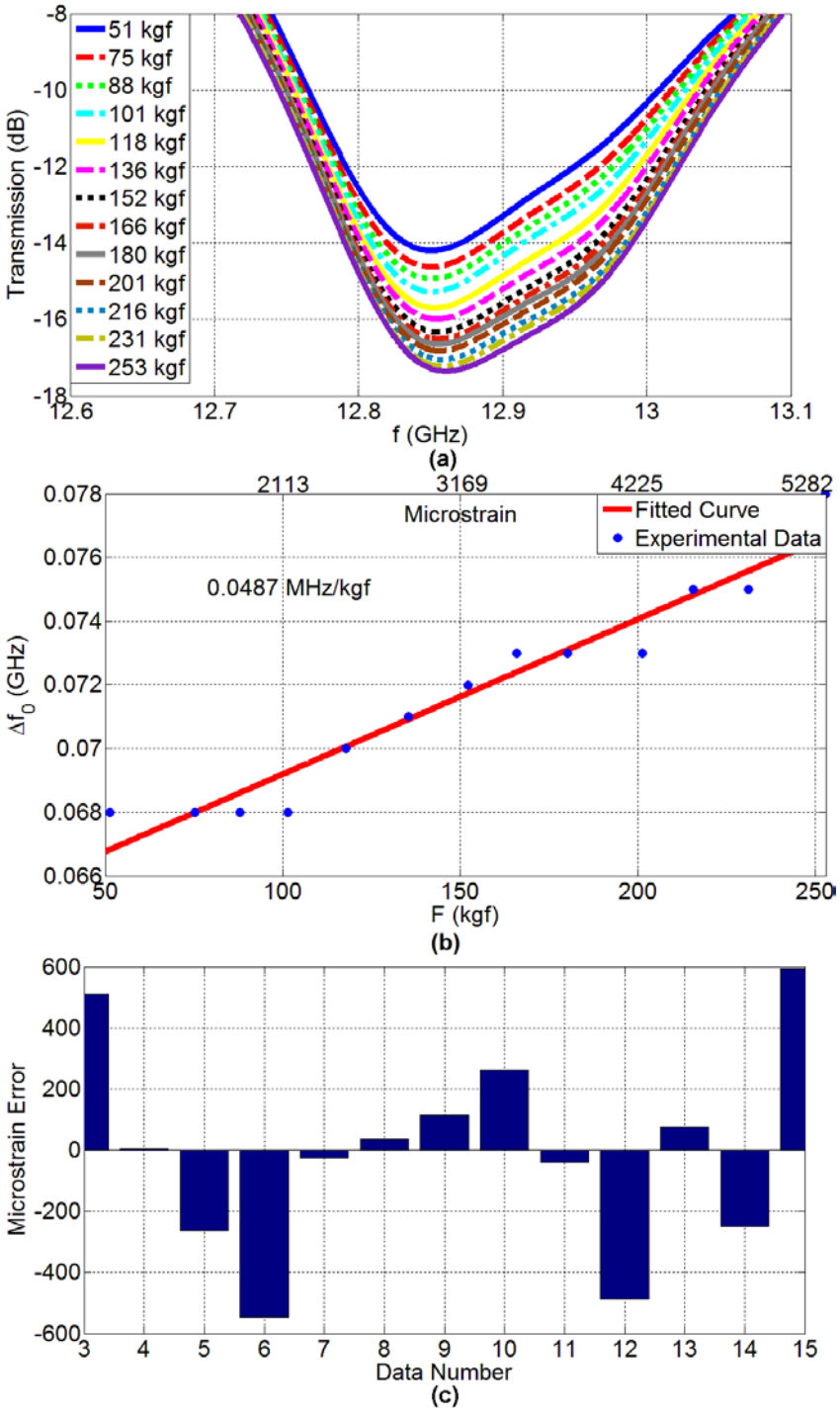


**Figure 5.2.2 (a) Transmission spectra of the silicon-based sensor parameterized with respect to the external force, (b) its F (and microstrain) *vs.* $\Delta f_0$, and (c) its errors in terms of microstrain.**

Fig. 5.2.3(a) depicts the relative transmission spectra (in dB) of the tape-based flexible metamaterial sensor. The data indicate that the no load operating frequency is 12.208 GHz and a greater than -10dB relative minimum in the transmission spectra for all loading cases. Fig. 5.2.3(b) demonstrates the applied load (F ~ 30 - 250 kgf) versus $\Delta f_0$ (the frequency shift with respect to the no load case). The data indicate that the flexible sensor delivers a 0.292 MHz/kgf sensitivity corresponding to $13.83 \times 10^{-3}$ MHz/microstrain sensitivity. The data exhibit a less than 80 microstrain error (as shown in Fig. 5.2.3(c)) with an associated 3% error [82]. Thus, there is an appreciable increase in sensitivity (6 times better) and a substantial decrease in error percentage (16 times better) in the tape-based flexible metamaterial as compared to the silicon-based metamaterial of the same design.

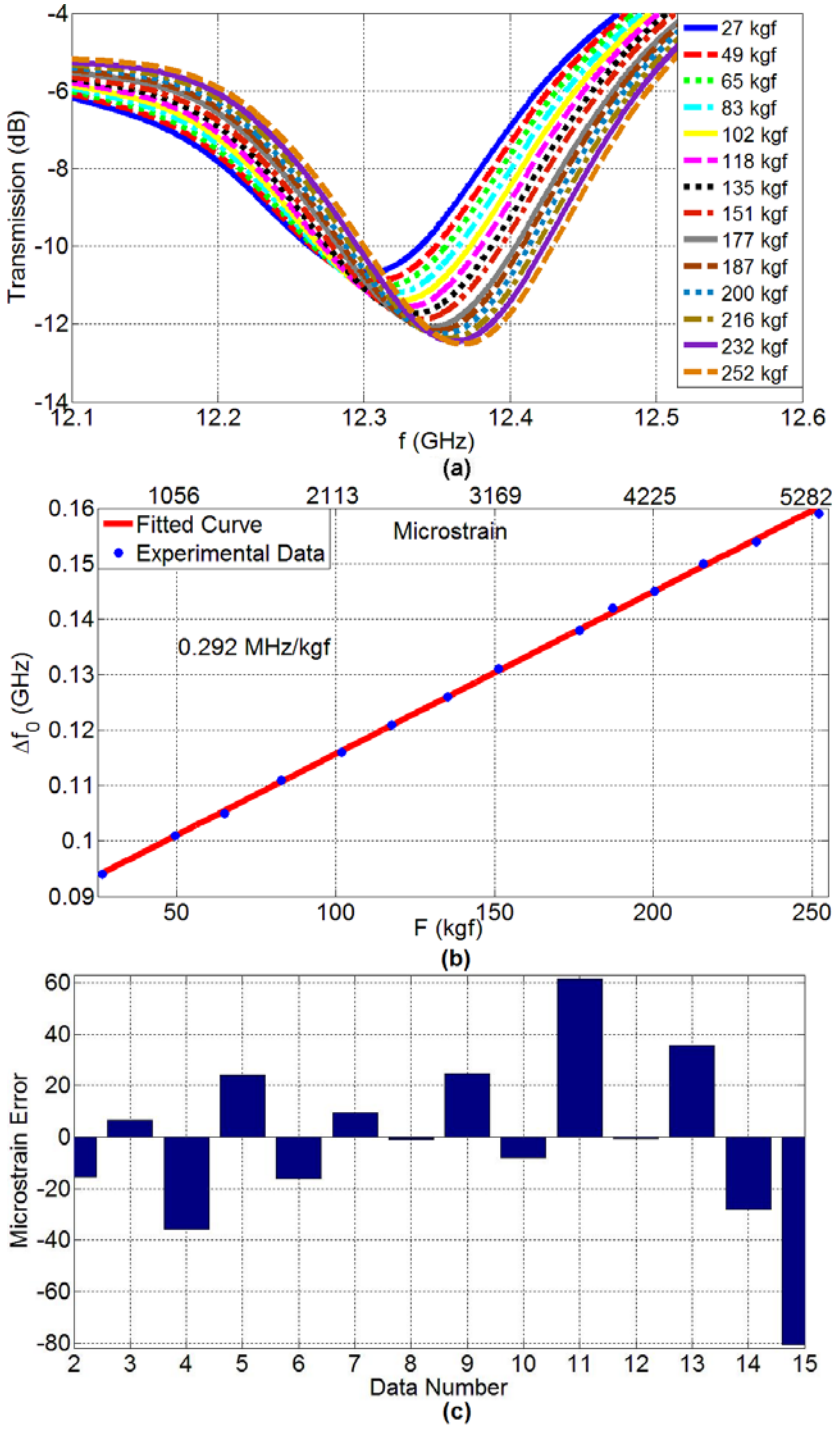


**Figure 5.2.3 (a) Transmission spectra of the tape-based flexible sensor parameterized with respect to the external force, (b) its F (and microstrain) *vs.* $\Delta f_0$, and (c) its errors in terms of microstrain.**

The data show that the tape-based flexible metamaterial is more sensitive and more linear compared to the silicon-based metamaterial. When considering these results, one must take into account both the RF and mechanical aspects of the system. The silicon-based sensor delivers a greater dip in transmission and higher Q-factors, and, hence delivers a higher signal-to-noise ratio as compared to tape-based flexible sensor. We postulate that this is because silicon is much thicker than the bottom gold layer on the vacuum tape, and, therefore, the silicon has a greater absorption at the resonance frequency. These factors account for the higher Q-factor obtained with the silicon sensor as compared to tape-based flexible sensor. Thus, by only considering RF portion of the system, it is not unexpected that the silicon-based sensor delivers a more linear response than the flexible metamaterial sensor. However, because of the mechanical aspect of the system, the sensor which incorporates the vacuum tape is more linear possibly because it uses a flexible substrate. Specifically, the flexible substrate has a lower elastic modulus and undergoes relatively greater mechanical deformation (for the same applied load), which results in a more sensitive construct. Since there are a limited number of datum points obtained in a single frequency scan by the network analyzer, it is easier to resolve smaller shifts in the transmission spectra in response to the externally applied load when the sensitivity is higher. If the network analyzer resolution is not sufficient to resolve the frequency shift with the applied load, then the resultant F *vs.* $\Delta f_o$ data becomes step-wise, which increases the errors, as is the case with the silicon-based metamaterial depicted in Fig. 5.2.2(b). The use of an external epoxy also plays an important role in the sensor's sensitivity and linearity. Since external epoxy is not required for fixation of the vacuum tape substrate to the test materials, the strain induced on the test materials directly propagates to the vacuum tape substrate. However, a thicker layer of external epoxy is required to attach the silicon substrate to the test materials. Hence, part of the applied strain may not be directly conferred to the silicon substrate. We hypothesize that this rationale may explain why the silicon substrate's frequency response does not change as linearly with respect to the applied load because of this mechanically composite structure. Therefore, the tape-based flexible sensor's response is more sensitive and more linear than the silicon-based sensor.

In conclusion, greater sensitivity and smaller error were achieved with the tape-based flexible sensor as compared to the silicon-based sensor. This is largely because of the greater compliance of the vacuum tape. In addition, the flexible tape sensor does not require the use of external epoxy between test material and vacuum tape substrate, which also contributes to its relatively greater sensitivity. The data indicate an improved sensitivity of 0.292 MHz/kgf, or $13.83 \times 10^{-3}$ MHz/microstrain, from the tape-based flexible sensor while the silicon-based sensor demonstrated a sensitivity of 0.0487 MHz/kgf or $2.303 \times 10^{-3}$ MHz/microstrain. In addition, reduced errors of less than 80 microstrain (less than 3%) in the tape-based flexible sensor was obtained as compared to errors less than 600 microstrain (50%) that were calculated from the silicon-based sensor data.

## 5.3 Metamaterial Based Telemetric Strain Sensing in Different Industrial Materials

This section is based on the publication "Metamaterial based telemetric strain sensing in different materials" **R. Melik,** E. Unal, N. K. Perkgoz, C. Puttlitz and H. V. Demir, *Optics Express 18, 5000-5007 (2010).* Reproduced (or 'Reproduced in part') with permission from Optical Society of America. Copyright 2010 Optical Society of America.

In this section [83], we present telemetric sensing of surface strains on different industrial materials using split-ring-resonator based metamaterials. For wireless strain sensing, we utilize metamaterial array architectures for high sensitivity and low errors in strain sensing. In this section, telemetric strain measurements in three test materials of cast polyamide, derlin and polyamide are performed by observing operating frequency shift under mechanical deformation and these data are compared with commercially-available wired strain gauges. We demonstrate that hard material (cast polyamide) showed low slope in frequency shift *vs.* applied load (corresponding to small mechanical deformation because of high Young's modulus), while soft material (polyamide) exhibited high slope (large mechanical deformation because of low Young's modulus).

Measuring strain telemetrically presents a large industrial challenge [39], [60]. To address this problem, we developed a metamaterial based wireless strain sensing method that monitors strain in real time by observing the operating frequency ($f_o$) shift under varying levels of strain [74]. This section extends these preliminary findings to different industrial materials to demonstrate the applicability of incorporating metamaterials for widespread applications.

The operating principle of our sensing approach is that when a force is applied to the sensor, the operating frequency of the metamaterial sensor is shifted, and, by observing this frequency change ($\Delta f_o$), we can monitor the strain in real time. In order to have an efficient wireless strain sensor working with this guiding principle, one must have the ability to easily measure the operating frequency. Thus, the sensor must provide a relatively high local minimum and sufficient sharpness at the minimum. Other desirable properties are high sensitivity and low error with loading. If the sensitivity is too low, then the shift of operating frequency will be insufficient and the strain will not be detectable. If there is too much error, then accurately relating the operating frequency to strain involves a more complicated readout process. The employment of metamaterials for use in the manufacture of wireless strain sensors is advantageous because of their unique structural properties. Metamaterials have gaps (splits) that have higher electric field intensity localization compared to conventional radio frequency (RF) – micro-electro-mechanical systems (MEMS) sensing structures. Hence, they yield higher signal-to-noise ratios, which results in better linearity. These additional gaps also yield greater relative deformation, which leads to better sensitivity. Since metamaterials demonstrate higher sensitivity and lower errors as compared to other conventional RF-MEMS sensing structures, we propose that metamaterials can be used for widespread wireless strain sensing applications in industry.

There are many proposed applications areas for metamaterials. Some of these applications include cloaking [84], negative refractive index [85]-[88], focusing light [89], subwavelength resolution [90] and laser manufacture [72], [91]. We have previously explained using metamaterials in the manufacture of telemetric sensors [74] for detecting mechanical strain telemetrically in real time. In this section, using test materials of cast polyamide, derlin and polyamide, we apply compressive loads to our sensors and observe significant operating frequency shifts with the deformation of these test materials. These data are compared to strain measurements using traditional, commercial wired strain gauges on the same test materials. In this section, different from the previous chapters, we study wireless sensors for different Young's modulus of materials telemetrically and show that they exhibit different slopes in the behavior of their frequency shift *vs.* the applied load (corresponding to different levels of Young's modulus). In addition to showing proof-of-concept demonstrations of using

metamaterials in widespread areas of industry where wireless strain sensing is required, we also present a different method for monitoring Young's modulus remotely by observing different slopes in *f vs. load* characterization (e.g., for the purpose of monitoring and assessment of fracture healing). Monitoring such an evolution of this slope in *f vs. load* for an implantable plate at different times potentially offers surgeons the ability to follow different phases of healing process remotely.

The metamaterial sensor fabrication starts with depositing 0.1 μm $Si_3N_4$ onto our silicon substrate via plasma enhanced chemical vapor deposition (PECVD) and is followed by lithography of our metamaterial pattern of split ring resonator array. Subsequent metallization using a box-coater allows for deposition of 0.1 μm Au to obtain the final structure. Fig. 5.3.1 shows the sensors adhered to the test materials of cast polyamide (in Fig. 5.3.1(a)), derlin (in Fig. 5.3.1(b)), and polyamide (in Fig. 5.3.1(c)). Each sensor chip has 5 x 5 repeating unit cells, yielding a 1.5 cm x 1.5 cm total chip size. Each sensing unit has a 2220 μm outer length denoted as $L_{out}$ and a 1380 μm inner length denoted as $L_{in}$, with 140 μm inner ($w_{in}$) and outer ($w_{out}$) widths, and 280 μm inner ($s_{in}$) and outer ($s_{out}$) spacings. The repeating length of this unit cell structure is 2780 μm. The sensor is shown with its dimensions in Fig. 5.3.1(d). Sensor chips are affixed onto the test materials using a standard hard epoxy. The compression apparatus applies loads to the test materials up to 300 kgf. To read telemetrically the strain on the test material with the metamaterial sensor chips, one antenna is used as the excitation transmitter and the other as the signal receiver. For this purpose, standard gain horn antennas are employed (shown in Fig. 5.3.1(e)).

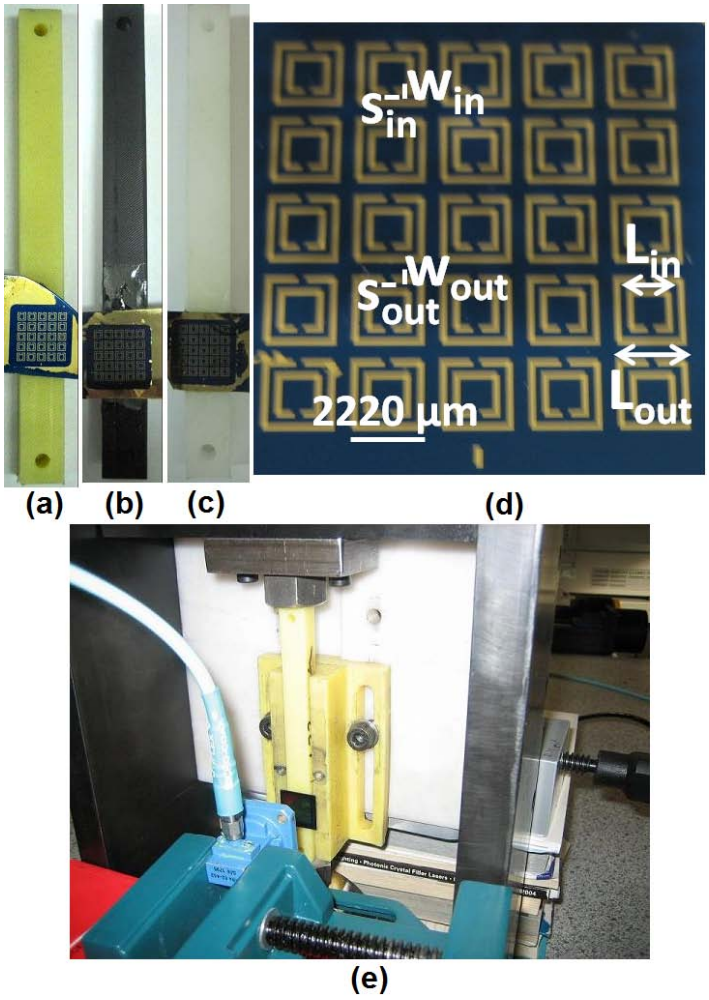


**Figure 5.3.1. The fabricated sensors fixated on different materials. The materials are (a) cast polyamide, (b) derlin and (c) polyamide. (d) The sensor shown with its dimensions. (e) Our compression setup.**

We apply the external load to the test materials in a controlled manner using our compression setup and, by knowing the Young's modulus and cross-sectional area of the specimen [92], we then calculate the theoretically imposed strain assuming linear elasticity. Finally, all strain measurements obtained with our wireless strain sensors and those of the commercial wired strain gauges are compared. The wired strain gauge used in this study was acquired from Tokyo Sokki Kenkyujo Co., Ltd., Tokyo, Japan (with a 2.1 gauge factor), which is one of the best semiconductor based wired gauges. The output resistance of the wired strain gauge was obtained using a standard parameter analyzer. In the strain gauges, the application of load to the test

material results in a Hall effect resistance change, and, dividing the applied stress by the Young's modulus, one can compute the applied microstrain. In all test materials, we set the working range over 2000 microstrain (for both wired measurements using the strain gauge and wireless measurements using the metamaterial chips). So, in all the cases, experimental data over 2000 microstrain are shown and compared.

For wireless measurements using the metamaterial chips, the transmission of the test material is measured when no sensor chip is attached to the test article in order to obtain the reference calibration. This measurement is repeated with the sensor under no load and then with the application of different compressive loads. Transmission spectra referenced relative to the no sensor case is obtained as a function of the applied load. From the transmission spectra of the sensor, we obtain the operating frequencies corresponding to different levels of applied loads. Then we subtract the no load operating frequency from these operating frequencies and obtain the relative operating frequency shifts ($\Delta f_0$). We obtain the operating frequency by looking at the minimum dip point in the range where we explore the shift with the applied load. Microstrain values are then obtained by dividing the applied stress by the Young's modulus for the test article. This gives the microstrain versus the relative frequency shift characteristics.

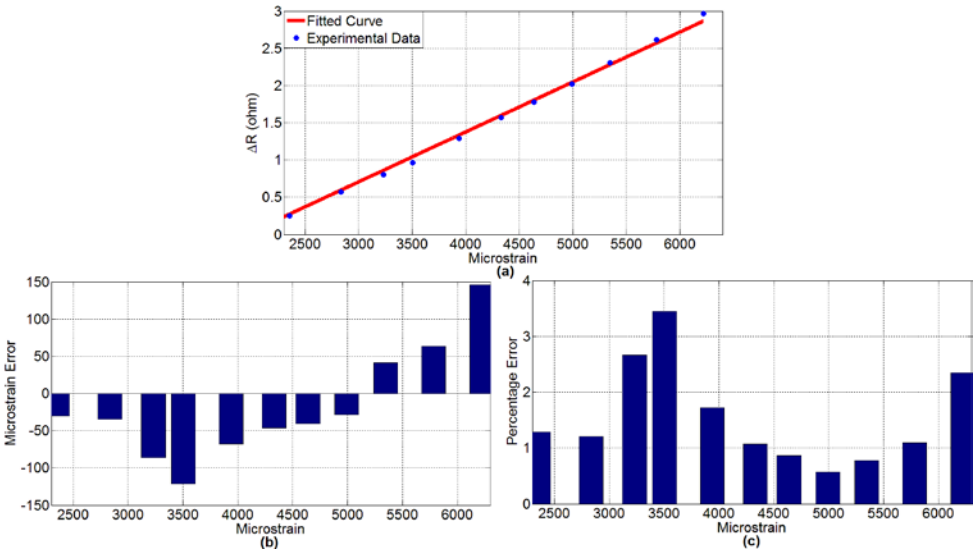


**Figure 5.3.2. Wired strain gauge measurements on cast polyamide test specimen. (a) Microstrain *vs.* ΔR, (b) microstrain error and (c) percentage error of the wired strain gauge measurements.**

Fig. 5.3.2(a) shows microstrain *vs.* ΔR data for the cast polyamide using the strain gauge, where ΔR is referenced to the no load condition measured as 351.239 Ω. Here the Young's modulus of the cast polyamide is taken to be 3.0 GPa. Here we obtain a maximum microstrain error of 150-microstrain given in Fig. 5.3.2(b) and a maximum error of 4% given in Fig. 5.3.2(c). The measurement sensitivity of the strain gauge on the cast polyamide is $6.708\times10^{-4}\,\Omega microstrain^{-1}$. Fig. 5.3.3(a) presents the transmission spectra of the metamaterial sensor on the cast polyamide with different applied loads changing from 28 to 271 kgf. The metamaterial sensor exhibits over a 10 dB dip in its transmission spectra where the no-load operating frequency is measured as 12.783 GHz. Fig. 5.3.3(b) shows the corresponding microstrain *vs.* $\Delta f_0$ characterization. The measurement sensitivity of the metamaterial sensor on the cast polyamide is 0.0543 MHz/kgf, or equivalently $2.348\times10^{-3}\,MHzmicrostrain^{-1}$. In Fig. 5.3.3(c), we see the microstrain error distribution of the metamaterial sensor that has a maximum error of 500-microstrain. In Fig. 5.3.3(d) we observe a maximum percentage error of 15%.

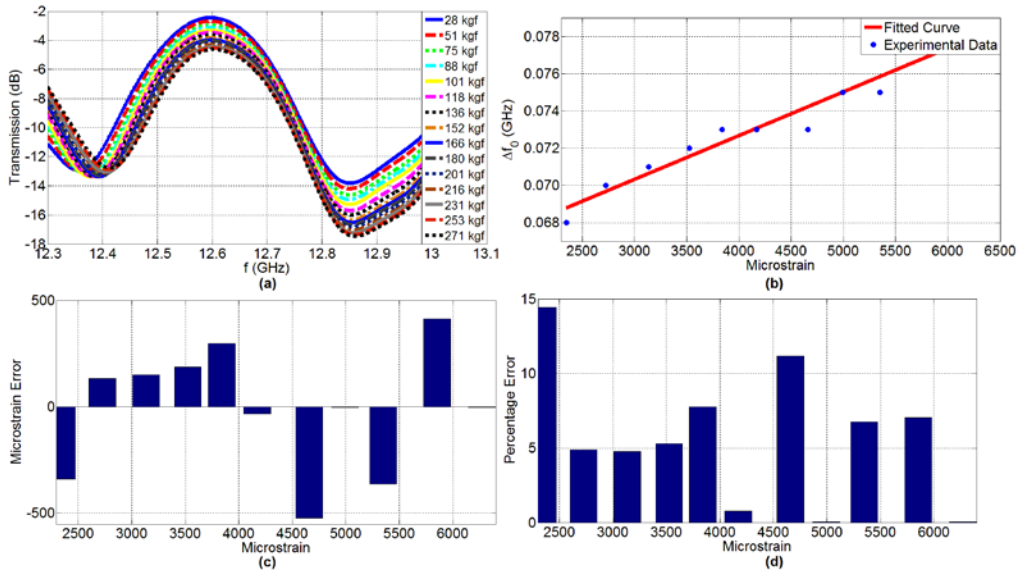


**Figure 5.3.3. Metamaterial measurements on cast polyamide stick. (a) Transmission spetra with respect to the case of no load, (b) microstrain *vs.* ΔR, (c) microstrain error and (d) percentage error of the wireless measurements.**

Fig. 5.3.4 shows measurements of the wired strain gauge on the derlin test specimen (with the Young's modulus of 2.7 GPa). When we apply strain to the test article, the resistance of the wired strain gauge (whose initial resistance is 350.783 Ω under no load) changes by a few ohms. This relative change of the resistance, ΔR, is obtained by subtracting the no load resistance from the measurements of resistances when different strains are applied. A linear microstrain *vs.* ΔR characteristics is obtained (presented in Fig. 5.3.4(a)), with a maximummicrostrain error less than 200 microstrain (shown in Fig. 5.3.4(b)). This represents an error percentage less than 4% (given in Fig. 5.3.4(c)). The measurement sensitivity of the wired gauge on the derlin is $6.8\times10^{-4}\Omega microstrain^{-1}$.

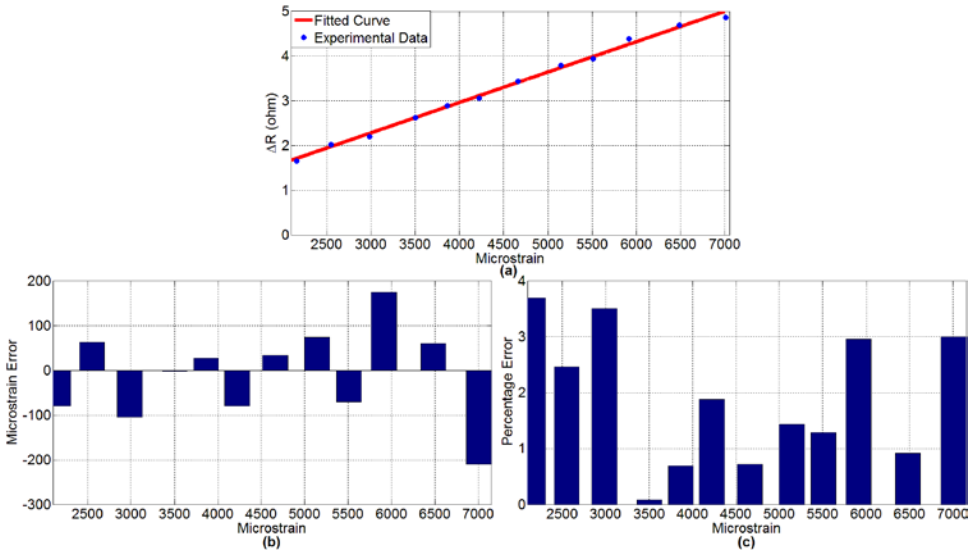


**Figure 5.3.4. Wired strain gauge measurements on derlin test specimen. (a) Microstrain *vs.* ΔR, (b) microstrain error and (c) percentage error of the wired strain gauge measurements.**

The transmission spectra of the metamaterial sensor are shown parameterized with respect to external loads applied to the derlin specimen in Fig. 5.3.5(a), where the operating frequency is measured as 12.737 GHz under no load and the observed dip is >10 dB. From these data, the microstrain *vs.* $\Delta f_0$ characteristics is obtained in Fig. 5.3.5(b). The measurement sensitivity of the wireless sensor on the derlin is 0.0577 MHz/kgf, or $2.224\times10^{-3} MHzmicrostrain^{-1}$. The maximum microstrain error (shown in Fig. 5.3.5(c)) is 300 microstrain, which represents a

maximum percentage error of 9% (given in Fig. 5.3.5(d)). From these results, we observe that the strain measurements obtained with the wireless metamaterial sensor closely approximates those obtained with the commercially available wired strain gauge. These data indicate that the wireless sensor is capable of measuring the strain remotely.

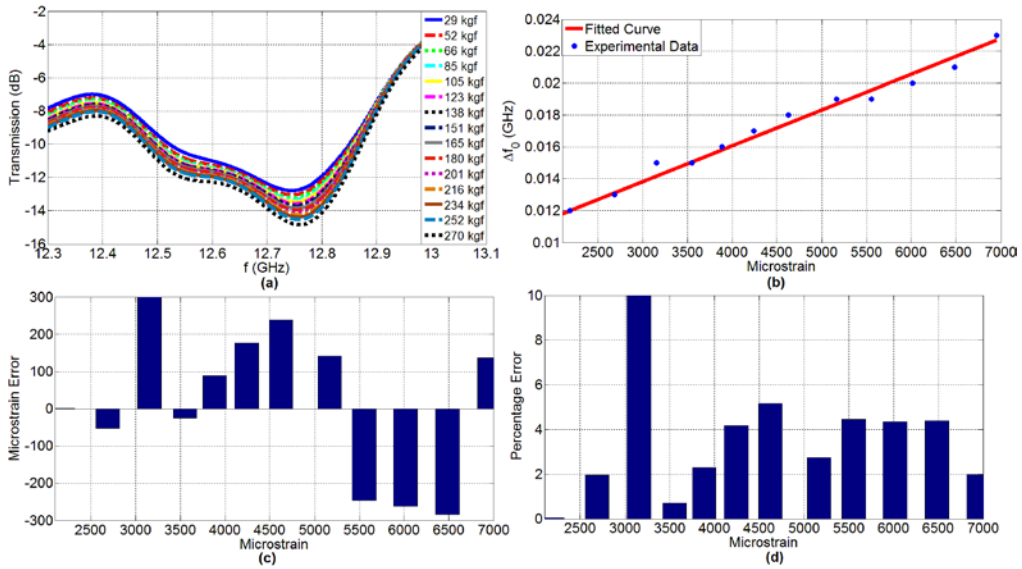


**Figure 5.3.5. Metamaterial measurements on derlin stick. (a) Transmission spectra with respect to the case of no load, (b) microstrain *vs.* ΔR, (c) microstrain error and (d) percentage error of the wireless measurements.**

In Fig. 5.3.6, we show the measurement results on the polyamide stick (with the Young's modulus of 1.8 GPa) with the wired strain gauge. The no load resistance is 351.1909 Ω. The microstrain error (presented in Fig. 5.3.6(b)) is less than a maximum level of 1000 microstrain, with a corresponding maximum percentage error of 10% (given in Fig. 5.3.6(c)). The measurement sensitivity of the wired gauge operating on the polyamide is $6.758\times10^{-4}\Omega microstrain^{-1}$. We also present the transmission spectra parameterized with respect to the applied loads on the polyamide specimen changing from 31 to 273 kgf in Fig. 5.3.7(a). The no load operating frequency is measured as 12.710 GHz, with a local dip of >10 dB. From Fig. 5.3.7(b) the measurement sensitivity of the wireless sensor on the polyamide is obtained to be 0.119 MHz/kgf, or $3.224\times10^{-3} MHzmicrostrain^{-1}$. The maximum microstrain error is 1500 microstrain (as illustrated in Fig. 5.3.7(c)) and the maximum percentage error is 19% (as

demonstrated in Fig. 5.3.7(d)). From these results, we conclude that the surface strain can be measured telemetrically with our wireless metamaterial sensor. In addition, all these data provide de facto evidence that metamaterials can be utilized as sensors for many application areas that require measuring mechanical strain remotely.

It is important to view these results within the context of the measurement capabilities used in this investigation. For the wireless experiments, the maximum number of points that the network analyzer can obtain is limited (which is 801 in our case). We focus on the spectral region around 800 MHz to facilitate identifying the transmission minimum (operating frequency). However, given the operating frequency of the sensor, this resolution may not be sufficient to accurately characterize the absolute local minimum. As a result, the error is truly a gestalt and represents the sum of the errors of the wireless sensor and the measurement system. For our wired strain gauge measurements, the measurements were taken with a parameter analyzer. Because of the resolution sufficiency of the parameter analyzer, the measured error is dominated by the error of the wired strain gauge, not the error of the measurement system. To illustrate the point, if the resistance measurements were instead taken with a multimeter, there would be much more error in the measurements because the multimeter's resolution is not as good as the parameter analyzer, resulting in a contribution to the overall error. For our wireless strain sensor measurements, since the network analyzer's maximum collection is 801 points over the defined frequency range, this is then analogous to making the wired strain gauge measurements with a standard multimeter. Conversely, if we had the capability to take 16001 points, we would then anticipate an associated reduction in the error.

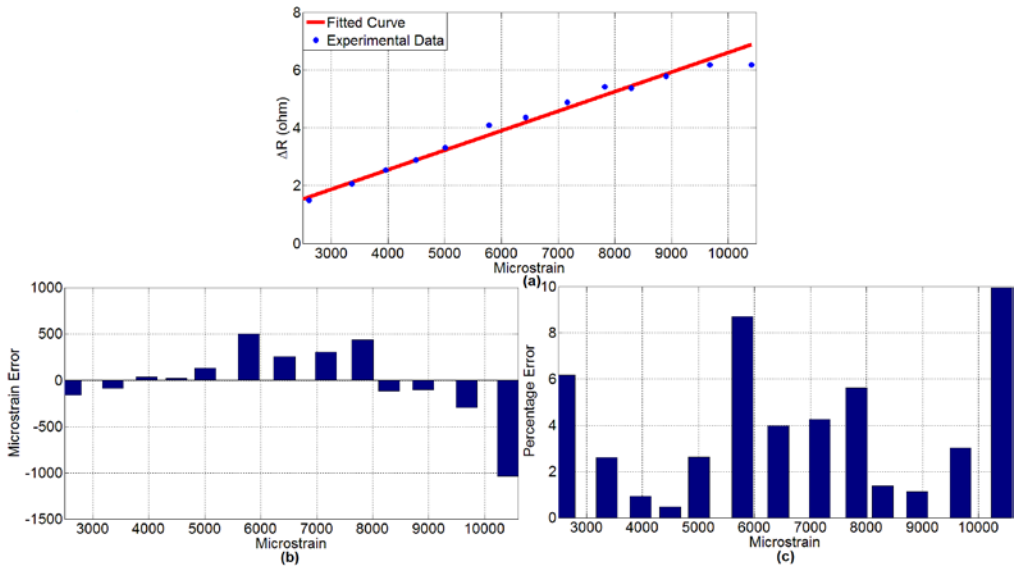


**Figure 5.3.6. Wired strain gauge measurements on polyamide test specimen. (a) Microstrain *vs.* ΔR, (b) microstrain error and (c) percentage error of the wired strain gauge measurements.**

Numerically, for the wireless sensor, the average sensitivity is found to be $2.5987\times10^{-3}\,MHzmicrostrain^{-1}$, resulting in 384.807 microstrain resolution (1/ (2.5987x10$^{-3}$)). For the wired strain gauge, the average sensitivity is $6.7553\times10^{-4}\,\Omega microstrain^{-1}$ and the minimally detectable current is 1μA (which corresponds to 0.123Ω), then we obtain 182.079 microstrain resolution (0.123/ (6.7553x10$^{-4}$)). For the wireless strain gauge, if we use a network analyzer, which can take up to 16001 points, the minimum resolution will be 1/20 of the current resolution (or 19.24 microstrain). If we also narrow down the frequency sweep band, this resolution will also be further reduced.

Finally, it is worth mentioning one important issue that relates to the thermal effects of wired strain gauges and wireless metamaterial sensors. It is well known that traditionally strain gauges that utilize the Hall effect display significant thermal drift due to their resistance dependent evolution of heat. This, in turn, can introduce significant error in their measurements. Given that the metamaterial sensors are not under constant current, this effect is all but eliminated in these wireless sensors.

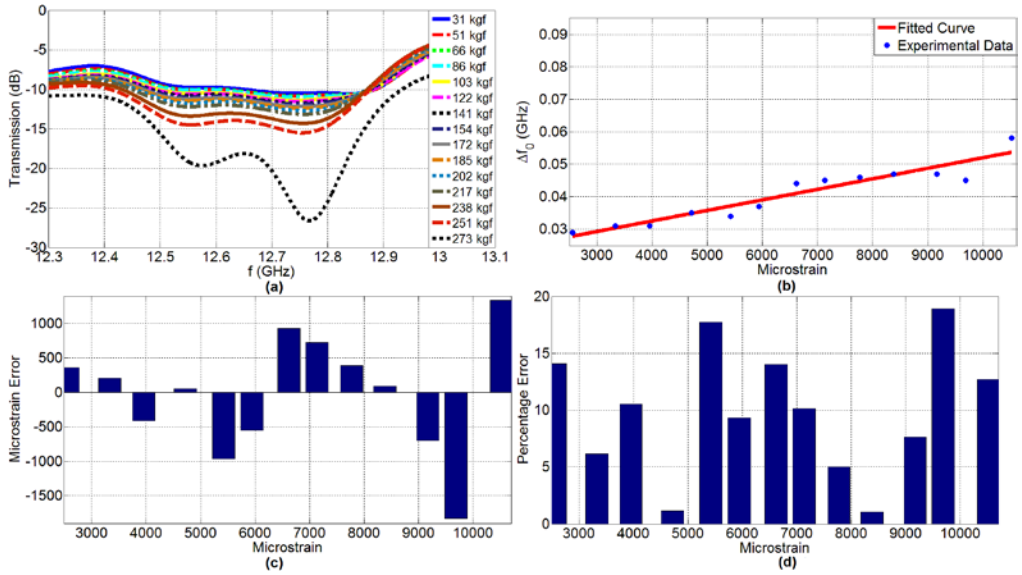


**Figure 5.3.7. Metamaterial measurements on polyamide stick. (a) Transmission spectra parameterized with respect to the case of no load, (b) microstrain *vs.* ΔR, (c) microstrain error and (d) the percentage error of the wireless measurements.**

In conclusion, we have experimentally showed that wireless metamaterial based strain sensors are capable of telemetrically measuring the surface strain on different materials including cast polyamide, derlin and polyamide. Because of the structural properties of the metamaterials, the wireless metamaterial sensors exhibit large frequency minima, leading to high sensitivity and low errors. They exhibit more than a 10 dB dip in transmission spectra, and the errors are reasonable when compared to those of the commercially available wired strain gauge, in spite of the addition of the measurement system error. The wireless sensor shows a $2.5987\times10^{-3}\,MHzmicrostrain^{-1}$ measurement sensitivity on the average, with a maximum error of 15% in cast polyamide, 9% in derlin, and 19% in polyamide. By measuring strain telemetrically in different industrial materials, we have presented a proof-of-concept demonstration that metamaterials can be used as wireless sensors for many application areas that require measuring mechanical strain telemetrically.

## 5.4 Metamaterial Parameters Affecting Wireless Strain Sensing

In this section, we will explore different metamaterials with different design parameters. We will show that how the gap of the metamaterial is sensitive to the mechanical deformation and also discuss the suitability of metamaterials for wireless strain sensing. By varying the gap, we will demonstrate the corresponding change in the sensitivity. Here we will show the best sensor performance of all devices up to this section. Also, we will compare the sensor performance of metamaterial structure with that of the other conventional RF structures and demonstrate better performance with metematerials compared to spiral structure.

We compare two metamaterial structures in this section. Meta-1 is the device with a larger gap which is the device shown in Section 5.1. Meta-2 is the device with a smaller gap. All the other device parameters are identical. The fabrication procedure, the experimental setup and the calibration procedure are completely the same as discussed in detail in Section 5.1.

**Table 5.4.1. The device parameters of meta-sensors.**

| | $L_{total}$ (μm) | $L_{unit}$ (μm) | $L_{out}$ (μm) | $L_{in}$ (μm) | $w_{out}$ (μm) | $s_{out}$ **(μm)** | $w_{in}$ (μm) | $s_{in}$ **(μm)** | $t_{film}$ (μm) | $t$ (μm) | N |
|---|---|---|---|---|---|---|---|---|---|---|---|
| Meta-1 | 15000 | 2780 | 2220 | 1500 | 80 | **280** | 80 | **280** | 0.1 | 0.1 | 5x5 |
| Meta-2 | 15000 | 2780 | 2220 | 1500 | 80 | **80** | 80 | **80** | 0.1 | 0.1 | 5x5 |

Before the observation of sensor performances, we will first present and discuss the simulation of metamaterial structure shown in Fig. 5.4.1. From this figure, we can see that the electric field is strongly localized between gaps. Hence, metamaterials emit stronger signal compared to conventional RF structures, e.g., spirals. Thus, they exhibit higher Q-factors. Since higher Q-

factor means higher SNR, the signal dominates the noise and metamaterials exhibit lower errors. Because of the gap, a metamaterial sensor will have additional capacitance hence with the same applied load, the change in its resonance frequency will be increased and its sensitivity will be increased. Also, because of this additional capacitance, it will demonstrate a lower resonance frequency per unit area, which is important for background absorption issues.

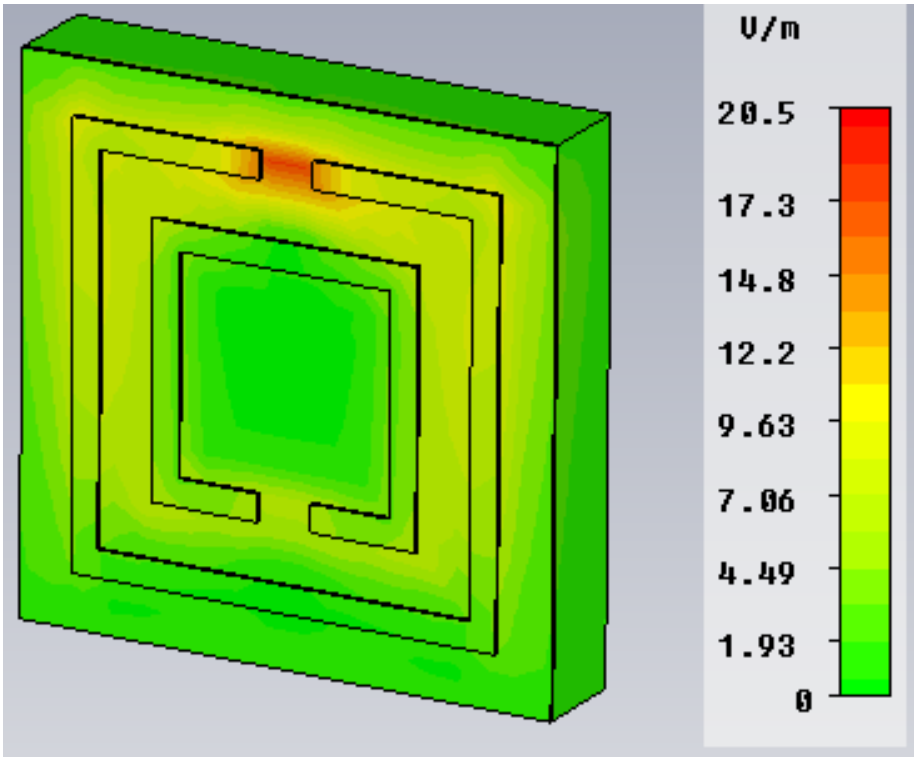


**Figure 5.4.1. The simulation of the meta-sensor. There is an E-field localization in the gap.**

In Fig. 5.4.2, we present the experimental results of Meta-2. The experimental results of Meta-1 were shown in Section 5.1. From the transmission, we can see that the no load frequency is 11.947 GHz. In Meta-1, the no load resonance frequency was 12.138 GHz. As expected, the no load resonance frequency is decreased compared to Meta-1 since the gap is smaller and hence the gap capacitance $C_{gap}$ is bigger. As in other metamaterial structures, Meta-2 exhibits a higher Q-factor and a larger transmission dip. It has 0.545 MHz/kgf (or 25.74 kHz/microstrain) sensitivity. It produces less than 7% error (or less than 300 microstrain error). With these

experimental results, Meta-2 shows the best sensor performance among all devices presented up to this section with its highest sensitivity, highest Q-factor and largest tranmission dip, and lowest errors.

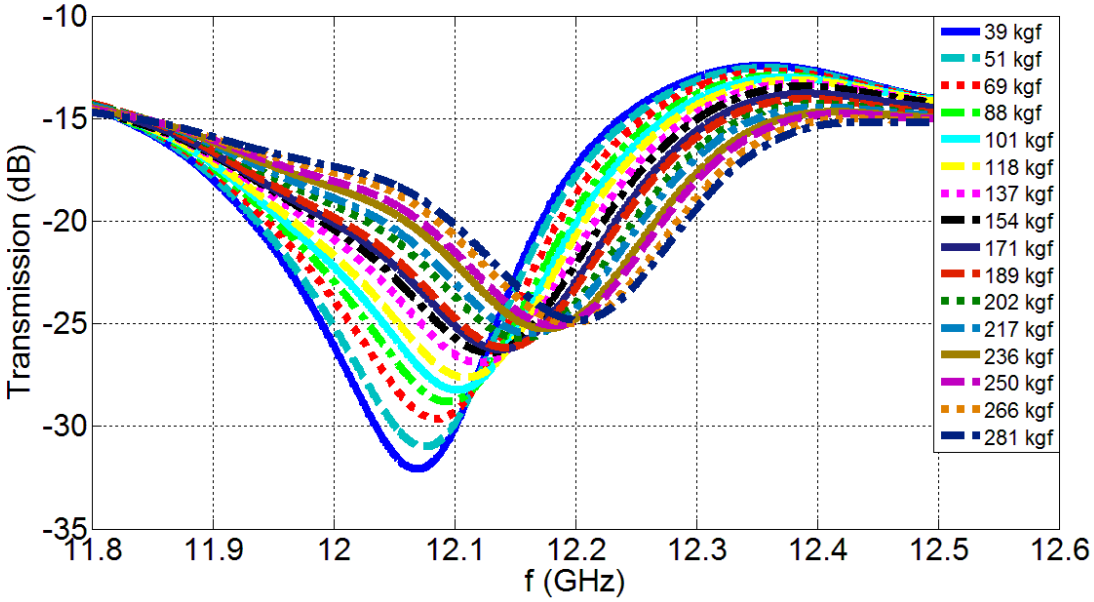


(a)

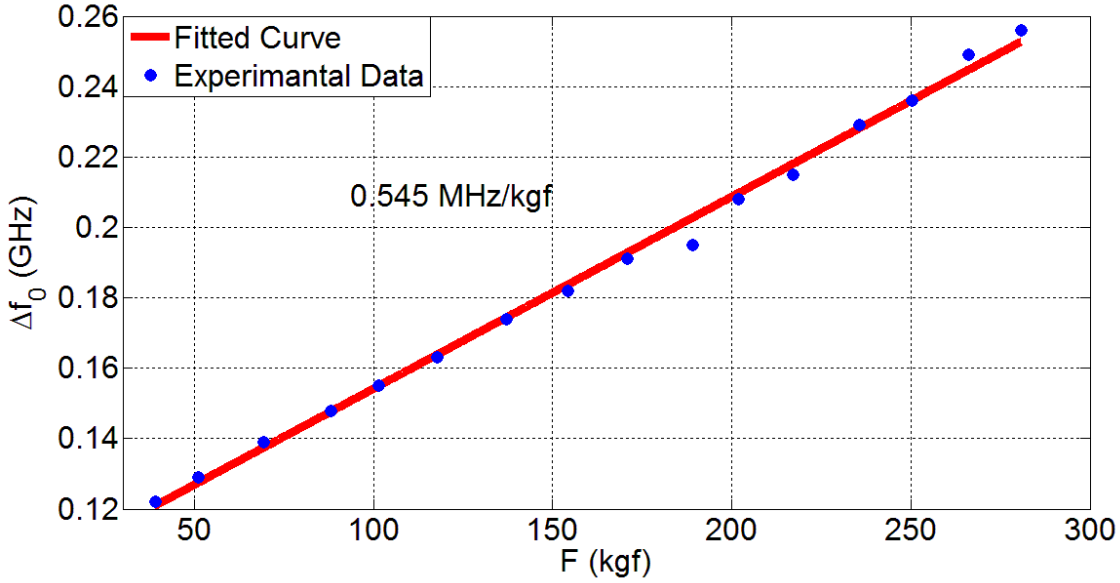


(b)

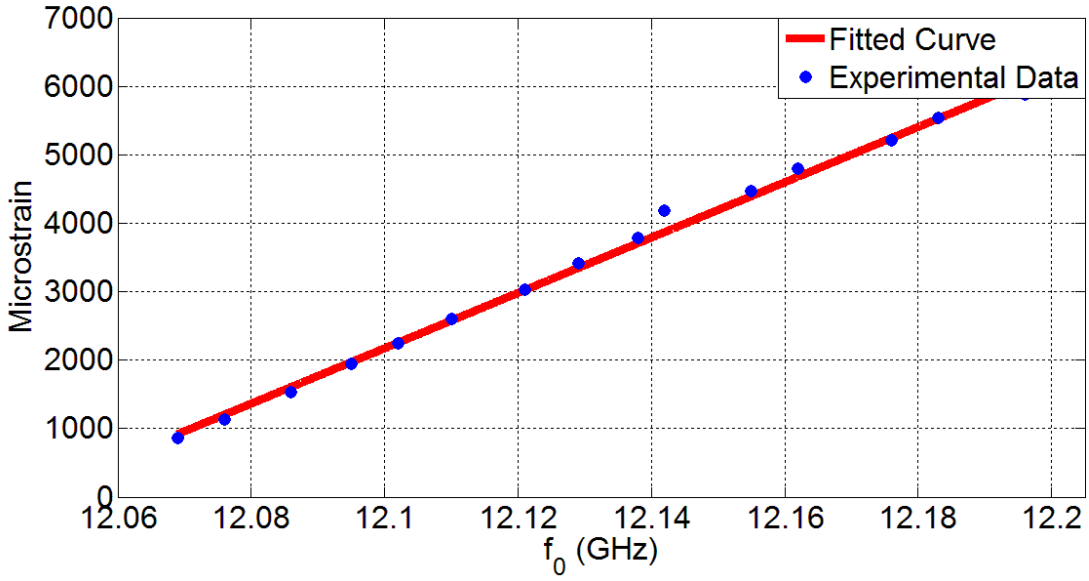
Fitted Curve
Experimental Data
Microstrain
7000
6000
5000
4000
3000
2000
1000
0
12.06
12.08
12.1
12.12
12.14
12.16
12.18
12.2
f0 (GHz)

(c)

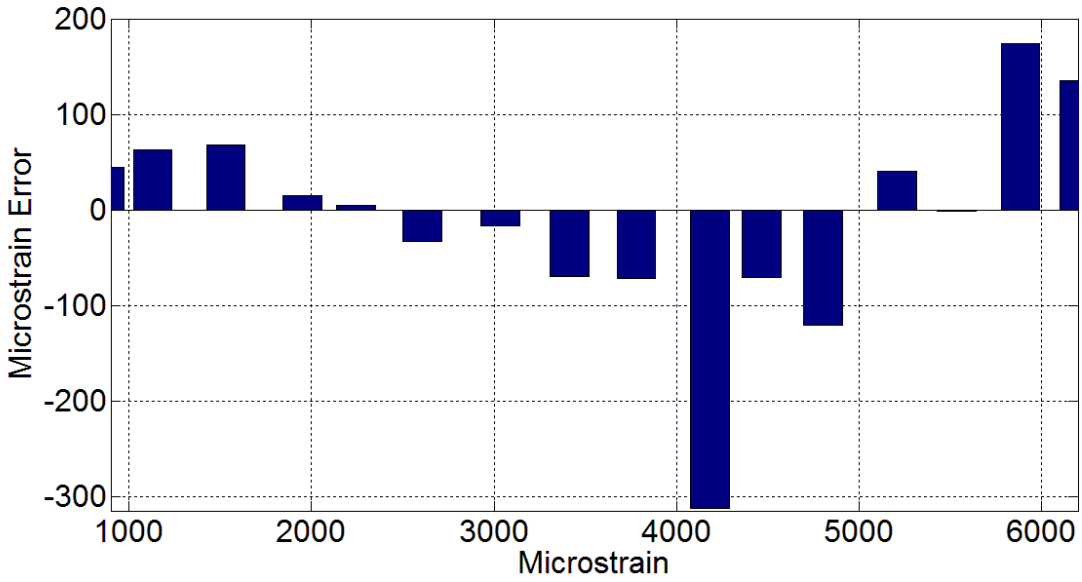
Microstrain Error
200
100
0
-100
-200
-300
1000
2000
3000
4000
5000
6000
Microstrain

(d)

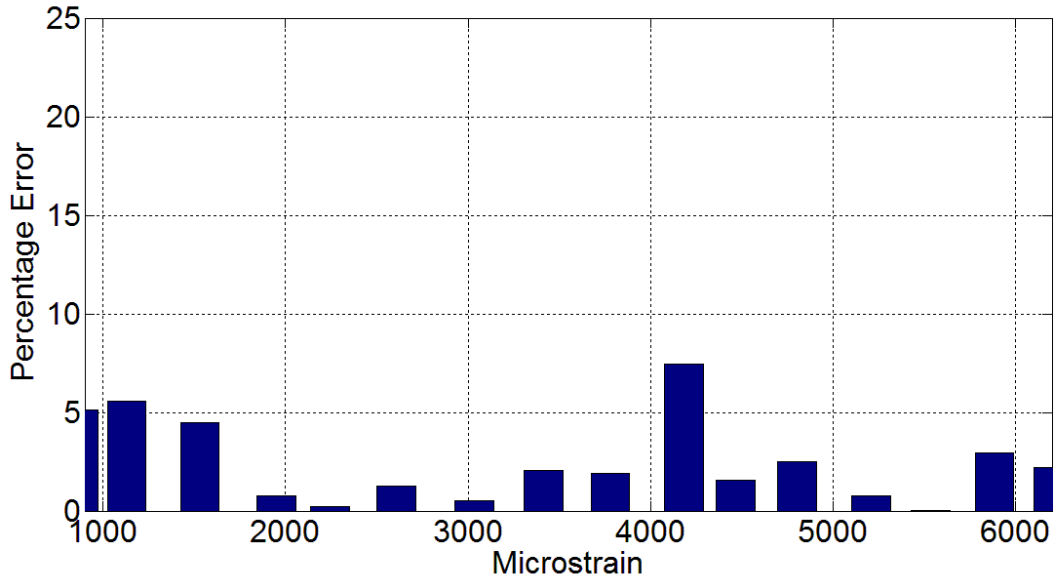


(e)

**Figure 5.4.2. Experimental measurements of Meta-2: (a) Transmission as a function of frequency with different applied loads, (b) F *vs.* $\Delta f_0$ graph, (c) $f_0$ *vs.* microstrain graph, (d) the error in terms of microstrain and (f) the error in terms of percentage.**

If we compare the results of Meta-1 and Meta-2 as in Fig. 5.4.3, we can see the significant increase of the sensitivity with the change of the gap. The increased sensitivity can visually be seen just by looking at their transmission curves. If the capacitance changes by the same amount, the percentage change of the capacitance is larger for smaller capacitance. Hence, the sensitivity is increased multiple times using a smaller gap. This experiment shows the importance of metamaterial structure for wireless strain sensing and demonstrates that the metamaterials with their gaps are very sensitive to the mechanical deformation. This also shows the importance of gaps (splits) for sensitivity and this unique structure of metamaterials make them apt for wireless strain sensing. Changing the dimensions of the gap is shown to significantly change the sensitivity. If we compare the errors, we can observe that they both feature low errors because of their strong enough transmission dips and high enough Q-factors.

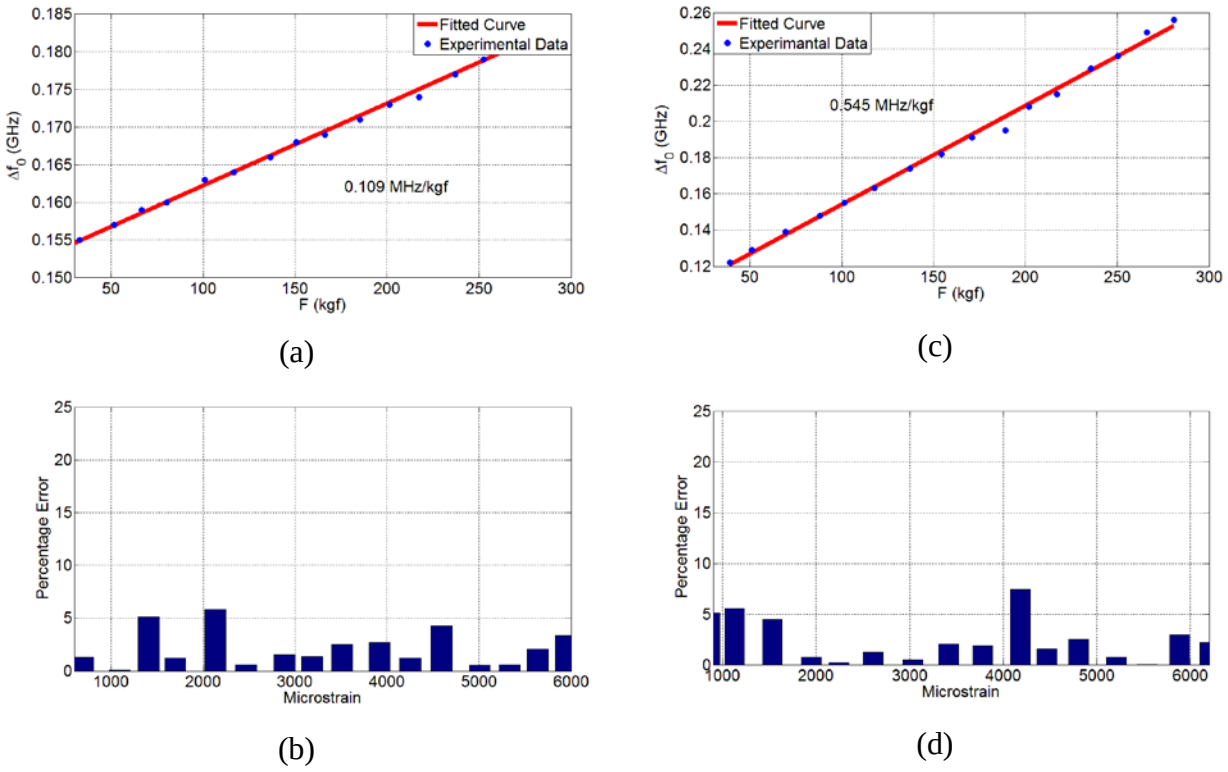


**Figure 5.4.3. Comparison of the experimental results of Meta-1 and Meta-2: (a) F *vs.* $\Delta f_0$ of Meta-1 (b) errors of Meta-1 in terms of percentage, (c) F *vs.* $\Delta f_0$ of Meta-2, and (d) errors of Meta-2 in terms of percentage.**

We can see comparison of the sensor performances of the spiral structure (single-device) which was shown is Section 4.1, and Meta-2 in Fig. 5.4.4. By looking at their corresponding transmission curves, we can see the significant increase of the sensitivity using metamaterial structures. First of all, the Meta-2 structure shows larger and sharper dips in transmission compared to the spiral structure. Furthermore, the Meta-2 has a higher Q-factor compared to that of the spiral structure. The sensitivity of the spiral structure is 0.218 MHz/kgf while the Meta-2 has 0.545 MHz/kgf sensitivity. Also, the spiral structure shows less than 25% errors while the Meta-2 shows less than 7% errors. From these results, we can understand that the metamaterials have the capability to exhibit higher Q-factors, better sensitivity and better linearity compared to conventional RF structures such as spiral coils.

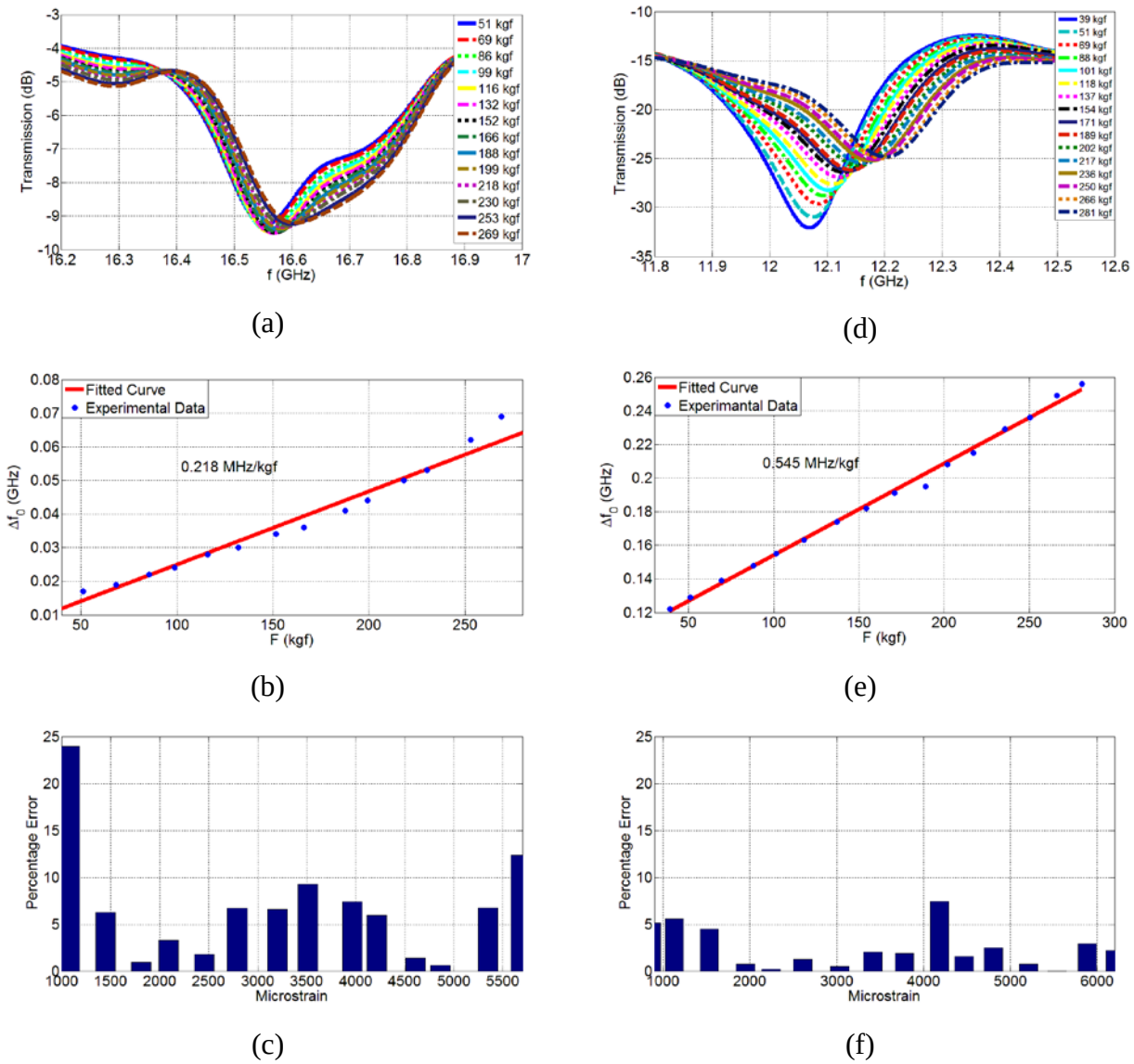


**Figure 5.4.4. Comparison of the experimental results of spiral structure (single-device), also previously shown in Section 4.1, and Meta-2: (a) Transmission spectra of the spiral structure under different levels of applied load, (b) F *vs.* $\Delta f_0$ of the spiral structure, (c) errors of the spiral structure in terms of percentage, (d) transmission spectra of the Meta-2 under different levels of applied load, (e) F *vs.* $\Delta f_0$ of the Meta-2, and (f) errors of the Meta-2 in terms of percentage.**

In conclusion, in this section, we showed that the metamaterials are very sensitive to the mechanical deformation. The gap is very important for sensitivity. It produces additional

capacitance and the change in this capacitance is very effective in shifting their resonance frequency. By changing the gap, we can affect the sensitivity significantly. Because metamaterials have strong electric field localized between the gaps, they radiate stronger signals and hence they demonstrate higher Q-factors, larger transmission dips, higher SNR, and lower errors compared to conventional RF structures such as the spiral structure. In addition, because of these gaps, they have additional capacitance and exhibit better sensitivity compared to the spiral coils. The meta-2 showed the best sensor performance of all devices presented up to this section and we can conclude that the metamaterials are very suitable structures for wireless strain sensing because of their unique structural properties (splits).

## 5.5 Metamaterials under Tension as Opposed to Compression

In this section, we will examine the tension behavior of the metamaterial sensors. Up to this point, metamaterials have been tested only under compression. As opposed to the compressive forces, the resonance frequency decreases with the tensile loads. This shows the sensitivity of our sensor to the direction of the applied force. We also observe that the softest material polyamide gives the highest slope in the response of frequency shift *vs.* applied load while the hardest material cast polyamide has the lowest slope. This will help surgeons to follow the phases of healing process by considering the changes in this slope of hardness. Also, the surgeon will be able to observe the direction of the force by looking at the sign of the slope. The Young's modulus of our tension setup is lower than that of our compression setup for each material. Thus, the slope response of our sensors under tension appears to be higher than that under compression. These data show consistent sensing behavior of the sensors under both tension and compression.

We can see the device parameters listed in Table 5.5.1. The device parameters are completely the same as in Section 5.3. Here we will examine three different test materials including cast polyamide, derlin, and polyamide, as in Section 5.3. However, this time as opposed to Section 5.5.3, we examine the tension behavior of these sensors. The hardest material is cast polyamide while the softest material is polyamide. The fabrication procedure of the sensors, the experimental setup and the calibration procedure are completely the same as discussed in detail in Section 5.1.

**Table 5.5.1. Our device parameters.**

| $L_{total}$ (μm) | $L_{unit}$ (μm) | $L_{out}$ (μm) | $L_{in}$ (μm) | $w_{out}$ (μm) | $s_{out}$ (μm) | $w_{in}$ (μm) | $s_{in}$ (μm) | $t_{film}$ (μm) | $t$ (μm) | N |
|---|---|---|---|---|---|---|---|---|---|---|
| 15000 | 2780 | 2220 | 1380 | 140 | 280 | 80 | 280 | 0.1 | 0.1 | 5x5 |

We can see the tension setup depicted in Fig. 5.5.1, which we built at Bilkent University. Under tension, both the gaps of metamaterials are decreased and the dielectric area between the substrate and metal layer is increased. Therefore, the capacitance between gaps ($C_{gap}$) and the dielectric capacitance ($C_{diel}$) are increased. Thus, the resonance frequency is decreased.

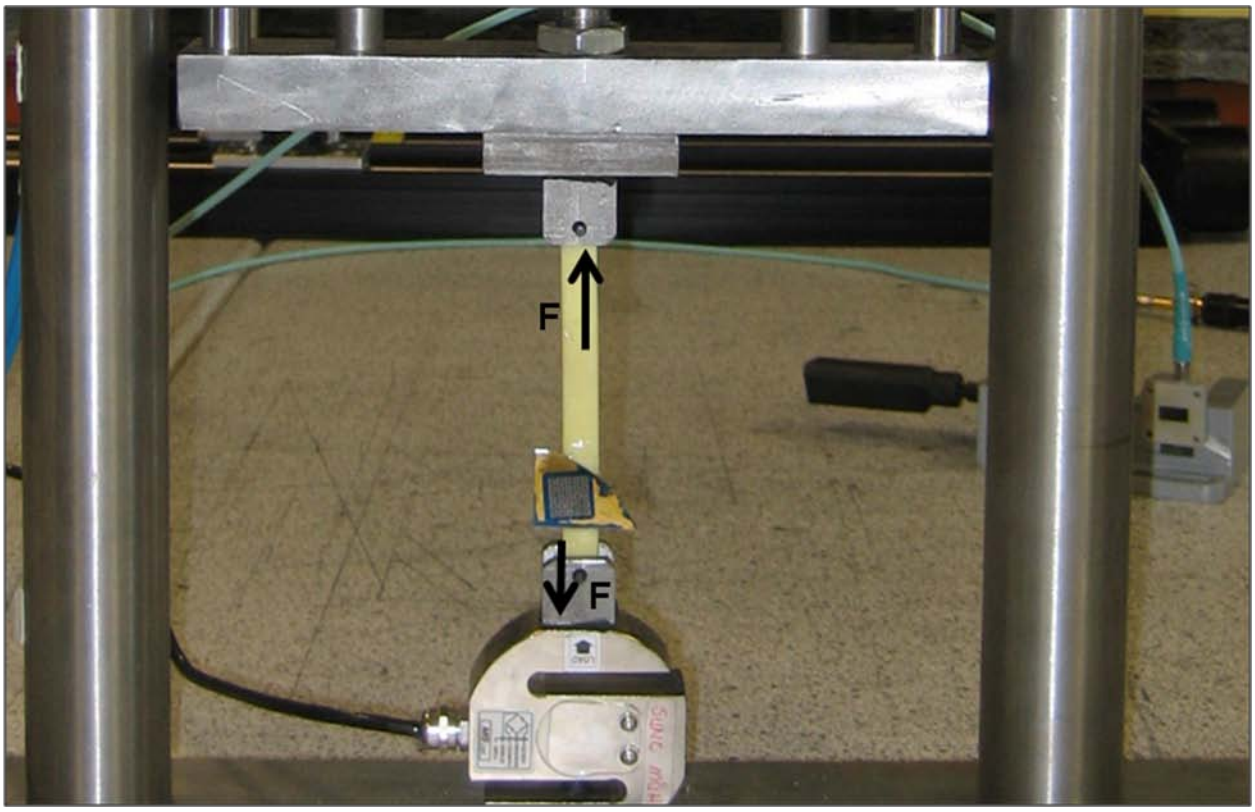


**Figure 5.5.1. Tension setup**

We present the experimental results of tensile loading on cast polyamide stick in Fig. 5.5.2. The tensile Young's modulus of cast polyamide is 2.371 GPa, which is lower than the compressive

Young’s modulus of cast polyamide stick (3.288 GPa). In this case, the sensitivity of the sensor is found to be -0.365 MHz/kgf, which is larger than the sensitivity of the sensor under compression. We measured the Young’s modulus of test materaials in both compression and tension setup using a commercially available wired strain gauge (Tokyo Sokki Kenkyujo Co., Ltd., with a gauge factor of 2.1). Since the Young’s modulus is lower, we obtain higher strain with the application of the same force, thus the shift of resonance frequency is increased and hence the sensor exhibits higher sensitivity. The sign of the slope is opposite to the sign of the slope under compression since the direction of the applied force is opposite. The sensor demonstrates less than 20% error, which proves reasonably correct read-out of the strain.

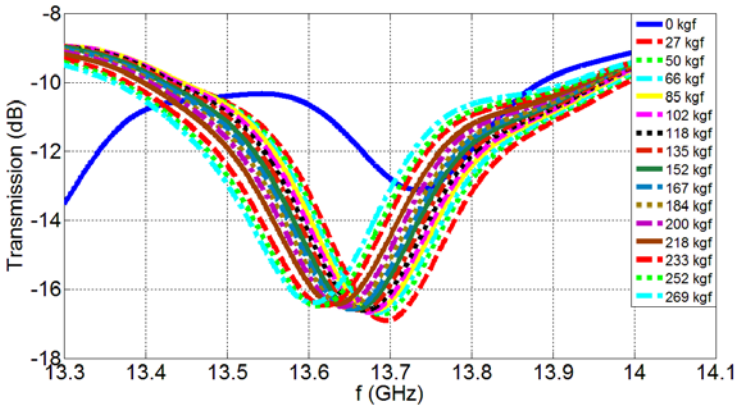


(a)

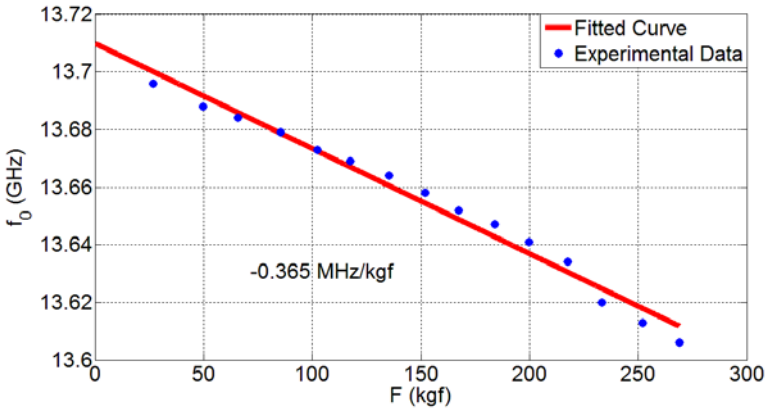


(b)

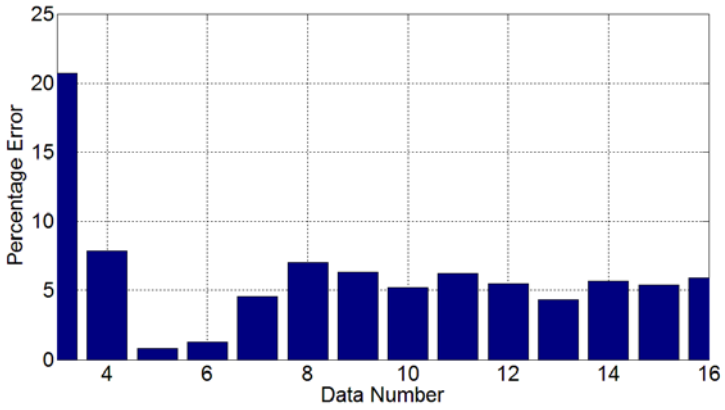


(c)

**Figure 5.5.2. Experimental results of tensile loading on cast polyamide: (a) Transmission spectra under different levels of applied loads, (b) F *vs.* $\Delta f_0$ and (c) error in terms of percentage.**

In Fig. 5.5.3, we can see the experimental results of the tension behavior on derlin. The tensile Young's modulus of derlin is 2.079 GPa which is lower than the compressive Young's modulus of derlin (2.896 GPa). The sensitivity of the sensor on derlin stick is -0.476 MHz/kgf, which is a larger slope in magnitude than that under compression. The sign of the slope under tension is different than the sign of the slope under compression. Also, the slope obtained on derlin stick is larger in magnitude than the slope obtained on cast polyamide stick, since the derlin is a softer material and we induce more strain with the same applied force and we thus get a higher sensitivity. The sensor shows less than 9% error under tension using derlin.

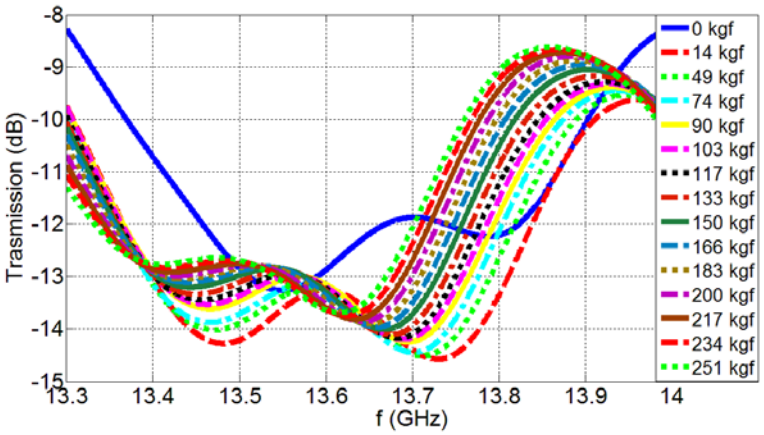


(a)

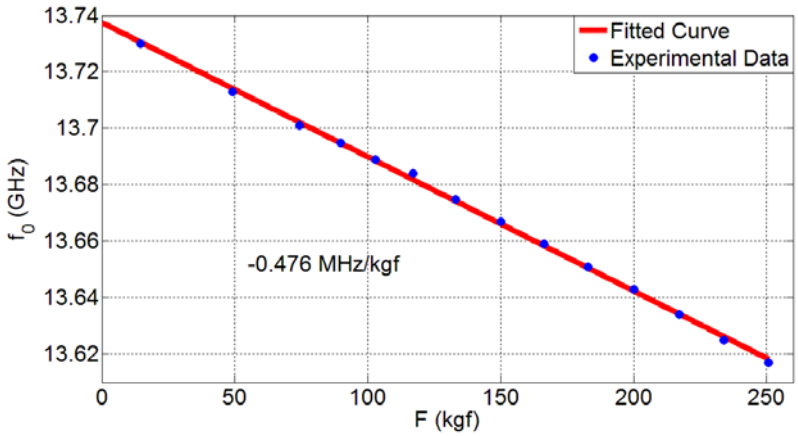


(b)

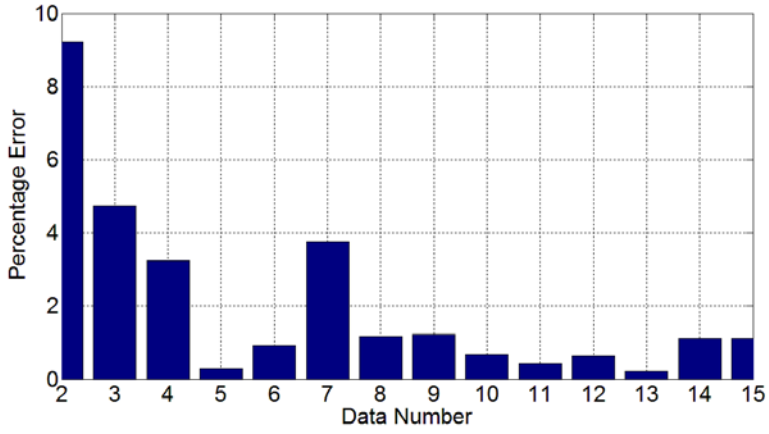


(c)

**Figure 5.5.3. Experimental results of tensile loading on derlin: (a) Transmission spectra under different levels of applied loads, (b) F *vs.* $\Delta f_0$ and (c) error in terms of percentage.**

The experimental results of tensile loading on polyamide stick are shown in Fig. 5.5.4. The Young's modulus of polyamide under tension (1.451 GPa) is also lower than its Young's modulus under compression (1.95 GPa). The sensor sensitivity is -0.656 MHz/kgf in this case, which is larger in magnitude than the slope under compression. The sign of the sensitivity under tension is also again opposite to the sign of the sensitivity under compression. Here we also obtain the largest slope of all test materials because the polyamide is the softest material. The error is less than 12%.

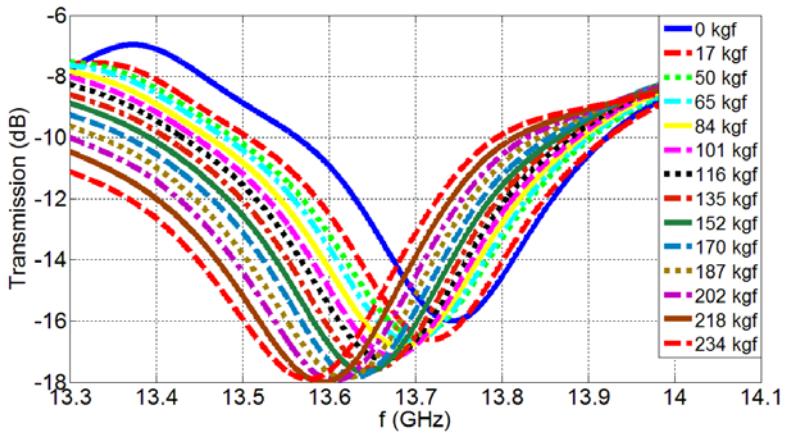


(a)

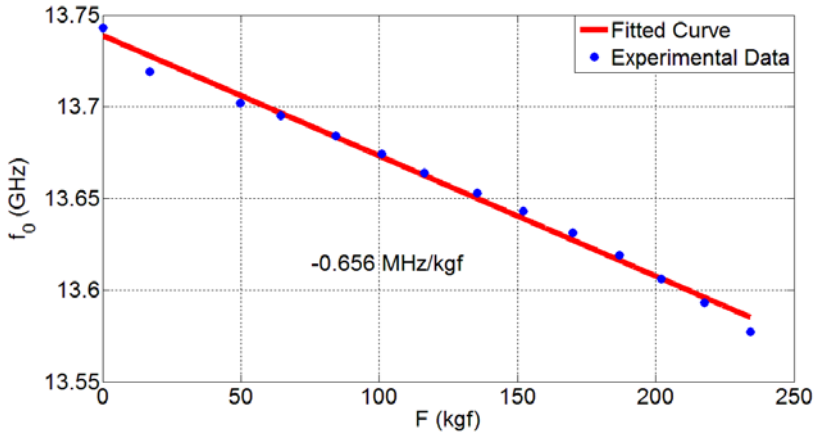


(b)

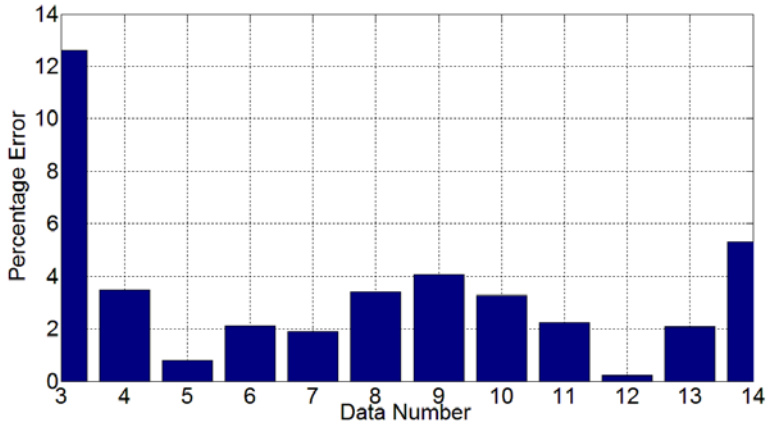


(c)

**Figure 5.5.4. Experimental results of tensile loading on polyamide: (a) Transmission spectra under different levels of applied loads, (b) F *vs.* $\Delta f_0$ and (c) error in terms of percentage.**

In conclusion, we measured the behavior of metamaterial sensors under tension. The resonance frequency shifts opposite to that under compression, which shows the sensitivity of metamaterial sensors to the direction of applied force. Since the tensile Young's modulus of test materials is lower than their compressive Young's modulus, the sensitivities are also measured to be larger in magnitude in tension. We measure the highest slope using the softest material, polyamide, while we observe the lowest slope using hardest material, cast polyamide. By observing the slopes and signs of the slopes, the surgeons can follow different phases of fracture healing.

# Chapter 6

# Wireless Strain Sensing Nested Metamaterials

In this chapter, we will demonstrate our novel architecture of nested metamaterials for wireless strain sensing. We will show the advantages of nested metamaterials compared to other structures such as classical metamaterial structure in wireless strain sensing. We will see that by playing with parameters of nested metamaterial structure, we can adjust resonance frequency and decrease the electrical lengths of the structure down to such as λ/400. We will also demonstrate the wireless strain sensing at 100 MHz using 0.8 cm × 0.8 cm sensor with different thicknesses of soft tissue and showcase strain sensing in sheep's metatarsal, femur and spine telemetrically.

## 6.1 Nested Metamaterials for Wireless Strain Sensing

This section is based on the publication "Nested Metamaterials for Wireless Strain Sensing" **R. Melik,** E. Unal, N. K. Perkgoz, B. Santoni, D. Kamstock, C.M. Puttlitz, and H. V. Demir, *IEEE*

*Journal of Selected Topics in Quantum Electronics 16, 450-458 (2010).* Reproduced (or 'Reproduced in part') with permission from IEEE. Copyright 2009 IEEE.

In this section [75], we designed, fabricated and characterized metamaterial-based RF-MEMS strain sensors that incorporate multiple split ring resonators (SRRs) in a compact nested architecture to measure strain telemetrically. Also, we showed biocompatibility of these strain sensors in an animal model. With these devices, our bioimplantable wireless metamaterial sensors are intended to enable clinicians to quantitatively evaluate the progression of long bone fracture healing by monitoring the strain on the implantable fracture fixation hardware in real-time. In operation, the transmission spectrum of the metamaterial sensor attached to the implantable fixture is changed when an external load is applied to the fixture, and from this change, the strain is recorded remotely. Employing telemetric characterizations we reduced the operating frequency and enhanced the sensitivity of our novel nested SRR architecture compared to the conventional SRR structure. The nested SRR structure exhibited a higher sensitivity of 1.09 kHz/kgf operating at a lower frequency compared to the classical SRR that demonstrated a sensitivity of 0.72 kHz/kgf. Using soft tissue medium, we achieved the best sensitivity level of 4.00 kHz/kgf with our nested SRR sensor. Ultimately, the laboratory characterization and *in vivo* biocompatibility studies support further development and characterization of a fracture healing system based on implantable nested SRR.

## 6.1.1. Introduction

The ability to telemetrically measure strain is important in many aspects of daily life. But such a task brings about important challenges. In many sectors such as in civil engineering, measuring the strength of materials (e.g., concrete) remotely in real time will help us to understand their transient structural behavior better (e.g., before and after an earthquake). Real-time measurement of the flexural rigidity of aircraft components during service in avionics is also an important application of telemetric strain sensing. Another unrealized, yet critical, application area is human medicine.

One important clinical issue in which we are currently interested is objectively monitoring the healing processes of fractured long bones [1]. Orthopaedic extremity injuries currently present a large medical and financial burden to both the United States and world-wide communities as can be seen in [2]. Severely comminuted fracture patterns, those commonly seen in high energy fractures, are difficult to treat due to the inherent absence of mechanical support through the native osseous tissue. In these cases, the implanted hardware (intramedullary rods, bone plates, screws, etc.) must assume the total mechanical load in the early post-operative term, which frequently results in an aberrant course of healing and the onset of delayed union or non-union. The most common treatment for these complications is additional surgery. These types of orthopaedic injuries require prolonged time before patients return to full activity [3].

Approximately six million long bone fractures are reported per annum in the United States. Surprisingly, approximately 10% of these fractures do not heal properly. Though the exact mechanism through which the healing progression becomes impaired is poorly understood, many of these non-unions or pseudoarthroses result when there is a severe or communited condition that does not proceed through a stabilized (intramembranous ossification) healing pathway [4]. Currently, clinicians may monitor healing visually by radiographs, and may examine the mechanical condition of the union through manually bending the bone at the fracture [5]. Unfortunately, the course of aberrant fracture healing is not easily diagnosed in the early time period when standard radiographic information of the fracture site is not capable of discriminating the healing pathway. Reference 6 shows us that manual assessment of fracture healing is also subjective and, therefore, inadequate as a diagnostic tool in the early stages of healing.

It has been shown in animal models that healing is critically important in the early time period. Animal studies have demonstrated that the callus and bone assume an increasing proportion of the load as healing proceeds, reducing the load carried by the implanted hardware [1]. However, to date, many of the technologies that seek to exploit this bone-implant load sharing phenomena have been considered too large in dimension or involve implantation of an associated power

supply. Previous investigations have been successful in determining forces in the hip [7]-[9], spine [10]-[12], and femur [13], [14]. However, due to the relatively large size of the sensors and associated hardware (signal conditioning, modulation, etc.), most of the aforementioned telemetry systems have been implanted inside of joint replacement components or bulky internal fixators. The result is that these devices have produced data that has been useful in the understanding of bone-implant loading, but have not been advantageous for large scale implementation as diagnostic and prognostic tools. Also, due to the complexity of the designs and requisite interconnectivity, manufacture of these systems could only be performed on a custom basis. The resulting expense could not justify their large scale manufacture.

To overcome the aforementioned shortcomings, we have developed radio frequency (RF) micro-electro-mechanical (MEMS) strain sensors that take advantage of the recent advances in metamaterials. To date metamaterials have been extensively investigated and exploited for various applications [61]-[66], [69]-[71], [73], [93]-[94]. In the previous literature, some of these applications include achieving negative refraction [65]-[66], [93], obtaining plasmons using nanowires [71], making metamaterial antennas [70], focusing light [73], cloaking [94], and building superlenses [69]. For metamaterials, sensing opens up a new direction where metametarials may provide unique benefits.

These SRR based sensors are passively powered devices (with no implantable power source), which we implement to monitor the surface bending strains on implanted fracture fixation hardware. Another important feature of these wireless sensors is that they do not require an internal-external physical connection to sense and transmit *in vivo* biological data. Finally, the miniaturization of these metamaterial-based sensors allows for their use in various implant applications that otherwise would not be possible. As the SRR based sensor displays a characteristic resonance frequency under no load, by measuring the magnitude of operating frequency shift under applied load, we are able to delineate the bending strain incurred in the fixation hardware and intend to relate this information to the progression of fracture healing.

For the sensing operation, four criteria are important and demonstrate the quality of the sensor. Firstly, the sensor must have a low enough operating frequency (sub GHz range) to avoid the background absorption of soft tissue. This poses a significant challenge as conventional fracture fixation devices have limited area to which the sensors can be affixed and such reduced space tends to increase the operating frequency of the sensor. This, in turn, undesirably increases the background absorption of human body (soft tissue). At higher frequencies, the soft tissue limits the penetration depth of electromagnetic waves. Therefore, it is required to maintain a small layout of the sensor while decreasing its operating frequency as much as possible.

Secondly, the sensors must emit a strong and measurable read-out signal with sharp enough resonance behavior (high enough quality-factor [Q-factor]) to accurately track the shift in transmission spectra. The third criterion pertains to the linearity of sensing, which is related to the quality factor of the sensor. A higher Q-factor leads to a higher signal to noise ratio (SNR), which reduces errors in the measurement (e.g., from the network analyzer) and decreases the error. The fourth criterion is sensor sensitivity. Since there are a limited number of data points in one frequency scan of the network analyzer, it is easier to resolve smaller shifts in the transmission spectra in response to the externally applied load when the sensitivity is higher. With the same level of induced strain, higher sensitivity yields larger shifts in transmission.

Metamaterials provide the ability to make better wireless sensors compared to conventional RF structures (e.g., spiral coils) because of their advantages over conventional structures with respect to four criteria listed above. The benefits of SRRs in telemetric sensing mainly stem from their unique structure, which features gaps (splits). Because of these gaps, SRRs exhibit lower resonance frequencies per unit area compared to spiral coils. This is critically important for bioimplant strain sensing within a limited space and in soft tissue environment. Furthermore, SRRs yield deeper and sharper dips at resonance in their transmission spectra compared to the spiral structures. The gaps of a SRR have much higher electric field density, which makes the resonance stronger and leads to a higher Q-factor, and, in turn, a higher signal-to-noise ratio. This makes the SRR sensor more linear compared to the spiral coil sensor. As a final consequence of gap presence in the SRRs, when an external load is applied, the change in the

additional capacitance further shifts the operating frequency, making the SRR more sensitive compared to the spiral structure. In our previous work as such, we used a single split ring resonator (SRR) structure in our strain sensor [58].

In this chapter, we present nested metamaterial-based strain sensors that are designed and fabricated to incorporate multiple SRRs in a compact nested architecture on a single chip to achieve significantly enhanced sensitivity in telemetric sensing. This architecture introduced for implant sensing features substantially more gaps compared to the structure of a conventional SRR. This decreases the operating resonance frequency of the resulting nested SRR sensor compared to the classical SRR sensor. Moreover, when the external load is applied, the capacitance of our nested SRR sensor is changed to a greater degree than the classical SRR, resulting in larger shifts in the transmission spectrum. This makes the nested SRR more sensitive than classical SRR in sensing.

Here we present the design, fabrication and characterization of our nested-metamaterial based RF-MEMS strain sensors and compare the telemetric sensing operation of the classical SRR and nested SRR based sensors in telemetric sensing. Further, we characterize the site-specific biocompatibility and wound-healing response elicited against these sensors in a small animal model. Finally, we present the proof-of concept telemetric demonstration of these nested SRR sensors using soft tissue in vitro.

## 6.1.2. Design and Fabrication

Fig. 6.1.1(a)-(c) show schematics of three designs of conventional split ring resonators, with two gaps (in two turns) in Fig. 6.1.1(a) (classical SRR), with a single gap (in one turn) in Fig. 6.1.1(b), and with four gaps (in four turns) in Fig. 6.1.1(c). Here increasing the number of turns decreases the operating resonance frequency because of the increased number of gaps and thus increased capacitance. However, the total possible reduction in the resonance frequency is limited by the space available on the chip, as each turn takes up a considerable amount of space.

To make a compact sensor, we propose nesting of SRRs that share the same sides except for where the gap is located, as depicted in Fig. 6.1.1(d) (nested SRR). With many more gaps available in the nested SRR, the resonance frequency is further reduced, consequently resulting in an increase in sensor sensitivity.

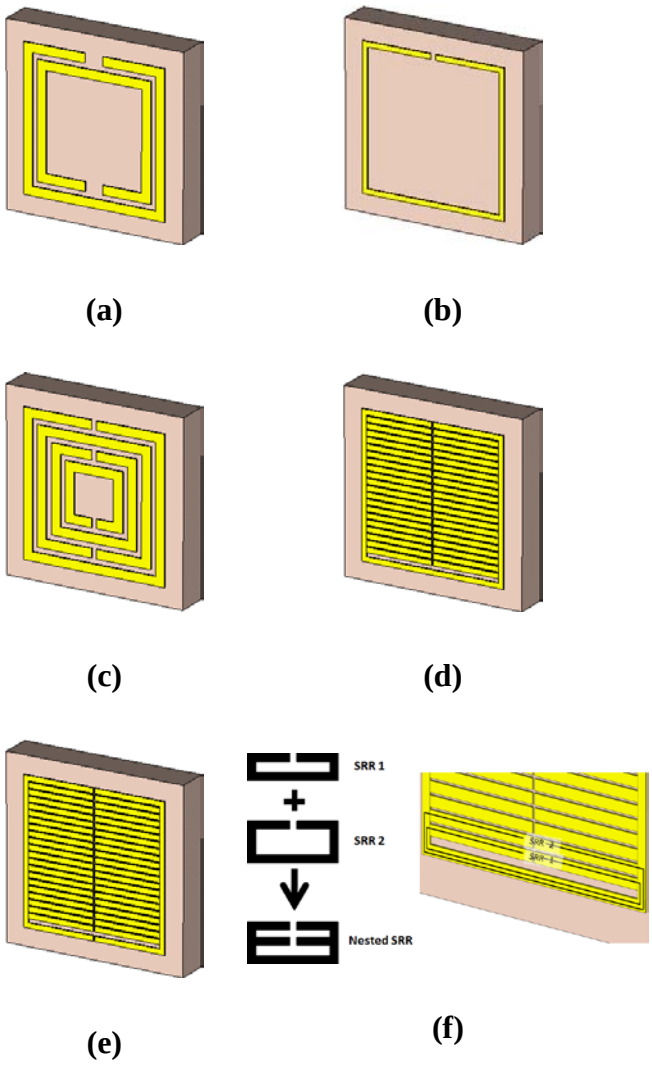


**Figure 6.1.1. Split ring resonator (SRR) with (a) two turns (classical SRR), (b) one turn, and (c) four turns; (d) our nested SRR architecture, (e) comb-like structure and (f) zoom-in of our nested SRR.**

A key feature of the nested architecture is the connected bottom line of the RF structure, which

confers continuity in our nested design. For comparison, Fig. 6.1.1(e) shows a pair of comb-like structures. These comb-like structures yield undesirably high resonance frequencies (even higher than that of the classical SRR) due to the discontinuous bottom line. As can be seen in the zoom-in of the nested SRR in Fig. 6.1.1(f), there are many SRRs nested together. These SRRs are added together with the same continuous bottom line, being the only difference with respect to Fig. 6.1.1(e).

For the classical SRR, we denote the total length of the outer coil as $L_{out}$, total length of the inner coil as $L_{in}$, width of the outer coil as $w_{out}$, width of the inner coil as $w_{in}$, spacing across the gap of the outer coil as $s_{out}$ and spacing across the gap of the inner coil as $s_{in}$. These parameters are depicted in Fig. 6.1.2(a). In the context of a design with fixed chip size (constant $L_{out}$), increasing $L_{in}$ decreases the resonance frequency. But making $L_{in}$ too much closer to $L_{out}$ decreases Q-factor due to the increased parasitic capacitance. Increasing $L_{in}$ increases the capacitance between substrate and metal ($C_{diel}$), decreasing the resonance frequency. Increasing $w_{in}$ and $w_{out}$, increases the capacitance between gaps ($C_{gap}$) as well as $C_{diel}$, which decreases the resonance frequency. Increasing $s_{in}$ and $s_{out}$ decreases $C_{gap}$, thus increasing the resonance frequency.

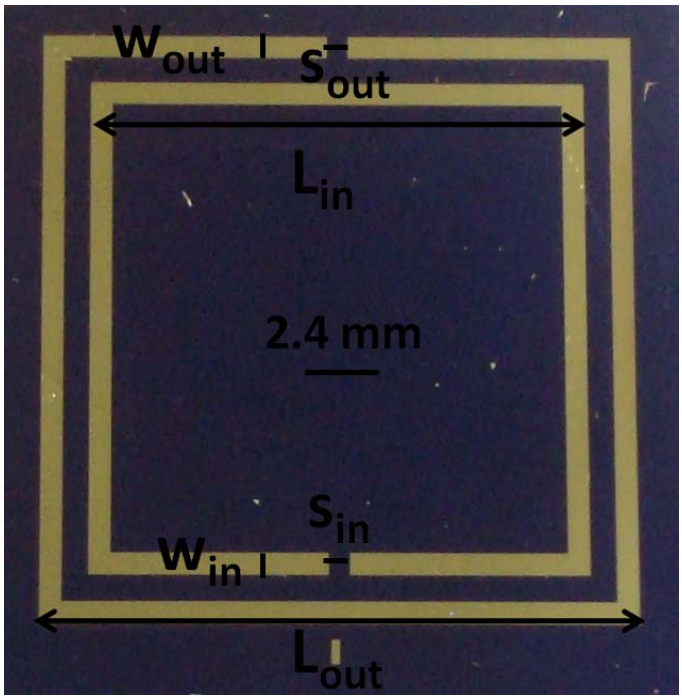


**(a)**

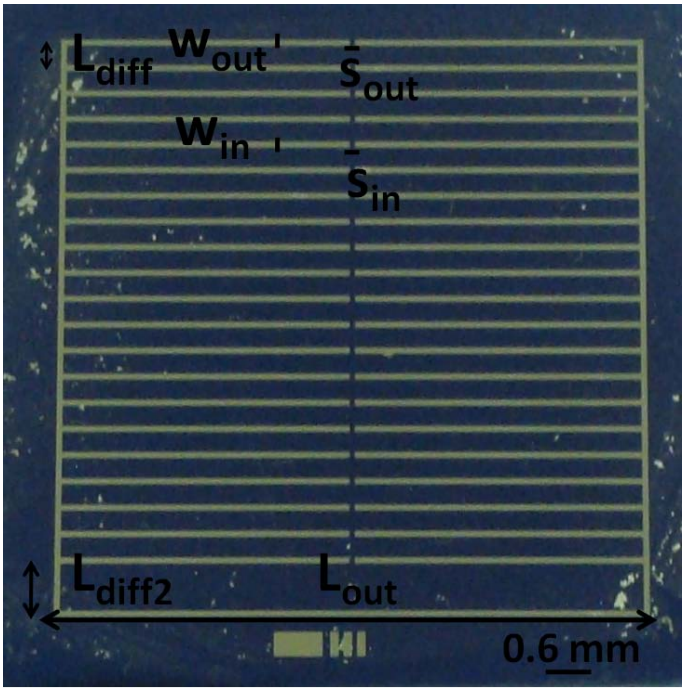


**(b)**

**Figure 6.1.2. Plan view pictures of (a) the classical SRR structure and (b) our nested SRR structure.**

The design parameters of the nested SRR are shown on a fabricated sample in Fig. 6.1.2(b). $L_{diff}$ is the distance between the combs and $L_{diff2}$ is the distance between the bottom line and the bottom comb teeth. The width of the top comb teeth is $w_{out}$, and the width of the nested comb teeth is $w_{in}$. The spacing across the gap of top comb teeth is $s_{out}$ and that of the others is $s_{in}$. $L_{out}$ is the total length of the structure. For the design parameters, the same conditions as in classical SRR apply in general. Increasing $w_{in}$ and $w_{out}$ decreases the resonance frequency. Increasing $s_{in}$ and $s_{out}$ increases the resonance frequency. If the width is much greater than the spacing, then the parasitic capacitance dominates so the Q-factor decreases. Therefore, we carefully choose the ratio of the width to the spacing.

The most important parameter for determining the resonance frequency of the nested SRR is the number of comb teeth (N) in the design. As N increases, both $C_{gap}$ and the $C_{diel}$ increase, thus decreasing the resonance frequency. Another parameter of interest in the nested SRR is $L_{diff}$. If we increase $L_{diff}$, then we decrease N. Subsequently, $C_{gap}$ and $C_{diel}$ are decreased, thereby increasing the resonance frequency. However, $L_{diff}$ should be greater than or equal to the width, otherwise the parasitic capacitance dominates. $L_{diff2}$ is another important parameter. We decrease $L_{diff2}$ as much as possible to decrease the resonance frequency since our goal is to maximize N. If $L_{diff2}$ is increased, then N is decreased. Therefore, $C_{gap}$ and $C_{diel}$ are decreased and the resonance frequency is increased. We make $L_{diff2}$ greater than or equal to $2L_{diff}+w_{in}$ so that we do not ruin the sequence of the combs and the parasitic capacitance does not dominate to decrease Q-factor.

The dielectric layer is also an important factor in our design. To have sufficient capacitance between the metal and the substrate, which serves as the distributed capacitance, we used a dielectric layer with a high dielectric constant [31]. On the other hand, to minimize the loss, a low-loss dielectric is required. Therefore, $Si_3N_4$ with a relative dielectric constant of 8 and a loss tangent of $5 \times 10^{-4}$ was chosen as the dielectric film to satisfy these conditions. Its film thickness was set to 0.1 $\mu$m to confer maximum capacitance over the minimum area.

The metal type and substrate used in the design are also critical, particularly for biocompatibility. We used Au as the metal layer and Si as the substrate. We chose $Si_3N_4$ as the dielectric layer also

because it is biocompatible [31]. For the fabrication process, we first deposited 0.1 µm thick $Si_3N_4$ onto our silicon substrate by plasma enhanced chemical vapor deposition (PECVD). Then by using standard lithography, metal evaporation, and lift-off, we deposited and patterned a 0.1 µm thick Au film to make our sensors. The design parameters for the optimized classical SRR and the optimized nested SRR used in the current study are provided in Table 6.1.1 and Table 6.1.2.

**Table 6.1.1. The parameters of classical SRR.**

| $L_{out}$ (mm) | $L_{in}$ (mm) | $w_{out}$ $w_{in}$ (mm) | $s_{out}$ $s_{in}$ (mm) | $t_{film}$ (µm) | $t_{metal}$ (µm) |
|---|---|---|---|---|---|
| **22.2** | **18.6** | **0.8** | **0.8** | **0.1** | **0.1** |

**Table 6.1.2. The parameters of nested SRR.**

| $L_{out}$ (mm) | $w_{out}$ $w_{in}$ (mm) | $s_{out}$ $s_{in}$ (mm) | $L_{diff}$ (mm) | $L_{diff2}$ (mm) | $t_{film}$ (µm) | $t_{metal}$ (µm) | N |
|---|---|---|---|---|---|---|---|
| **22.2** | **0.2** | **0.2** | **0.8** | **1.8** | **0.1** | **0.1** | **20** |

# 6.1.3. Experimental Characterization

In this section, we characterized differences in telemetric strain sensing ability between the classical SRR and nested SRR based sensors. We then evaluated the biocompatibility of our sensors over a six month time period in a small animal model. Finally, we demonstrated telemetric operation in soft tissue using our nested SRR sensor as a proof-of-concept demonstration for implant applications.

*Comparison of Classical and Nested SRR Strain Sensors*

We experimentally characterized the metamaterial based sensors using a custom-design mechanical testing setup. In the current study, a uniaxial traction force was applied in a controlled manner to a polyamide beam rigidly coupled to a load cell and actuator as shown in Fig. 6.1.3(a). Using this apparatus constructed at Bilkent University, loads were applied incrementally up to 300 kgf. The classic SRR and the nested SRR sensors were rigidly affixed to the polyamide beams with hard epoxy prior to testing.

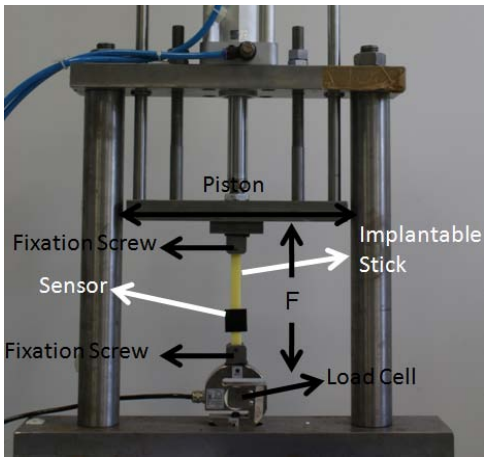


**(a)**

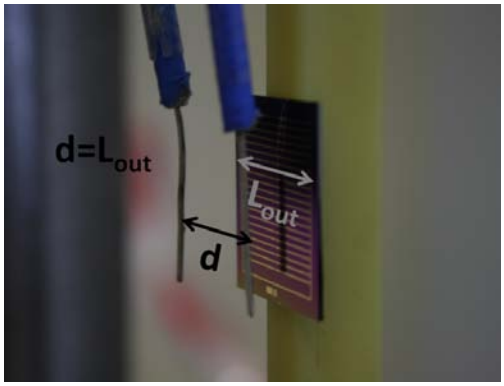


**(b)**

**Figure 6.1.3. (a) Mechanical apparatus and (b) coaxial probe antennas.**

Antennae made of coaxial probes with the same ground to decrease the noise during characterization were used to measure the change in RF spectrum of the loaded sensors during

testing (Fig. 6.1.3(b)). The length of these probes was set to 2.5 cm, which was comparable to the size of our sensors. Because our sensors are small in size ($\lambda_o/30$ - $\lambda_o/25$) in comparison to their operating wavelength, it was rather difficult to use standard antennas with sizes comparable to our sensors to measure their transmission spectra. The distance between these probe antennas was set equal to $L_{out}$ and they were placed 0.5 cm away from the sensor as shown in Fig. 6.1.3(b). In this configuration, the best signal is obtained with the probes parallel to the sensor. All these distance parameters were kept fixed throughout the calibration process and characterization process. For calibration purposes, the transmission of the polyamide beam was measured first with no sensor chip attached. Subsequently the same measurement was repeated with the sensor attached under no load and then also following application of discrete tensile loads. Transmission spectra referenced relative to the no sensor condition were obtained as a function of the applied load.

Relative transmission spectra (in dB) are presented in Fig. 6.1.4 and Fig. 6.1.5 for the classical SRR and nested SRR sensors, respectively, with respect to the case of no sensor in semi-log scale. Under no load, the operating frequency of the classic SRR was 529.8 MHz. At this point, the size of this classical SRR sensor corresponded to $\lambda_o/25.5$. With the applied load, the operating frequency decreased as seen in Fig. 6.1.4(a) and 6.1.4(b). Under the applied tensile load, the gaps of SRR are decreased, hence $C_{gap}$ is increased. Also the dielectric area between substrate and metal layer is increased, thus $C_{diel}$ is increased [39]. Fig. 6.1.4(c) plots the operating frequency shift (with respect to the case of no load) as a function the applied load and indicates a sensitivity of 0.723 kHz/kgf for the classic SRR. Fig. 6.1.4(d) presents the induced strain (in microstrain) as a function of operating frequency shift. Here Young's modulus of the cast polyamide beam was taken to be 2.37 GPa, which is separately verified using a wired strain gauge (Tokyo Sokki Kenkyujo Co., Ltd. Strain Gauges with a gauge factor of 2.1). This SRR sensor demonstrates a sensitivity of 0.0259 kHz/microstrain. In Fig. 6.1.4(e), we observed that this sensor had less than 500 microstrain error, which corresponded to 16% error as shown in Fig. 6.1.4(f).

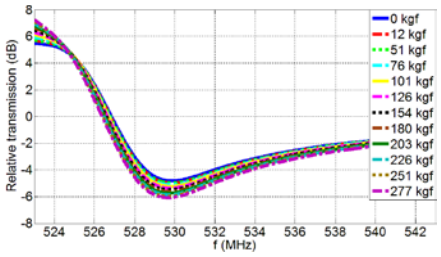
Relative transmission (dB)
f (MHz)
0 kgf
12 kgf
51 kgf
76 kgf
101 kgf
126 kgf
154 kgf
180 kgf
203 kgf
226 kgf
251 kgf
277 kgf

**(a)**

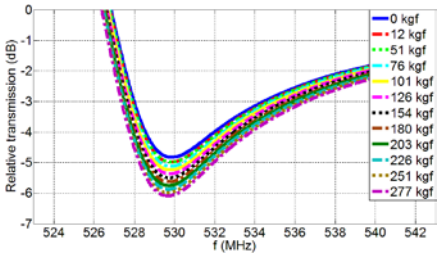
Relative transmission (dB)
f (MHz)
0 kgf
12 kgf
51 kgf
76 kgf
101 kgf
126 kgf
154 kgf
180 kgf
203 kgf
226 kgf
251 kgf
277 kgf

**(b)**

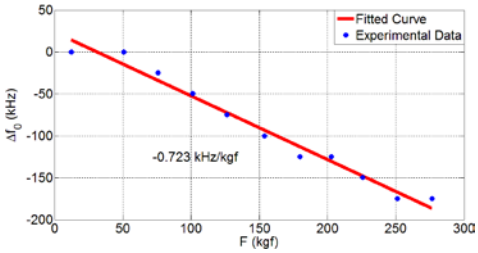
Fitted Curve
Experimental Data
-0.723 kHz/kgf
Δf0 (kHz)
F (kgf)

**(c)**

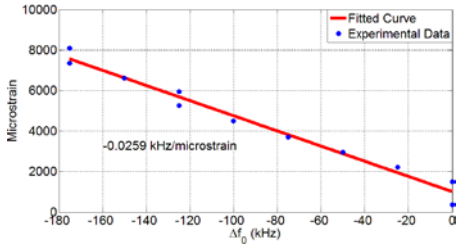
Fitted Curve
Experimental Data
-0.0259 kHz/microstrain
Microstrain
Δf0 (kHz)

**(d)**

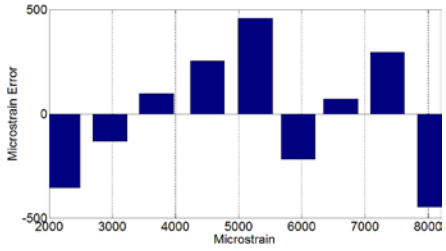
Microstrain Error
Microstrain

**(e)**

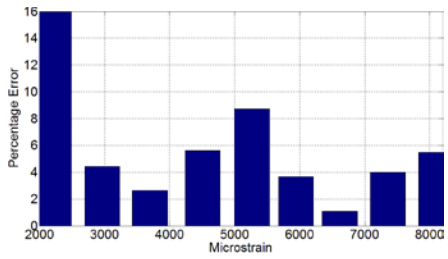


**(f)**

**Figure 6.1.4. Experimental characterization of the classical SRR sensor under tension: (a) relative transmission spectra, (b) zoom-in of the transmission shift, (c) frequency shift ($\Delta f_o$) *vs.* applied load (F), (d) induced strain (microstrain) *vs.* frequency shift ($\Delta f_o$), (e) error (in microstrain), and (f) error percentage.**

Transmission spectra of our novel SRR structure (nested SRR) for different levels of the applied load are illustrated in Fig. 6.1.5(a) and with zoom-in in Fig. 6.1.5(b). Here the operating frequency was 506.2 MHz under no load, which was lower than that of the classical SRR. The size of this nested SRR corresponded to $\lambda_o/26.7$. Fig. 6.1.5(c) plots the change in the operating frequency with respect to the case of no load as a function of the applied load and indicates a sensitivity of 1.09 kHz/kgf. The sensitivity of the nested SRR was significantly increased compared to the classical SRR as a result of the multiple gaps used in the nested SRR. Fig. 6.1.5(d) plots the strain *vs.* frequency shift demonstrating a sensitivity of 0.0369 kHz/microstrain. In Fig. 6.1.5(e), the nested SRR sensor had less than 600 microstrain error, corresponding to less than 16% error in Fig. 6.1.5(f). The errors of the nested SRR sensors are nearly the same as those of the classical SRR. However, the nested SRR sensor exhibited reduced operating frequency and increased sensitivity.

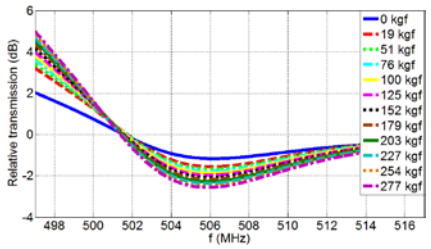
Relative transmission (dB)
f (MHz)
0 kgf
19 kgf
51 kgf
76 kgf
100 kgf
125 kgf
152 kgf
179 kgf
203 kgf
227 kgf
254 kgf
277 kgf

**(a)**

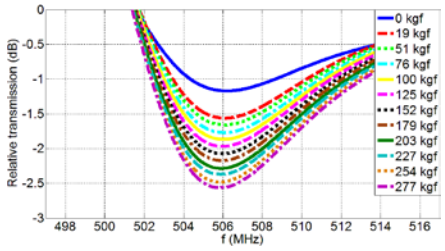
Relative transmission (dB)
f (MHz)
0 kgf
19 kgf
51 kgf
76 kgf
100 kgf
125 kgf
152 kgf
179 kgf
203 kgf
227 kgf
254 kgf
277 kgf

**(b)**

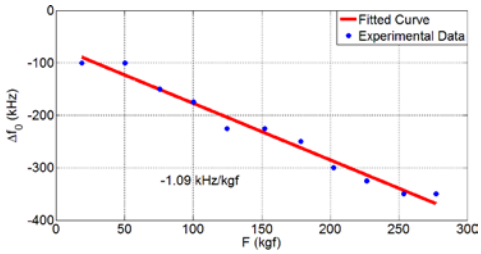
Fitted Curve
Experimental Data
-1.09 kHz/kgf
Δf0 (kHz)
F (kgf)

**(c)**

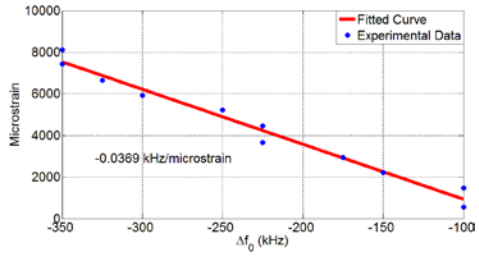
Fitted Curve
Experimental Data
-0.0369 kHz/microstrain
Microstrain
Δf0 (kHz)

**(d)**

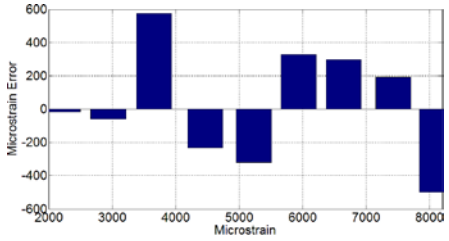
Microstrain Error
Microstrain

**(e)**

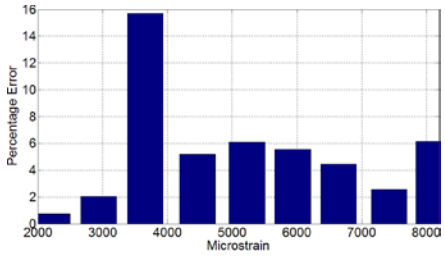


**(f)**

**Figure 6.1.5. Experimental characterization of the nested SRR sensor under tension: (a) relative transmission spectra, (b) zoom-in of the transmission shift, (c) frequency shift ($\Delta f_0$) *vs.* applied load (F), (d) induced strain (microstrain) *vs.* frequency shift ($\Delta f_0$), (e) error (in microstrain), and (f) error percentage.**

*Bio-compatibility Experiments of Our Sensors*

New Zealand white rabbits (Harlan Inc., Indianapolis, IN) were chosen as an appropriate animal model to investigate the site-specific biocompatibility of our MEMS sensors due to their size and ability to house multiple sensor chips. A total of four rabbits each implanted with 4 sensors and 2 control material implants (6 implants / rabbit; 16 sensors and 8 controls total) were used to investigate the biocompatibility in accordance with ASTM Standards F981-04 and F763-04. Animals were humanely euthanized six months post-operatively at which time critical gross pathology and microscopic evaluation of the implant sites for an implant-associated tissue reaction was pursued. This studies were supervised by our collaborator Dr. Christian Puttlitz.

This study was approved by the Institutional Animal Care and Use Committee (IACUC #07-057A-01) at Colorado State University. New Zealand white rabbits were placed on a constant temperature-heating pad (32 to 37°C), and pre-medicated and sedated with intramuscular acepromazine (1 mg/kg) and anesthetized by inhalation of 4% isoflurane delivered after intubation with a cuffed 3 mm endotracheal tube (Harvard Apparatus Dual Phase Control Respiratory Pump-Canine, Harvard Apparatus Co., South Natic, MA). Respiration was accomplished with a tidal volume of 15 ml/kg and frequency of 20-30/min. The peak airway pressure was 20 $cmH_20$. Anesthesia was maintained by 1.5% isoflurane.

Prior to surgery, all implant sensors were terminally sterilized via two cycles of autoclave for 25 min/10 min dry at 121°C. The surgical sites were denuded of all hair on both sides of the spinal

column. The skin was swabbed lightly with diluted alcohol and dried prior to sample implantation. Each rabbit received six (n=6) sterilized samples (four test materials and two controls) each implanted in individual sites of the lumbar paravertebral musculature. Two sensor chips (5 mm x 5 mm) and one control specimen (aluminum oxide, $Al_2O_3$; ASTM F603-00) were placed parallel to and on either side of the spinal column approximately 2.5 to 5 from midline and 2.5 cm apart from each other resulting in a total of 3 implants per side.

Animals were euthanized six months postoperatively by intravenous injection of sodium pentobarbital (150 mg/kg). This method is consistent with the recommendations of the Panel on Euthanasia of the American Veterinary Medical Association. The tissue surrounding and overlying each implant, both for the sensor material and the $Al_2O_3$ control material, was macroscopically evaluated for evidence of internal and external lesions in accordance with a semi-quantitative scoring system developed in our laboratory. Each implant was then removed with an intact envelope (~ 4 mm) of surrounding tissue and fixed for 24 hours in 10% neutral buffered formalin. After fixation, each implant was removed from the tissue envelope and the tissue specimens were routinely processed, embedded in paraffin, sectioned at 5 μm, and stained with Hematoxylin and Eosin (H&E) for semi-quantitative evaluation of the cellular and tissue response to the sensor and control materials. Microscopic evaluation was performed by a single board certified pathologist who was blinded to the treatment groups so as to avoid observer bias.

The animal surgeries were uneventful and vital signs were normal. During convalescence, there were no complications resulting from the surgical procedure, no evidence of post-operative infection, and no mortality in the six-month survival period. Gross examination of tissue adjacent to these sensor materials did not reveal any visible signs of adverse reactions manifested as external or internal lesions to the test materials. No infection or inflammation was grossly noted in the musculature surrounding implanted materials.

Microscopic examination of the H&E stained slides confirmed that there was no adverse tissue reaction to the sensor materials either immediately adjacent to or peripheral to the implantation site as shown in Fig. 6.1.6. Examination of histological slides confirmed the absence of abnormal macrophage or lymphocytic cellular activity. Resultantly, inflammation scores for the

sensor and $Al_2O_3$ control materials were 0 ± 0 and 0 ± 0 (mean ± stdev), respectively. Minimal fibrosis was noted surrounding both the control and sensor materials (1.0 ± 0.5 and 0.94 ± 0.24, respectively) and the general toxicity score for the test and control materials was zero.

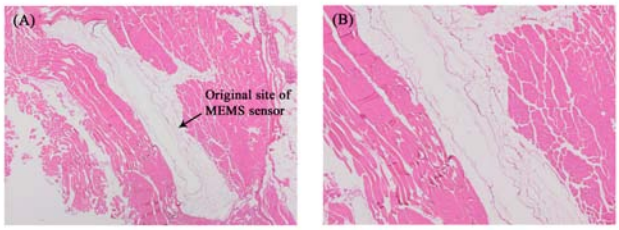


**Figure 6.1.6. 2x (A) and 4x (B) images of the H&E stained tissue adjacent to the implanted sensor. After six months *in vivo*, no evidence of inflammation or adverse tissue response was documented adjacent to any of the implanted sensors demonstrating adequate biocompatibility.**

*Soft Tissue Experiments*

After showing enhanced functional performance with the nested SRR sensor relative to the classic SRR design and demonstrating biocompatibility of our sensors, we investigated the fidelity with which we could detect the shift in transmission spectra in a scenario that more closely resembles the intended application of the device: one in which soft tissue separates the sensor and the antennae, as would be the case while monitoring bending strains on internal hardware in human patients (Fig. 6.1.7(a) and Fig. 6.1.7(b)). Fig. 6.1.8(a) and Fig. 6.1.8(b) depict the transmission spectra of the nested SRR with the soft tissue parameterized with respect to the applied load. In the soft tissue experiment, the operating frequency of the nested SRR was 474.2 MHz under no load, which was lower than that measured in free space (Fig. 6.1.5). This is an exact consequence of the soft tissue as it has a very high dielectric constant of 56.445 around 500 MHz [95] resultantly decreasing the resonance frequency of the device. The sensitivity of the sensor (Fig. 6.1.8(c)) under these test conditions was also increased to 4.00 kHz/kgf because the soft tissue helps to better focus electromagnetic waves compared to the free space because of its high dielectric constant at low frequencies. Consequently, the mechanical deformation under load affects the operating frequency more strongly, which leads to better sensitivity in the soft tissue.

**(a)** **(b)**

**Figure 6.1.7.** ***In vitro*** **characterization with soft tissue (a) in front view showing antennas (b) in back view showing the sensor.**

Using the soft tissue medium is advantageous for our sensing application since the operating frequency is lowered. It should be noted that the space between the antennae and soft tissue should be kept at an absolute minimum. If there is sufficient free space between them, then the antenna signal dramatically decreases. Also, in Fig. 6.1.8(d), we show the strain *vs.* operating frequency shift and obtain 0.17 kHz/microstrain sensitivity here. In Fig. 6.1.8(e), the nested SRR sensor had a maximum of 1500 microstrain error, corresponding to 35% error as shown in Fig. 6.1.8(f), in the soft tissue, which is larger than in the free space.

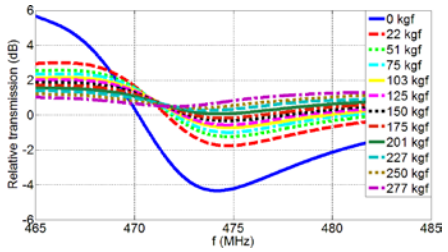
Relative transmission (dB)
f (MHz)
0 kgf
22 kgf
51 kgf
75 kgf
103 kgf
125 kgf
150 kgf
175 kgf
201 kgf
227 kgf
250 kgf
277 kgf

**(a)**

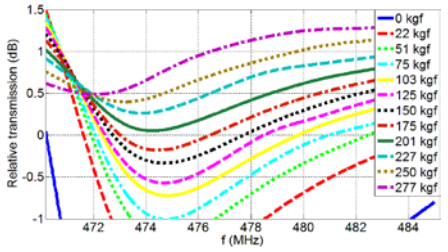
Relative transmission (dB)
f (MHz)
0 kgf
22 kgf
51 kgf
75 kgf
103 kgf
125 kgf
150 kgf
175 kgf
201 kgf
227 kgf
250 kgf
277 kgf

**(b)**

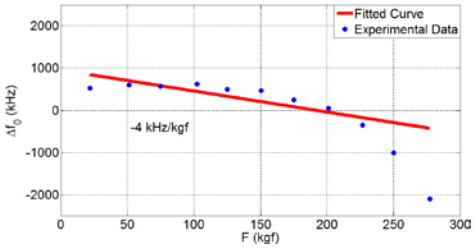
Fitted Curve
Experimental Data
-4 kHz/kgf
Δf0 (kHz)
F (kgf)

**(c)**

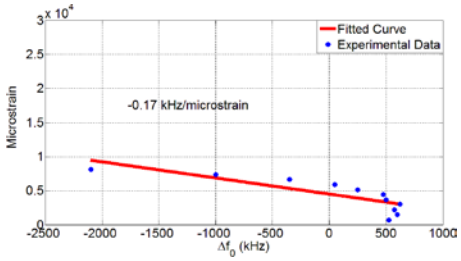
x 10^4
Fitted Curve
Experimental Data
-0.17 kHz/microstrain
Microstrain
Δf0 (kHz)

**(d)**

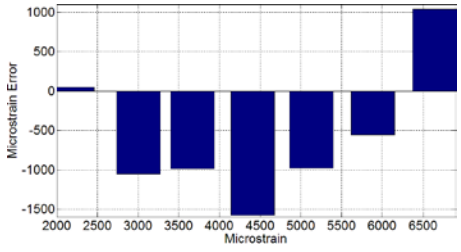
Microstrain Error
Microstrain

**(e)**

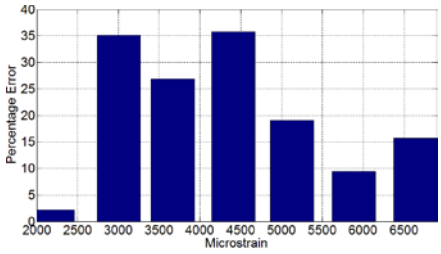


**(f)**

**Figure 6.1.8. Experimental characterization of the nested SRR sensor using soft tissue under tension: (a) relative transmission spectra, (b) zoom-in of the transmission shift, (c) frequency shift ($\Delta f_o$) *vs.* applied load (F), (d) induced strain (microstrain) *vs.* frequency shift ($\Delta f_o$), (e) error (in microstrain), and (f) error percentage.**

# 6.1.3. Conclusion

In conclusion, we designed, fabricated and characterized a novel nested SRR for implant strain sensing. We demonstrated that the nested SRR sensor outperforms the classical SRR sensor with regard to operating frequency and sensitivity, which was a direct result of the increased number of gaps in the nested architecture. The unloaded operating frequency of nested SRR (506.2 MHz) was decreased relative to the classical SRR (529.8 MHz) in the free space experiments. Further, the sensitivity of the nested SRR (1.09 kHz/kgf) was increased with respect to the classical SRR (0.72 kHz/kgf) in the free space.

We also demonstrated biocompatibility of our metamaterial sensors by implanting them into New Zealand white rabbits and observing no evidence of inflammation or adverse tissue response over a period of six months. As a first proof-of-concept demonstration using soft tissue in a situation that approximates the clinical condition, we demonstrated that the unloaded operating frequency and sensitivity of the nested sensor were 474.2 MHz and 4.00 kHz/kgf, respectively. These findings were a direct consequence of the interposed soft tissue, which exhibits a very high dielectric constant at the operating frequencies. The results presented herein support the continued development and characterization of a fracture healing system based on these implantable metamaterial sensors with nested architecture.

## 6.2 Further Investigation of Nested Metamaterial Design

In this section, we will investigate where the received signal and observed resonance result from during the operation of the sensor. We will show different experiments using different device architectures for the same structures with different device parameters, and also experiments with different building blocks of the sensor. We will explain the experimental configuration in detail and discuss the calibration method and the effect of soft tissue in our experiments.

In this section, we will consider two different nested metamatarial designs. The parameters of these Nested-1 and Nested-2 structures are listed in Table 6.2.1. The fabrication procedure of these devices is the same as in Section 6.1. Here we first performed experiments with Nested-1 structure under compression. The test material is cast polyamide and the sensor chip is attached to the test material. The calibration method is the same as we used in Section 6.1. In calibration, the transmission of the test material is first measured with no sensor chip attached. Subsequently, the same measurement is repeated with the sensor attached under no load and then also following application of discrete compressive loads. Transmission spectra referenced relative to the no-sensor condition are obtained as a function of the applied load. We show the resulting relative transmission spectra as in Fig. 6.2.1(a). We observe multiple resonances. We observe the shift of the first two modes of the resonances with the applied loads in Fig. 6.2.1(b). This suggests that these dips correspond to the resonance frequencies which can be meaningfully changed with mechanical loading.

**Table 6.2.1. The parameters of nested metamaterials.**

| | $L_{out}$ (mm) | $w_{out}$ $w_{in}$ (mm) | $s_{out}$ $s_{in}$ (mm) | $L_{diff}$ (mm) | $t_{film}$ (μm) | $t_{metal}$ (μm) | N |
|---|---|---|---|---|---|---|---|
| **Nested-1** | **22.2** | **0.04** | **0.04** | **0.04** | **0.1** | **0.1** | **276** |
| **Nested-2** | **5.55** | **0.01** | **0.01** | **0.01** | **0.1** | **0.1** | **276** |

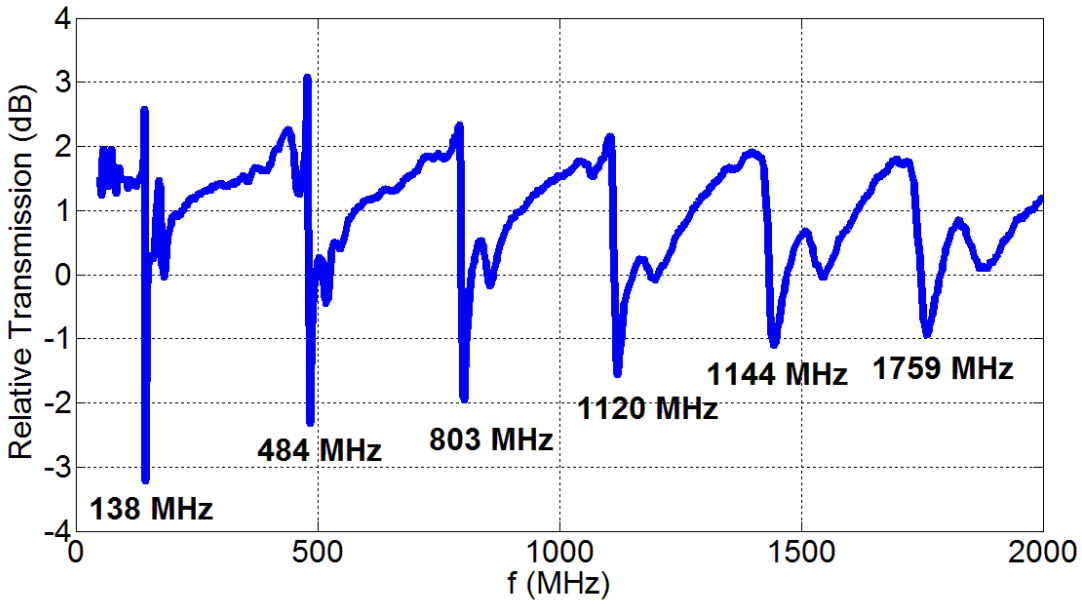


**Figure 6.2.1 Experimental relative transmission measurement of Nested-1 structure.**

We can see the shift of the first resonance in the range of 137 - 140 MHz in Fig. 6.2.2.

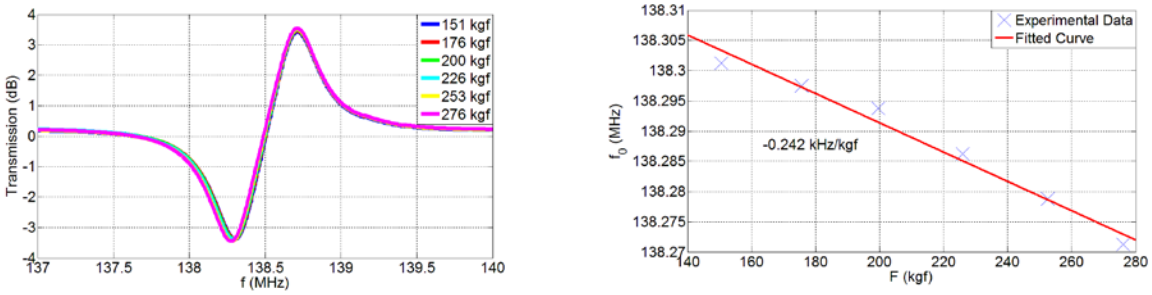


(a) (b)

**Figure 6.2.2 Experimental transmission measurement of Nested-1 structure in the range of 137 -140 MHz. (a) Transmission spectra (around the first resonance) under different applied loads and (b) F *vs.* $\Delta f_0$.**

For observing whether the signal is coming from the sensor, we made negative control group experiments with only substrate (but no sensor structure on it) as in Fig. 6.2.3 and with silicon plus the dielectric $Si_3N_4$ (but no sensor structure on them) in Fig. 6.2.4. We observed no meaningful sensing signal in these measurements. These negative control group studies indicate that the substrate and/or the dielectric film does not deliver a meaningful signal, and that a sensor

design made of a patterned metal film structure on top of the dielectric film laid on the substrate is required to observe resonance behavior meaningfully shifting under mechanical deformation.

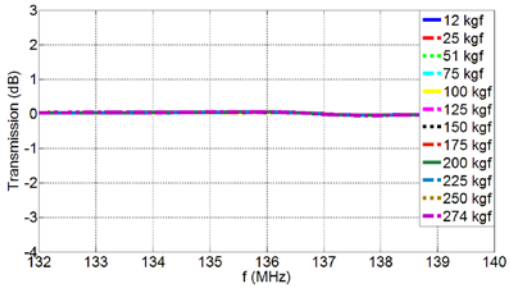


**Figure 6.2.3 Experimental transmission measurement of 2.5 cm × 2.5 cm silicon substrate (with no sensor structure on it) in the same frequency range of the first mode.**

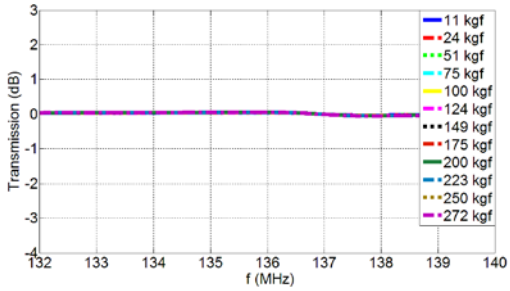


**Figure 6.2.4 Experimental transmission measurement of 2.5 cm × 2.5 cm silicon plus $Si_3N_4$ film on it (with no sensor structure on them) in the same frequency range of the first mode.**

We also performed experiments using structures with different design parameters in the same frequency range to see whether the resonance is coming specifically from this Nested-1 structure with 276 legs. We first tested the nested metamaterial structure with only 20 legs, which was previously used in Section 6.1. We observed no sensing signal from this structure in this frequency range as shown in Fig. 6.2.5. The resonance frequency of this structure is 500 MHz because of its fewer legs as was previously studied. We can also observe that by playing with the number of legs, one can change the resonance frequency of the resulting nested metamaterial. We find out that increasing the number of legs decreases resonance frequency as a result of increased gap capacitances with increasing leg number. We also performed experiments using Nested-1 structure but this time with its legs being distorted shown in Fig. 6.2.6. In this test structure, we placed a gap in the bottom metal line. We did not obtain any meaningful sensing

signal with this structure. We see that the bottom continuous metal line of the nested metamaterial is critically important for its proper operation.

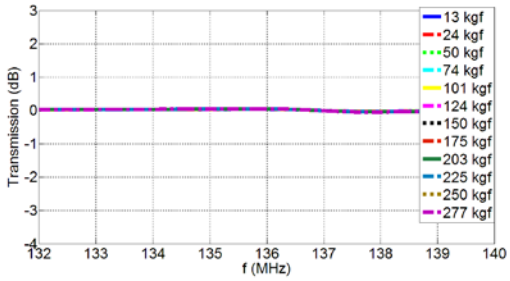


**Figure 6.2.5 Experimental transmission measurement of the sensor with 20 legs in the same frequency range of the first mode. (Its resonance is in the 500 MHz range.)**

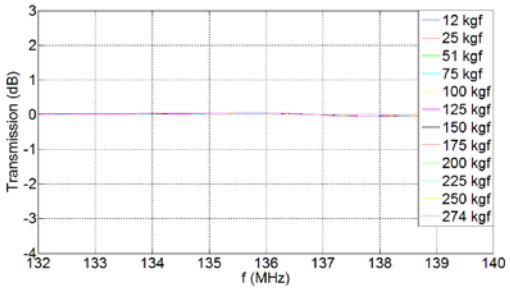


**Figure 6.2.6 Experimental transmission measurement of the distorted Nested-1 sensor with a gap in the bottom metal line in the same frequency range of the first mode.**

By applying load to the sensor, we also investigated the shift of the second resonance frequency as shown in Fig. 6.2.7. Observing the shift with applied loads in these two different resonance modes indicates that the resonance behavior of the sensor is critical in receiving meaningful sensing signal. We also repeated the same set of negative control group experiments for this second mode as in the first mode. Again, we observed no meaningful sensing signal using only silicon substrate (Fig. 6.2.8) or silicon plus the dielectric $Si_3N_4$ film on it (Fig. 6.2.9) in this frequency range, either.

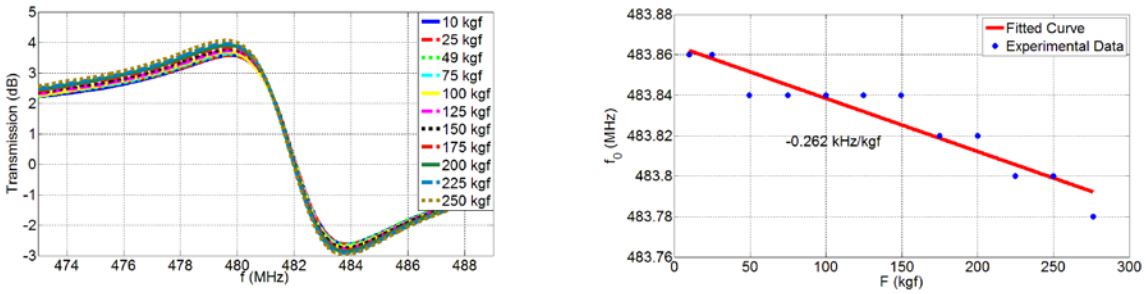


(a) (b)

**Figure 6.2.7 Experimental transmission measurement of Nested-1 structure in the proper range of 473-489 MHz. (a) transmission spectra (around the second resonance) under different applied loads and (b) F *vs.* $\Delta f_0$.**

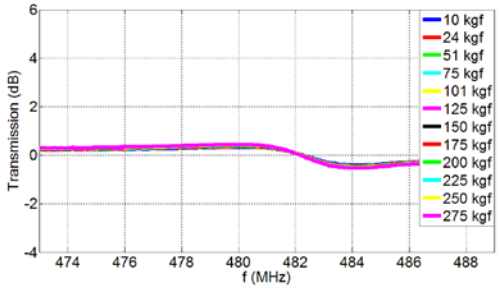


**Figure 6.2.8 Experimental transmission measurement of 2.5 cm × 2.5 cm silicon substrate in the same frequency range of the second mode.**

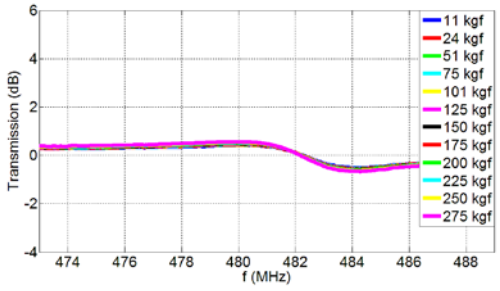


**Figure 6.2.9 Experimental transmission measurement of 2.5 cm × 2.5 cm silicon substrate plus $Si_3N_4$ film in the same frequency range of the second mode.**

We also conducted experiments using Nested-2 structure. In this set of experiments, there is a broken wood to experimentally simulate the broken bone and the stainless steel plate implant is fixed on two broken pieces of the wood as in the real case. We also changed the calibration method for this case. In real life, we cannot take the sensor out of the body first and then attach the sensor to the implantable plate to perform calibration. Because of this reason, we devised a new calibration method with the sensor still being on the implantable plate. In this calibration procedure, the transmission of the test material is first measured with the sensor chip attached but under no load. Subsequently the same measurement is repeated under different discrete compressive loads. Transmission spectra referenced with respect to the no load condition are obtained as a function of the applied load as shown in Fig. 6.2.10(a). We observe the resonance frequency shift of Nested-2 structure in Fig. 6.2.10(b). Again, we made negative control group experiments with the silicon substrate (Fig. 6.2.11) and silicon substrate plus the dielectric $Si_3N_4$ film (Fig. 6.2.12), which yielded no meaningful sensing signal. We also tested the flexible Nested-2 structure and observed meaningful shift of the resonance frequency as in Fig. 6.2.13.

We also performed negative control group experiments with only stick, vacuum tape plus gold and vacuum tape plus gold plus dielectric $Si_3N_4$ film, none of which returned a meaningful sensing signal as in the previous cases (in Fig. 6.2.14, Fig. 6.2.15, and Fig. 6.2.16). These experiments show that it is necessary to use a sensor chip to obtain meaningful data in response to mechanical loading.

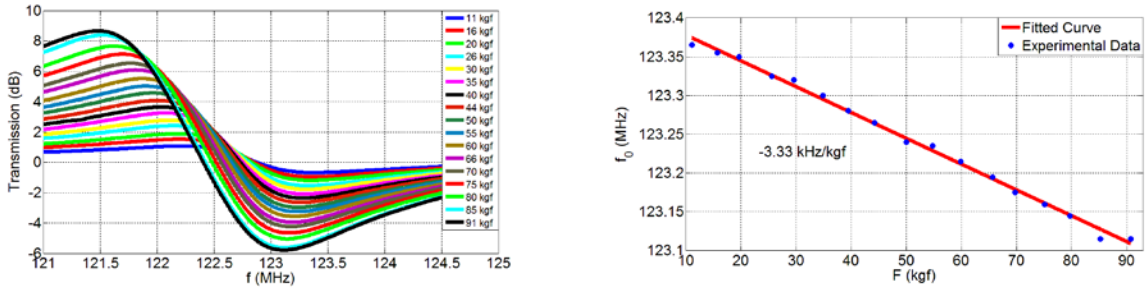


(a) (b)

**Figure 6.2.10 Experimental transmission measurement of Nested-2 structure. (a) Transmission spectra under different applied loads and (b) F *vs.* $\Delta f_0$.**

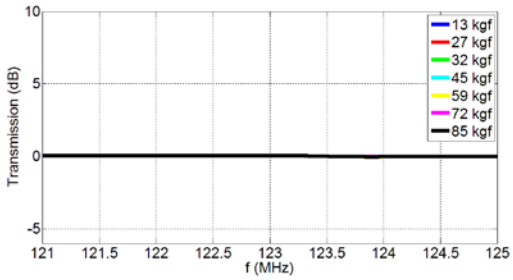


**Figure 6.2.11 Experimental transmission measurement of 0.8 cm × 0.8 cm silicon substrate.**

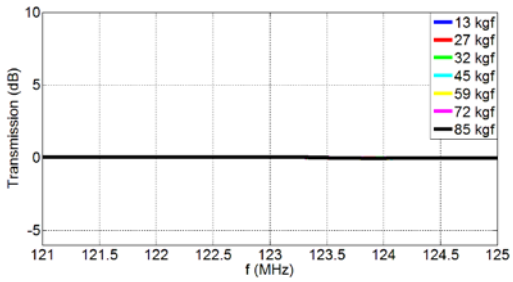


**Figure 6.2.12 Experimental transmission measurement of 0.8 cm × 0.8 cm silicon substrate plus $Si_3N_4$ film.**

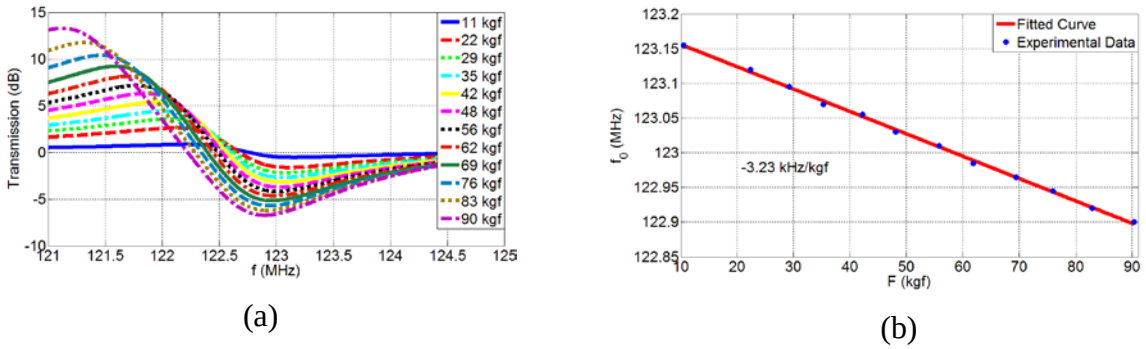


**Figure 6.2.13 Experimental transmission measurement of flexible Nested-2 structure. (a) Transmission spectra under different applied loads and (b) F *vs.* $\Delta f_0$.**

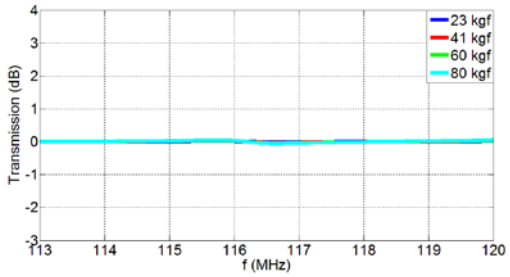


**Figure 6.2.14 Experimental transmission measurement of only stick.**

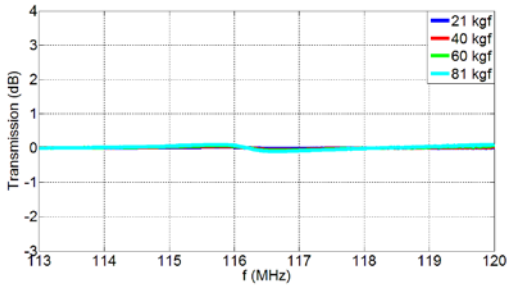


**Figure 6.2.15 Experimental transmission measurement of vacuum tape plus gold film.**

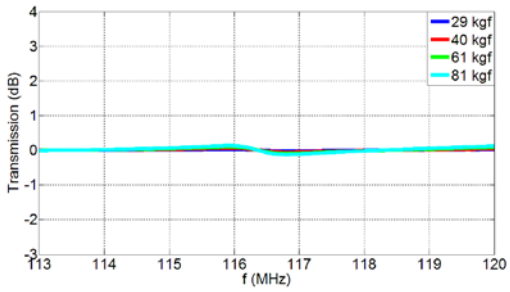


**Figure 6.2.16 Experimental transmission measurement of vacuum tape plus gold plus $Si_3N_4$ film.**

The metamaterial structure exhibits strong E-field between the gaps as was previously discussed and shown in Fig. 5.4.1. Here we also observe in Fig. 6.2.17 that metamaterial has a high electric energy density between the gaps and its surface current of is in the same line on resonance. These gaps are important for the resonance frequency shift as was shown in Section 5.4. We also performed a parametric study with metamaterials of different design parameters and obtained different resonance frequencies for each case. For example, we increased the resonance frequency of Meta-1 structure in Section 5.3 by decreasing the inner length while keeping everything else the same. Also, by decreasing the gap of Meta-1 structure alone, we increased the capacitance and decreased the resonance frequency of Meta-2 structure with respect to Meta-1 structure in Section 5.4.

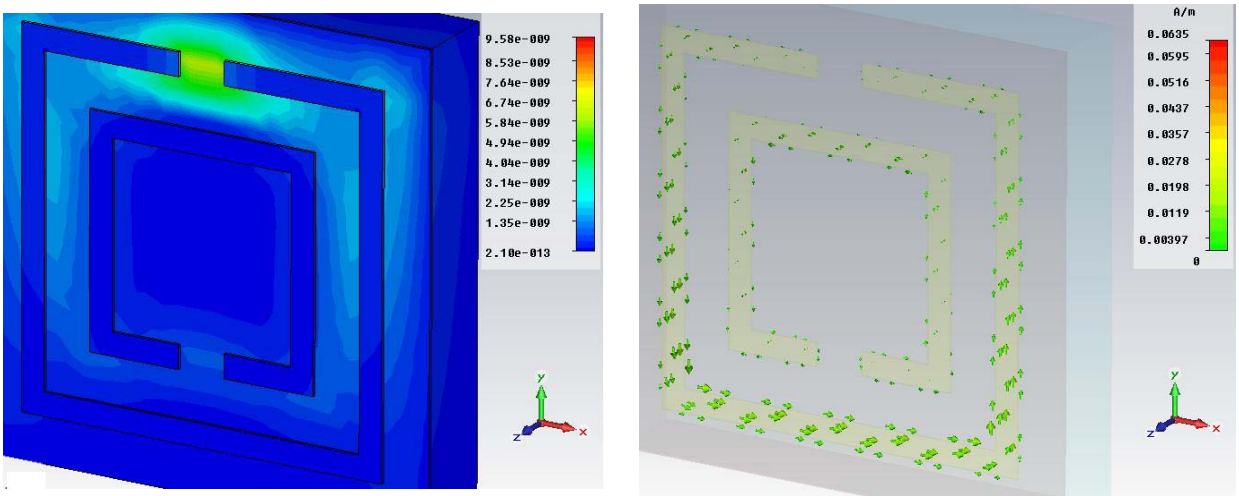


(a) (b)

**Figure 6.2.17 The simulated field maps of a meta-structure. (a) Electric energy density and (b) surface current distribution.**

We show the electric field ($\vec{E}$), magnetic field ($\vec{H}$) and the propagation direction ($\vec{k}$) in Fig. 6.2.21. To get a strong resonance, the H-field should go through the sensor [96]. Since the E-field can be expressed as $\vec{E} = |\sin(\theta)|\hat{\theta}$ in [97], the E-field is in the direction as shown in Fig. 6.2.18. The signal goes from one probe to another, and thus $\vec{k}$ is in the direction as illustrated in Fig. 6.2.18. Also from the relation of the electric field and magnetic field $\vec{k} \times \vec{E} = \vec{H}$ [98], we again find that H field goes through the sensor to get a strong resonance signal. If H-field goes through the sensor, the power of E-field is negligible; hence, any orientation of the sensor gives similar results. The gaps of the metamaterial structure increase the induced current density. Since we have multiple gaps in nested metamaterial, we observe strong resonance.

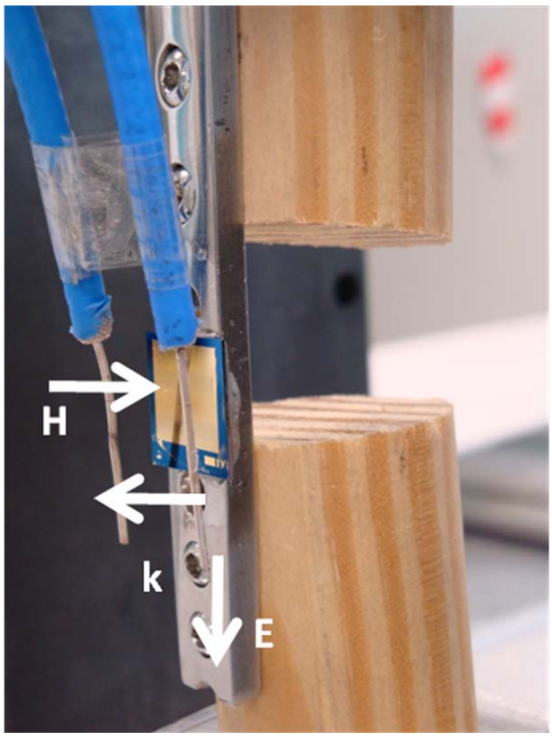


**Figure 6.2.18 $\vec{E}$, $\vec{H}$, and $\vec{k}$ configurations of the experimental setup.**

We also characterized the nested metamaterial sensor in Section 6.1 as an antenna by itself (although this particular nested metamaterial design that we implemented with a very thin dielectric film leads to loss through displacement current across the dielectric film). By wire

bonding the sensor to the connectors, we tested it as an antenna. Our nested metamaterial is of course lossy and very small compared to its wavelength. We show its reflection in Fig. 6.2.19(a), and its E-field radiation pattern in Fig. 6.2.19(b). From these results, we observe that its signal level decreases after $30^0$. This implies that one cannot get good signal levels with misalignments of the external antenna and the sensor above $30^0$.

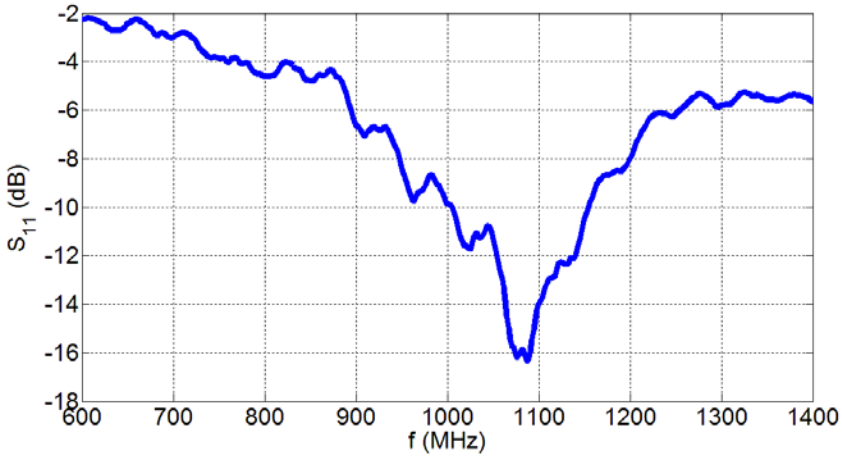


(a)

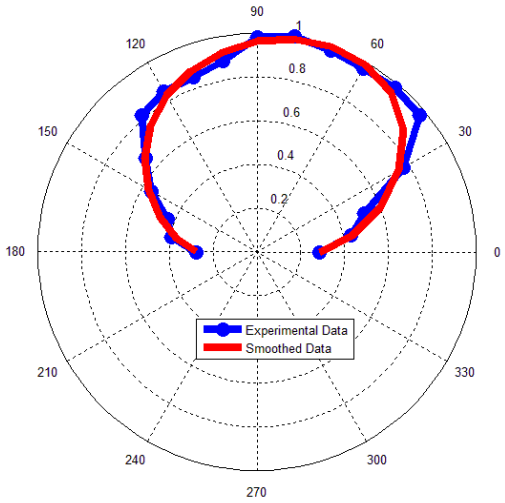


(b)

**Figure 6.2.19 Experimental measurement of our nested metamaterial chip as an antenna. (a) Its reflection spectrum and (b) E-plane radiation pattern.**

In these experiments, we place the sensor between two coaxial probes as the external antennas. Even when the size of the metamaterial chip is 1/3 or 1/4 of the size of the probe, this approach is effective. For example, when we use standard gain horn antenna, the cross-sectional area is high, and the cross-section of the antenna will not be comparable with the size of the sensor chip. Hence, EM wave is scattered. On the other hand, loop antennas act as point source and EM wave is again scattered off them. Because of this reason, it is useful to use loop antenna only for big slabs of metamaterials. It is better to use coaxial probes to examine the performance of small size metamaterial chips, although coaxial probes are weaker than the loop antennas in general.

We can also compare coaxial probe antennas with loop antennas in another perspective. In these experiments, we used two coaxial probe antennas operating in the reactive near-field region as the coupled transmitter and receiver antennas. We also performed similar experiments by using loop antennas instead of coaxial probes. The alignment of the sensor was much easier for the cases when we used the probe antennas as opposed to the loop antennas. For the loop antenna measurements, we had to move the two loop antennas individually and it was difficult to see the particular chip under test during the measurement. Also, it is easier to couple the probe antennas to the sensor compared to the loop antennas. Additionally, it may be difficult to use loop antennas because their physical sizes are larger and it is hard to place them close enough to receive good signal. Because of these reasons, we preferred using probe antennas instead of loop antennas in our experiments.

In soft tissue, it is important to decrease the operating frequency to receive a good signal. The soft tissue has a higher penetration depth and a lower absorption coefficient at lower operating frequencies. Because of this reason, decreasing the operating frequency to 100 MHz is critical. We could not get a good signal level across a thick body of soft tissue (over 1 cm) at 500 MHz using the sensor in Section 6.1. Moreover, the soft tissue has a higher dielectric constant compared to the air. At 100 MHz, the dielectric constant (relative permittivity) of the soft tissue is about 66, which is much higher than the air's (1). Also, when the sensor is between the two external antennas (two coaxial probes), it gives the best signal level. If we put the two probes further away, EM wave will have to come at an angle and the signal level will decrease. We

cannot get high enough signal levels when the distance between the probes and sensor is over 1 cm in the air as shown in Fig. 6.2.20. However, with soft tissue, we can receive a reasonable signal up to 20 cm separation in soft tissue. This is because the soft tissue environment has a higher dielectric constant (and a higher refractive index). Hence, we think that EM wave even for far distances comes at an angle almost equal to the angle when the sensor is close to the two external antennas. Indeed, inserting a high dielectric medium between the source and target is a used method for EM wave (or light) focused in a tighter spot.

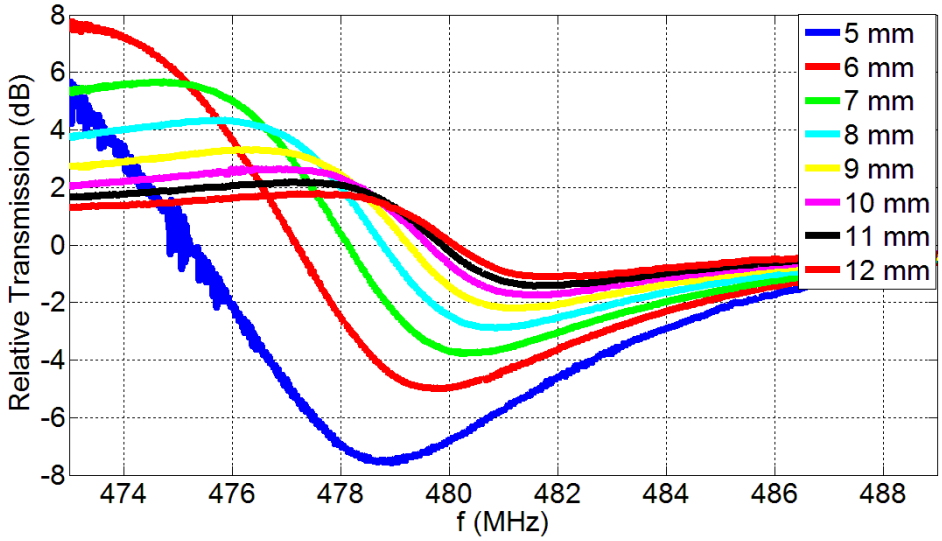


**Figure 6.2.20 Experimental transmission measurement of 2.5 cm × 2.5 cm nested metamaterial sensor chip at different distances from the external antenna. No meaningful sensing is possible after 1 cm in air.**

In our experiments, we take transmission measurements, either with respect to the stick (test material with no sensor) or with respect to the sensor under 0 kgf (no load). Thus, in our calibration method, we set the signal from the no-sensor stick or the no-load sensor to be 0 dB. Therefore, this 0 dB level is not an absolute value; it is only meaningful in the relative sense. Hence looking at the relative transmission of the sensor while we apply external load, the received signal level can exceed this artificial 0 dB level. The measured relative transmission spectra exhibit dips and peaks around this assigned 0 dB level. This is because of the probe antennas are not tuned. The two probes and the sensor are all coupled in the near-field region. That is, we cannot measure the real signal coming from the sensor alone because of the coupled

probes whatever calibration method is used and, hence, because of the un-tuned coupling between them, we will always see peaks and dips in transmission measurements. We also performed measurements using two uncoupled loop antennas such that the receiving antenna does not see the transmitting antenna. Because of the unsuitability of these loop antennas for small size metamaterial chips as explained above, we could however not obtain any meaningful sensing signal. For these reasons, the most convenient configuration in our experiments was the usage of a coupled pair of coaxial probes in the near field of our metamaterial sensor, which leads to meaningful relative transmission measurement for telemetric sensing purposes (but no absolute transmission level measurement).

## 6.3 Experiments with Nested Metamaterials Operating at Low Frequency

In this section, we will present experimental measurements with nested metamaterials at low frequency (135 - 140 MHz). In Section 6.1, we only obtained $\lambda_o/30$ electrical length of the sensor. Since nested metamaterials made it possible to easily adjust the operating frequency, we were able to decrease the electrical length of the sensor to $\lambda_o/400$. In 500 MHz experiments in Section 6.1, we received sensing signal only through 0.5 cm thick soft tissue; however, by decreasing the operating frequency, we were able to obtain sensing signal up to 20 cm thick soft tissue. The signal-to-noise ratio (SNR) received level of the signal was better around 100 MHz with 20 cm thick soft tissue compared to the SNR level of the signal in Section 6.1 at 500 MHz with 0.5 cm thick soft tissue. Additionally, we will demonstrate the miniaturization steps of the sensor in this section. We will also examine the sensing operation starting from the simplest case (sensor on the cast polyamide test material) to the real case (sensing in sheep's metatarsal, femur and spine).

### 6.3.1 Experiments with 2.5 cm × 2.5 cm sensor chip on cast polyamide implant

The fabrication procedure of the nested metamaterial, whose design parameters can be seen in Table 6.3.1, is the same as in Section 6.1. The calibration method is also the same as that described in Section 6.1 such that the transmission of the cast polyamide stick was first measured with no sensor chip attached. After that, the same measurement was repeated with the sensor attached under no load and then also following application of discrete compressive loads. Transmission spectra referenced with respect to the no-sensor condition were obtained as a function of the applied load.

**Table 6.3.1. The parameters of nested metamaterials.**

| $L_{out}$ (mm) | $w_{out}$-$w_{in}$ (mm) | $s_{out}$-$s_{in}$ (mm) | $L_{diff}$ (mm) | $t_{film}$ (μm) | $t_{metal}$ (μm) | N |
|---|---|---|---|---|---|---|
| **22.2** | **0.04** | **0.04** | **0.04** | **0.1** | **0.1** | **276** |

We present the experimental setup in Fig. 6.3.1. We use two coaxial probes as the external antennas. The soft tissue is placed before the sensor while the sensor is attached to the test material cast polyamide via hard epoxy. The load is applied by the compression setup.

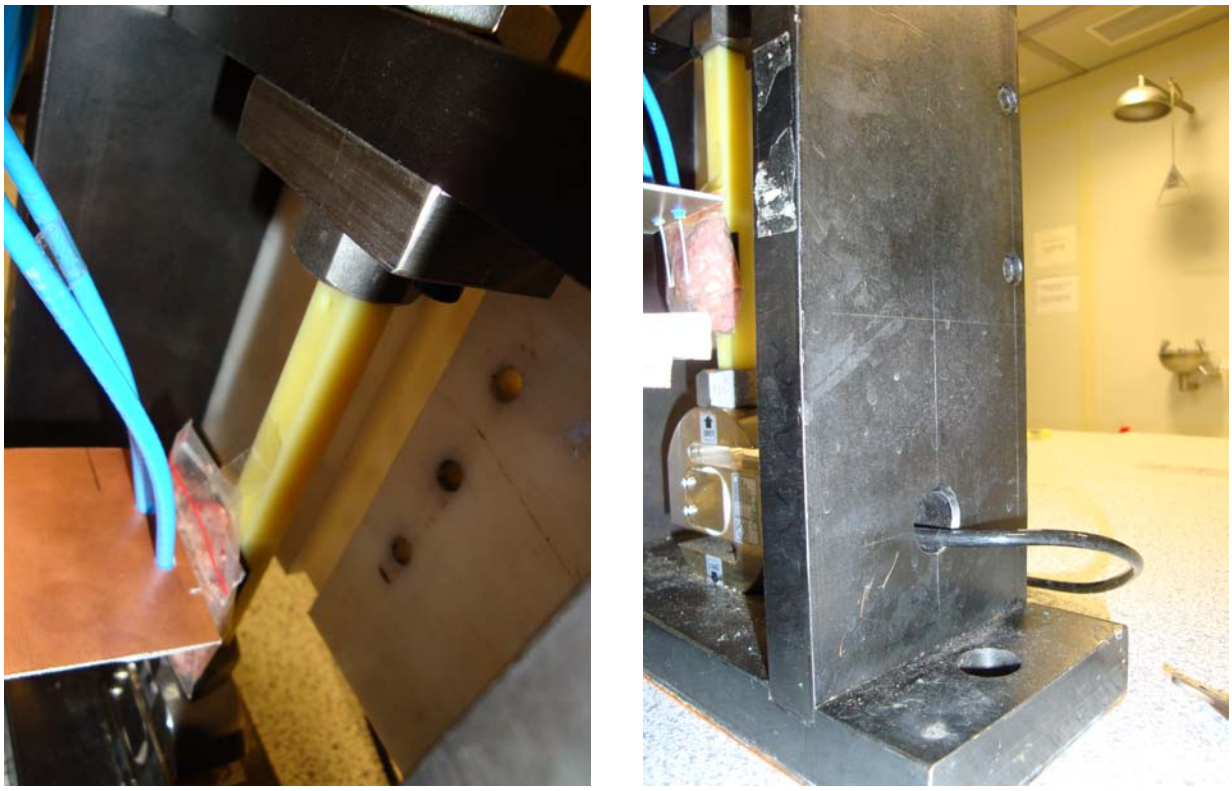

(a) (b)

**Figure 6.3.1. (a) The experimental setup for 100 MHz measurements. (b) The compression setup.**

We show the experimental results of the nested metamaterial sensor when there is no soft tissue in Fig. 6.3.2. The distance between the sensor and the external antenna is 0.5 cm. Since the strain values are low, it is difficult to sense the strain when the external load is under 150 kgf. Hence, we assume the working range of the sensor over 150 kgf of applied load and we perform extra

analysis to the loads greater than or equal to 150 kgf. From the experimental results, we observe that the wireless strain sensing is detected correctly when there is no soft tissue. Moreover, no sensing signal is observed when we apply load to empty stick as presented in Fig. 6.3.2. We can also see the sharpness of the resonance from Fig. 6.3.2(b). By using nested metamaterials, we both decrease the operating frequency and preserve the Q-factor. The no-load operating frequency of the sensor is 138.3012 MHz, while the no-load Q-factor is 240.273. The electrical length of the sensor is $\frac{\lambda}{97.71}$.

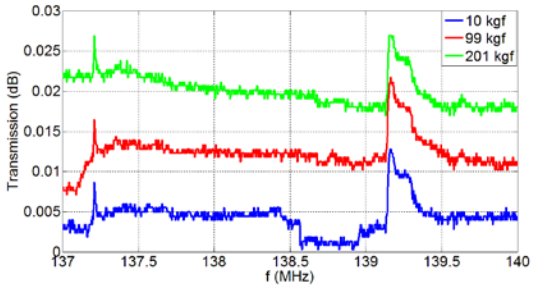


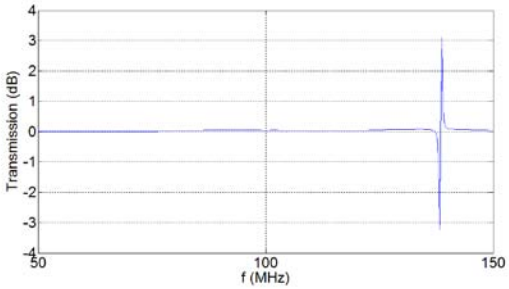


(a)

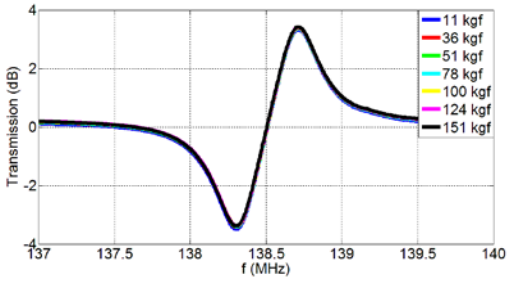


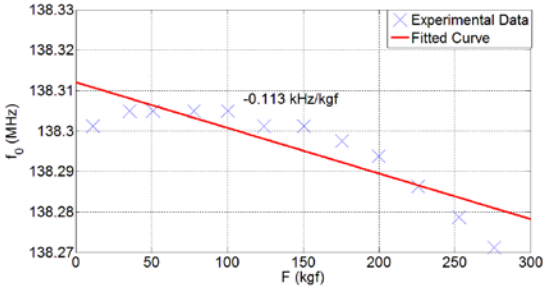


(c)

(d)

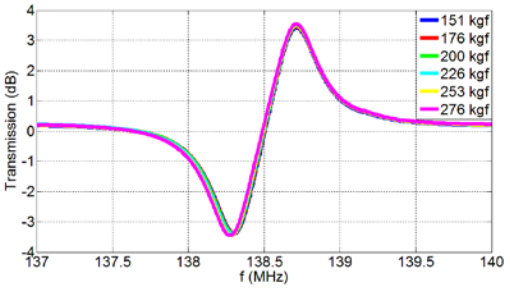


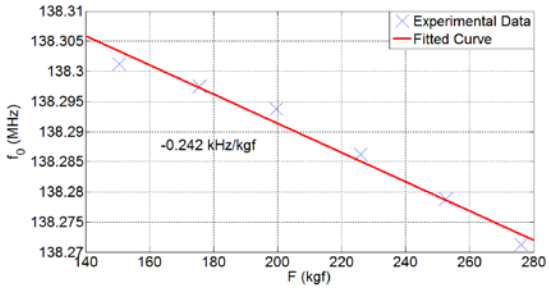


(e)

(f)

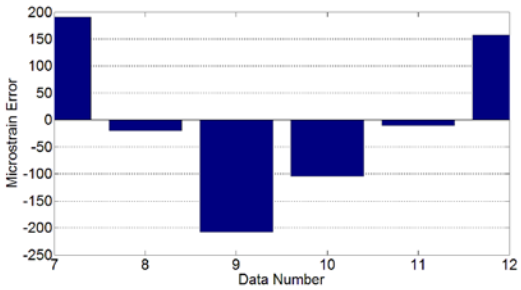


(g)

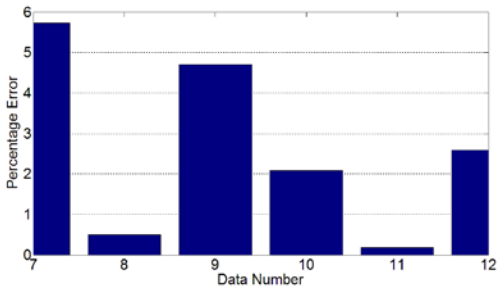


(h)

**Figure 6.3.2. Experimental measurements of 2.5 cm × 2.5 cm nested metamaterial sensor on the cast polyamide test material: (a) Transmission spectra of the stick, (b) transmission spectra for 50 MHz -150 MHz, (c) transmission spectra under 150 kgf applied load, (d) F *vs.* $f_0$, (e) transmission spectra over 150 kgf applied load, (f) F *vs.* $f_0$ over 150 kgf applied load, (g) the error in terms of microstrain over 150 kgf applied load, and (h) the error in terms of percentage over 150 kgf applied load.**

The experimental results of the nested metamaterial sensor when there is 0.5 cm thick soft tissue can be seen in Fig. 6.3.3. Since we are operating in 100 MHz range, the soft tissue does not affect the signal quality; hence, we obtain high signal level through soft tissue and a good linearity of sensing. Since we accept the working range of the sensor as the applied loads above 150 kgf, we again make analysis over 150 kgf applied load. We will perform this analysis for also 1 cm and 2 cm soft tissue thicknesses with cast polyamide stick. The no load operating frequency of the sensor is 137.56 MHz, the no load Q-factor is 127.065 and the electrical length of the sensor is $\frac{\lambda}{98.24}$.

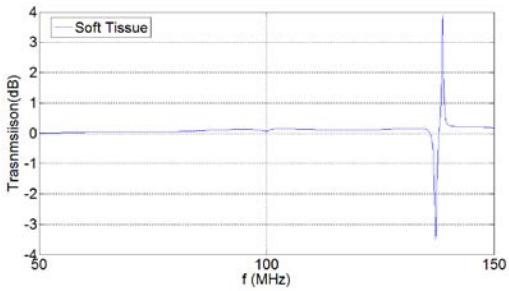


(a)

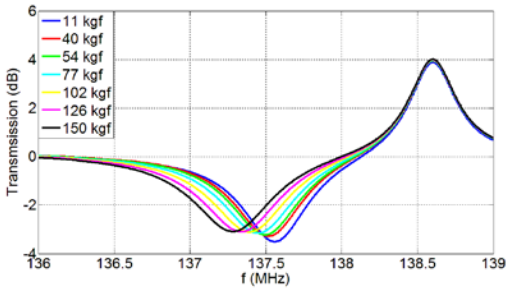


(b)

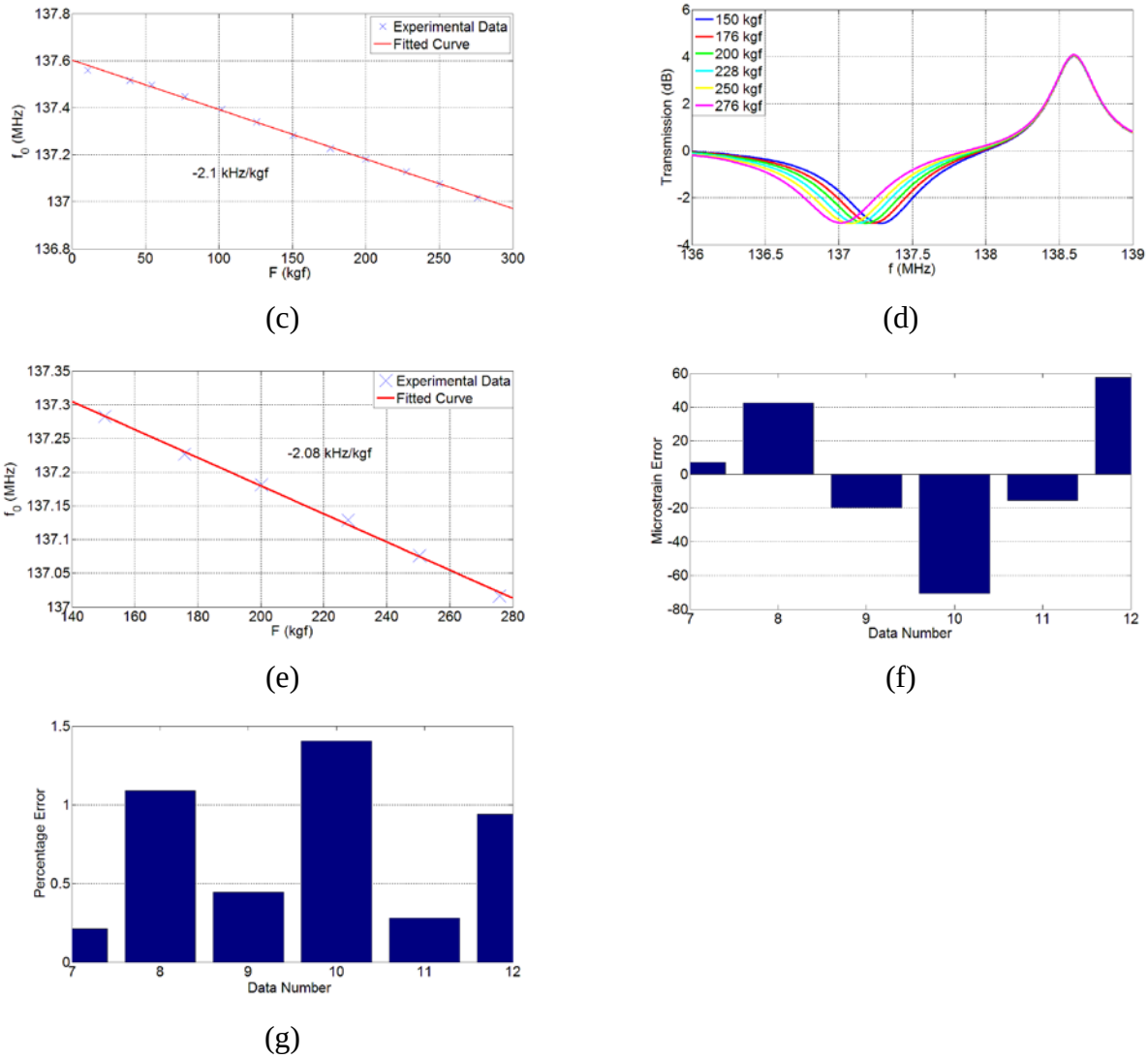


**Figure 6.3.3. Experimental measurements of 2.5 cm × 2.5 cm nested metamaterial sensor with 0.5 cm thick soft tissue on the cast polyamide test material: (a) Transmission spectra for 50 MHz -150 MHz, (b) transmission spectra under 150 kgf applied load, (c) F *vs.* $f_0$, (d) transmission spectra over 150 kgf applied load, (e) F *vs.* $f_0$ over 150 kgf applied load, (f) the error in terms of microstrain over 150 kgf applied load, and (g) the error in terms of percentage over 150 kgf applied load.**

The experimental results of the nested metamaterial sensor when there is 1 cm thick soft tissue are depicted in Fig. 6.3.4. We again receive a high signal level with 1 cm thick soft tissue and sense strain telemetrically. The no load operating frequency of the sensor is 137.7625 MHz, the no-load Q-factor is 189.26, and the electrical size of the sensor is $\frac{\lambda}{98.09}$.

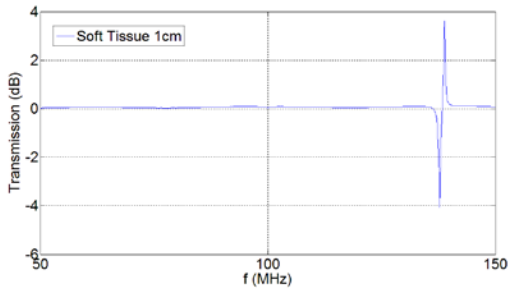


(a)

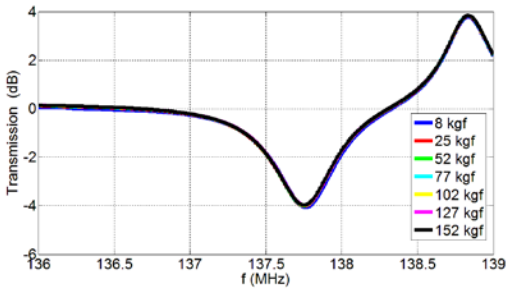


(b)

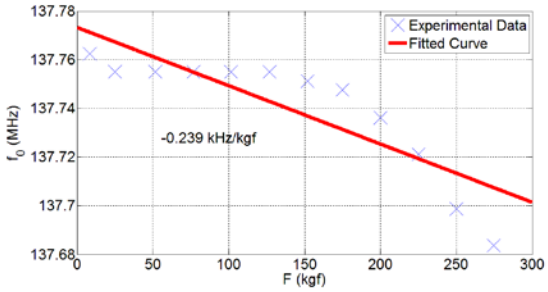


(c)

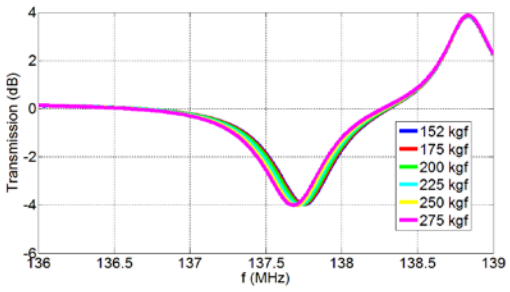


(d)

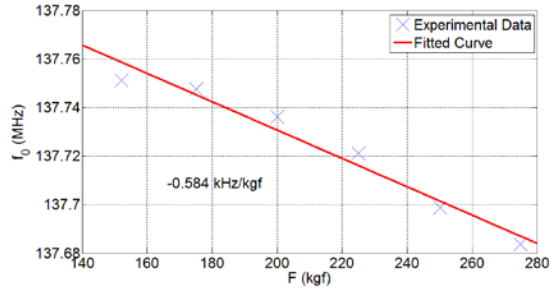


(e)

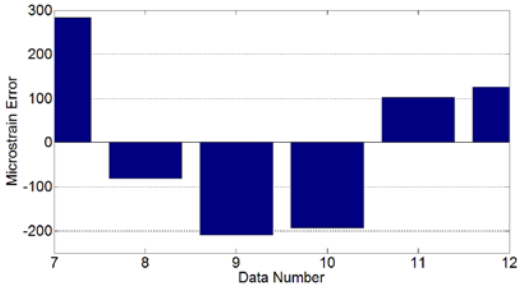


(f)

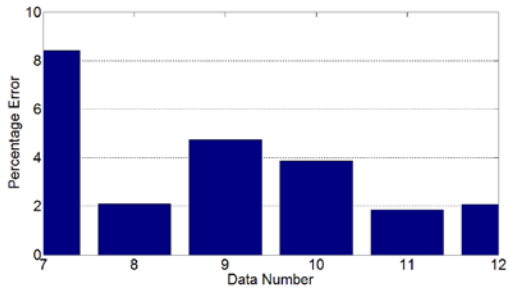


(g)

**Figure 6.3.4. Experimental measurements of 2.5 cm × 2.5 cm nested metamaterial sensor with 1 cm thick soft tissue on the cast polyamide test material: (a) Transmission spectra for 50 MHz -150 MHz, (b) transmission spectra under 150 kgf applied load, (c) F *vs.* $f_0$, (d) transmission spectra over 150 kgf applied load, (e) F *vs.* $f_0$ over 150 kgf applied load, (f) the error in terms of microstrain over 150 kgf applied load, and (g) the error in terms of percentage over 150 kgf applied load.**

The experimental results of the nested metamaterial sensor when there is 2 cm thick soft tissue is given in Fig. 6.3.5. With 2 cm thick soft tissue, we again acquire a high signal level and measure strain telemetrically. The sensor features 137.3425 MHz no-load operating frequency, $\frac{\lambda}{98.39}$ electrical length with 133.2 no-load Q-factor.

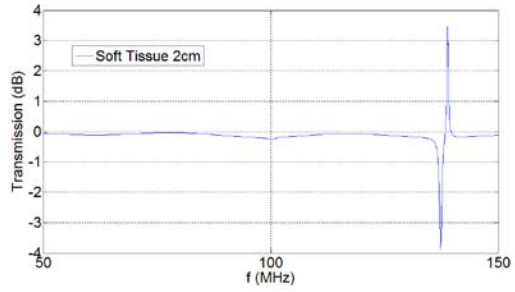


(a)

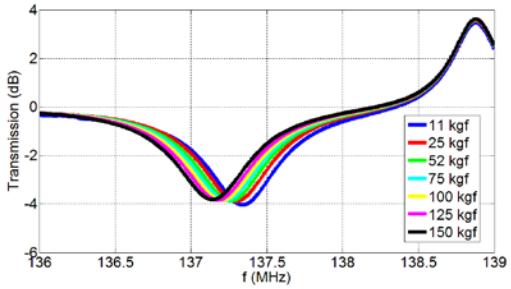


(b)

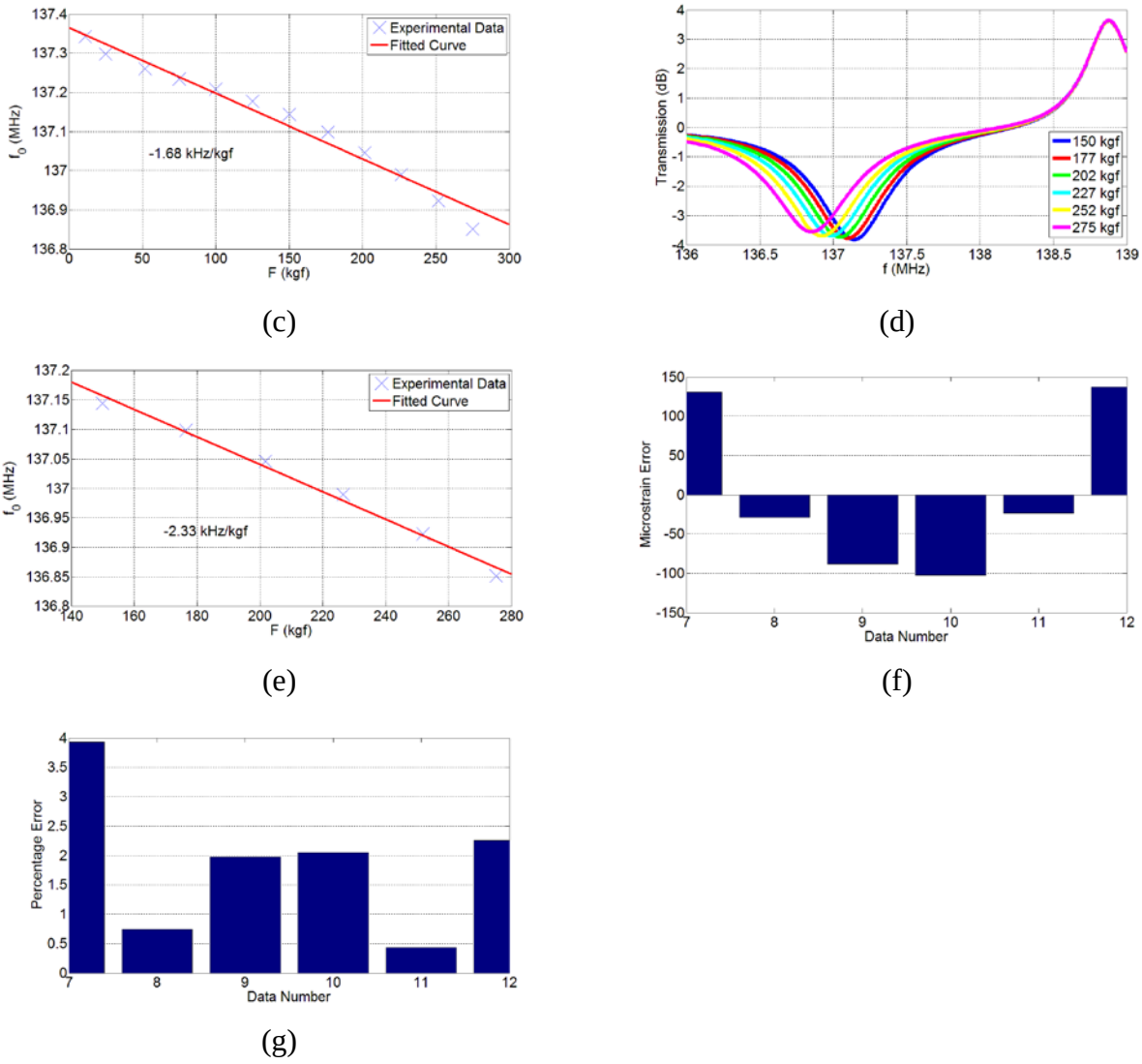


**Figure 6.3.5. Experimental measurements of 2.5 cm × 2.5 cm nested metamaterial sensor with 2 cm thick soft tissue on the cast polyamide test material: (a) Transmission spectra for 50 MHz -150 MHz, (b) transmission spectra under 150 kgf applied load, (c) F *vs.* $f_0$, (d) transmission spectra over 150 kgf applied load, (e) F *vs.* $f_0$ over 150 kgf applied load, (f) the error in terms of microstrain over 150 kgf applied load, and (g) the error in terms of percentage over 150 kgf applied load.**

We present the experimental results of the nested metamaterial sensor when there is 5 cm thick soft tissue in Fig. 6.3.6. The wireless strain sensing is measured correctly with 5 cm thick soft tissue, which has a 137.6162 MHz no-load operating frequency, a 195.644 no-load Q-factor and

a $\frac{\lambda}{98.2}$ electrical length. Because of the buckling of the test material under high stress, the sign of the slope may change. In our experimental setups with the wood test material, we solved this problem as it is impossible for the wood test material to move or buckle. Hence, we always obtain the same sign of the slope in all experiments performed with the wood test material. Also, we change the investigation of the applied load range from over 150 kgf applied loads to the applied loads between 80 and 220 kgf for 5 cm, 10 cm and 20 cm thicknesses of soft tissue.

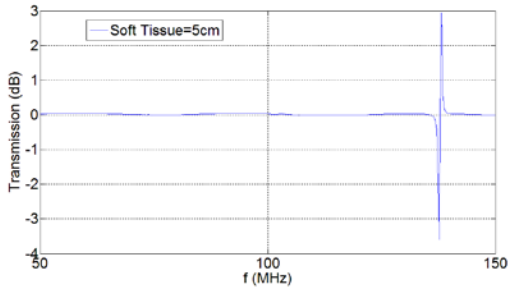


(a)

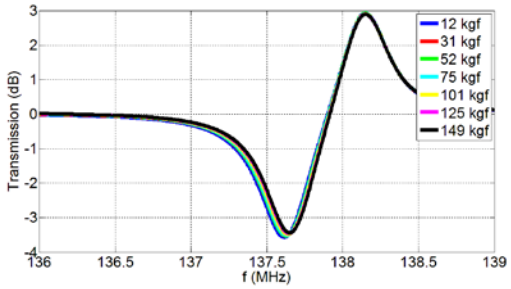


(b)

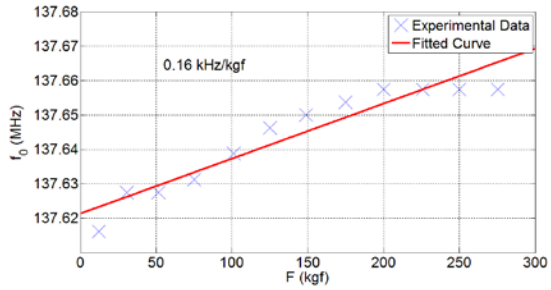


(c)

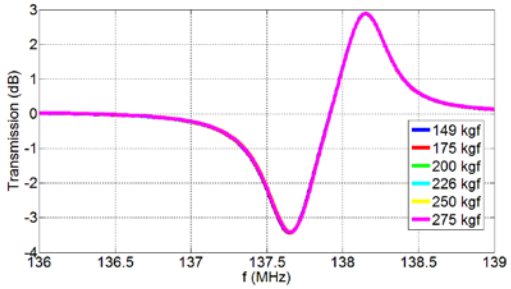


(d)

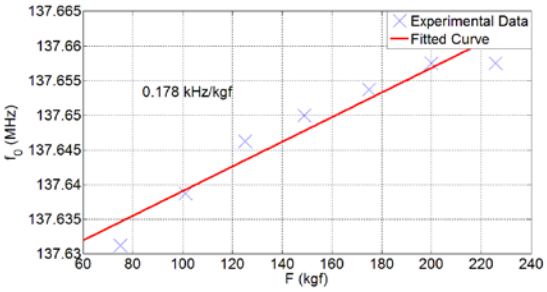


(e)

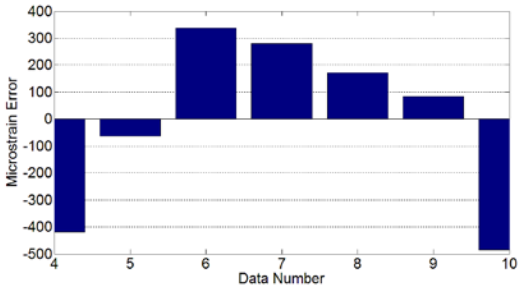


(f)

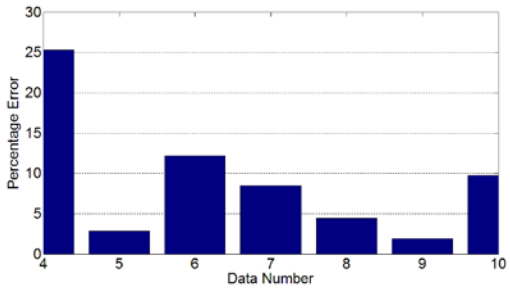


(g)

**Figure 6.3.6. Experimental measurements of 2.5 cm × 2.5 cm nested metamaterial sensor with 5 cm thick soft tissue on the cast polyamide test material: (a) Transmission spectra for 50 MHz -150 MHz, (b) transmission spectra under 150 kgf applied load, (c) F *vs.* $f_0$, (d) transmission spectra over 150 kgf applied load, (e) F *vs.* $f_0$ between 80 kgf -220 kgf applied load, (f) the error in terms of microstrain between 80 kgf -220 kgf applied load, and (g) the error in terms of percentage between 80 kgf -220 kgf applied load.**

We depict the experimental results of the nested metamaterial sensor when there is 10 cm thick soft tissue in Fig. 6.3.7. Even with such a high thickness of soft tissue, we are able to observe telemetric strain sensing. Different soft tissue thicknesses are important in real life. For example, if the bone is near to skin such as in the cases of metatarsal, the soft tissue thickness can be 0.5, 1 or 2 cm, depending of the weight of the person. For the femur, the thickness can be 5, 10 cm or more. For a overweight person, the spine could be 20 cm away from the skin. To use our sensor for monitoring fracture healing in different places of the body, we should be able to measure strain telemetrically for all these different thicknesses of soft tissue. The sensor exhibits a 137.7025 MHz no-load operating frequency with a $\frac{\lambda}{98.14}$ electrical length.

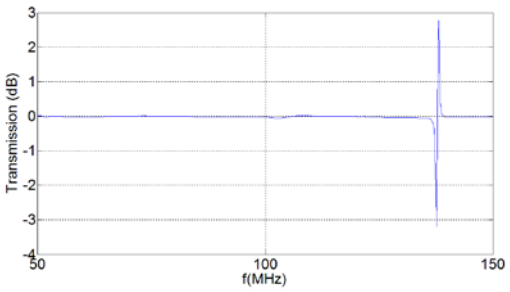


(a)

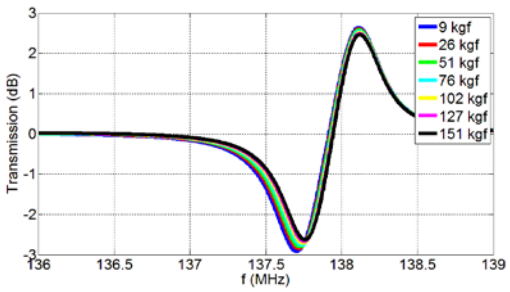


(b)

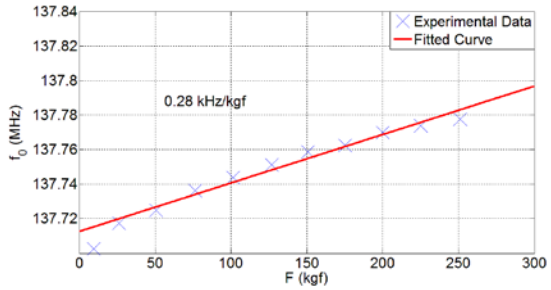


(c)

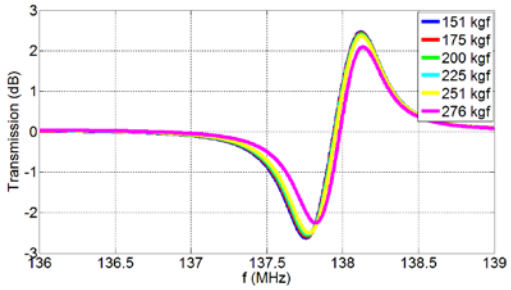


(d)

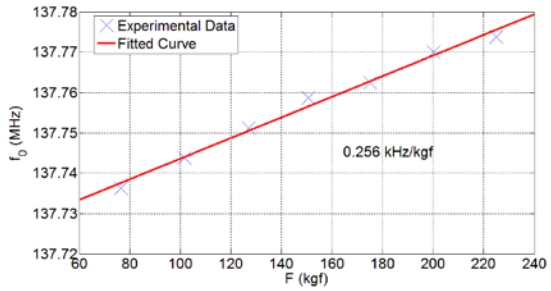


(e)

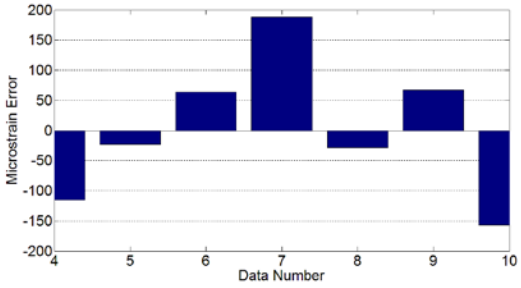


(f)

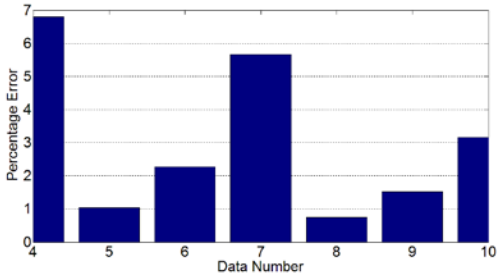


(g)

**Figure 6.3.7. Experimental measurements of 2.5 cm × 2.5 cm nested metamaterial sensor with 10 cm thick soft tissue on the cast polyamide test material: (a) Transmission spectra for 50 MHz -150 MHz, (b) transmission spectra under 150 kgf applied load, (c) F *vs.* $f_0$, (d) transmission spectra over 150 kgf applied load, (e) F *vs.* $f_0$ between 80 kgf -220 kgf applied load, (f) the error in terms of microstrain between 80 kgf -220 kgf applied load (g) the error in terms of percentage between 80 kgf -220 kgf applied load.**

We show the experimental results of the nested metamaterial sensor when there is 20 cm thick soft tissue in Fig. 6.3.8. Even with this thickness of the soft tissue, we perform strain sensing telemetrically at 137.8863 MHz of no-load operating frequency with a $\frac{\lambda}{98}$ electrical length.

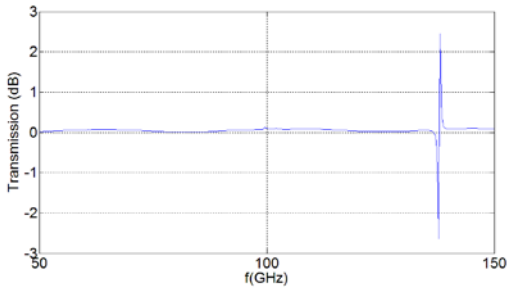


(a)

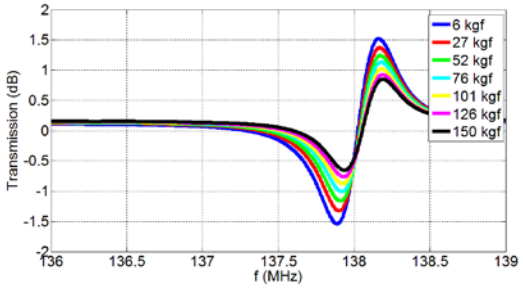


(b)

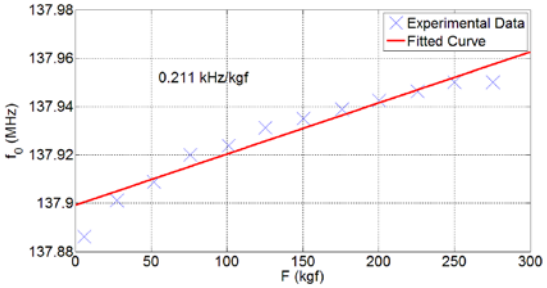


(c)

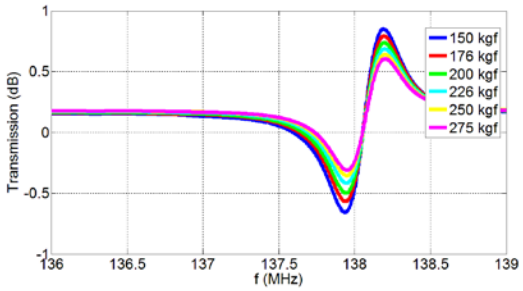


(d)

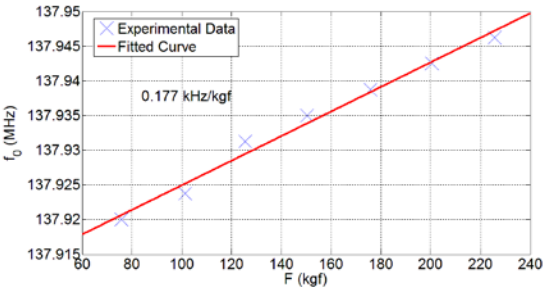


(e)

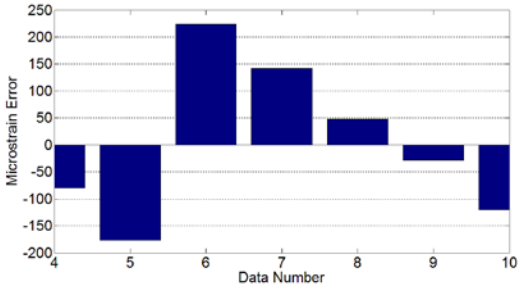


(f)

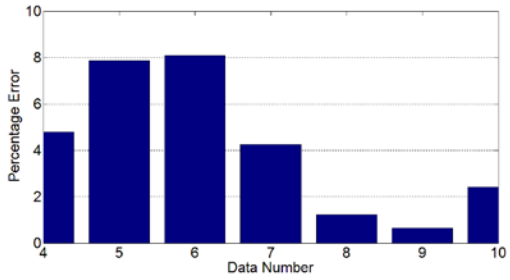


(g)

**Figure 6.3.8. Experimental measurements of 2.5 cm × 2.5 cm nested metamaterial sensor with 20 cm thick soft tissue on the cast polyamide test material: (a) Transmission spectra for 50 MHz -150 MHz, (b) transmission spectra under 150 kgf applied load, (c) F *vs.* $f_0$, (d) transmission spectra over 150 kgf applied load, (e) F *vs.* $f_0$ between 80 kgf -220 kgf applied load, (f) the error in terms of microstrain between 80 kgf -220 kgf applied load (g) the error in terms of percentage between 80 kgf -220 kgf applied load.**

## 6.3.2 Experiments with 2.5 cm × 2.5 cm sensor chip on metal implant

In this section, we explain our additional experiments with the nested memtamaterial in Section 6.3.1. The calibration method is also the same as that described in Section 6.3.1. However, this time, instead of cast polyamide, we use metal implant stick as the test material to observe whether the metal stick blocks the signal and hinders us from measuring strain telemetrically. We observe from our experiments that the metal stick does not have any disadvantage compared to the plastic stick for wireless strain sensing in our configuration. Since, our antennas are in front of the stick, the metal stick does not degrade the signal level and does not prevent telemetric strain sensing compared to plastic stick. Also, from Section 6.2, we learned that the antennae should not be over 0.5 cm away from the sensor chip to obtain good signal. Hence, we put our sensor 0.5 cm away from the soft tissue. Moreover, because of the buckling of the metal stick, we can see changes in the sign of the slope. We observe strain telemetrically with our 2.5 cm × 2.5 cm nested metamaterial sensor attached to the metal stick using 5 cm thick soft tissue in

Fig. 6.3.9, with 10 cm thick soft tissue in Fig. 6.3.10, and with 20 cm thick soft tissue in Fig. 6.3.11. For all these thicknesses, we measure strain remotely.

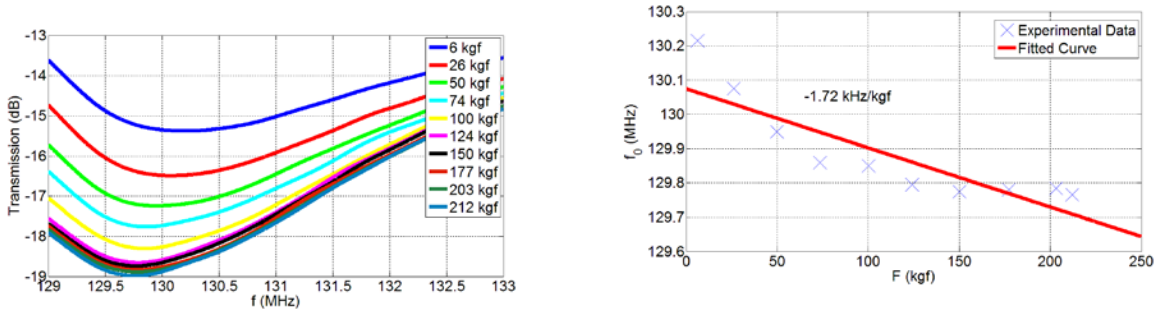


(a) (b)

**Figure 6.3.9. Experimental measurements of our 2.5 cm × 2.5 cm nested metamaterial sensor with 5 cm thick soft tissue on the metal stick test material: (a) Transmission spectra under different applied loads and (b) F *vs.* $f_0$.**

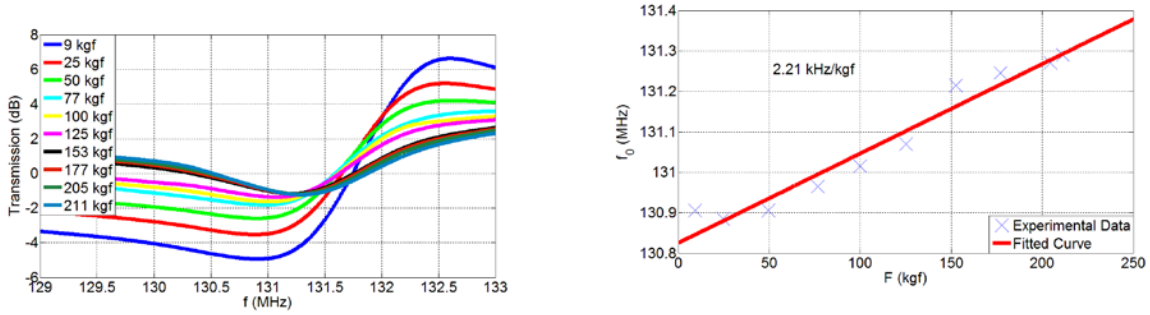


(a) (b)

**Figure 6.3.10. Experimental measurements of our 2.5 cm × 2.5 cm nested metamaterial sensor with 10 cm thick soft tissue on the metal stick test material: (a) Transmission spectra under different applied loads and (b) F *vs.* $f_0$.**

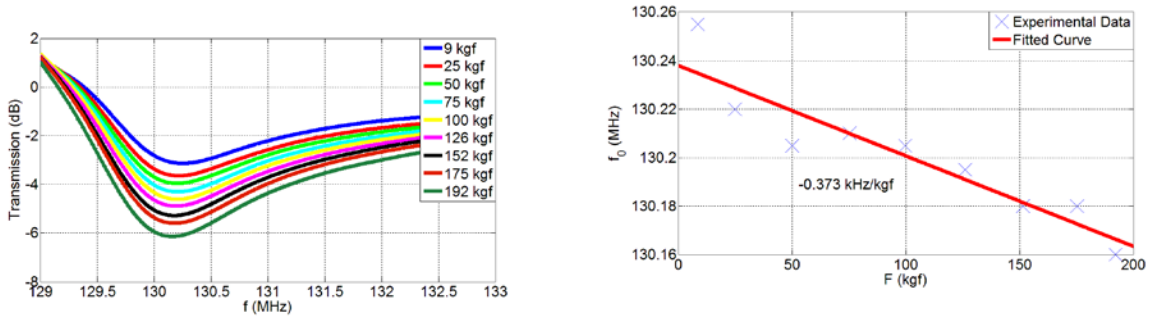


(a) (b)

**Figure 6.3.11. Experimental measurements of our 2.5 cm × 2.5 cm nested metamaterial sensor with 20 cm thick soft tissue on the metal stick test material: (a) Transmission spectra under different applied loads and (b) F *vs.* $f_0$.**

# 6.3.3 Experiments with 2.5 cm × 2.5 cm sensor chip on wood test material

In this section, our experimental setup is adapted towards the real-life application. We use wood to simulate the bone, insert stainless steel plate over the wood, and attach our sensor to the stainless steel plate via hard epoxy. We also solve the problem of the movement of the test material; hence, there is no buckling problem in this section. We always get the same sign of the slope. We expect increased operating frequency with the applied load in compression setup. In the previous chapters, sensor was on cast polyamide stick. The compression setup applied load to the cast polyamide stick; hence, the force applied to the sensor was in opposite direction to the applied load. This time, load is applied to the wood; thus, the force applied to the sensor is in the same direction. Therefore, here we expect decreased operating frequency with the applied load.

We show the experimental setup apparatus (for the case of no fracture) in Fig. 6.3.12. Wood is used to simulate the bone. As in real case, the stainless steel is used as the implantable stick, which is attached to the wood, and our sensor is in turn attached to the stainless steel plate via

hard epoxy. We use the sensor in Section 6.3.1 and the calibration method we use is the same as that described in Section 6.3.1.

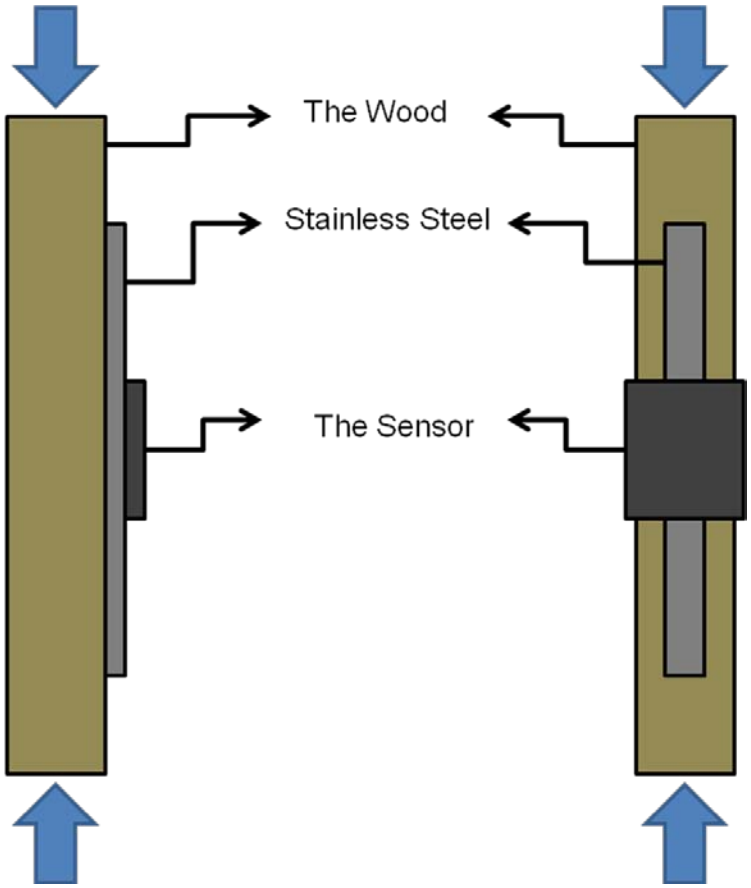


**Figure 6.3.12. Schematic sketch of the experimental apparatus for the case of non-fracture. Wood is used to simulate the bone.**

We present the experimental results of our 2.5 cm × 2.5 cm nested metamaterial sensor for the case of non-fracture case in Fig. 6.3.13. We sense the strain on the implantable plate wirelessly.

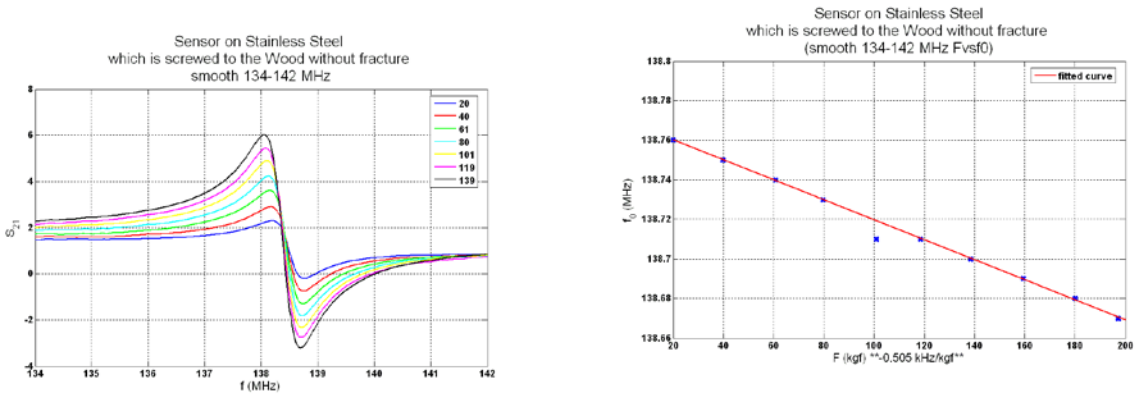


(a) (b)

**Figure 6.3.13. Experimental measurements of 2.5 cm × 2.5 cm nested metamaterial sensor for the case of non-fracture (a) transmission spectra under different applied loads and (b) F *vs.* $f_0$.**

We show the experimental apparatus for the case of non-fracture with an angle to the surface normal in Fig. 6.3.14 and the experimental results of this experiment in Fig. 6.3.15. In real case, the bone does not have to be fixed perpendicular to the surface. There may be some angle. To simulate this situation, we have performed this experiment. In this case, there is also strain induced on the implantable plate with an angle to the ground.

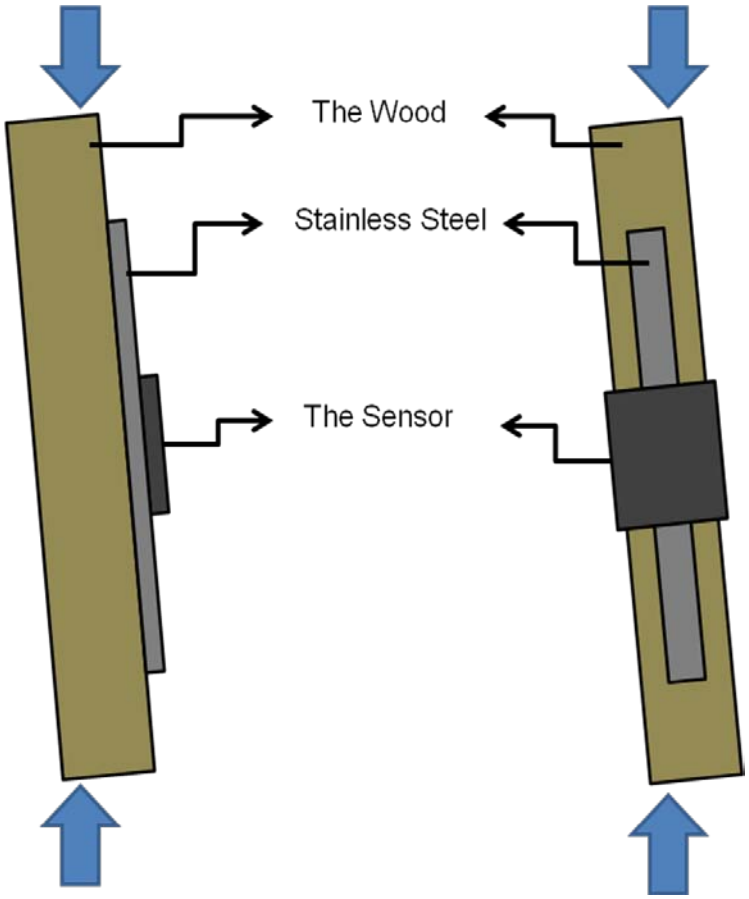


**Figure 6.3.14. Schematic illustration of the experimental apparatus for the case of non-fracture with an angle to the ground. Wood is used to simulate the bone.**

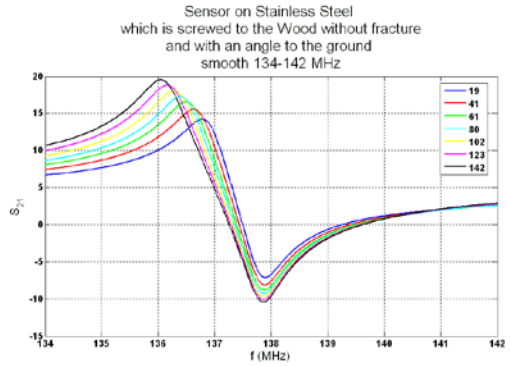


(a)

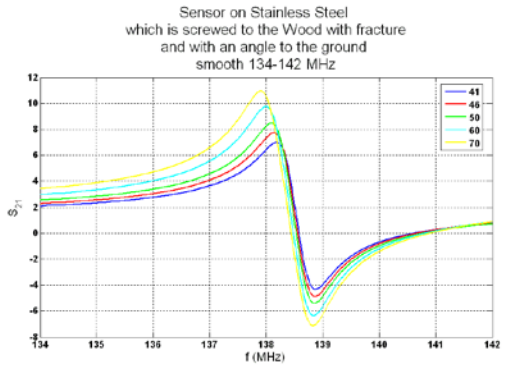


(b)

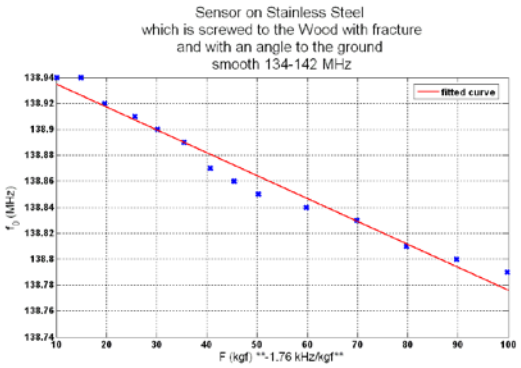


(c)

**Figure 6.3.15. Experimental measurement of 2.5 cm × 2.5 cm nested metamaterial sensor for the case of non-fracture with an angle to the ground: (a) transmission spectra under different applied loads, (b) transmission spectra under different applied loads between 40 and 70 kgf, and (c) F *vs.* $f_0$.**

The experimental apparatus for the case of fracture is demonstrated in Fig. 6.3.16 where the plastic is used to simulate the bone. To simulate a full fracture case, we cut the middle part of the plastic. The experimental results for this case are shown in Fig. 6.3.17. From these results, we see that the wireless strain sensing is achieved. Since this plastic is harder than wood, we have lower sensitivity in this case. We changed the material to simulate the bone from wood to this plastic material because we can insert additional various materials between middle part of the plastic sections.

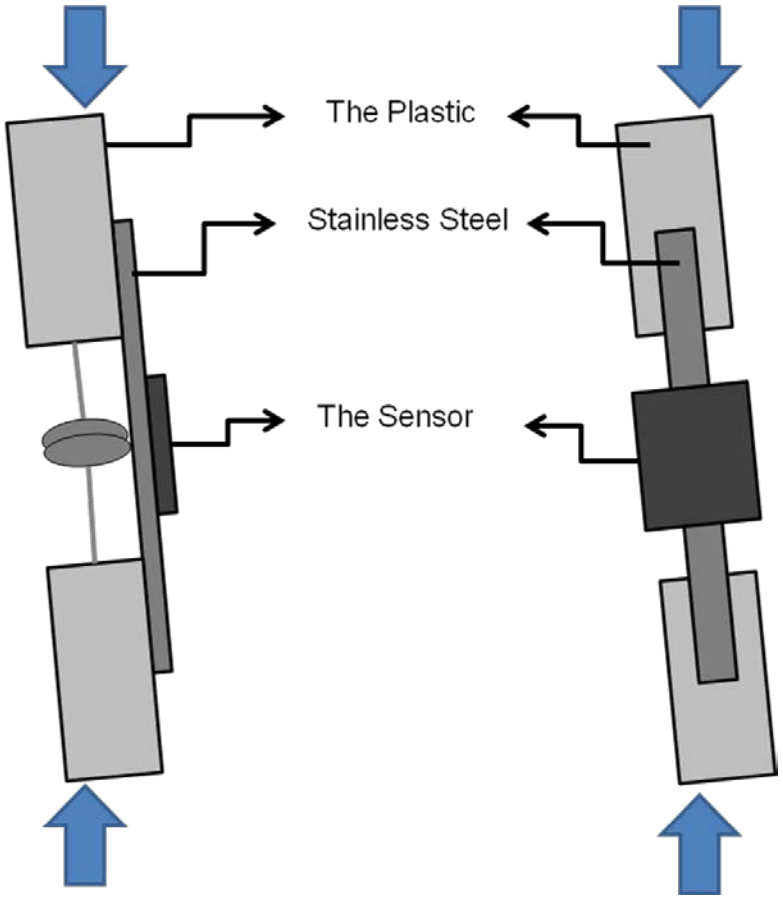


**Figure 6.3.16. Schematic illustration of the experimental apparatus for the full fracture case. Plastic is used to simulate the bone.**

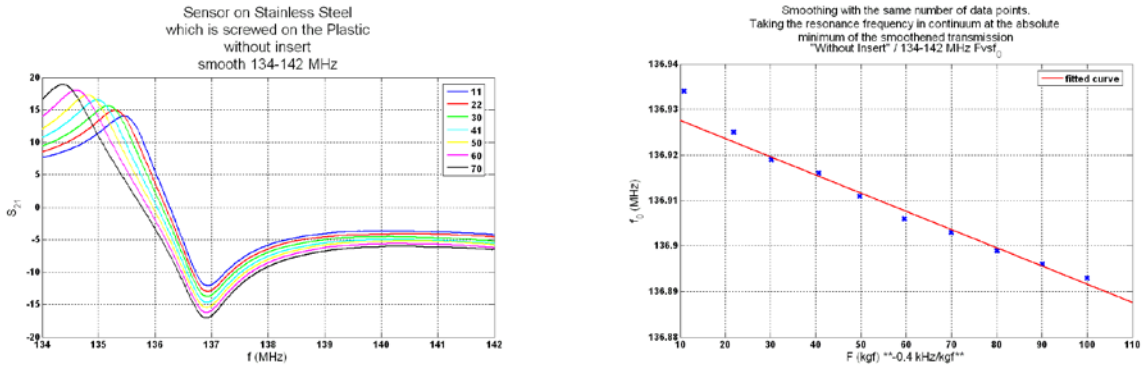


(a) (b)

**Figure 6.3.17. Experimental measurement of our 2.5 cm × 2.5 cm nested metamaterial sensor for the full fracture case: (a) Transmission spectra under different applied loads and (b) F *vs.* $f_0$.**

The experimental apparatus for the case of fracture with an insert is depicted in Fig. 6.3.18. Again, the plastic is used to simulate the bone. By inserting materials between the parts of the plastics, we simulate different phases of the fracture. At the beginning, the tissue filling the space of the fractured bone is soft. As the time passes, the bone tissue builds up, becoming harder. To simulate this situation, we first used the softest insert into the plastic as illustrated in Fig. 6.3.19. The slope of $\Delta f_0$ *vs.* F decreased compared to the full fracture case. Then we used a harder insert and measured strain telemetrically as depicted in Fig. 6.3.20. We observed that the slope decreased compared to the case of softer insert. Finally, we inserted the hardest insert and obtained the lowest slope of all cases shown in Fig. 6.3.21. Thus, we show in these experiments that it is possible to monitor different phases of fracture healing by observing the changes in $\Delta f_0$ *vs.* F slope of the sensor.

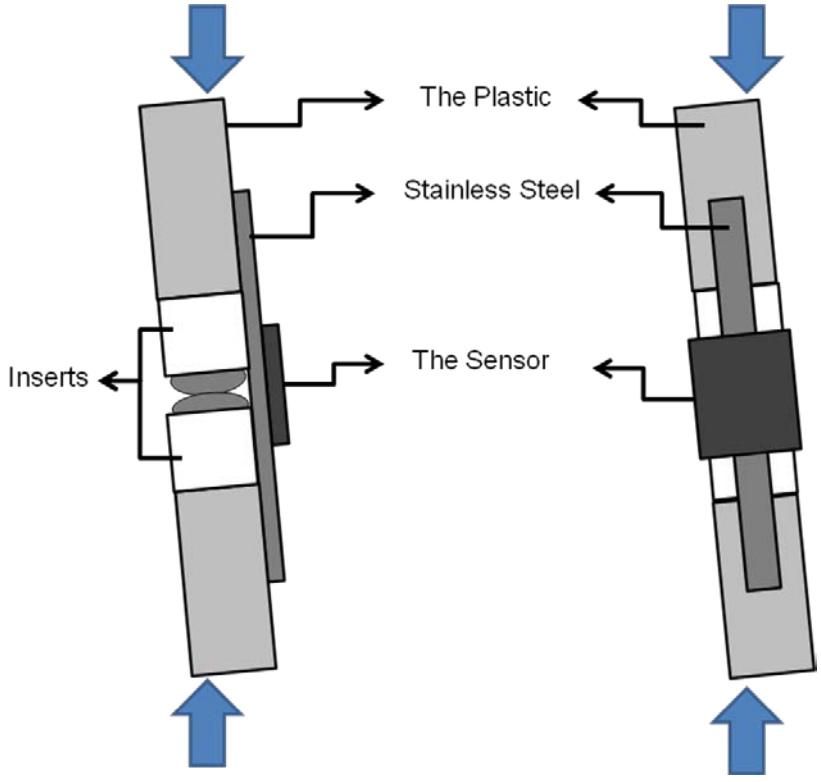


**Figure 6.3.18. Schematic illustration of the experimental apparatus for the case of fracture with an insert. Plastic is used to simulate the bone.**

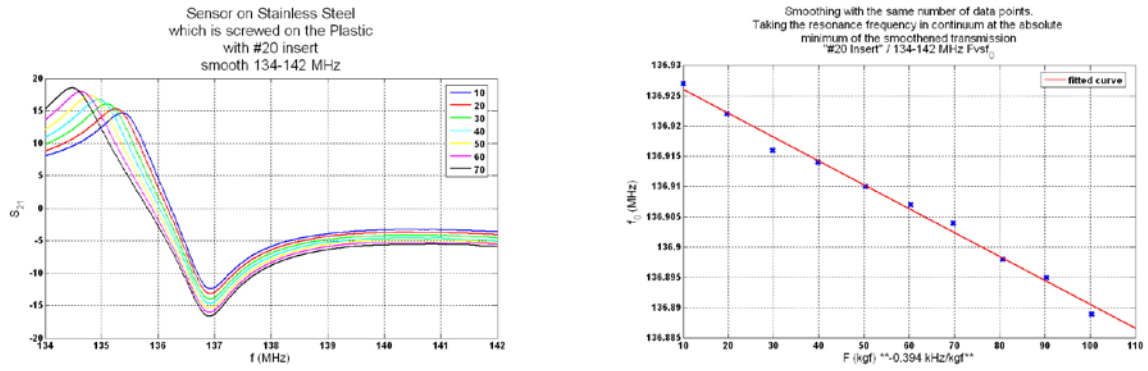


(a) (b)

**Figure 6.3.19. Experimental measurement of our 2.5 cm × 2.5 cm nested metamaterial sensor for the case of fracture with the first (softest) insert: (a) Transmission spectra under different applied loads and (b) F *vs.* $f_0$.**

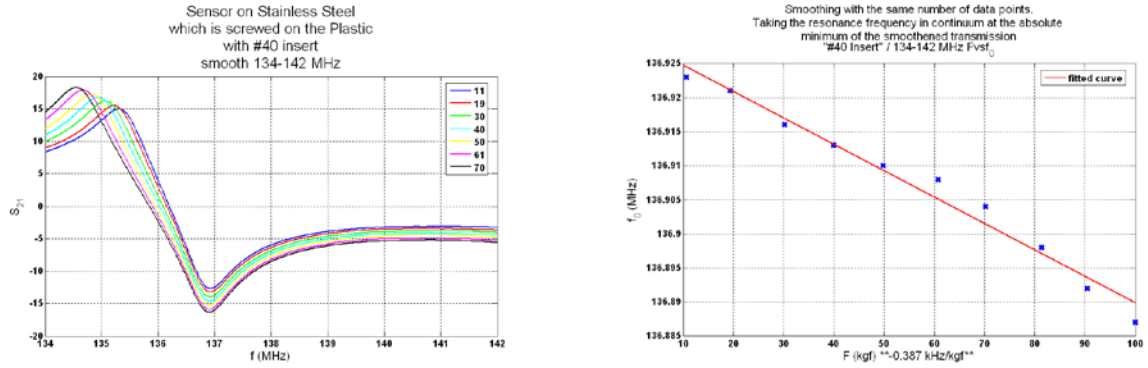


(a) (b)

**Figure 6.3.20. Experimental measurement of our 2.5 cm × 2.5 cm nested metamaterial sensor for the case of fracture with the second insert: (a) Transmission spectra under different applied loads and (b) F *vs.* $f_0$.**

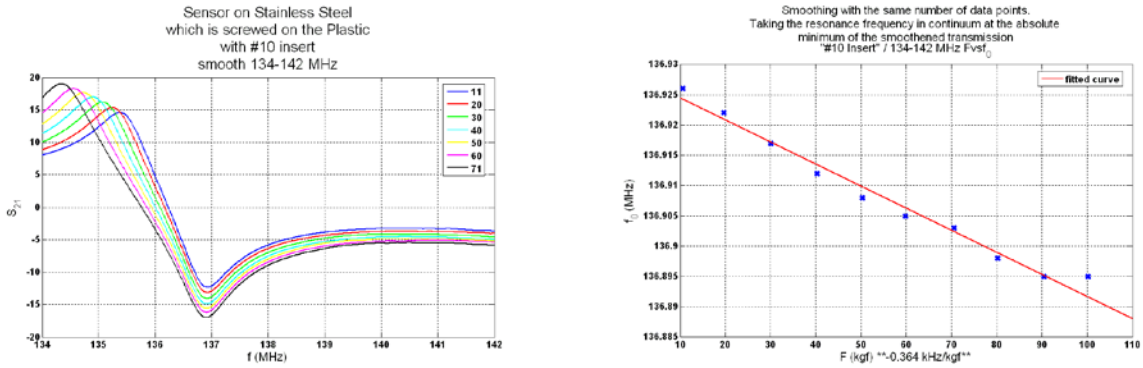


(a) (b)

**Figure 6.3.21. Experimental measurement of our 2.5 cm × 2.5 cm nested metamaterial sensor for the case of fracture with the last (hardest) insert: (a) Transmission spectra under different applied loads and (b) F *vs.* $f_0$.**

## 6.3.4 Experiments with 1.25 cm × 1.25 cm sensor chip on wood test material

The device parameters of our 1.25 cm × 1.25 cm nested metamaterial sensor are shown in Table 6.3.2. We miniaturized the sensor to 1.25 cm; however, this level of miniaturization is yet not sufficient for our sensors to be used on commercial implants. To place our sensor on implantable stick, we need to further miniaturize the sensor <1cm. We also used baluns for external antennas. By this way, we made our experimental setup less insensitive to the environment and made our experiments more robust. We show schematic illustrations of our apparatus in Fig. 6.3.22, photographs of our experimental setup in Fig. 6.3.23 and the zoomed-in pictures of our experimental setup in Fig. 6.3.24.

**Table 6.3.2. The parameters of our 1.25 cm × 1.25 cm nested metamaterial sensor.**

| | $L_{total}$ (μm) | $L_{out}$ (μm) | $L_{in}$ (μm) | $w_{out}$ (μm) | $s_{out}$ (μm) | $w_{in}$ (μm) | $s_{in}$ (μm) | $L_{diff}$ (μm) | $t_{film}$ (μm) | $t$ (μm) | N |
|---|---|---|---|---|---|---|---|---|---|---|---|
| Nested SRR | 12500 | 11100 | 8900 | 20 | 20 | 20 | 20 | 20 | 0.1 | 0.1 | 276 |

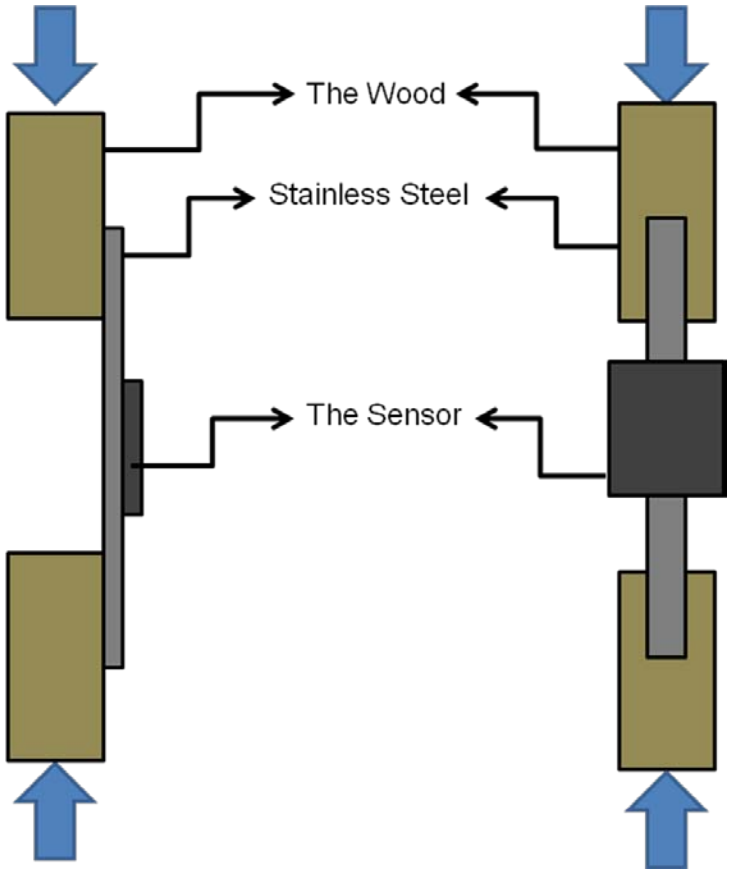


**Figure 6.3.22. Schematic illustration of the experimental apparatus.**

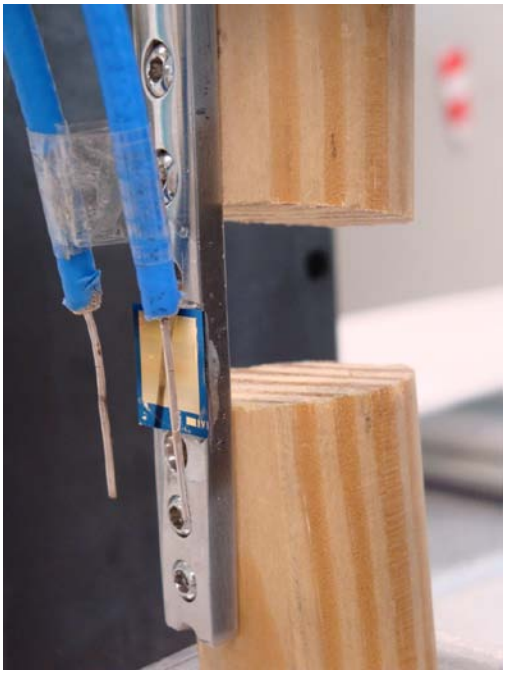

**Figure 6.3.23. Photograph of the experimental setup.**

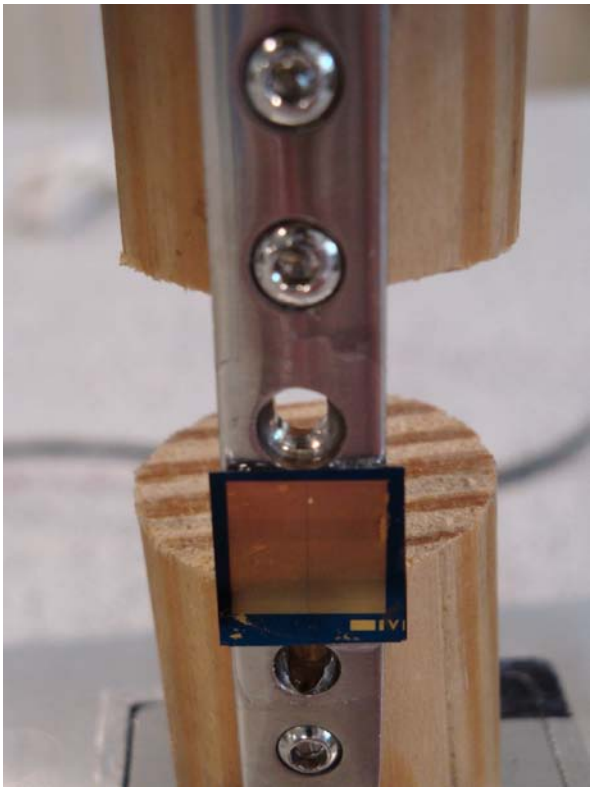

(a)

(b)

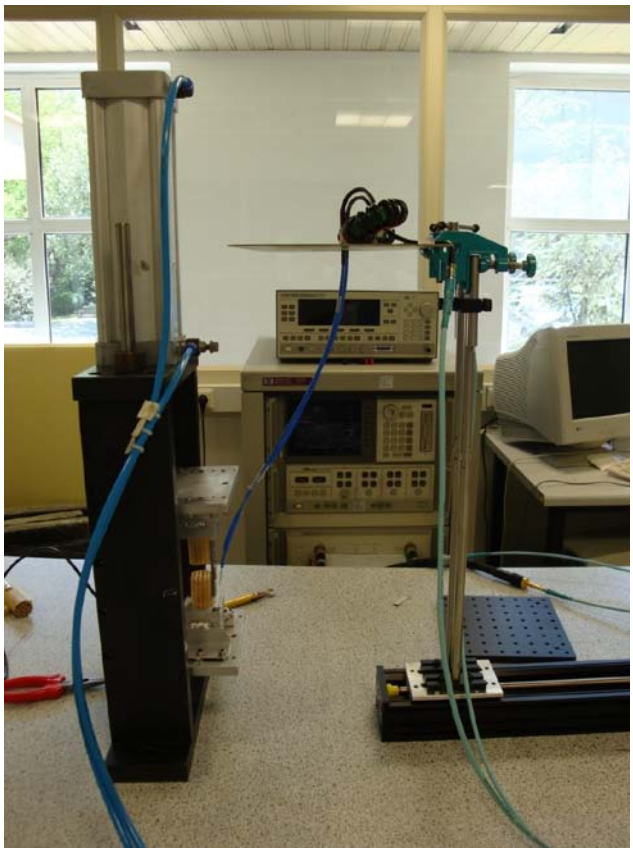

(c)

(d)

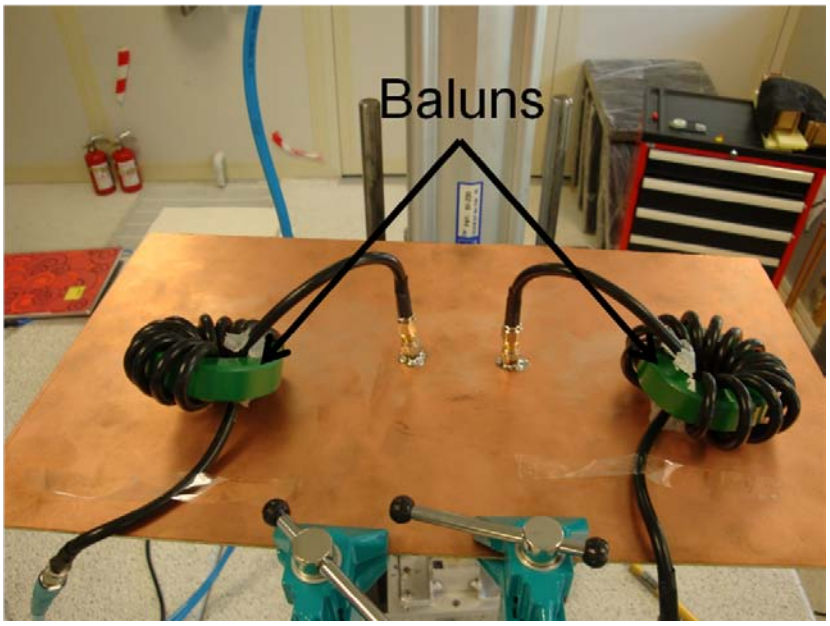


(e)

**Figure 6.3.24. Zoomed-in pictures of the experimental setup from different angles (a) – (e).**

We also changed the calibration method in this experiment. In real-life application, we cannot take the sensor out of the body first to make a measurement and then attach the sensor to the implantable plate. Because of this reason, we performed calibration when the sensor is on the implantable plate. For calibration purposes, the transmission of the test material was first measured with sensor chip attached. Subsequently, the same measurement was repeated with different discrete compressive loads. Transmission spectra referenced with respect to the no-load condition were obtained as a function of the applied load. We observe the shift of operating frequency with our 1.25 cm × 1.25 cm sensor as presented in Fig. 6.3.25.

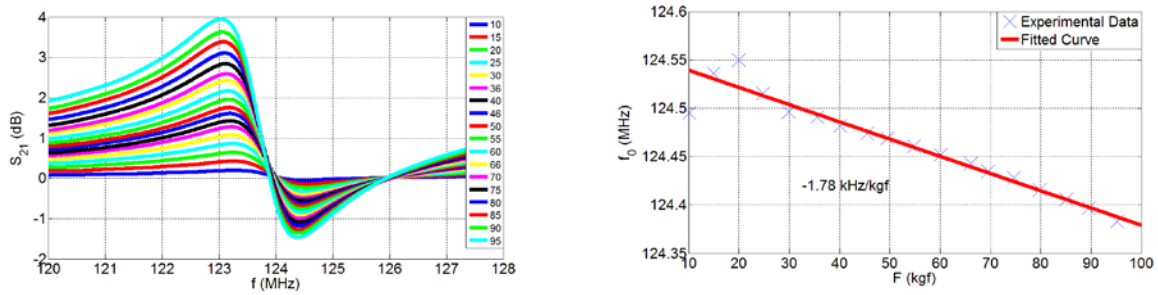


(a) (b)

**Figure 6.3.25. Experimental results of our 1.25 cm × 1.25 cm sensor with new calibration method.**

## 6.3.5 Experiments with our 0.8 cm × 0.8 cm sensor chip on wood test material

We need to decrease the size of our sensor to sub-cm range for the use of our sensors in real-life application. We can place our sensor to commercial implantable sticks when they are sub-cm sized. Thus, we decreased the size of our sensor down to 0.8 cm. We also need to decrease the operating frequency down to the range of 100 MHz since we want to use our sensor in the body, e.g., for spine avoiding the background of soft tissue. So, our sensor should provide wireless strain measurement even through 20 cm thick soft tissue (An overweight person's spine can be 20 cm away from his skin). At 100 MHz, there will be very small absorption coefficient of soft tissue; thus, the signal level will not degrade, and there will be no strong absorption by soft

tissue. At 100 MHz, the soft tissue will have a high dielectric constant; therefore, EM waves will have high penetration depth in to soft tissue. As a result, we will have wireless sensing possible at deeper levels of the body (e.g., spine) at 100 MHz. Therefore, we decreased the electrical length of the sensor to $\lambda_o/400$ by decreasing the sensor size to 0.8 cm while operating in the range of 100 MHz. This enabled us to demonstrate the use of our sensors in deep sites of the body fractured as in real-life applications. The device parameters are presented in Table 6.3.3 and the photograph of the sensor is given in Fig. 6.3.26.

**Table 6.3.3. The parameters of 0.8 cm nested metamaterials.**

| | $L_{total}$ (μm) | $L_{out}$ (μm) | $L_{in}$ (μm) | $w_{out}$ (μm) | $s_{out}$ (μm) | $w_{in}$ (μm) | $s_{in}$ (μm) | $L_{diff}$ (μm) | $t_{film}$ (μm) | $t$ (μm) | N |
|---|---|---|---|---|---|---|---|---|---|---|---|
| Nested SRR | 8000 | 5550 | 4450 | 10 | 10 | 10 | 10 | 10 | 0.1 | 0.1 | 276 |

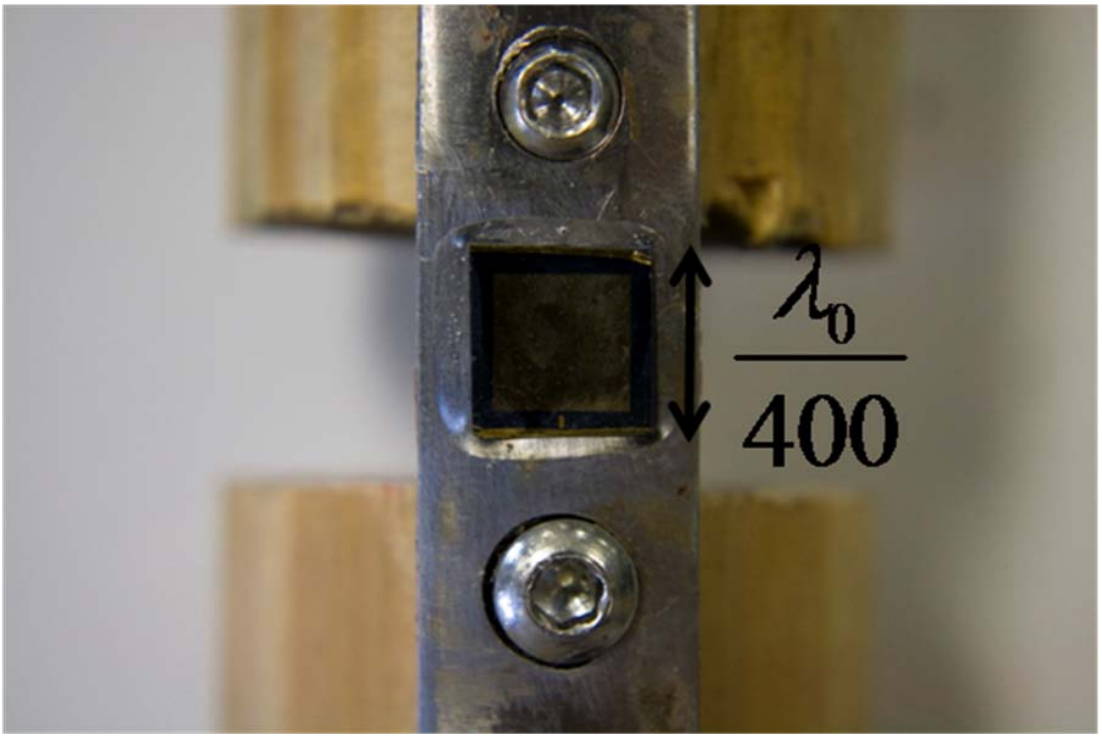


**Figure 6.3.26. Photograph of our 0.8 cm × 0.8 cm sensor attached to the implantable stick.**

By decreasing the size of the sensor to 0.8 cm and operating it up to a soft tissue thickness of 20 cm, we have being granted the first US National Institute of Health (NIH) grant of these RF-bioMEMS wireless sensors with a subcontract to Bilkent University (NIH 5R01EB010035, Co-PI H.V. Demir). We have also made a US patent application of our sensors sponsored by "Synthes" [99]. They also produced sample implants for our sensors as demonstrated in Fig. 6.3.27. Our sub-cm sized sensors working in the range of 100 MHz are also promising for applications other than monitoring fracture healing.

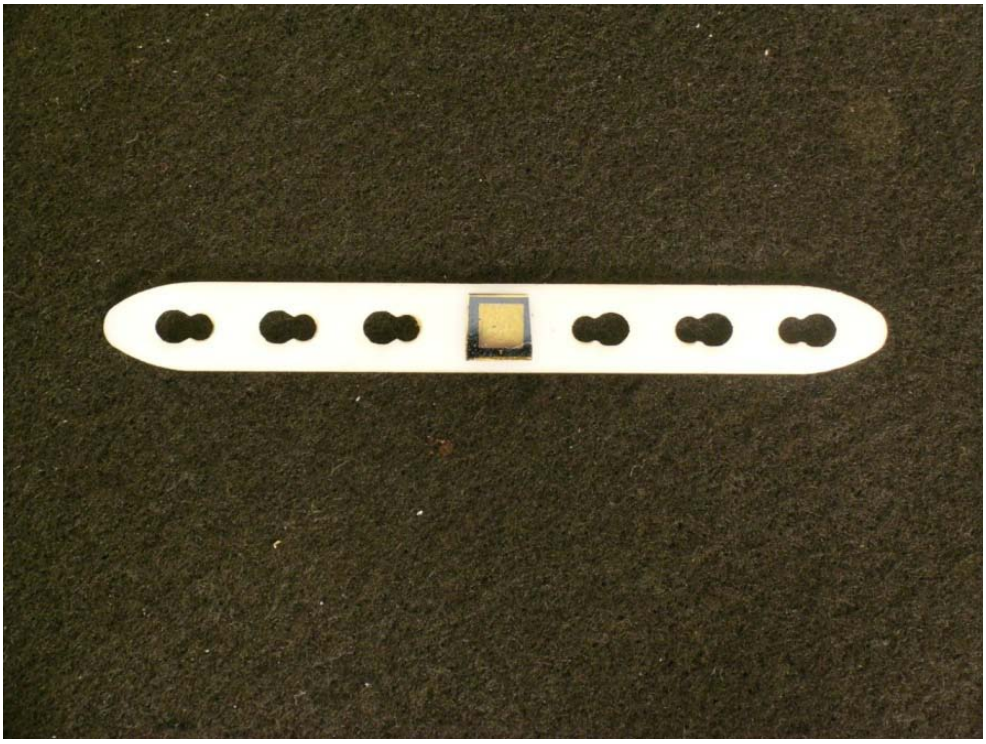

**Figure 6.3.27. Photograph of the sample implant produced by the company "Synthes" specially for our sensor.**

We performed our soft tissue experiments with the experimental setup shown in Fig. 6.3.28. The two-sectioned wood is used to simulate the broken bone, the implantable stick is attached to the wood and our sensor is attached to the implantable stick via hard epoxy. We use probe antennas as the external antennas.

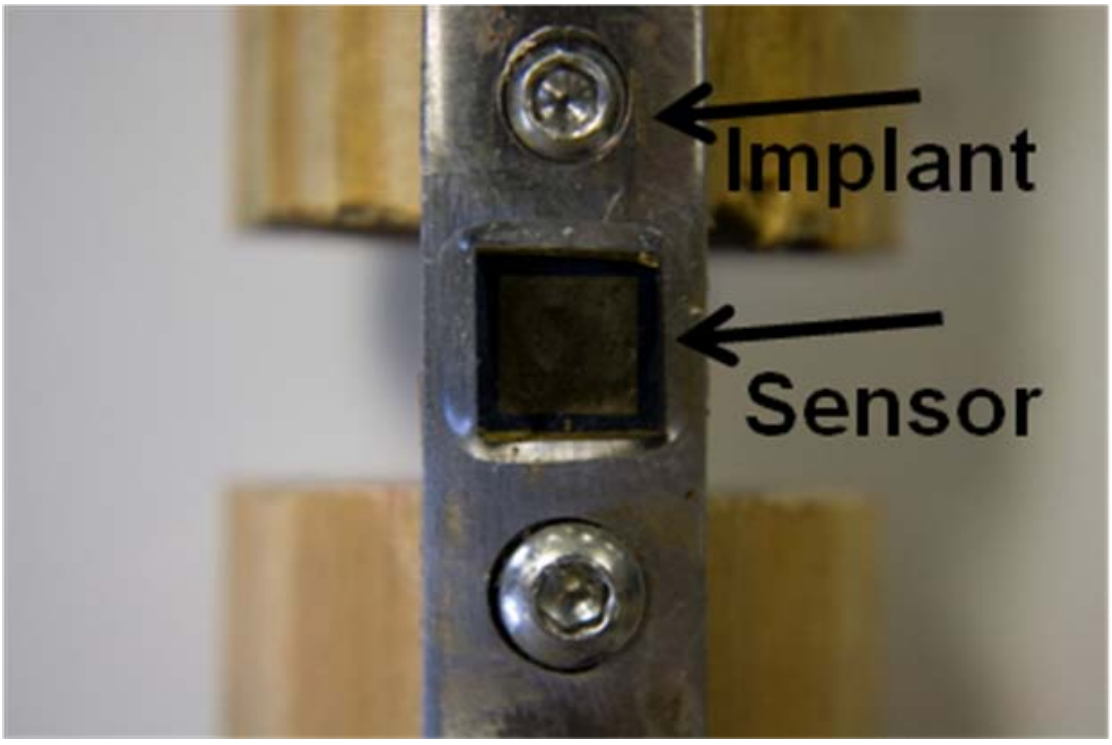


(a)

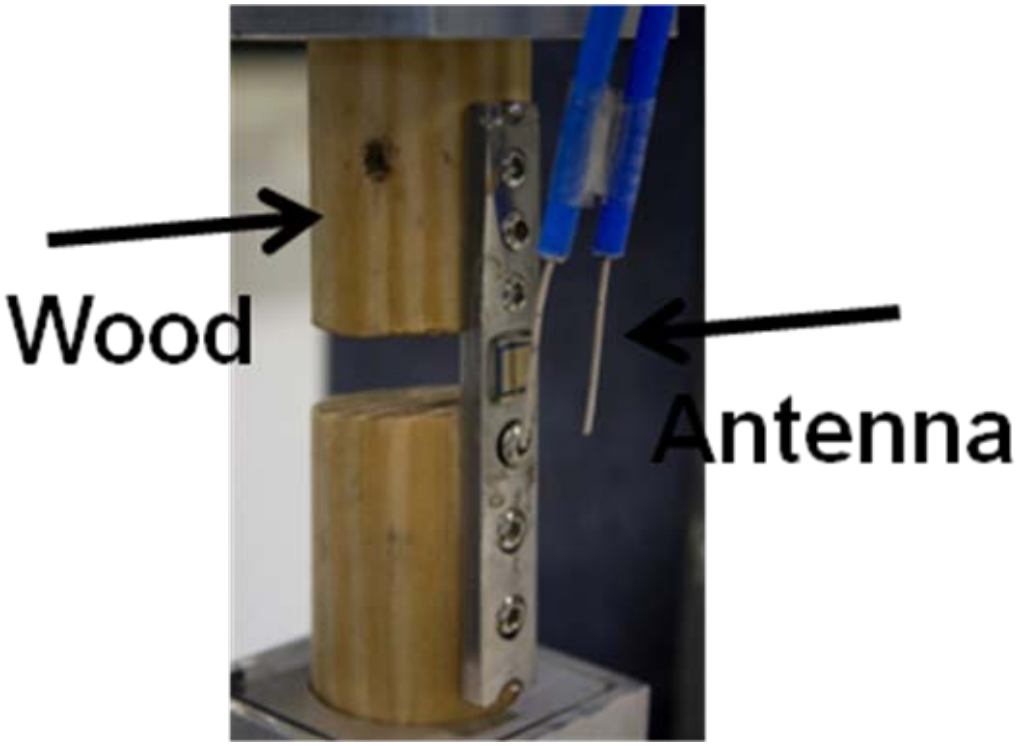


(b)

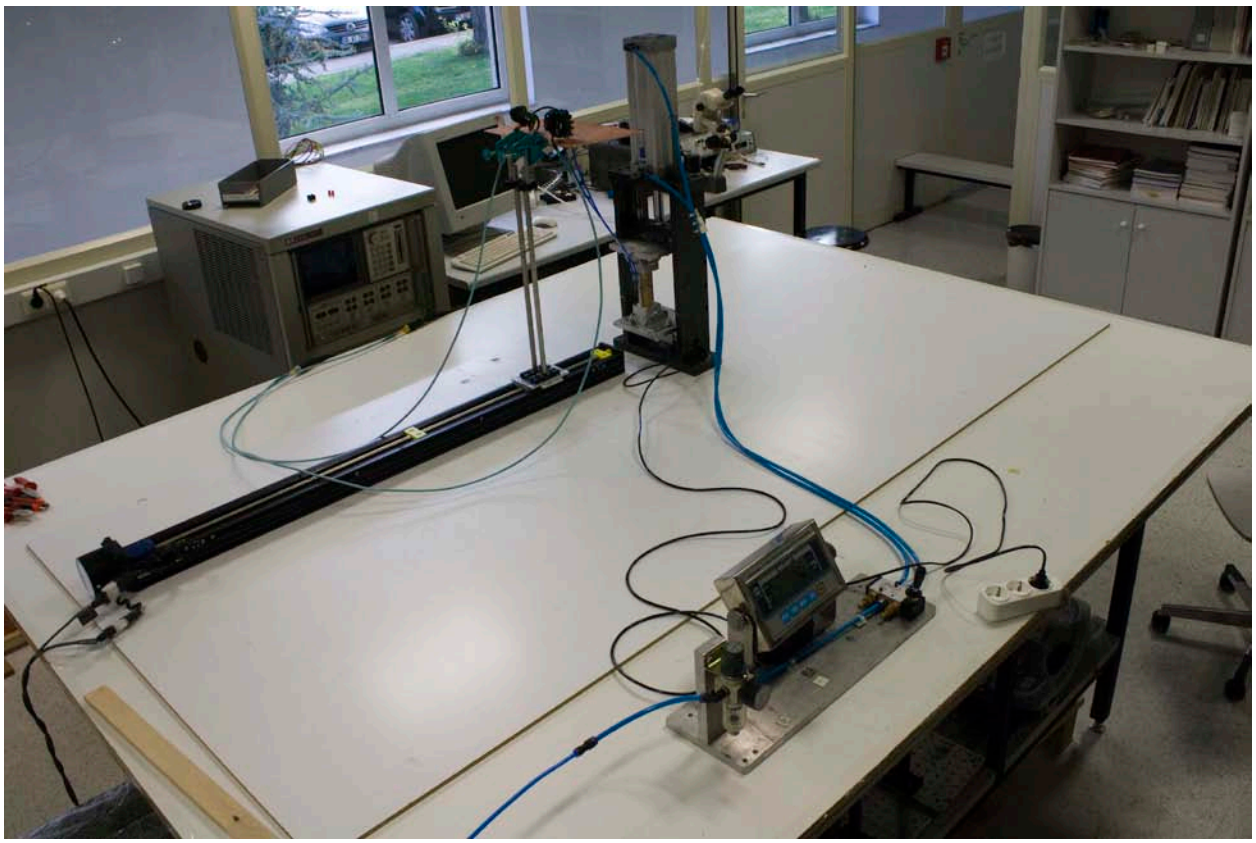

(c)

**Figure 6.3.28. Photographs of the experimental setup from different angles (a) – (c).**

## A) Perpendicular Load Application:

We performed our experiments using the perpendicular load application setup shown in Fig. 6.3.29. Wireless sensing is tested with our 0.8 cm × 0.8 cm nested metamaterial sensor. The calibration is the same as that described in Section 6.3.4 and the fabrication procedure of the sensors is the same as in Section 6.1. Fig. 6.3.30 shows the no soft tissue case, while Fig. 6.3.31 depicts 0.5 cm thick soft tissue case and Fig. 6.3.32 demonstrates 1 cm thick soft tissue case. The 2 cm thick soft tissue case can be seen in Fig. 6.3.33, the 5 cm thick soft tissue case is shown in Fig. 6.3.34, the 10 cm thick soft tissue case is depicted in Fig. 6.3.35 and the 20 cm thick soft tissue case is demonstrated in Fig. 6.3.36. Although the linearity is not good for 5 cm thick and

20 cm thick soft tissue cases, wireless sensing is still achieved. To demonstrate this, we divided the working range of the sensor into narrower ranges.

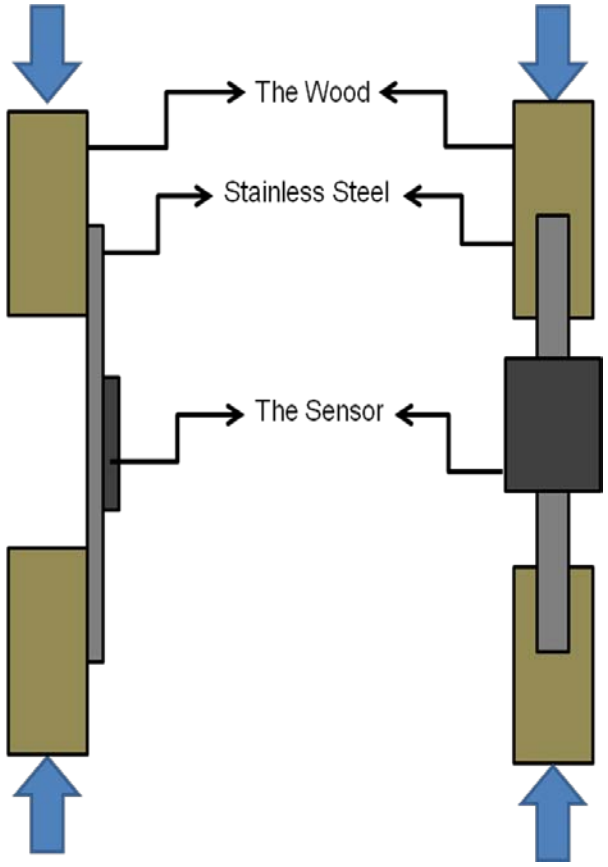


**Figure 6.3.29. Schematic illustration of the perpendicular load application apparatus.**

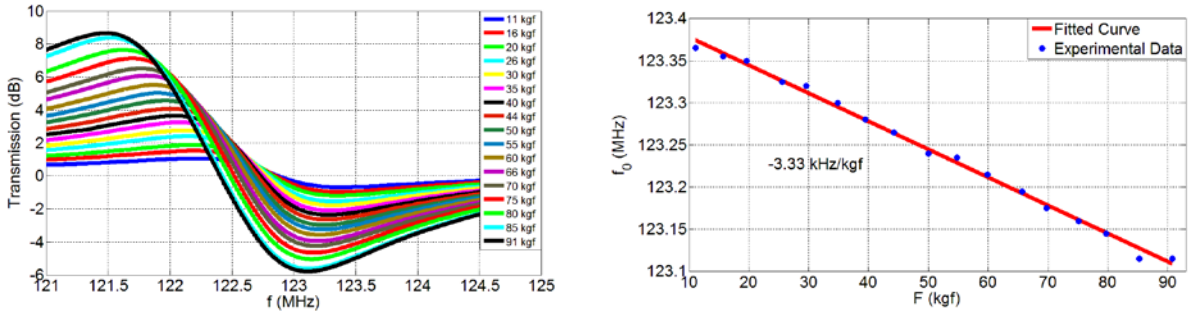


(a) (b)

**Figure 6.3.30. Experimental measurement of our 0.8 cm × 0.8 cm nested metamaterial sensor with no soft tissue: (a) Transmission spectra and (b) F *vs.* $f_0$.**

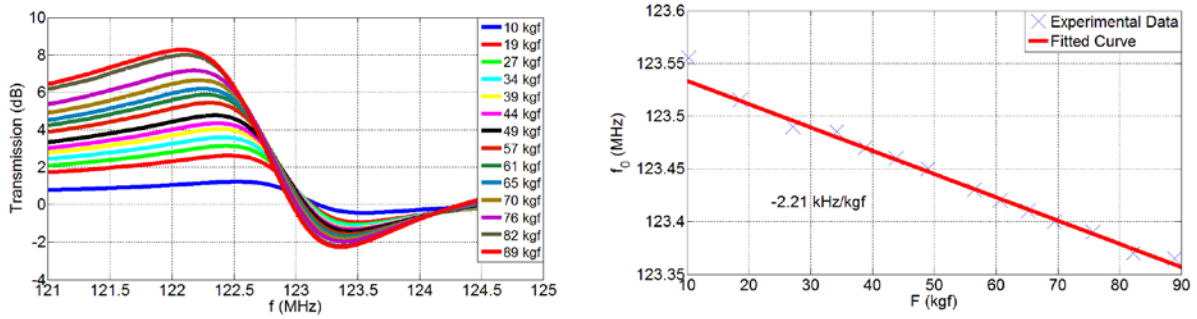


(a) (b)

**Figure 6.3.31. Experimental measurement of our 0.8 cm × 0.8 cm nested metamaterial sensor across 0.5 cm thick soft tissue: (a) Transmission spectra and (b) F *vs.* $f_0$.**

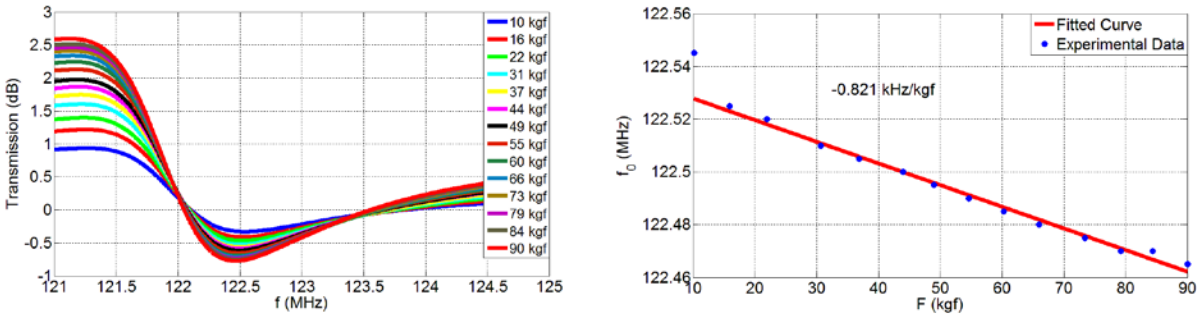


(a) (b)

**Figure 6.3.32. Experimental measurement of our 0.8 cm × 0.8 cm nested metamaterial sensor across 1 cm thick soft tissue: (a) Transmission spectra and (b) F *vs.* $f_0$.**

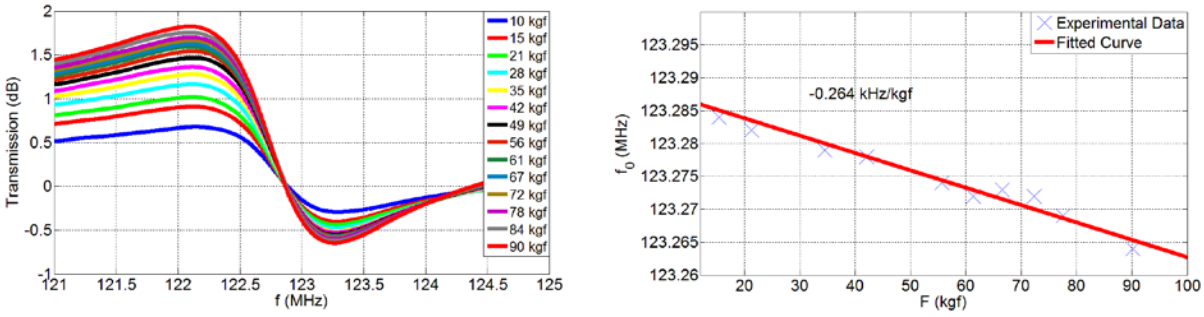


(a) (b)

**Figure 6.3.33. Experimental measurement of our 0.8 cm × 0.8 cm nested metamaterial sensor across 2 cm thick soft tissue: (a) Transmission spectra and (b) F *vs.* $f_0$.**

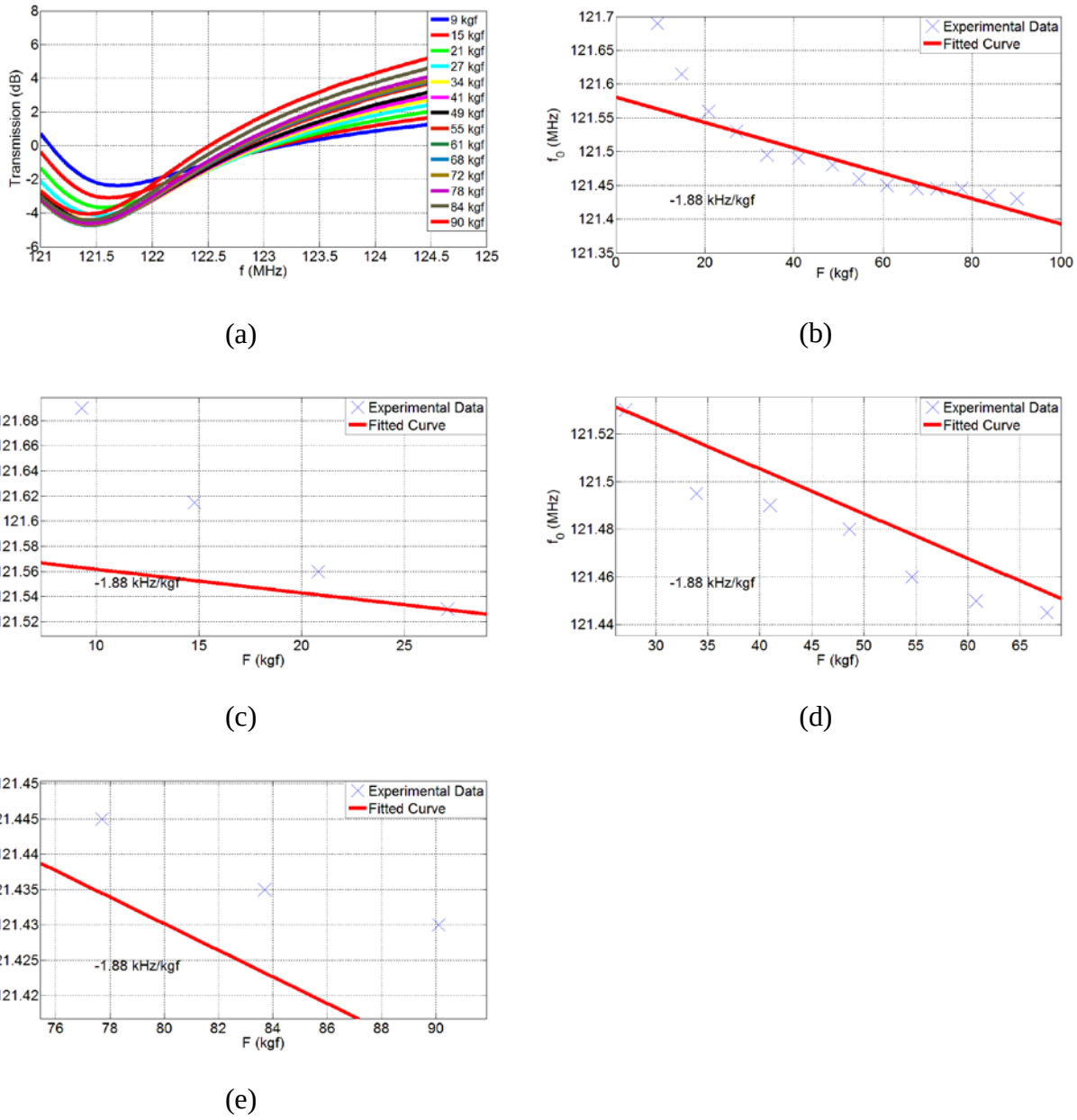


**Figure 6.3.34. Experimental measurement of our 0.8 cm × 0.8 cm nested metamaterial sensor across 5 cm thick soft tissue: (a) Transmission spectra, (b) F *vs.* $f_0$, (c) narrower working range 1, (d) narrower working range 2, and (e) narrower working range 3.**

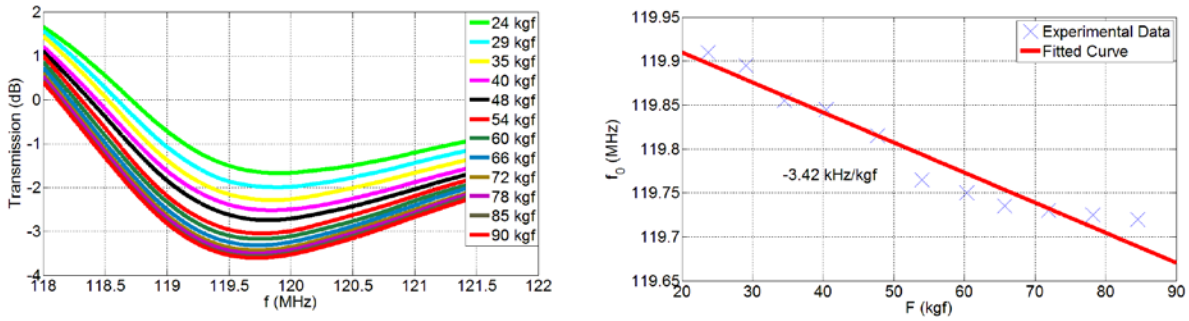


(a) (b)

**Figure 6.3.35. Experimental measurement of our 0.8 cm × 0.8 cm nested metamaterial sensor across 10 cm thick soft tissue: (a) Transmission spectra and (b) F *vs.* $f_0$.**

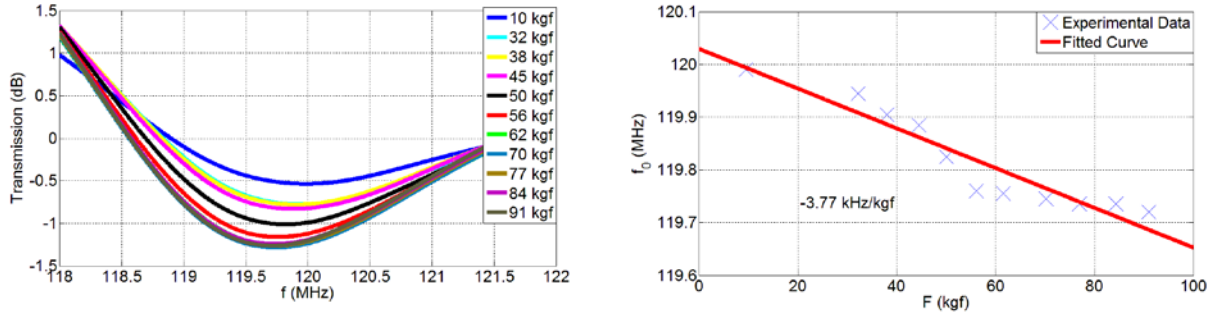


(a) (b)

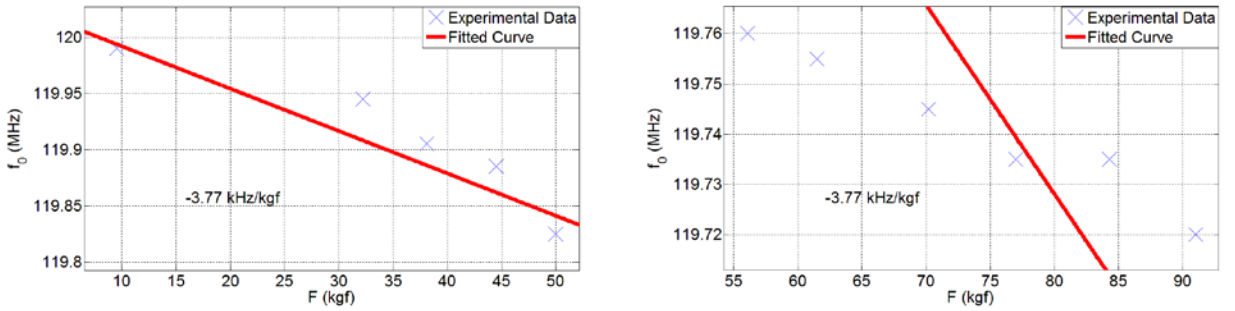


(c) (d)

**Figure 6.3.36. Experimental measurement of our 0.8 cm × 0.8 cm nested metamaterial sensor across 20 cm thick soft tissue: (a) Transmission spectra, (b) F *vs.* $f_0$, (c) narrower working range 1, and (d) narrower working range 2.**

## B) Angular (Twisted) Load Application:

In real-life application, the bone does not have to be fixed perpendicularly to the ground. There may be some angle different than $90^0$ between the fixation plate of the bone and the ground. To simulate this situation, we performed experiments with angular load application apparatus. We demonstrate the twisted load application setup in Fig. 6.3.37. Sensing with no soft tissue case is shown in Fig. 6.3.38, sensing with 0.5 cm thick soft tissue is depicted in Fig. 6.3.39 and that with 5 cm thick soft tissue is presented in Fig. 6.3.40. Although the linearity is not good in 5 cm thick soft tissue case, the sensing is still possible. In order to illustrate this, we divided the working range of the sensor into narrower ranges.

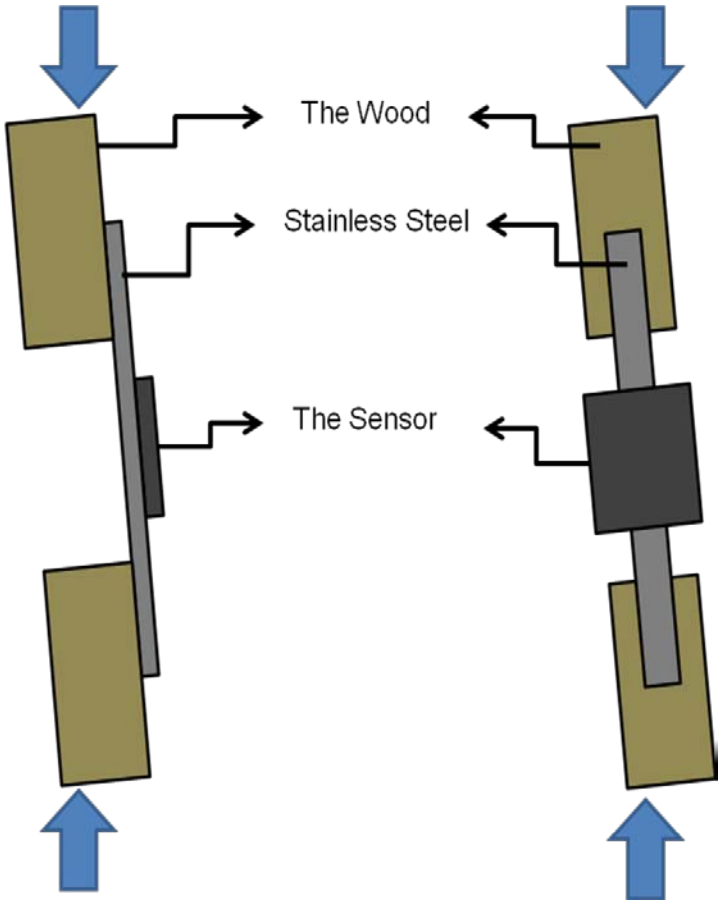


**Figure 6.3.37. Schematic illustration of the angular load application apparatus.**

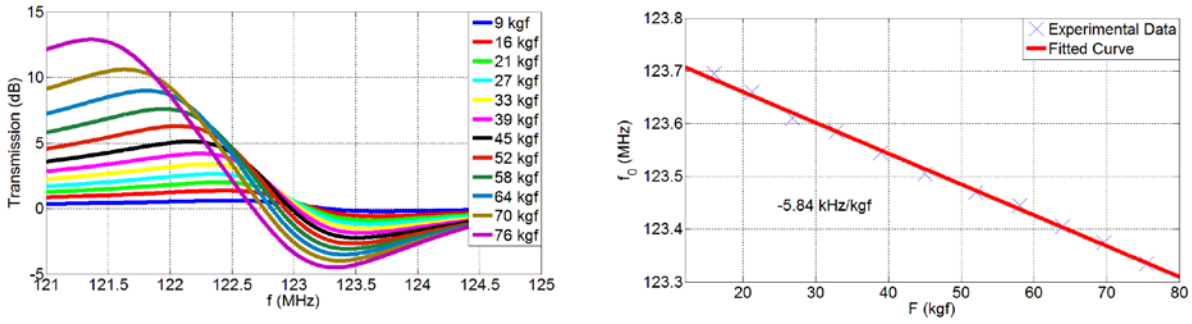


(a) (b)

**Figure 6.3.38. Experimental measurement of our 0.8 cm × 0.8 cm nested metamaterial sensor with no soft tissue: (a) Transmission spectra and (b) F *vs.* $f_0$.**

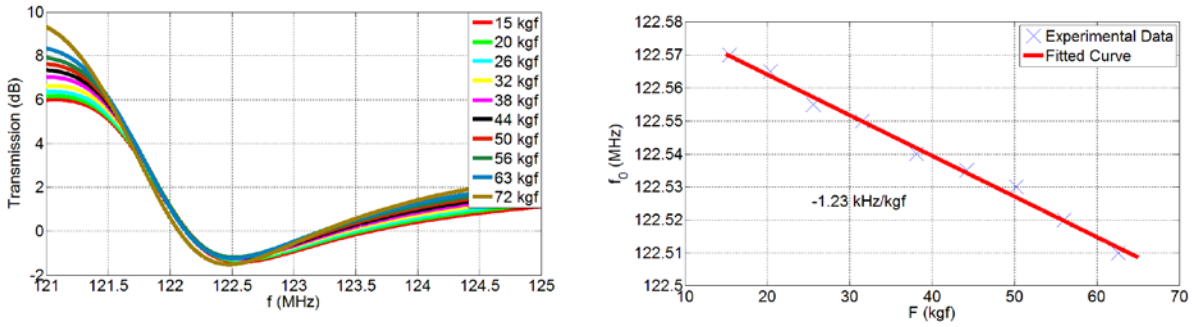


(a) (b)

**Figure 6.3.39. Experimental measurement of our 0.8 cm × 0.8 cm nested metamaterial sensor across 0.5 cm thick soft tissue: (a) Transmission spectra and (b) F *vs.* $f_0$.**

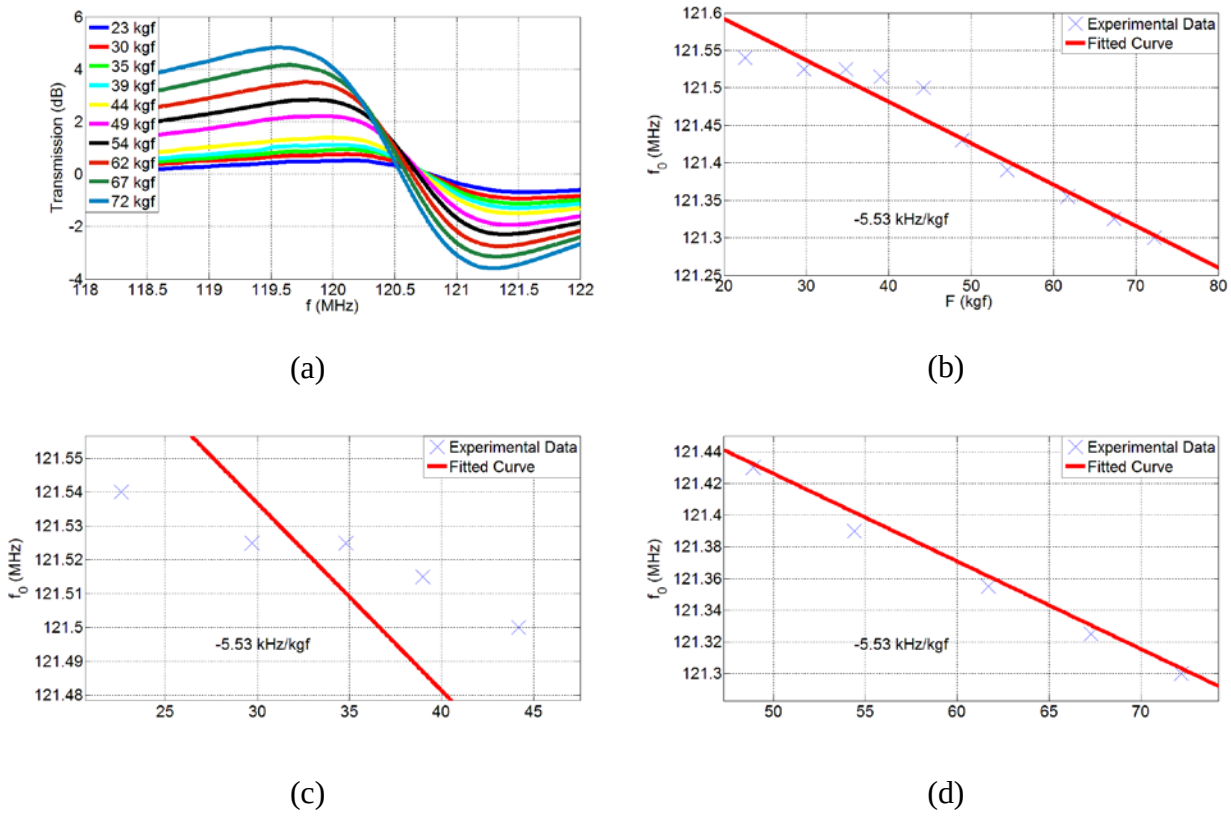


**Figure 6.3.40. Experimental measurement of our 0.8 cm × 0.8 cm nested metamaterial sensor across 5 cm thick soft tissue: (a) Transmission spectra, (b) F *vs.* $f_0$, (c) narrower working range 1, and (d) narrower working range 2.**

# 6.3.6 Experiments with 0.8 cm × 0.8 cm flexible sensor chip on wood test material

In this section, we observe the performance of the vacuum tape-based flexible 0.8 cm × 0.8 cm nested metamaterial sensor. The fabrication procedure of the sensor is the same as in Section 5.2. The calibration method used in this section is the same as that described in Section 6.3.4. The vacuum tape-based flexible sensor is shown in Fig. 6.3.41. The vacuum tape-based flexible sensor shows better performance as wireless strain sensors compared to the silicon-based sensor in Section 6.3.5. Since the sensor is flexible, it can be used on non-flat surfaces. The flexible

sensor also exhibits better linearity compared to the silicon-based sensor. Because flexible sensor features better linearity and it is usable on non-flat surfaces, the vacuum tape-based flexible sensor makes a better sensor compared to silicon-based sensor for wireless strain sensing.

We observe lower errors with flexible sensor because of the mechanical aspects of the system. This flexible sensor, which incorporates the vacuum tape, is more linear possibly because it uses a flexible substrate. The flexible substrate propagates the strain regardless of the orientation; however, the silicon substrate captures the strain depending on the orientation, and hence the sensor with flexible substrate is more linear. The use of an external epoxy also plays an important role in the sensor's linearity. Since external epoxy is not required for fixation of the vacuum tape substrate to the test materials, the strain induced on the test materials directly propagates to the vacuum tape substrate. However, external epoxy is required to attach the silicon substrate to the test materials. Hence, part of the applied strain may not be directly conferred to the silicon substrate. We hypothesize that this rationale may explain why the silicon substrate's frequency response does not change linearly with respect to the applied load because of this mechanically composite structure. Therefore, the tape-based flexible sensor's response is more linear than the silicon-based sensor's response.

There is no significant difference using small thickness of soft tissue (thinner than 5 cm) between the silicon-based sensor and the vacuum tape-based flexible sensor. However, for large thicknesses soft tissue (thicker than 5 cm), we observe a huge difference between the sensor performance of the silicon-based sensor and the vacuum tape-based flexible sensor in terms of the error. Because obtaining high level of signal with higher thickness of soft tissue is more difficult, the mechanical aspects of the system become more important for sensing operation. Hence, the difference of the sensor performance between the silicon-based sensor and the vacuum tape-based flexible sensor in terms of error becomes clearer.

We divided our experimental procedures into experiments with perpendicular load application and experiments with angular load application. We observed the performance of the flexible sensor and compared it against silicon-based sensor. In all cases, the flexible sensor performed

wireless sensing and exhibited better linearity compared to the silicon-based sensor. In perpendicular load application, Fig. 6.3.42 shows sensing with no soft tissue case. Fig. 6.3.43 presents a comparison of the sensing performances of the silicon-based sensor and the vacuum tape-based flexible sensor with no soft tissue case. Fig. 6.3.44 presents sensing with 0.5 cm thick soft tissue case. Fig. 6.3.45 depicts comparison of the sensing performances of the silicon-based sensor and the vacuum tape-based flexible sensor with 0.5 cm thick soft tissue case. Fig. 6.3.46 shows sensing with 1 cm thick soft tissue case, while Fig. 6.3.47 shows comparison of the sensing performances of the silicon-based sensor and the vacuum tape-based flexible sensor with 1 cm thick soft tissue. Fig. 6.3.48 demonstrates sensing with 2 cm thick soft tissue, while Fig. 6.3.49 presents a comparison of the sensing performances of the silicon-based sensor and the vacuum tape-based flexible sensor with 2 cm thick soft tissue. Fig. 6.3.50 depicts sensing with 5 cm thick soft tissue, whereas Fig. 6.3.51 shows a comparison of the sensing performances of the silicon-based sensor and the vacuum tape-based flexible sensor with 5 cm thick soft tissue. Fig. 6.3.52 demonstrates sensing with 10 cm thick soft tissue, while Fig. 6.3.53 presents a comparison of the sensing performances of silicon-based sensor and vacuum tape-based flexible sensor with 10 cm thick soft tissue. Fig. 6.3.54 presents sensing with 20 cm thick soft tissue, while Fig. 6.3.55 depicts comparison of the sensing performances of the silicon-based sensor and the vacuum tape-based flexible sensor with 20 cm thick soft tissue.

For angular load application, sensing with no soft tissue is shown in Fig. 6.3.56, comparison of the silicon-based sensor and vacuum tape-based flexible sensor with no soft tissue is demonstrated in Fig. 6.3.57; sensing with 0.5 cm thick soft tissue is depicted in Fig. 6.3.58, comparison of the silicon-based sensor and the vacuum tape-based flexible sensor with 0.5 cm thick soft tissue is presented in Fig. 6.3.59; sensing with 5 cm thick soft tissue is depicted in Fig. 6.3.60 and comparison of the silicon-based sensor and the vacuum tape-based flexible sensor with 5 cm thick soft tissue is shown in Fig. 6.3.61.

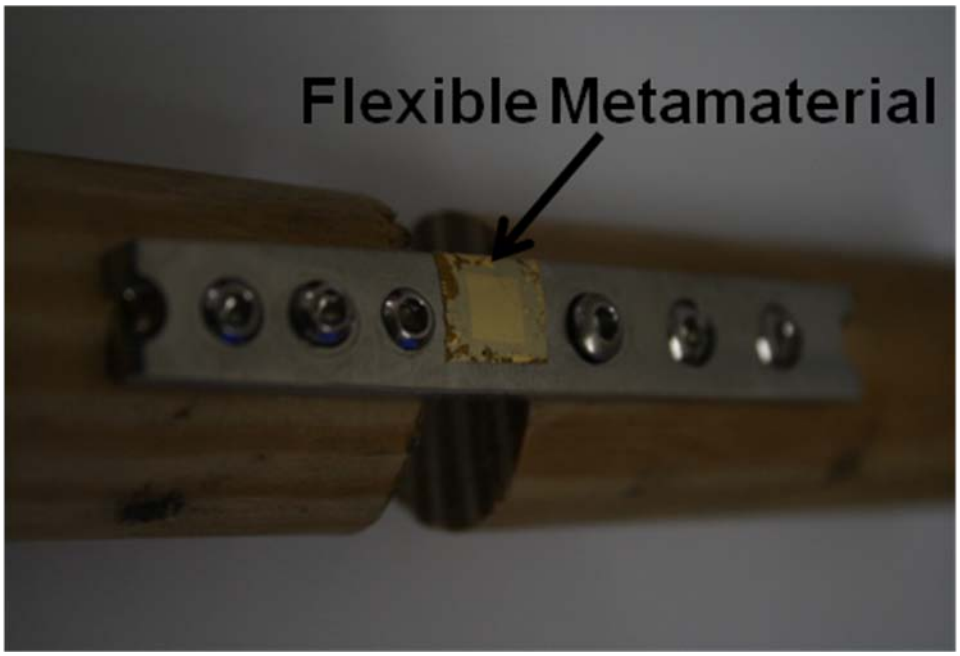


(a)

(b)

(c)

**Figure 6.3.41. Photographs of our flexible sensors from different angles (a) – (c).**

## A) Perpendicular Load Application:

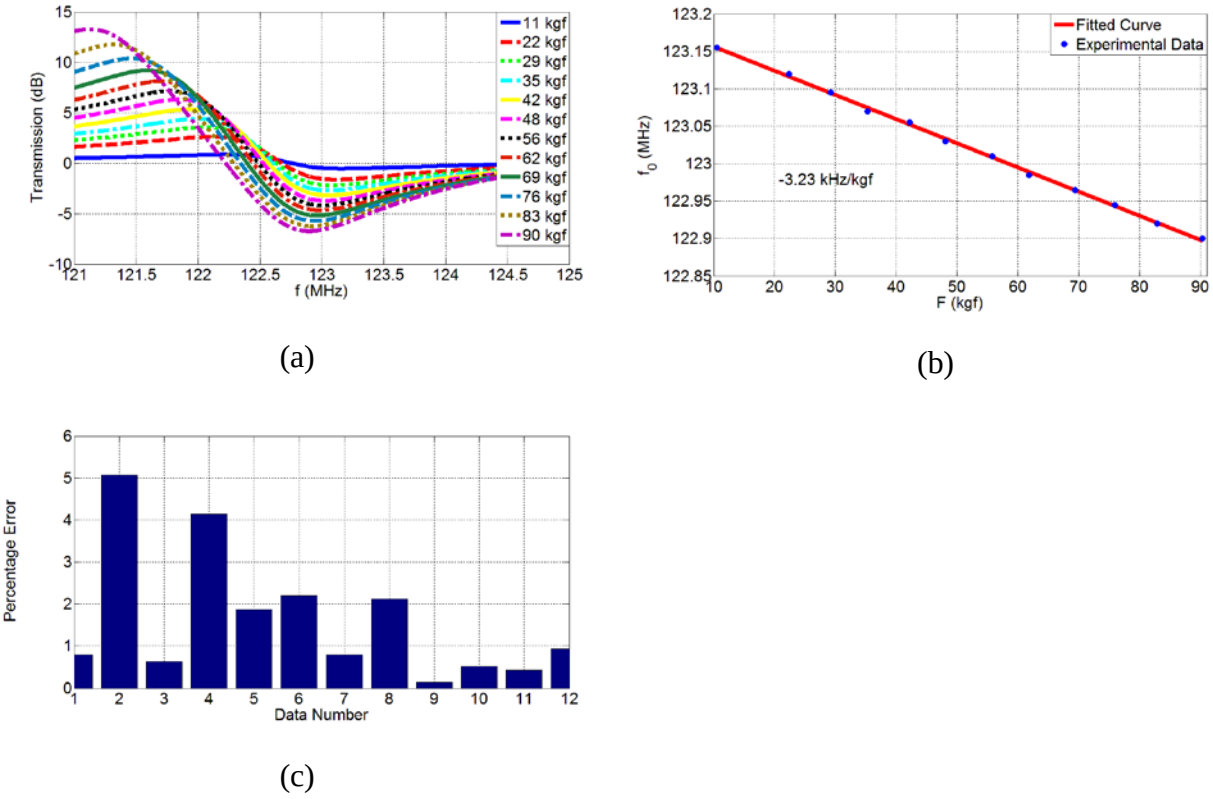


**Figure 6.3.42. Experimental measurement of our flexible 0.8 cm × 0.8 cm nested metamaterial sensor with no soft tissue: (a) Transmission spectra, (b) F *vs.* $f_0$, and (c) errors in terms of percentage.**

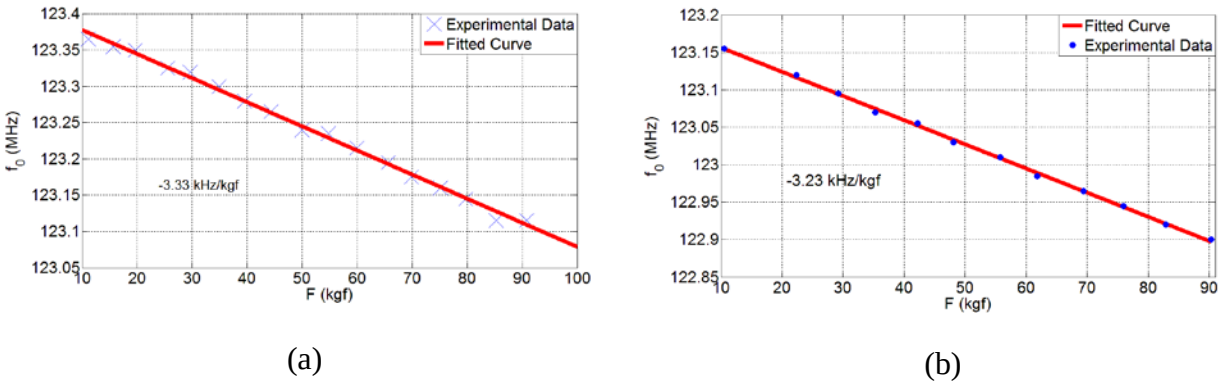


**Figure 6.3.43. Comparison of the sensing performances of the silicon-based sensor and the vacuum tape-based flexible sensor with no soft tissue: (a) The silicon-based sensor and (b) the vacuum tape-based flexible sensor.**

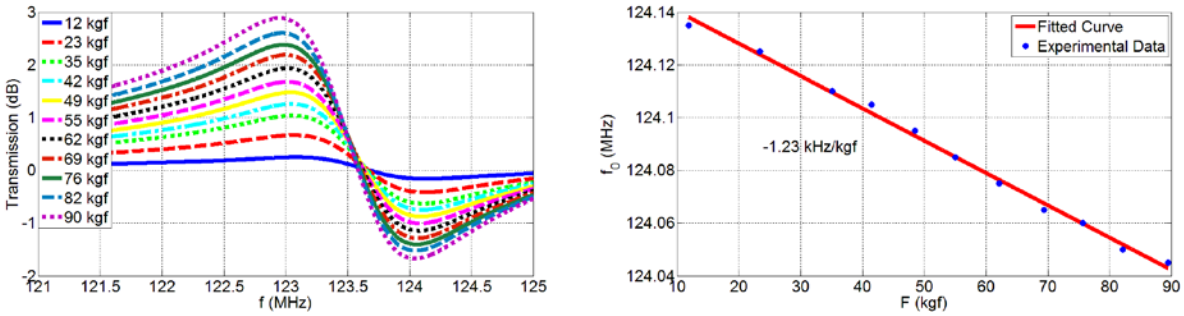


(a) (b)

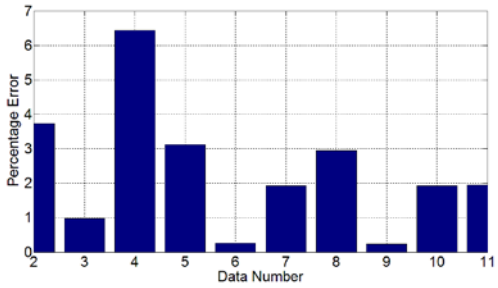


(c)

**Figure 6.3.44. Experimental measurement of our flexible 0.8 cm × 0.8 cm nested metamaterial sensor using 0.5 cm thick soft tissue: (a) Transmission spectra, (b) F *vs.* $f_0$, and (c) errors in terms of percentage.**

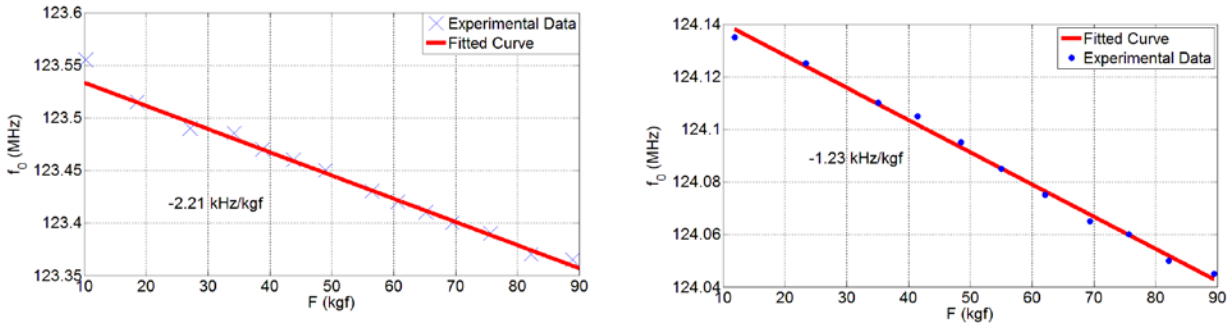


(a) (b)

**Figure 6.3.45. Comparison of the sensing performances of the silicon-based sensor and the vacuum tape-based flexible sensor using 0.5 cm thick soft tissue: (a) The silicon-based sensor and (b) the vacuum tape-based flexible sensor.**

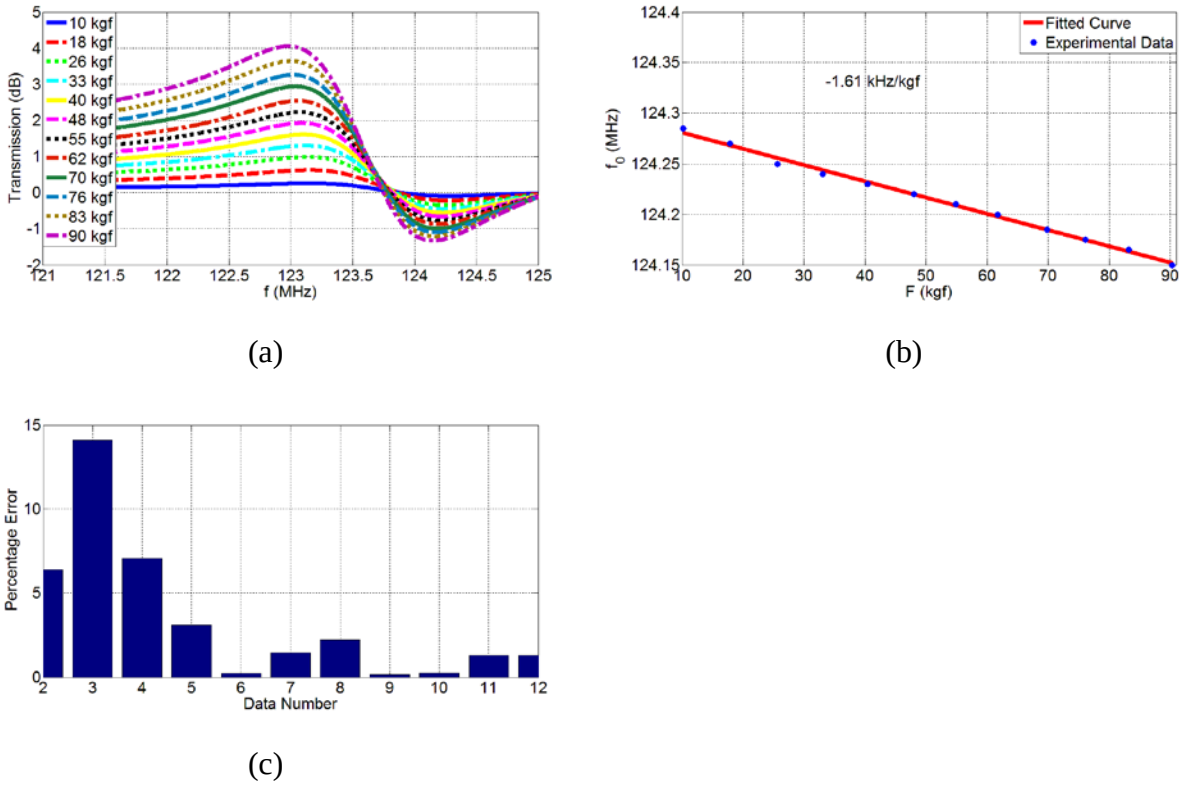


**Figure 6.3.46. Experimental measurement of our flexible 0.8 cm × 0.8 cm nested metamaterial sensor using 1 cm thick soft tissue: (a) Transmission spectra, (b) F *vs.* $f_0$, and (c) errors in terms of percentage.**

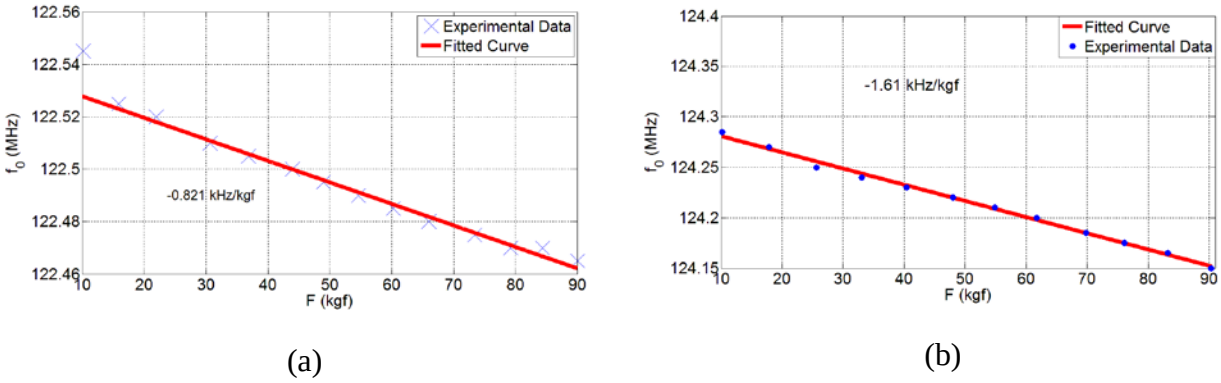


**Figure 6.3.47. Comparison of the sensing performances of the silicon-based sensor and the vacuum tape-based flexible sensor using 1 cm thick soft tissue: (a) The silicon-based sensor and (b) the vacuum tape-based flexible sensor.**

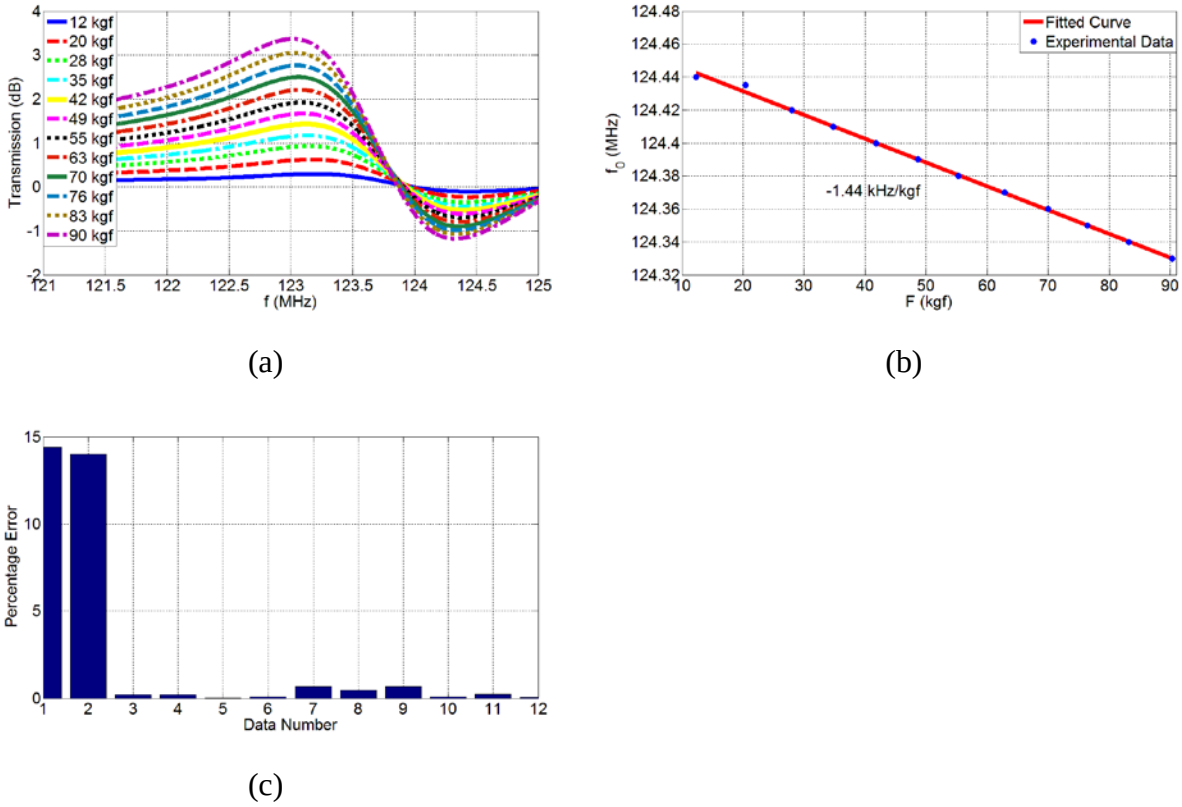


**Figure 6.3.48. Experimental measurement of our flexible 0.8 cm × 0.8 cm nested metamaterial sensor using 2 cm thick soft tissue: (a) Transmission spectra, (b) F *vs.* $f_0$, and (c) errors in terms of percentage.**

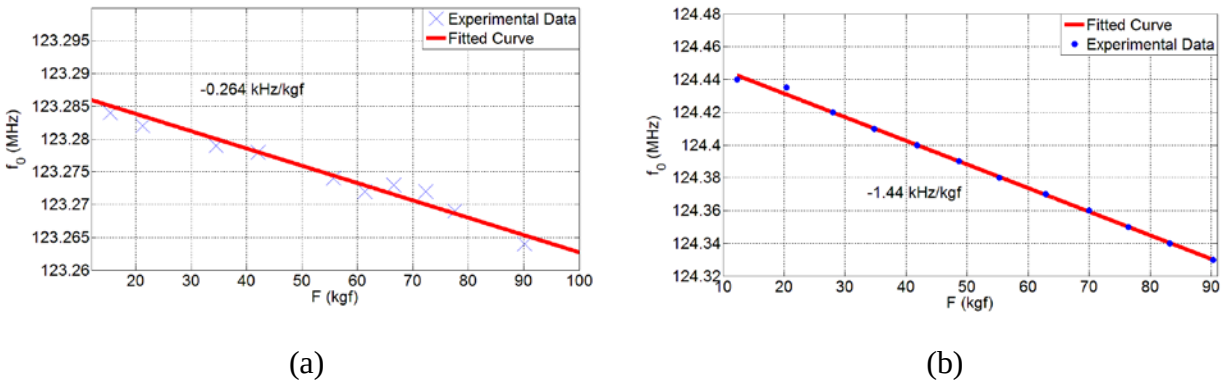


**Figure 6.3.49. Comparison of the sensing performances of the silicon-based sensor and the vacuum tape-based flexible sensor using 2 cm thick soft tissue: (a) The silicon-based sensor and (b) the vacuum tape-based flexible sensor.**

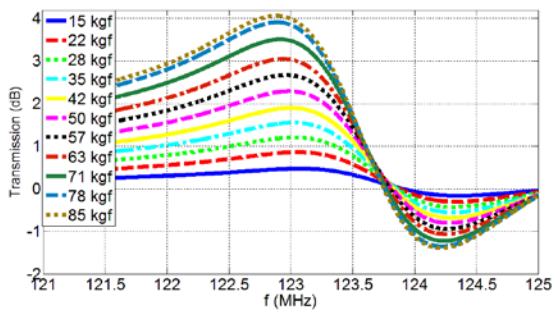


(a)

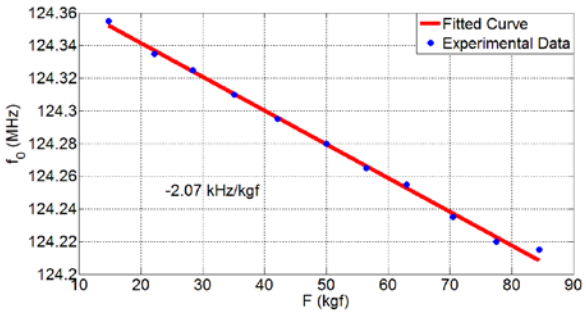


(b)

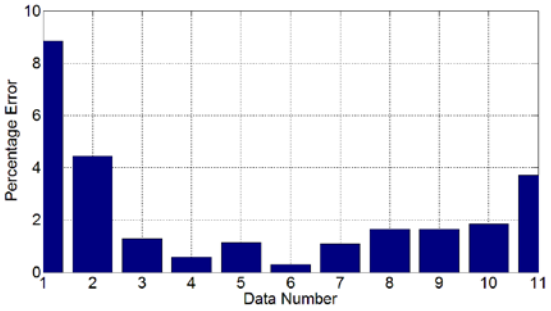


(c)

**Figure 6.3.50. Experimental measurement of our flexible 0.8 cm × 0.8 cm nested metamaterial sensor using 5 cm thick soft tissue: (a) Transmission spectra, (b) F *vs.* $f_0$, and (c) errors in terms of percentage.**

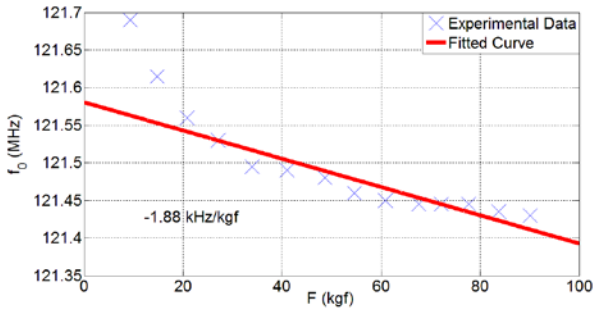


(a)

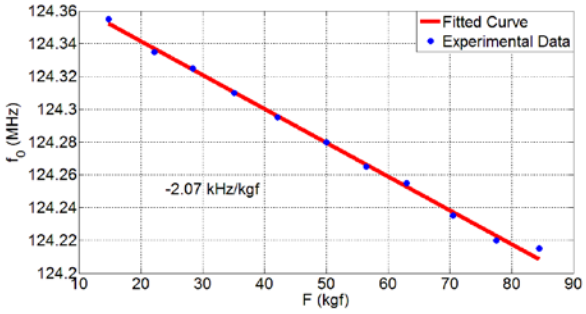


(b)

**Figure 6.3.51. Comparison of the sensing performances of the silicon-based sensor and the vacuum tape-based flexible sensor using 5 cm thick soft tissue: (a) The silicon-based sensor and (b) the vacuum tape-based flexible sensor.**

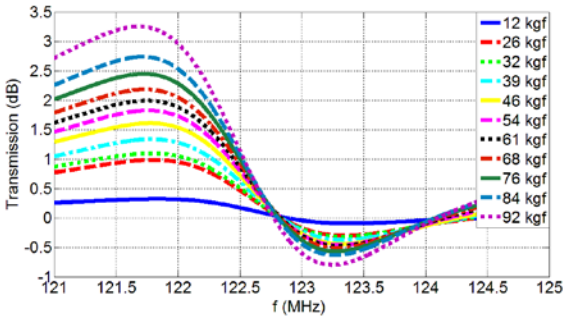


(a)

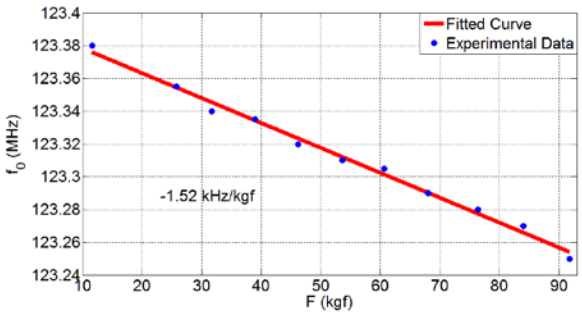


(b)

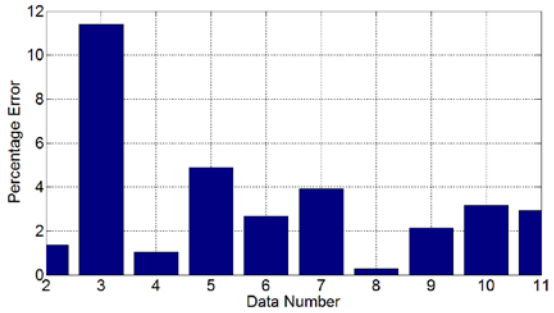


(c)

**Figure 6.3.52. Experimental measurement of our flexible 0.8 cm × 0.8 cm nested metamaterial sensor using 10 cm thick soft tissue: (a) Transmission spectra, (b) F *vs.* $f_0$, and (c) errors in terms of percentage.**

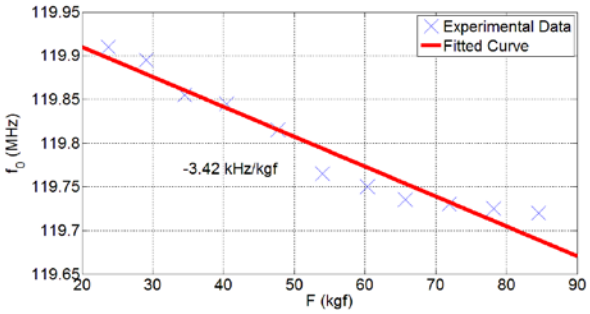


(a)

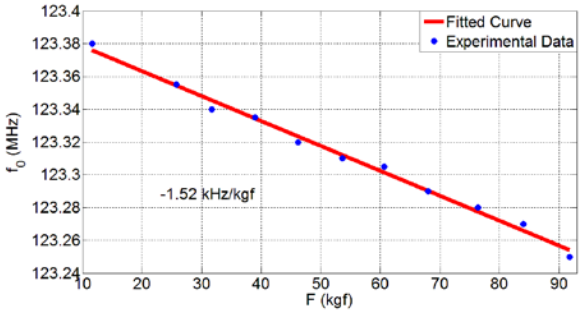


(b)

**Figure 6.3.53. Comparison of the sensing performances of the silicon-based sensor and the vacuum tape-based flexible sensor using 10 cm thick soft tissue: (a) The silicon-based sensor and (b) the vacuum tape-based flexible sensor.**

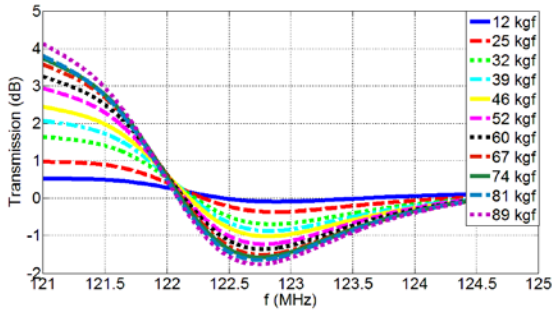


(a)

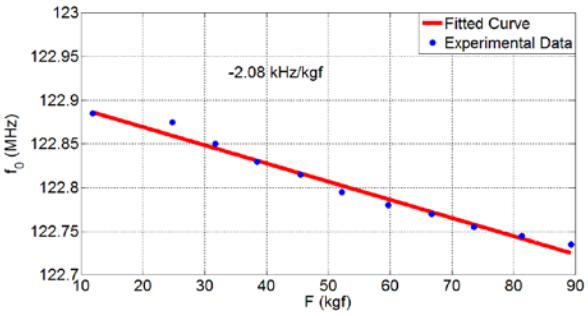


(b)

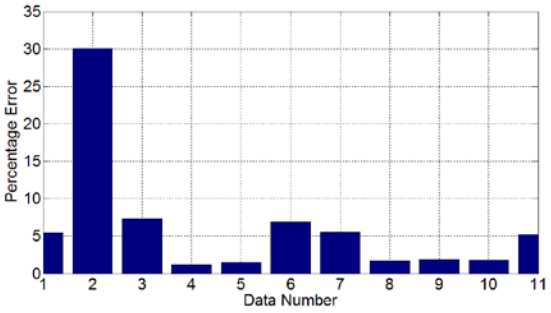


(c)

**Figure 6.3.54. Experimental measurement of our flexible 0.8 cm × 0.8 cm nested metamaterial sensor using 20 cm thick soft tissue: (a) Transmission spectra, (b) F *vs.* $f_0$, and (c) errors in terms of percentage.**

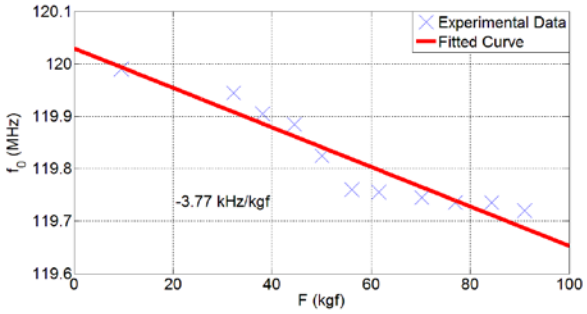


(a)

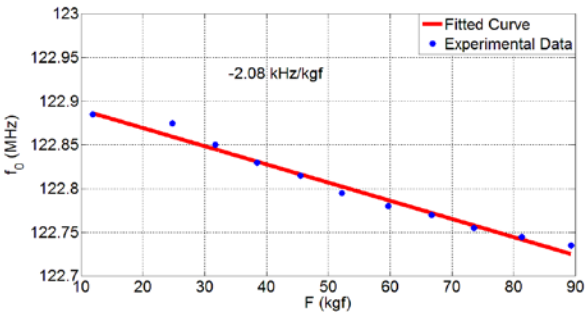


(b)

**Figure 6.3.55. Comparison of the sensing performances of the silicon-based sensor and the vacuum tape-based flexible sensor using 20 cm thick soft tissue: (a) The silicon-based sensor and (b) the vacuum tape-based flexible sensor.**

## B) Angular (Twisted) Load Application:

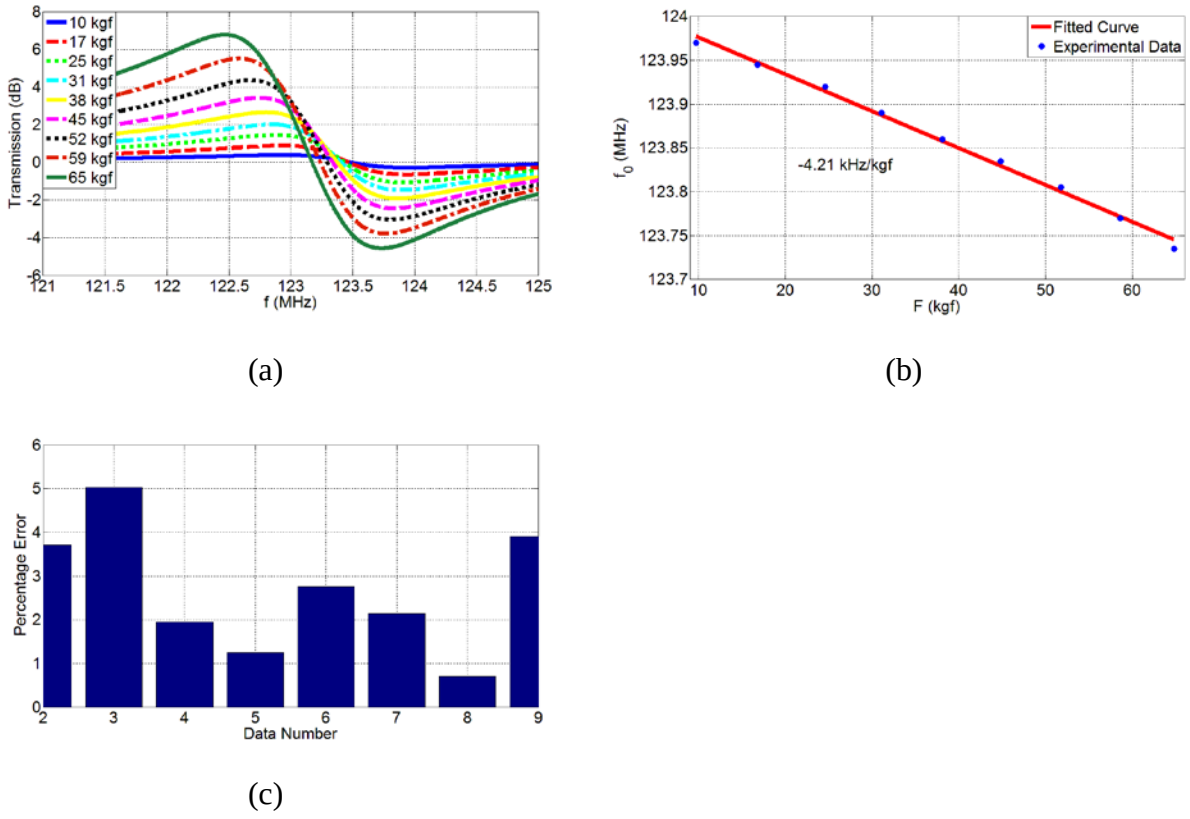


**Figure 6.3.56. Experimental measurement of our flexible 0.8 cm × 0.8 cm nested metamaterial sensor with no soft tissue: (a) Transmission spectra, (b) F *vs.* $f_0$, and (c) errors in terms of percentage.**

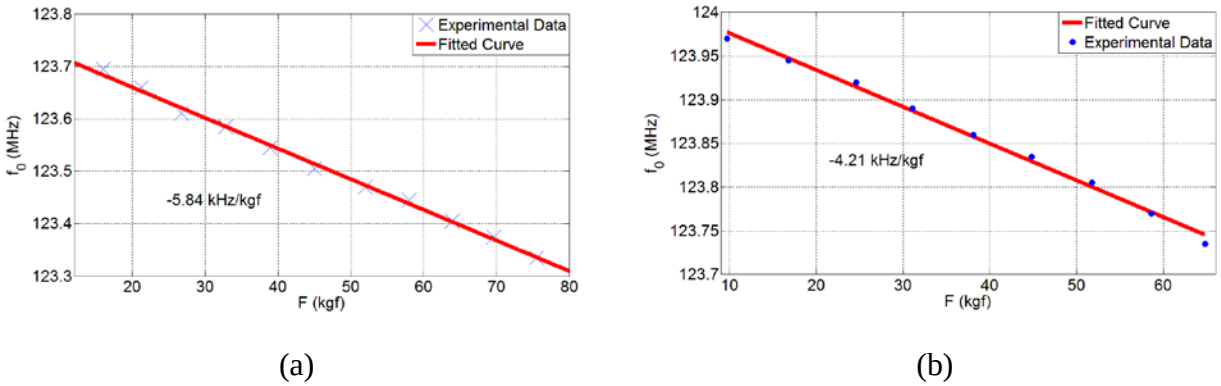


**Figure 6.3.57. Comparison of the sensing performances of the silicon-based sensor and the vacuum tape-based flexible sensor with no soft tissue: (a) The silicon-based sensor and (b) the vacuum tape-based flexible sensor.**

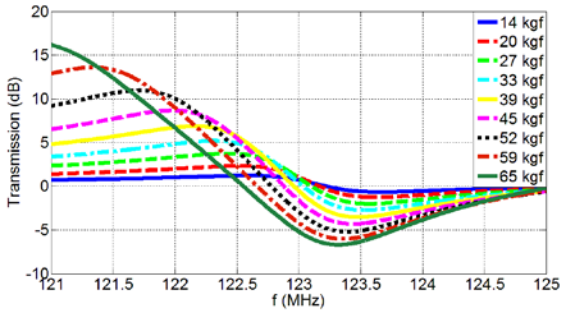


(a)

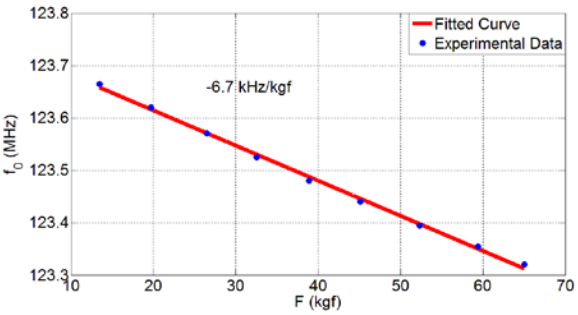


(b)

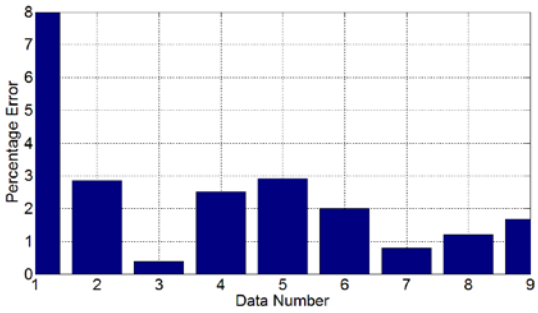


(c)

**Figure 6.3.58. Experimental measurement of our flexible 0.8 cm × 0.8 cm nested metamaterial sensor using 0.5 cm thick soft tissue: (a) Transmission spectra, (b) F *vs.* $f_0$, and (c) errors in terms of percentage.**

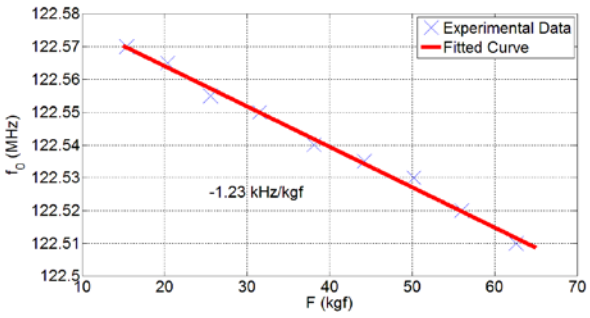


(a)

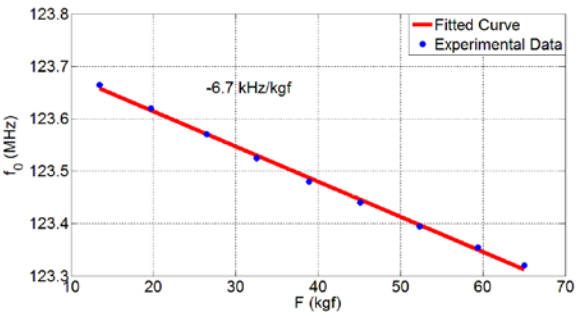


(b)

**Figure 6.3.59. Comparison of the sensing performances of the silicon-based sensor and the vacuum tape-based flexible sensor using 0.5 cm thick soft tissue: (a) The silicon-based sensor and (b) the vacuum tape-based flexible sensor.**

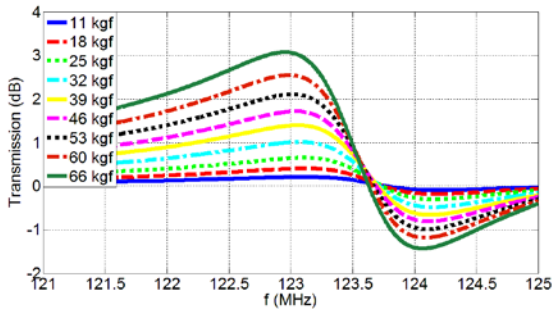


(a)

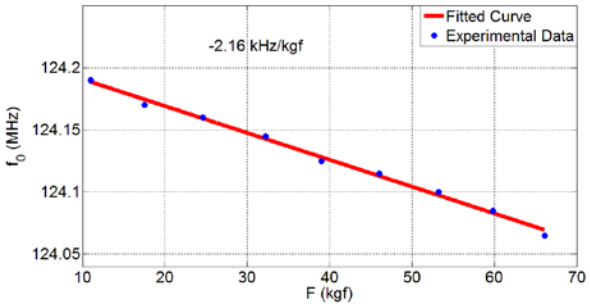


(b)

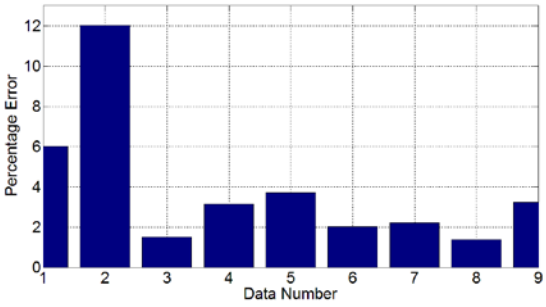


(c)

**Figure 6.3.60. Experimental measurement of our flexible 0.8 cm × 0.8 cm nested metamaterial sensor using 5 cm thick soft tissue: (a) Transmission spectra, (b) F *vs.* $f_0$, and (c) errors in terms of percentage.**

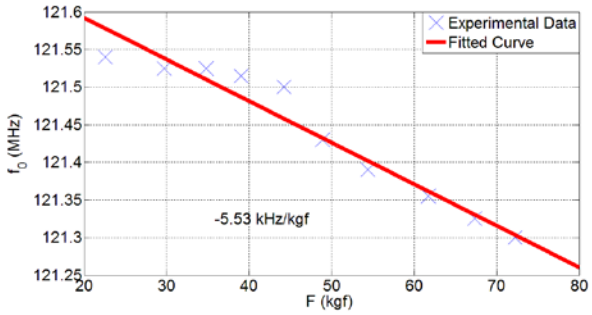


(a)

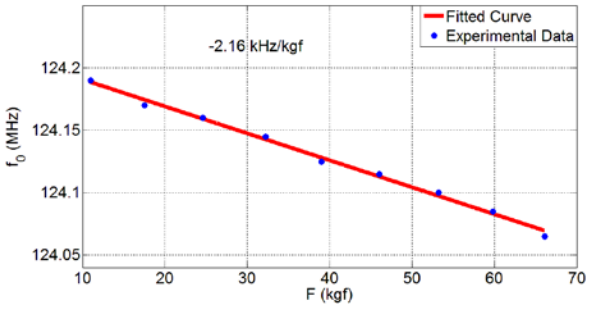


(b)

**Figure 6.3.61. Comparison of the sensing performances of the silicon-based sensor and the vacuum tape-based flexible sensor using 5 cm thick soft tissue: (a) The silicon-based sensor and (b) the vacuum tape-based flexible sensor.**

## 6.3.7 *Ex vivo* experiments with 0.8 cm chip

In this section, we performed *ex vivo* experiments supervised by Dr. Christian Puttlitz. Thus, we made experiments with the bone of sheep. We demonstrated that our sensor works in sheep's metatarsal, femur and spine. By using our sensors, we can monitor fracture healing in the body, even the fracture on spine.

In *ex vivo* experiments, we used sheep bone as depicted in Fig. 6.3.62. We attached the implantable plate to the bones and our sensor was attached to the implantable plate via hard epoxy. Here we used our 0.8 cm × 0.8 cm nested metamaterial sensor whose design parameters are given in Section 6.3.5. We also used the same calibration method as that described in Section 6.3.5.

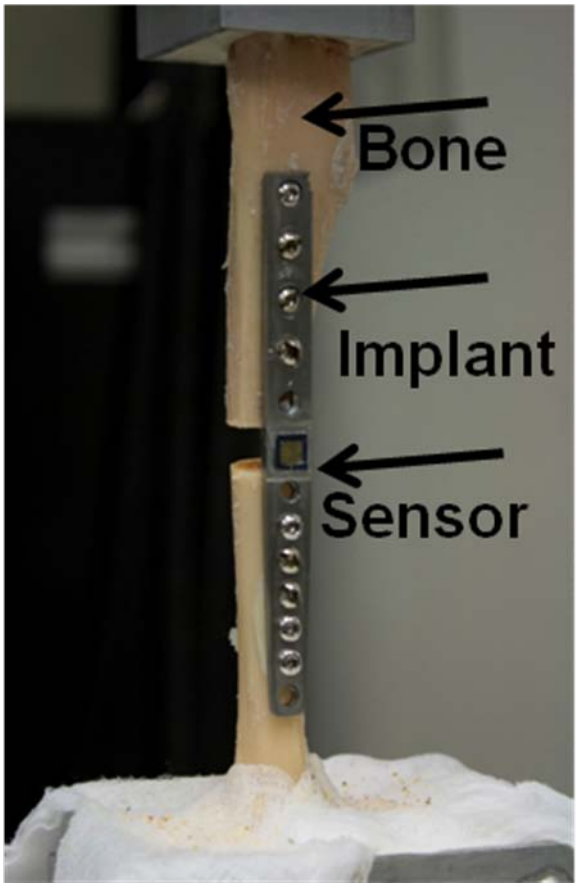


**Figure 6.3.62. Experimental apparatus for *ex vivo* experiments.**

We present the experimental setup for sheep's metatarsal in Fig. 6.3.63. As in real application, we put the cast over the bone. The stainless steel plate is attached to the bone while the sensor is attached to the stainless steel plate. The external antennas are in front of the cast, and we measure the transmission behavior of the sensor under different applied loads as demonstrated in Fig. 6.3.64. We observe that the wireless strain sensing is achieved in sheep's metatarsal. The metatarsal experiments resemble the *in vitro* experiments with no soft tissue because there is only skin in front of the metatarsal. Moreover, different from *in vitro* experiments on wood test material, we put cast over the bone. However, we again obtain similar results from metatarsal experiments when compared to the *in vitro* experiments performed with wood test material.

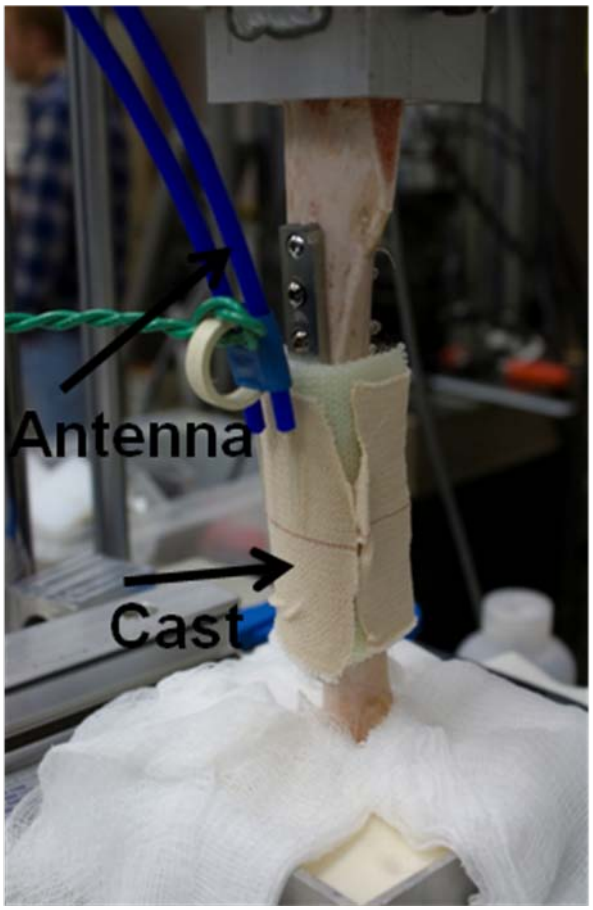


**Figure 6.3.63. Experimental setup for sheep's metatarsal.**

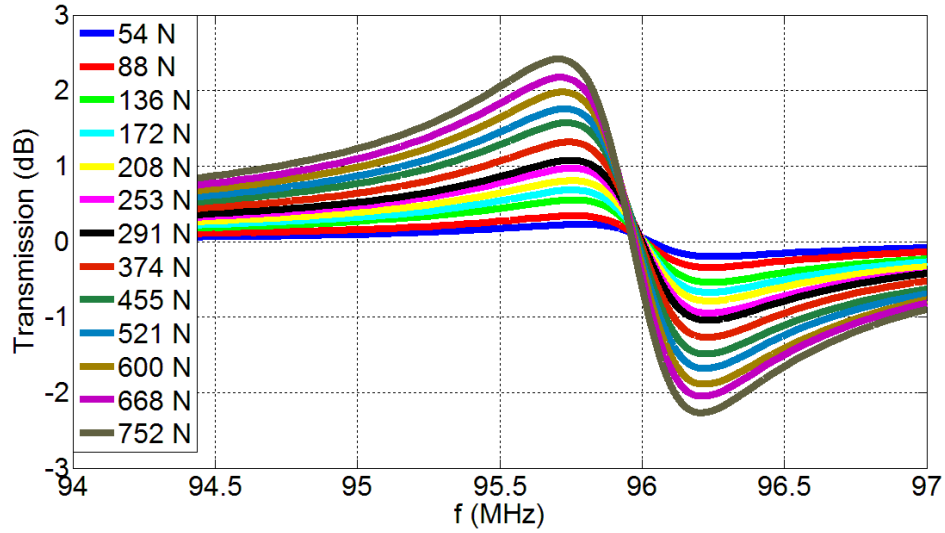


(a)

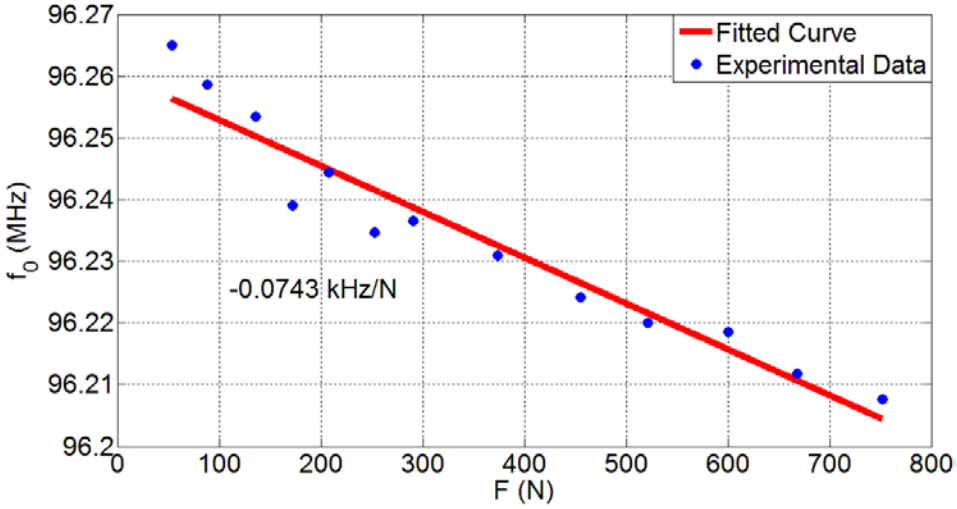


(b)

**Figure 6.3.64. Experimental measurement of our 0.8 cm × 0.8 cm nested metamaterial sensor on sheep's metatarsal: (a) Transmission spectra and (b) F *vs.* $f_0$.**

We also observe the case of the metatarsal without fracture. In this case, we do not observe sufficient sensing behavior from the sensor since the bone is very hard in this case and the strain on the bone passing onto the stainless steel implant is negligible. The results of metatarsal without fracture is depicted in Fig. 6.3.65.

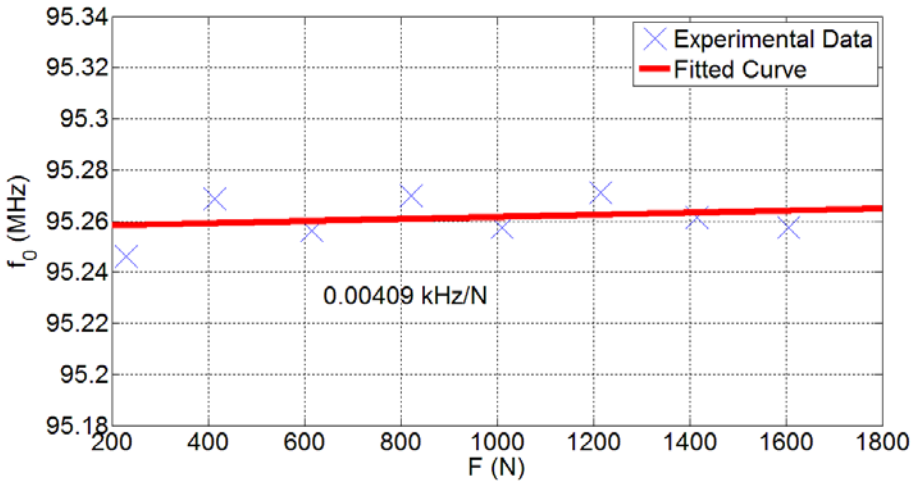


**Figure 6.3.65. Experimental measurement of our 0.8 cm × 0.8 cm nested metamaterial sensor on sheep's metatarsal without fracture.**

We demonstrate the experimental setup for sheep's femur in Fig. 6.3.66. The stainless steel plate is placed on the broken femur by surgery, and the sensor is attached to the stainless steel implant. There is thick soft tissue (almost 15 cm thick) in front of the femur. This case is similar to the *in vitro* experiments on wood test material with 20 cm thick soft tissue. However, in this case, we additionally put cast in front of the soft tissue. Similar to the *in vitro* experiments on wood test material, we succeeded in the observation of the strain telemetrically in sheep's femur as shown in Fig. 6.3.67.

**Figure 6.3.66. Experimental setup for sheep's femur.**

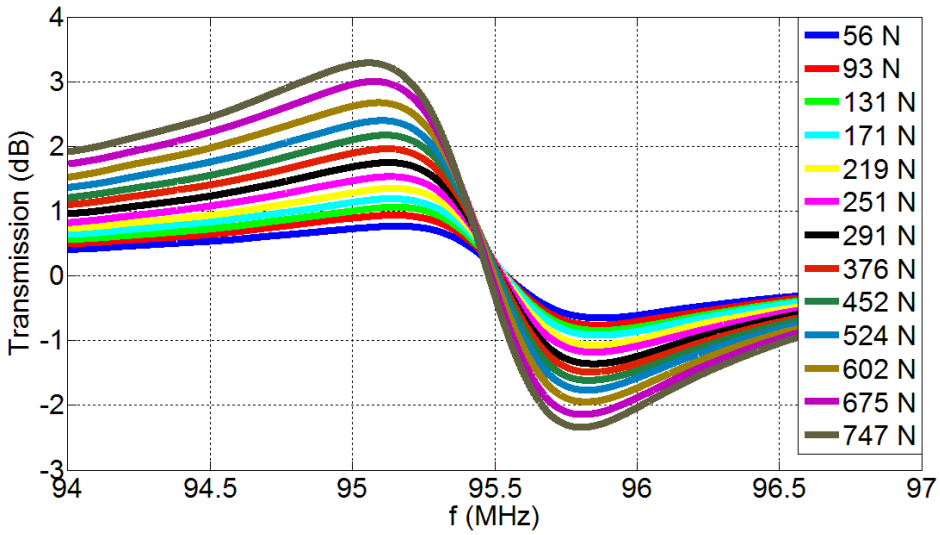


(a)

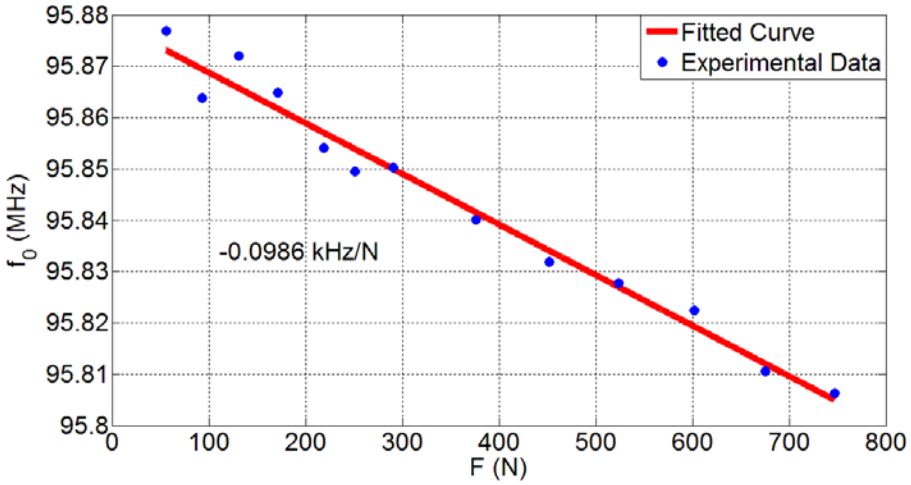


(b)

**Figure 6.3.67. Experimental measurement of our 0.8 cm × 0.8 cm nested metamaterial sensor on sheep's femur: (a) Transmission spectra and (b) F *vs.* $f_0$.**

We show the experimental setup for sheep's spine in Fig. 6.3.68. Different from metatarsal and femur, we apply moment to the spine in this case. Like metatarsal and femur, we are successful in monitoring strain telemetrically as depicted in Fig. 6.3.69. These experiments show that it is possible to monitor fracture healing in different parts of the body including spine by using our sensors.

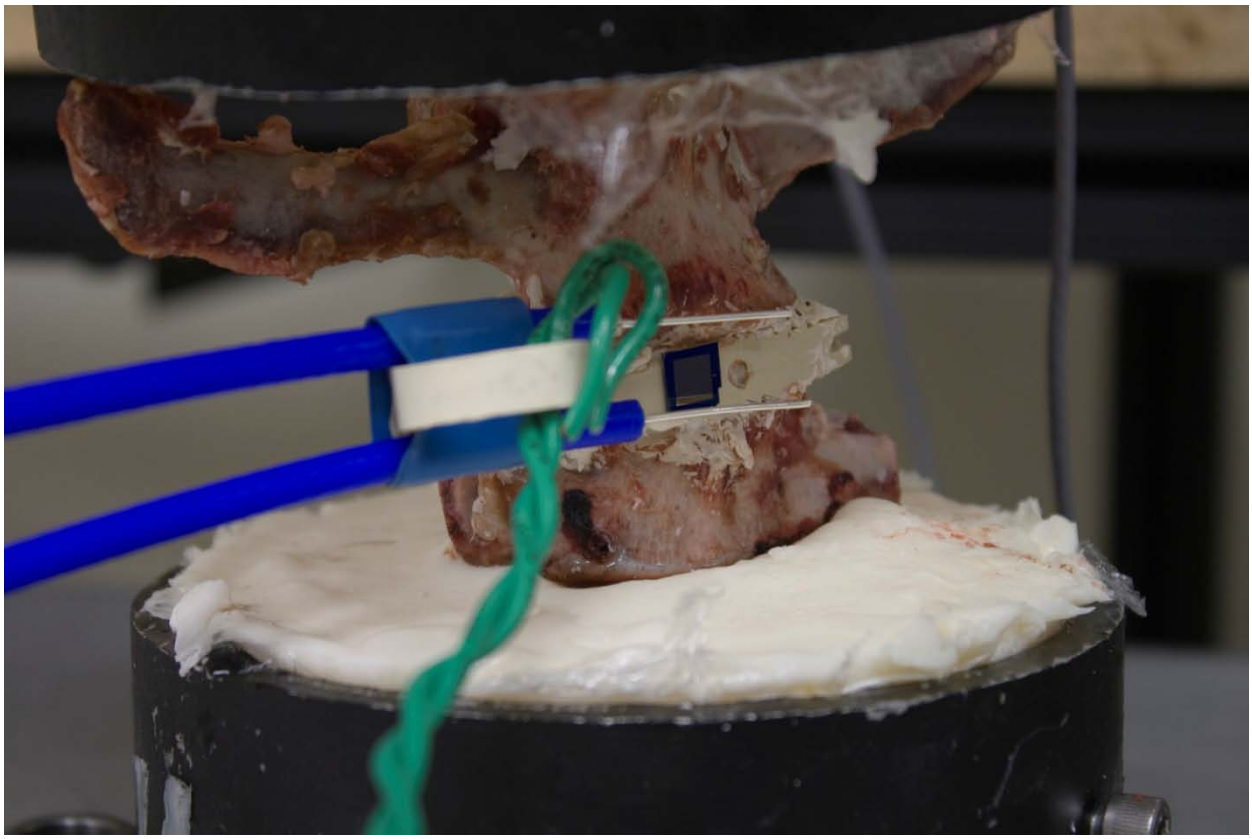

**Figure 6.3.68. Experimental setup for sheep's spine.**

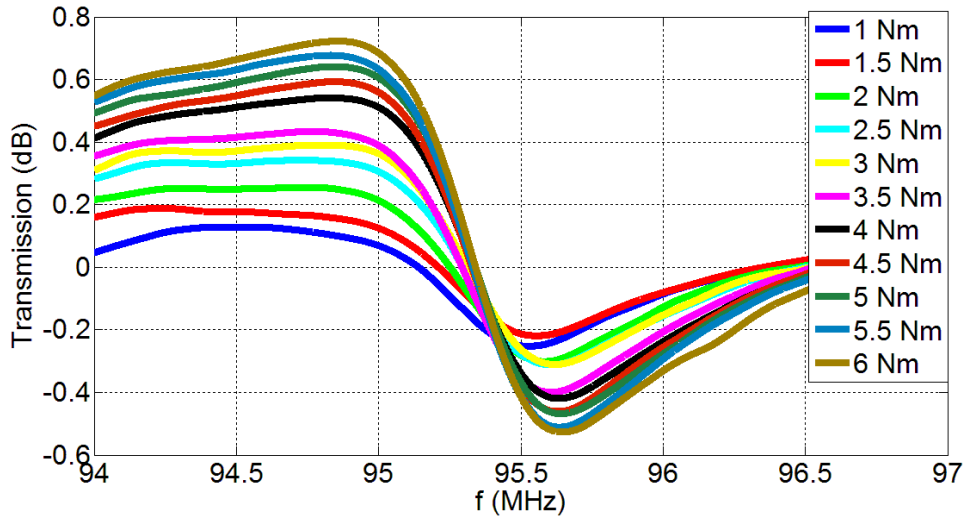


(a)

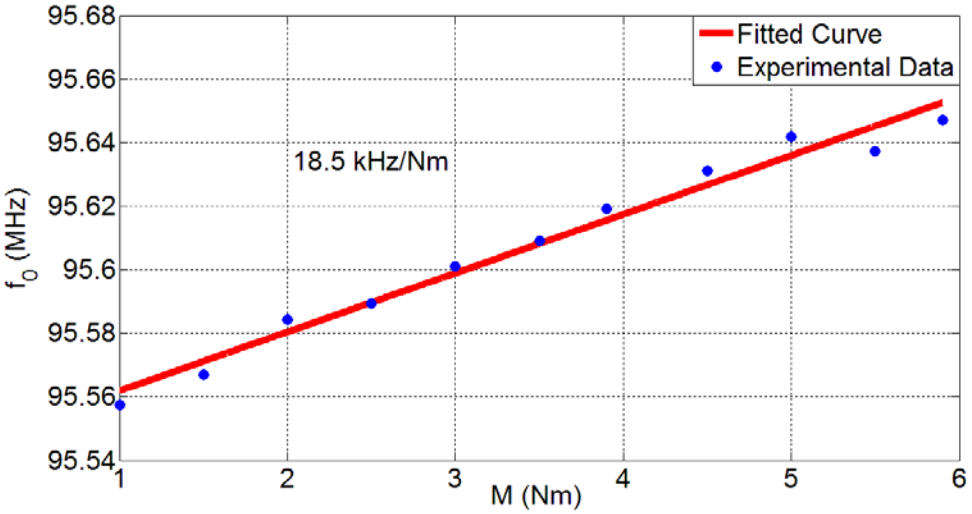


(b)

**Figure 6.3.69. Experimental measurement of our 0.8 cm × 0.8 cm nested metamaterial sensor on sheep's spine: (a) Transmission spectra and (b) M (moment) *vs.* $f_0$.**

Our sensor is also tested for mechanical hysteresis effect and is found to be sensitive enough that it can help to observe the hysteresis behavior on the implantable stick. Here we observe the hysteresis of the stainless steel plate on the femur in Fig. 6.3.70. From this figure, we again see that our sensor monitors strain in real time. If we change the applied load, the strain on the implantable plate changes in real time, and the transmission behavior of the sensor changes in response to the mechanical deformation. For example, if the applied strain increases in real time after a cycle of increasing and decreasing loads (where we gradually increase the load and then then gradually decrease the load and we complete a cycle when we reach the starting point), the response of the sensor also changes accordingly while going through the cycles.

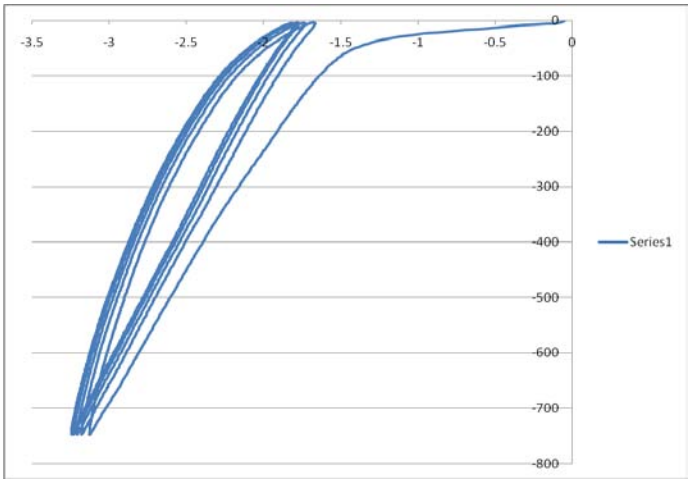


(a)

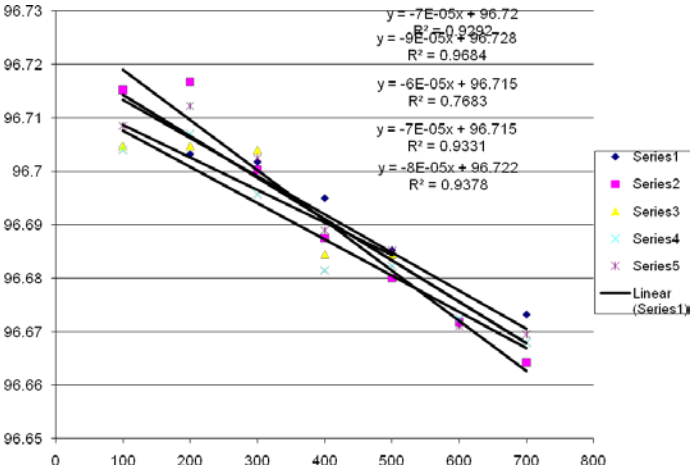


(b)

**Figure 6.3.70. Hysteresis behavior observed by our sensor: (a) Load cycles and (b) response of the sensor.**

We show the experimental setups from different angles in Fig. 6.3.71-6.3.74. The *ex vivo* experimental setup is pictured in Fig. 6.3.71. The metatarsal experiments is presented in Fig. 6.3.72, while Fig. 6.3.73 shows the femur experiments and Fig. 6.3.74 depicts the spine experiments.

(a)

(b)

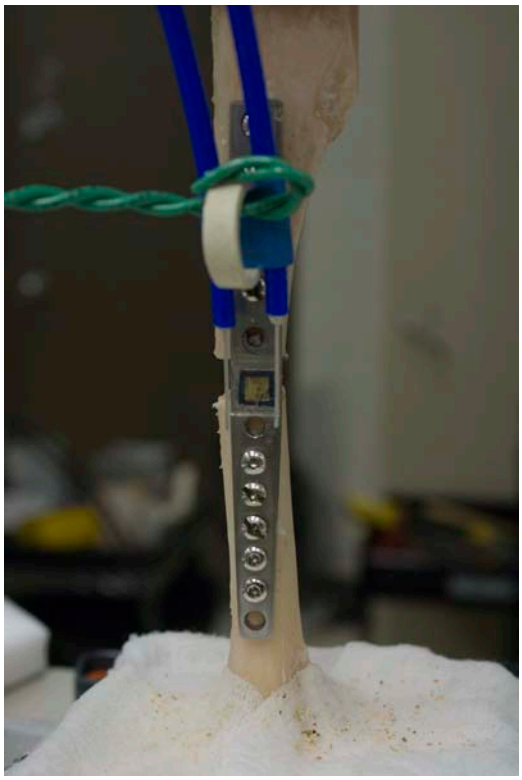

(c)

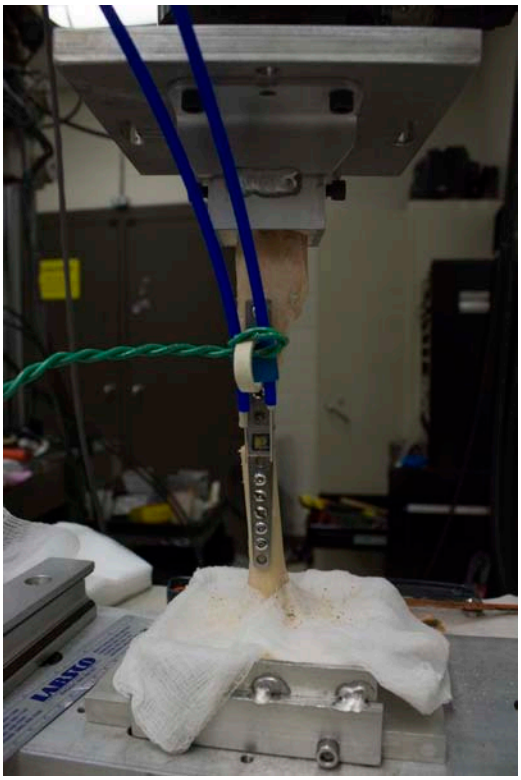

(d)

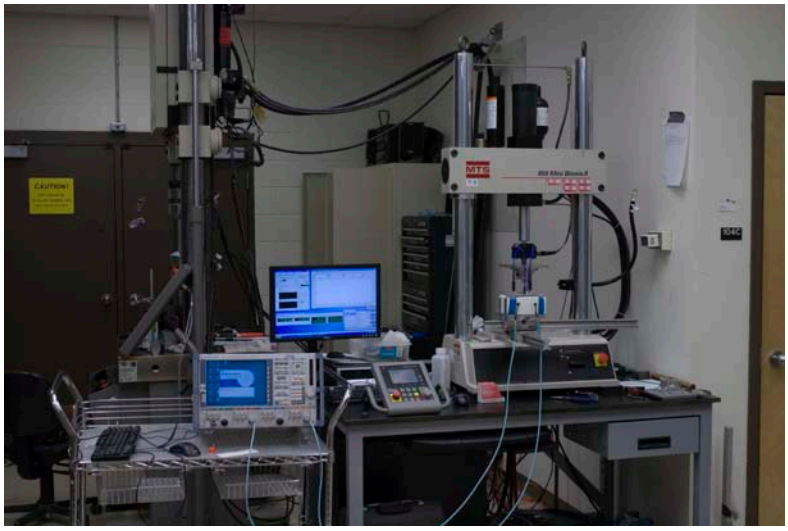

(e)

**Figure 6.3.71.** ***Ex vivo*** **experimental setup from different angles (a) – (e).**

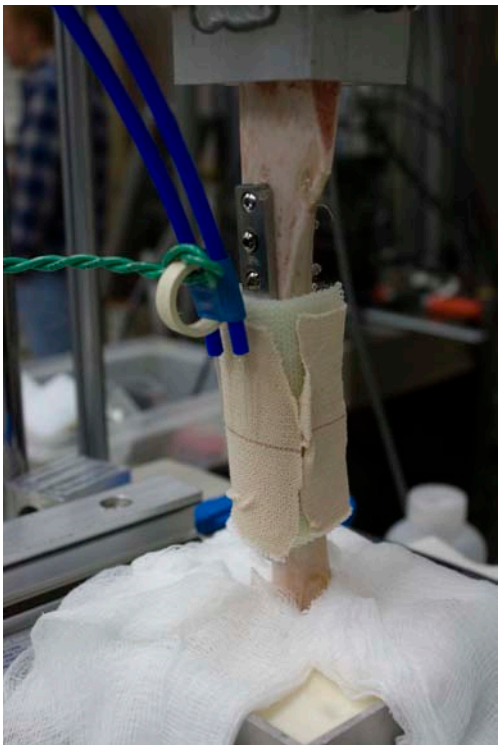

(a)

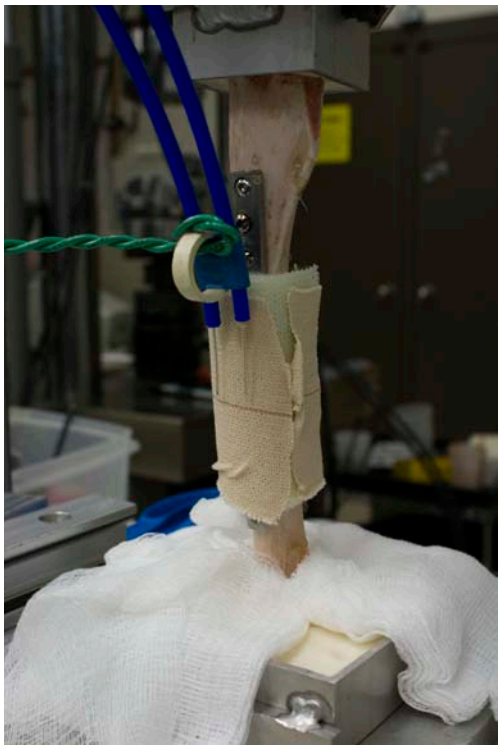

(b)

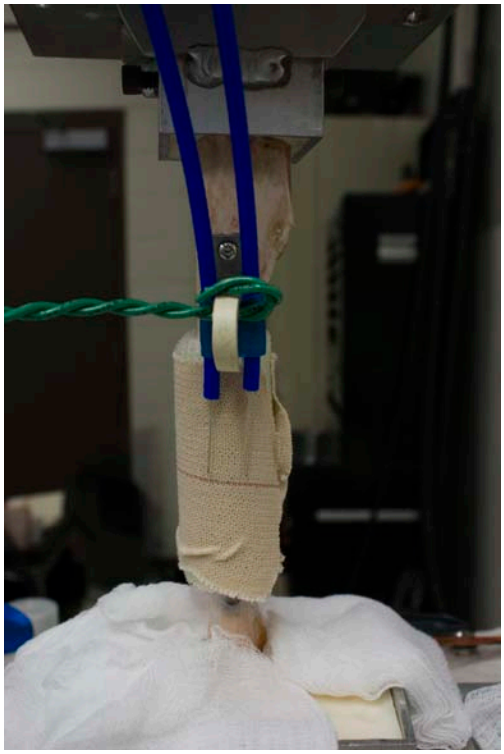

(c)

(d)

**Figure 6.3.72. Experimental setup for sheep's metatarsal experiments from different angles (a) – (d).**

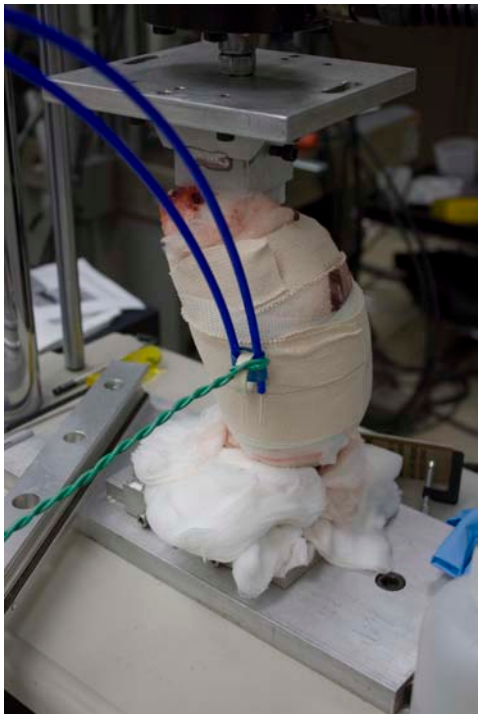

(a)

(b)

(c)

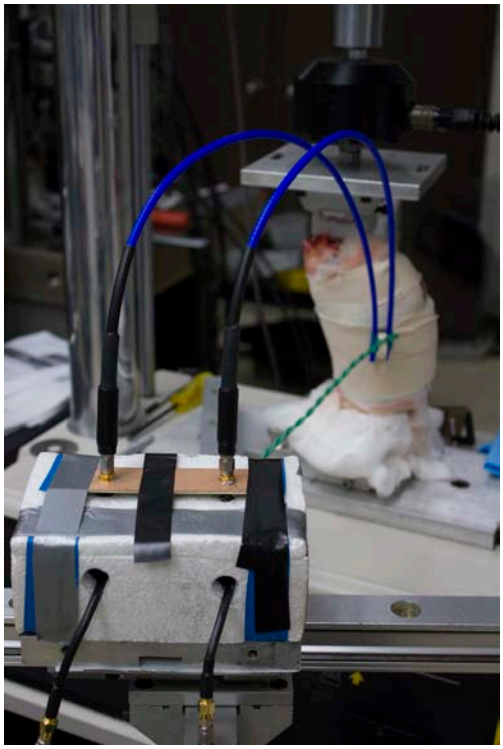

(d)

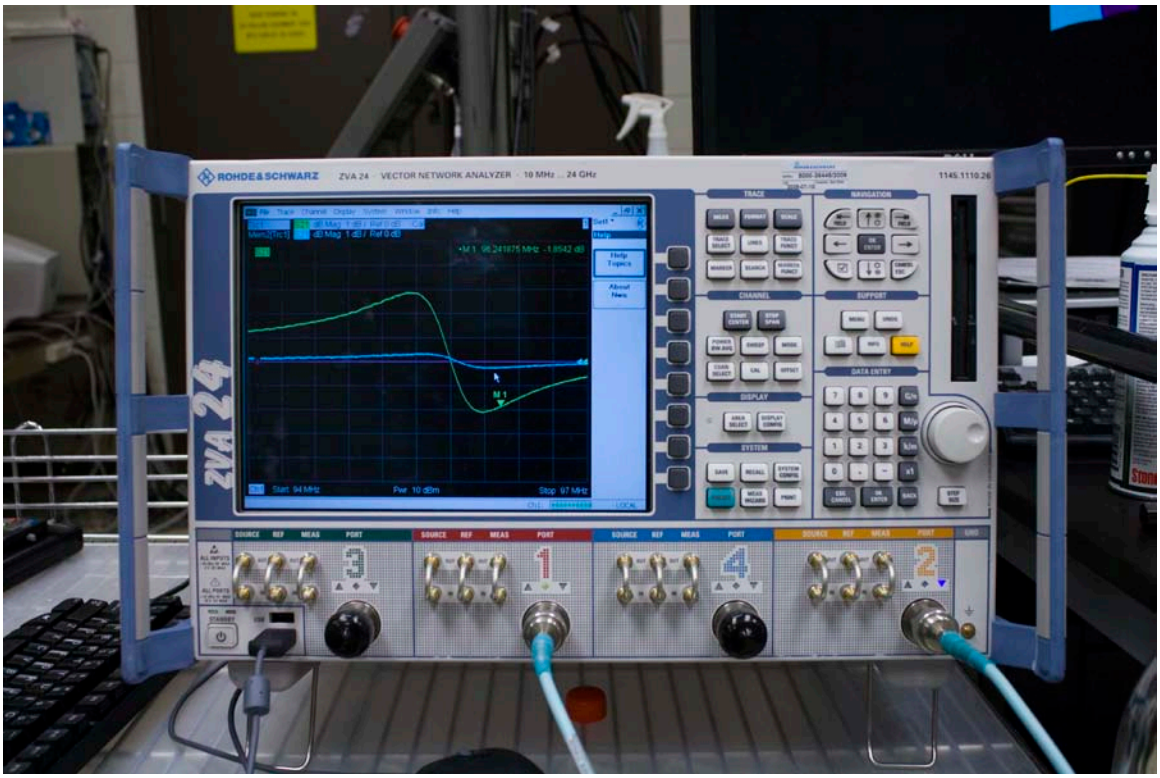
ROHDE&SCHWARZ
ZVA 24 · VECTOR NETWORK ANALYZER · 10 MHz ... 24 GHz
ZVA 24

(e)


Remote Station Control

(f)


-7.96 mm
-25.4353 N
14.18 N
-785.25 N
34.725 mm
-11.327 mm
DELL

(g)


(h)

**Figure 6.3.73. Experimental setup for sheep's femur experiments from different angles (a) – (h).**

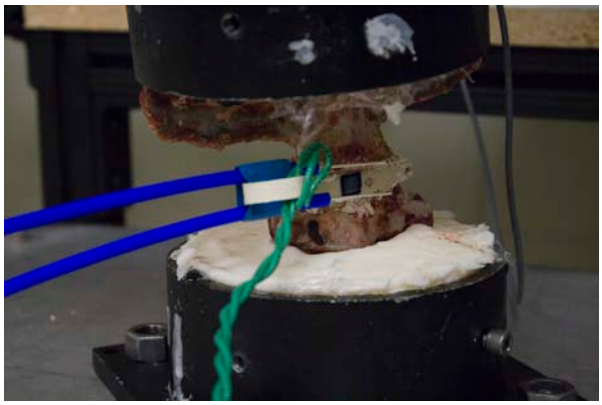

(a)

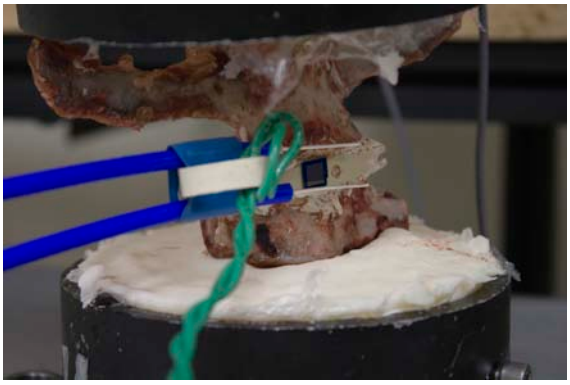

(b)

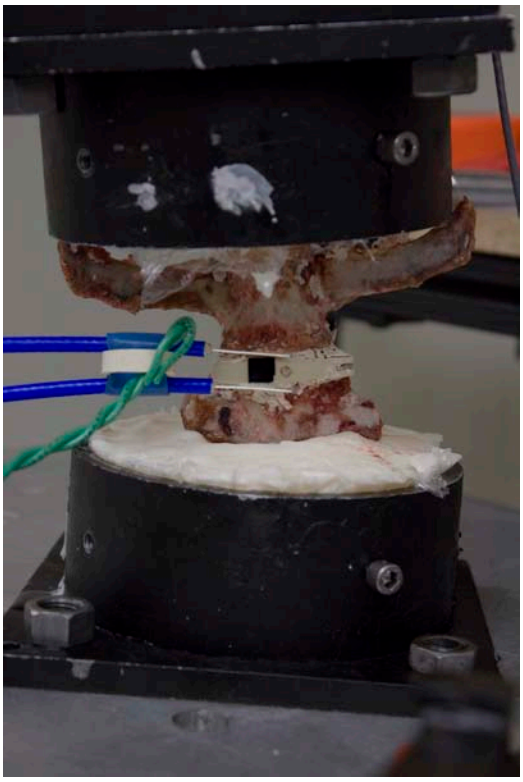

(c)

(d)

**Figure 6.3.74. Experimental setup for sheep's spine experiments from different angles (a) – (d).**

# Chapter 7

# Conclusion

In conclusion, we presented the conception, theoretical modeling, design, fabrication, and experimental characterization of our implantable RF-bioMEMS sensors to be implanted in human beings.

Because we intend to use these sensors in human body, we are limited with the available chip area of the sensors for implanting. Hence, we need to substantially miniaturize the sensors given their operating wavelength. In order to miniaturize the sensors, we first developed a new structural concept of high Q-factor on-chip resonators based on employing thin film capacitor of the chip; avoiding the need for using an external capacitor. We utilized this concept throughout the whole thesis (including the wireless devices at later stages as well); and designed and fabricated our first proof-of-concept wired sensors that rely on this architectural concept. We showed high Q-factor on-chip resonators at 7 GHz and at 15 GHz.

We applied external load to these on-chip resonators and observed the proof-of-concept demonstration of resonance frequency shift with mechanical deformation. We understood that

the shift is due to the change in the capacitance under mechanical loading. We then employed a circular geometry and increased the sensor performance, and then developed a suspended architecture and even further increased the performance of the sensors.

We also showed the proof of concept of fully telemetric sensing using spiral architecture. We examined single type, array type, hybrid array type, and multi-turn type spiral sensors and experimentally showed the importance of sensitivity, Q-factor and linearity for sensing operation, and the ways to increase sensitivity, Q-factor and linearity. We found out that the single-type sensor shows better sensitivity compared to array-type sensor because of its fewer structures on it. However, the array-type sensor represents smaller errors because it has more structures, which produces a higher Q-factor, higher SNR, and lower errors. By using hybrid array structures, we increased sensitivity and Q-factor, and decreased errors at the same time compared to single-type and array-type cases. The multi-turn spirals showed the best performance as sensors compared to the other spiral structure cases.

Subsequently, we designed and implemented wireless strain sensors of metamaterials for the first time, which opened up possibly a new direction for metamaterial applications. Metamaterials make better sensors compared to conventional RF structures (e.g., spiral coils) because of their unique structural properties (their splits). Because of these gaps in metamaterial structure, we obtain higher Q-factors, higher dips, higher sensitivities, better linearity, and lower resonance frequency per unit area compared to spiral coil structure. We also demonstrated flexible metamaterials, which outperform silicon-based metamaterials as wireless strain sensors. They can be used on non-flat surfaces and exhibit better linearity in sensing compared to silicon-based sensors. We also demonstrated metamaterial sensors serving for different test materials and showed that metamaterials exhibit the lowest *f vs. load* slope for the hardest material while it presents the highest slope for the softest one. Monitoring such an evolution of this slope for an implantable plate at different times potentially offers surgeons the ability to follow different phases of healing process remotely. We also made parametric study for understanding the sensing mechanism of metamaterials. We showed that the gaps of the metamaterials are very sensitive to the mechanical deformation. Changing the dimension of the gap significantly affects

the sensitivity. In addition to compressive force, we also applied tensile forces to metamaterials. Since the tensile force is opposite to the compressive force, the frequency shift under tension is opposite to that under compression. This proved that our metamaterial sensors are sensitive to the direction of the applied force.

We proposed and developed our novel structure of nested metamaterial, which outperforms classical metamaterials as wireless strain sensors. Since they have more gaps compared to classical metamaterial structure, they exhibit better linearity and lower resonance frequency per unit area. We achieved successful operation of nested metamaterial sensors using a 0.8 cm × 0.8 cm footprint operating at 100 MHz using silicon substrate and flexible substrate. Because of the architecture of the nested metamaterials, we easily tuned the operating frequency and decreased the electrical length of the sensor chip to $\lambda_o/400$. By decreasing the operating frequency to 100 MHz, we were able to achieve telemetric sensing across even up to 20 cm thick soft tissue. For the nested metamaterial case, flexible-based sensor outperformed silicon-based sensor since they exhibit better linearity in sensing compared to silicon-based sensors and they can additionally be used on non-flat surfaces. We also achieved successful operation of nested metamaterial sensors using 0.8 cm × 0.8 cm chip size in sheep's metatarsal, femur and spine. Our novel wireless RF-MEMS sensors hold great promise for applications in future healthcare (also for those other than monitoring fracture healing) and in other industries.

# BIBLIOGRAPHY


**[1]** K. Stoffel, K. Klaue and S. M. Perren, "Functional load of plates in fracture fixation in vivo and its correlate in bone healing," *Injury*, **31**, 37–50 (2000).

**[2]** J.D. Heckman and J. Sarasohn-Kahn, "The economics of treating tibia fractures. The cost of delayed unions," *Bulletin-Hospital for Joint Diseases*, **56**, 63-72 (1997).

**[3]** E.W. Lambert, R.B. Simpson, A. Marzouk, and D.V. Unger, "Orthopaedic injuries among survivors of USS COLE attack," *J Orthop Trauma*, **17**, 436-441 (2003).

**[4]** M.S. Gaston and A.H. Simpson, "Inhibition of fracture healing," *J Bone Joint Surg Br.*, **89**, 1553-1560 (2007).

**[5]** A.H. Simpson, T.N. Gardner, M. Evans, J. Kenwright, "Stiffness, strength and healing assessment in different bone fractures--a simple mathematical model," *Injury*, **31**, 777-781 (2000).

**[6]** J. Webb, G. Herling, T. Gardner, J. Kenwright, and A.H. Simpson, "Manual assessment of fracture stiffness," *Injury*, **27**, 319-320 (1996).

**[7]** G.M. Kotzar, D.T. Davy, J. Berilla, and V.M. Goldberg, "Torsional loads in the early postoperative period following total hip replacement," *J Orthop Res.*, **13**, 945-955 (1995).

**[8]** G.M. Kotzar, D.T. Davy, V.M. Goldberg, Heiple KG, J. Berilla, Jr. K.G. Heiple, R.H. Brown, and A.H. Burstein, "Telemeterized in vivo hip joint force data: a report on two patients after total hip surgery," *J Orthop Res.*, **9**, 621-633 (1991).

**[9]** D.T. Davy, G.M. Kotzar, R.H. Brown, K.G. Heiple, V.M. Goldberg, K.G. Heiple, J. Berilla, and A.H. Burstein , "Telemetric force measurements across the hip after total arthroplasty," *J Bone Joint Surg Am.*, **70**, 45-50 (1998).

**[10]** A. Rohlmann, F. Graichen, R. Kayser, A. Bender, and G. Bergmann, "Loads on a telemeterized vertebral body replacement measured in two patients," *Spine*, **33**, 1170-1179 (2008).

**[11]** A. Rohlmann, F. Graichen, and G. Bergmann, "Loads on an internal spinal fixation device during physical therapy," *Phys Ther.*, **82**, 44-52 (2002).

**[12]** A. Rohlmann, F. Graichen, U. Weber, and G. Bergmann, "2000 Volvo Award winner in biomechanical studies: Monitoring in vivo implant loads with a telemeterized internal spinal fixation device," *Spine*, **25**, 2981-2986 (2000).

**[13]** S.J. Taylor and P.S. Walker, "Forces and moments telemetered from two distal femoral replacements during various activities," *J Biomech*, **34**, 839-48 (2001).

**[14]** S.J. Taylor, P.S. Walker, J.S. Perry, S.R. Cannon, and R. Woledge, "The forces in the distal femur and the knee during walking and other activities measured by telemetry," *J Arthroplasty*, **13**, 428-437 (1998).

**[15]** R. Melik and H.V. Demir, "Implementation of High Quality-Factor On-Chip Tuned Microwave Resonators at 7 GHz," *Microwave and Optical Technology Letters,* **51,** 497-501 (2009).

**[16]** J. N. Burghartz, D. C. Edelstein, K. A. Jenkins, and Y. H. Kwark, "Spiral Inductors and Transmission Lines in Silicon Technology Using Copper–Damascene Interconnects and Low-Loss Substrates," *IEEE Transactions on Microwave Theory and Techniques*, **45,** 1961-1968 (1997).

**[17]** K. Okada, H. Sugawara, H. Ito, K. Itoi, M. Sato, H. Abe, T. Ito, and K. Masu, "On-Chip High-Q Variable Inductor Using Wafer-Level Chip-Scale Package Technology," *IEEE Transactions on Electron Devices*, **53,** 2401-2406 (2006).

**[18]** P. Wu and Z. Yu, "A Micromechanical High-Q Resonator Based on Hybrid Cavity," *Microwave Conference Proc.*, (Dec. 2005).

**[19]** I. Bahl, "Lumped Elements for RF and Microwave Circuits," *London: Artech Hous*e, (2003).

**[20]** C. A. Tavernier, R. M. Henderson, and J. Papapolymerou, "A Hybrid Micromachined High - Q Cavity Resonator at 5.8 GHz," *Proc. of the 30th European Microwave Conference*, (Oct. 2000).

**[21]** H.-ju Hsu, M. J. Hill, R. W. Ziolkowski, and J. Papapolymerou, "A Duroid-Based Planar EBG Cavity Resonator Filter With Improved Quality Factor," *IEEE Antennas and Wireless Propagation Letters*, **1**, 67-70 (2002).

**[22]** D. M. Pozar, "Microwave Engineering," *New York: John Wiley and Sons*, (2005).

**[23]** Y.K. Koutsoyannopoulos and Y. Papananos, "Systematic Analysis and Modeling of Integrated Inductors and Transformers in RF IC Design", *IEEE Transactions on Circuits and Systems*, **47**, 699-713 (2000).

**[24]** J. R. Long and M. A. Copeland, "The Modeling, Characterization, and Design of Monolithic Inductors for Silicon RF IC's," *IEEE Journal of Solid-State Circuits*, **32**, 357-369 (1997).

**[25]** C.P. Yue, C. Ryu, J. Lau, T.H. Lee, and S.S. Wong, "A Physical Model for Planar Spiral Inductors on Silicon," *IEEE International Electron Device Meeting*, (Dec. 1996)

**[26]** R. Ludwig, and P. Bretchko, "RF Circuit Design," *New Jersey: Prentice Hall*, (2000).

**[27]** H. M. Greenhouse, "Design of Planar Rectangular Microelectronic Inductors," *IEEE Transactions on Parts, Hybrids and Packaging*, **10**, 101-109 (1974).

**[28]** T. H. Lee, "The Design of CMOS Radio-Frequency Integrated Circuits," *New York: Cambridge University Press*, (1998).

**[29]** A. Zolfaghari, A. Chan, and B. Razavi, "Stacked Inductors and Transformers in CMOS Technology," *IEEE Journal of Solid-State Circuits*, **36**, 620-628 (2001).

**[30]** C.P. Yue and S. S. Wong, "On-Chip Spiral Inductors with Patterned Ground Shields for Si-Based RF IC's," *IEEE Journal of Solid-State Circuits*, **33**, 743-752 (1998).

**[31]** R. Melik, N.K. Perkgoz, E. Unal, Z. Dilli and H.V. Demir, "Design and Realization of a Fully On-Chip High-Q Resonator at 15 GHz on Silicon," *IEEE Transactions on Electron Devices*, **55,** 3459-3466 (2008).

**[32]** C. A. Tavernier, R. M. Henderson, and J. Papapolymerou, "A Reduced-Size Silicon Micromachined High-Q Resonator at 5.7 GHz," *IEEE Trans. Microwave Theory & Tech.*, **50,** 2305-2314 (2002).

**[33]** C. C. Tang, C.H. Wu, and S.I. Liu, "Miniature 3-D inductors in standard CMOS process," *IEEE Journal of Solid-State Circuits*, **37,** 471-480 (2002).

**[34]** W. Y. Yin, S. J. Pan, and L. W. Li, "Double-level spiral inductors with multiple-via interconnects on GaAs substrates," *IEEE Transaction on Magnetics*, **40,** 1756-1758 (2004).

**[35]** W. Y. Yin, S. J. Pan, and L. W. Li, "Comparative characteristics of on-chip single- and double-level square inductors," *IEEE Transaction on Magnetics,* **39,** 1778-1783 (2003).

**[36]** W. Y. Yin, S. J. Pan, L. W. Li, and Y. B. Gan, "Experimental characterization of coupling effects between two on-chip neighboring square inductors," *IEEE Transactions on Electromagnetic Compatibility,* **45,** 557-561 (2003).

**[37]** M. Park, S. Lee, C. S. Kim, H. K. Yu, and K. S. Nam, "The Detailed Analysis of High CMOS-Compatible Microwave Spiral Inductors in Silicon Technology," *IEEE Transactions on Electron Devices,* **45**, 1953-1959 (1998).

**[38]** R.E. Collin, "Foundations for Microwave Engineering," *New York: McGraw Hill,* (1992).

**[39]** R. Melik, N.K. Perkgoz, E. Unal, C.M. Puttlitz, and H.V. Demir, "Bioimplantable passive on-chip RF-MEMS strain sensing resonators for orthopeadic applications," *Journal of Micromechanics and Microengineering, **18,** 115017 (2008).*

**[40]** K.V. Schuylenbergh, R. Puers, F. Rodes, F. Burny, M. Donkenvolcke, and F. Moulart, "Monitoring orthopaedic implants using active telemetry," *Proceedings of the Annual International Conference of the IEEE,* **6**, 2672-2673 (1992).

**[41]** T.A. Einhorn, "Enhancement of fracture healing," *Journal of Bone and Joint Surgery*, **77,** 940-956 (1995).

**[42]** A.C.R. Grayson, R.S. Shawgo, A.M. Johnson, N.T. Flynn, Y. Li, M.J. Cima, and R.A. Langer, "BioMEMS review: MEMS technology for physiologically integrated devices," *Proceedings of the IEEE,* **92,** 6-21 (2004).

**[43]** R.N. Simons and F.A. Miranda, "Radiation characteristics of miniature silicon square spiral chip antenna for implantable bio-MEMS sensors," *Antennas and Propagation Society International Symposium, IEEE,* **1B**, 836-839 (2005).

**[44]** R.N. Simons, D.G. Hall, and F.A. Miranda, "RF Telemetry System for an Implantable Bio-MEMS Sensor," *IEEE MTT-S Inter. Microwave Symp. Digest,* **3,** 1433-1436 (2004).

**[45]** R.N. Simons, D.G. Hall, and F.A. Miranda, "Spiral Chip Implantable Radiator and Printed Loop External Receptor for RF Telemetry in Bio-Sensor Systems," *Radio and Wireless Conference, IEEE,* (2004).

**[46]** F.A. Miranda, R.N. Simons, and D.G. Hall, "Validation of Radio Frequency Telemetry Concept in the Presence of Biological Tissue-Like Stratified Media" *IEEE Antennas and Propagation Society Inter. Symp. Digest*, **2,** 1335-1338 (2004).

**[47]** R.N. Simons and F.A. Miranda, "Radio Frequency Telemetry System for Sensors and Actuators," *U.S. Patent* **6667725 (**2003).

**[48]** S.D. Senturia, "Microsystem Design," *Kluwer Academic publishers*, (2001).

**[49]** R. Melik, E. Unal,N. K. Perkgoz, C.M. Puttlitz, and H. V. Demir, "Circular High-Q Resonating Isotropic Strain Sensors with Large Shift of Resonance Frequency under Stress," *Sensors*, **9**, 9444-9451 (2009).

**[50]** M. Suster, J. Guo, N. Chaimanonart, W.H. Ko, and D.J. Young, "Low-noise CMOS integrated sensing electronics for capacitive MEMS strain sensors," *Proceedings of the IEEE 2004 Custom Integrated Circuits Conference*, Orlando, FL, USA (October, 2004).

**[51]** K.E. Wojciechowski, B.E. Boser, and A.P. Pisano, "A MEMS resonant strain sensor with 33 nano-strain resolution in a 10 kHz bandwidth," *Proceedings of 2005 IEEE Sensors*, Irvine, CA, USA (October 30–November 3, 2005).

**[52]** R. Melik, E. Unal, N. K. Perkgoz, C.M. Puttlitz, and H. V. Demir, "RF-MEMS Load Sensor with Enhanced Q-factor and Sensitivity in a Suspended Architecture", in review.

**[53]** M. Ahmadian, B.W. Flynn, A.F. Murray, and D.R.S. Cumming, "Miniature Transmitter for Implantable Micro Systems," *Proc. of the 25th Annual Inter. Conf. of the IEEE Engineering in Medicine and Biology Society*,**4**, 3028-3031, Cancun, Mexico (Sept. 17-21, 2003).

**[54]** S. Ullerich, W. Mokwa, G. V. Bogel, and U. Schnakenberg, "Micro Coils for an Advanced System for Measuring Intraocular Pressure," *Proc. of The 1st Annual Inter. IEEE-EMBS Special Topic Conf. on Microtechnologies in Medicine And Biology*, (2000).

**[55]** W. Mokwa, "Ophthalmic Implants," *Proc. of the 2nd IEEE Inter. Conf. on Sensors*, (2003).

**[56]** T. Akin, K. Najafi, and R.M. Bradley, "An Implantable Multichannel Digital Neural Recording System for a Micromachined Sieve Electrode," *IEEE Jour. Solid-State Circuits*, **33**, 109-118 (1998).

**[57]** R. Melik, E. Unal, C.M. Puttlitz, and H. V. Demir, "Wireless Bio-implantable RF-MEMS strain sensors", submitted.

**[58]** R. Melik, E. Unal, N. K. Perkgoz, C. Puttlitz and H. V. Demir, "Metamaterial-based wireless strain sensors," *Applied Physics Letters*, **95**, *011106 (2009)*.

**[59]** R. Park and T. Paulay, "Reinforced Concrete Structures," *John Wiley & Sons, NY*, (1975).

**[60]** A. Ghali and R. Favre, "Concrete Structures: Stresses and Deformations," *E & FN Spon, London*, (1994).

**[61]** W. E. Kock, "Metal-lens antennas," *IRE Proc.*, **34,** 828-836 (1946).

**[62]** V. G. Veselago, "The electrodynamics of substances with simultaneously negative values of ε and μ," *Usp. Fiz. Nauk*, **92**, 517–526 (1967).

**[63]** J. B. Pendry, A. J. Holden, W. J. Stewan and I. Younes, "Extremely Low Frequency Plasmons in Metallic Mesostructures," *Phys. Rev. Letters*, **76**, 4473-4776 (1996).

**[64]** R. M. Walser, "Introduction to Complex Mediums for Electromagnetics and Optics," *SPIE Press, Bellingham, WA, USA*, (2003).

**[65]** D. R. Smith, "The reality of negative refraction," *Physics World*, **16**, 23 (2003).

**[66]** D. R. Smith, J. B. Pendry and M. C. K. Wiltshire, "Metamaterials and negative refractive index," *Science*, **305**, 788-792 (2004).

**[67]** U. K. Chettiar, S. Xiao, A. V. Kildishev, W. Cai, H.-K. Yuan, V. P. Drachev, and V. M. Shalaev, "Optical metamagnetism and negative index metamaterials," *MRS Bulletin*, **33**, 921-926 (2008).

**[68]** W. Cai, U. K. Chettiar, A. V. Kildishev, and V. M. Shalaev, "Optical cloaking with metamaterials," *Nature Photonics*, **1**, 224-227 (2007).

**[69]** D. R. Smith, "How to build a superlens," *Science*, **308**, 502-503 (2005).

**[70]** K. B. Alici and E. Ozbay, "Electrically small split ring resonator antennas," *J. Appl. Phys*, **101**, 083104 (2007).

**[71]** V. A. Podolskiy, A. K. Sarychev, V. M. Shalaev, "Plasmon modes in metal nanowires and left-handed materials" *J. of Nonlinear Optical Physics and Materials*, **11**, 3, 65-74 (2002).

**[72]** M. S. Rill, C. Plet, M. Thiel, I. Staude, G. von Freymann, S. Linden, and M. Wegener, "Photonic metamaterials by direct laser writing and silver chemical vapour deposition," *Nature Mater*, **7**, 543-546 (2008).

**[73]** J. B. Pendry and S. A. Ramakrishna, "Focusing light using negative refraction," *J. Phys. [Condensed Matter]*, **15**, 6345-64 (2003).

**[74]** R. Melik, E. Unal, N. K. Perkgoz, C.M. Puttlitz, and H. V. Demir, "Flexible Metamaterials for Wireless Strain Sensing," *Applied Physics Letters*, **95**, 181105 (2009).

**[75]** R. Melik, E. Unal, N. K. Perkgoz, B. Santoni, D. Kamstock, C.M. Puttlitz, and H. V. Demir, "Nested Metamaterials for Wireless Strain Sensing," *IEEE Journal of Selected Topics in Quantum Electronics*, **16**, 450-458 (2010).

**[76]** J. B. Pendry, A. J. Holden, D. J. Robbins, and W. J. Stewart, "Low frequency plasmons in thin-wire structures," *J. Phys.: Condens. Matter*, **10**, 4785-4809 (1998).

**[77]** X. Wang, D.-H. Kwon, D.H. Werner, and I.-C. Khoo, A.V. Kildishev, and V.M. Shalaev, "Tunable optical negative-index metamaterials employing anisotropic liquid crystals,"*Appl. Phys. Lett.*, **91**, 143122 (2007).

**[78]** J. B. Pendry, "Negative Refraction Makes a Perfect Lens," *Phys. Rev. Lett.*, **85**, 3966-3969 (2000).

**[79]** Z. W. Liu, N. Fang, T. J. Yen, X. Zhang, "Rapid Growth of Evanescent Wave with a Silver Superlens," *Appl. Phys. Lett.*, **83**, 5184 (2003).

**[80]** D. Schurig, J. J. Mock, B. J. Justice, S. A. Cummer, J. B. Pendry, A. F. Starr, D. R. Smith, "Metamaterial Electromagnetic Cloak at Microwave Frequencies," *Science*, **314**, 977-980 (2006).

**[81]** D. J. Quinn, "Microstructure, residual stress, and mechanical properties of thin film materials for a microfabricated solid oxide fuel cell," *M.S. thesis, Massachusetts Institute of Technology*, (2006).

**[82]** See EPAPS supplementary material at http://dx.doi.org/10.1063/1.3250175 for errors of silicon-based sensor and tape-based flexible sensor in terms of percentage.

**[83]** R. Melik, E.Unal, N. K. Perkgoz, C. Puttlitz, and H. V. Demir, "Metamaterial based telemetric strain sensing in different materials," *Optics Express*, **18**, 5000-5007 (2010).

**[84]** H. Chen, B.-I. Wu, B. Zhang, and J. A. Kong1, "Electromagnetic wave interactions with a metamaterial cloak," *Physical Review Letters*, **99**, 063903 (2007).

**[85]** R. A. Shelby, D. R. Smith, and S. Schultz, "Experimental verification of a negative index of refraction," *Science*, **292**, 77-79 (2001).

**[86]** S. Zhang, W. Fan, B. K. Minhas, A. Frauenglass, K. J. Malloy, and S. R. J. Brueck, "Mid-infrared resonant magnetic nanostructures exhibiting a negative permeability," *Physical Review Letters*, **94**, 037402 (2005).

**[87]** V.M. Shalaev, "Optical negative-index metamaterials", *Nature Photonics*, **1**, 41-48 (2007).

**[88]** C. G. Parazzoli, R. B. Greegor, K. Li, B. E. C. Koltenbah, and M. Tanielian, "Experimental Verification and Simulation of Negative Index of Refraction Using Snell's Law," *Physical Review Letters*, **90**, 107401 (2003).

**[89]** J. D. Wilson, and Z. D. Schwartz, "Multifocal flat lens with left-handed metamaterial," *Applied Physics Letters*, **86**, 021113 (2005).

**[90]** A. Salandrino, and N. Engheta, "Far-field subdiffraction optical microscopy using metamaterial crystals: Theory and simulations," *Physical Review B*, **74**, 075103 (2006).

**[91]** G. Dolling, C. Enkrich, M. Wegener, C. M. Soukoulis, and S. Linden, "Simultaneous negative phase and group velocity of light in a metamaterial," *Science*, **312**, 892-894 (2006).

**[92]** http://www.mathweb.com

**[93]** V.M. Shalaev, W. Cai, U.K. Chettiar, H.-K. Yuan, A.K. Sarychev, V.P. Drachev, and A.V. Kildishev, "Negative index of refraction in optical metamaterials," *Optics Letters*, **30**, 3356-3358 (2005).

**[94]** http://news.bbc.co.uk/1/hi/sci/tech/5016068.stm

**[95]** http://niremf.ifac.cnr.it/tissprop/htmlclie/htmlclie.htm

**[96]** P.G. Balmaz and O.J.F. Martin, "Electromagnetic resonances in individual and coupled split-ring resonators," *Journal of Applied Physics*, **92**, 2929-2936 (2002).

**[97]** C. A. Balanis, "Antenna Theory," *John Wiley & Sons, 3rd Edition*, (2005).

**[98]** C. A. Balanis, "Advanced Engineering Electromagnetics," *John Wiley & Sons*, (1989).

**[99]** H.V.Demir, R. Melik, and C. M. Puttlitz, "Bioimplant strain sensors," US patent pending.